Title
Mass-Transport Phenomena in Fuel-Cell Membranes and Catalyst Layers

Author
Petrovick, John G.

Publication Date
2023

Peer reviewed|Thesis/dissertation

Mass-Transport Phenomena in Fuel-Cell Membranes and Catalyst Layers

By

John George Petrovick III

A dissertation submitted in partial satisfaction of the

requirements for the degree of

Doctor of Philosophy

in

Chemical Engineering

in the

Graduate Division

of the

University of California, Berkeley

Committee in charge:

Dr. Adam Z. Weber, Co-Chair
Professor Clayton J. Radke, Co-Chair
Professor Alexis T. Bell
Professor Philip S. Marcus

Summer 2023

Abstract

Mass-Transport Phenomena in Fuel-Cell Membranes and Catalyst Layers

by

John George Petrovick III

Doctor of Philosophy in Chemical Engineering

University of California, Berkeley

Dr. Adam Z. Weber, Co-Chair
Professor Clayton J. Radke, Co-Chair

Fuel cells are a next-generation, clean energy-conversion technology designed to replace existing internal combustion engines. Their implementation is important in reducing carbon emissions and addressing the world climate crisis. However, many system limitations still need to be resolved before fuel cells can enter widespread use, particularly with regard to transport of chemical species within the fuel cell. Fuel cells are composed of several key components, but paramount among them are the fuel-cell catalyst layers, responsible for the fuel-cell reactions that produce electricity, and the fuel-cell membrane, responsible for transporting ions within the system. Transport of chemical species is irrevocably tied to the performance of each component. Improving fuel-cell efficiency by minimizing gas crossover requires understanding gas transport within fuel-cell membranes. Addressing the issue of fuel-cell flooding and the associated reduction in performance requires study of water transport within the membranes, as well as gas transport within the catalyst layers. This dissertation studies these phenomena and provides guidance on proper measurement techniques as well as the transport properties of current state-of-the-art materials.

Following an Introduction in Chapter 1, the dissertation begins with a detailed examination of the use of microelectrodes to study the properties of fuel-cell membranes, particularly gas transport. There is an extensive history of using microelectrodes to study fuel-cell membranes *ex-situ*, but little standardization of cell design and technique. Different designs available in the literature are discussed as are the results of prior studies. Author recommendations are made for proper use of microelectrode systems to ensure consistent experimental results. Then, a new flow-through microelectrode cell design that ameliorates several of the key issues with prior designs, such as equilibration time, is presented. The cell design is evaluated in several ways, including the impact of applied mechanical pressure, impact of gas flowrate, ability to measure both hydrogen oxidation and oxygen reduction, and minimization of equilibration time. Chapter 2 thus provides a foundation for the study of membrane transport properties in the next two chapters.

Chapter 3 provides a comprehensive examination of measuring gas transport using a microelectrode system. The flowthrough cell discussed in Chapter 2 measures the diffusivity,

Henry's constant, and permeability of Nafion and Nafion XL to hydrogen and oxygen gas as a function of water content. Flaws with the existing analytical solutions for analyzing current transients in these systems are discussed, and a 2D numerical model is developed to account accurately for the finite membrane thickness. In addition, the impact of surface roughness at very short times (< 1 s) is quantified and included in the analysis. Finally, a simple multiphase parallel-diffusion model interprets the measured gas-transport parameters. Hydrogen has a higher diffusivity and permeability than does oxygen, but a lower Henry's constant. Diffusivity and permeability both increase with water content whereas Henry's constant decreases. This is due to the impact of the hydrophilic phase, as both gases have a higher diffusion coefficient and lower Henry's constant in the hydrophilic phase compared to the hydrophobic polymer backbone. The parameters presented in Chapter 3 allow for a more accurate picture of gas crossover within fuel cells and assist in creating accurate models of this phenomenon.

Electro-osmosis, or coupled ion-water transport, in fuel-cell membranes is the focus of Chapter 4. Once again, the microelectrode cell described in Chapter 2 studies this effect, in both proton- and anion-exchange membranes. Electro-osmosis is examined by measuring the open-circuit voltage as the relative humidity changes within the cell. The necessary background in thermodynamics and transport phenomena is provided to interpret the experimental data. A Nafion membrane is the baseline case and exhibits a higher water transport number than previously reported. However, more focus is given to the measurement of electro-osmosis in anion-exchange membranes. Anion type in the anion-exchange membrane is studied; it is found that the solvation shell of the ions has a significant effect on the measured water transport number, consistent with studies in Nafion. The larger is the solvation shell, the higher is the measured coefficient. Essentially, ions primarily move the water that is directly associated with them. In addition, temperature has little impact on the water transport number in anion-exchange membranes. Finally, a Stefan-Maxwell-Onsager framework and the measured water transport number of Versogen is used to extract the water permeability as a function of water content. Permeability tends to increase with water content, as it is easier for water to move through the membrane when more water is present. Chapter 4 presents all of the water transport parameters necessary to define fully the water balance in fuel-cell membranes.

Chapter 5 studies the impact of water droplet growth on platinum catalyst particles within the catalyst layer and whether the transport of oxygen gas to the platinum catalyst is inhibited by drop growth. A moving-mesh numerical model is developed to study this droplet growth. The Navier-Stokes equation captures convection within the water droplet, and Fick's law models oxygen transport within the expanding drop. Tafel kinetics quantifies the current at the platinum surface. Four different cases are considered: growth of a pinned and advancing drop on a bare platinum surface, growth of an advancing drop on a thin layer of Nafion, and growth of a water layer within a carbon nanopore. In all cases, water droplet growth does not inhibit oxygen transport due to a funneling effect, where the larger gas/water interface compensates for the increasing diffusion length as the drop grows. In the Nafion-layer case, the Nafion membrane is much more mass-transfer resistive than is the droplet, minimizing the impact of the droplet if the platinum is covered in Nafion. In the carbon nanopore, the produced water layer can become limiting, but only at pore lengths much larger than is typically found in porous carbon particles. The formation of local water droplets is thus not mass-transfer limiting in the catalyst layer. Catalyst-layer design should instead focus on reducing the impact of full catalyst-layer flooding

or the placement of platinum within the catalyst layer rather than focusing on the formation of water nanodroplets.

Overall, this dissertation explores how a microelectrode cell can be used to ascertain critical membrane transport properties including how system geometry plays a key role in the proper measurement of transport properties. The findings quantify the importance of water content on transport properties and how it is the most powerful variable controlling them. Proposed future work includes extending the study to gas transport in novel ion-conducting polymers (ionomers), examining gas and water transport in ionomer thin films, and modeling local bubble growth on platinum nanoparticles in electrolyzer catalyst layers.

To my parents, for their unwavering support throughout my graduate school career.

Contents

List of Figures

List of Tables

Acknowledgements

Completing a PhD thesis is hard, and I received help from so many people along the way. From those directly involved in my research to those that kept me sane, it would not have been possible without you all.

First, I would like to thank my advisers, Adam Weber and Clay Radke. None of this work would have been possible without their guidance, mentorship, and support, and I am confident that I am leaving Berkeley a better scientist and a better person due in no small part to our work together. I will miss the research and hard science we tackled together, but I will also miss the small moments – chatting with Adam in the office in between his endless meetings, listening to Clay's stories in our weekly meetings. Thank you again for your support on this journey.

The camaraderie of the Weber lab, and my interactions with group members past and present, was essential to learning as much as I did and becoming the scientist I am today, and I made many wonderful friends in the group. There are almost too many people to list – Andy Crothers and Pete Dudenas, your mentorship when I first joined the lab set the culture and how grad students should interact. Meron Tesfaye, for introducing me to microelectrodes, casting, and the joys of thin films. Yagya Regmi and Mike Gerhardt, thank you for always being willing to listen when I needed to talk, and for teaching me the basics of experiments and modeling. Priyam, thank you for discussing Stefan-Maxwell-Onsager theory, and its many equations and complexities, whenever I asked. Ahmet Kusoglu, thank you for the many coffee chats and "working" discussions. Philomena Weng, thank you for being the best North Berkeley shuttle buddy I could have asked for.

Those who worked with me on the joys, trials, and tribulations of microelectrodes deserve a special shoutout. Thank you, Nem Danilovic, for training me in electrochemistry when I first joined the group, helping tremendously with the experimental aspects of microelectrodes, and being a great mentor to me when I needed it. Doug Kushner – thank you for everything, from the coffee chats to the troubleshooting to the microelectrode cell design and fabrication, and everything in-between. It is no understatement that this PhD would not have been completed without your assistance. And finally, Grace Anderson – my microelectrode partner-in-crime, my troubleshooting confidant, and my great friend. I cannot imagine working on microelectrodes without you.

To (some of) the fantastic friends I made in the group: Claire Arthurs, from desk mate to office mate to cubicle mate, thank you for the happy hours, the hangouts, and for being an overall great friend. Hailey Boyer, I will miss our happy hours (as difficult to plan as they may be), and talking about whatever comes to mind. Catherine Weiss and Sidd Rajupet, you both may have arrived near the end of my PhD, but I have greatly enjoyed the happy hours, the wok nights, and chatting about things both science and non-science. Harsh Srivastav, thank you for the modeling discussions and the Korean bbq, even if I kept bailing on you. And finally, Ashley Bird, thank you for being a great friend and letting me watch Ion. It was truly a pleasure.

To those of you who left the group before me: Anamika Chowdhury, thank you for being a wonderful friend and role model of "chill". Sarah Berlinger, you were the best office mate I could have asked for, and a great friend – I will miss excursions to the best restaurants in the East

Bay with you. And finally, Julie Fornaciari, my wonderful friend – I cannot imagine doing my PhD without having had you in the group. Our daily messages and distractions were truly a highlight. The pep talks from all three of you were essential in stressful times (quals comes to mind), and I look forward to continuing our friendships.

I would be remiss to not mention my friends in the larger CBE department, who kept me distracted with fun activities as a necessary break from research. Neel Shah, thank you for being an amazing friend, always down for a hangout when needed (and who makes the best pizza). Eric Taw, thank you for the dinner parties, playing way too much Siege with me (even when we both know we shouldn't), and being an all-around great person. Zach Hoffman, Alec Ho, Natalie Lefton, Ana Carneiro, Sam Crowe, and Emily Carvalho – thank you all for being great friends. Whether it was going climbing, on hikes, to the movies, or to parties, I have had a great deal of fun with you all and appreciated all the adventures.

My housemates at 1513 Hearst Ave also deserve a shoutout – thank you Zach Konz, Branden Leonhardt, Clay Batton, and Justin Baerwald for being great roommates and friends. We survived the pandemic together, and I cannot imagine doing it with anyone else. Weekly house dinners were always a highlight that I am happy we kept going for over 3 years. Zach, I will miss our chats about topics large and small, and Clay, I already miss our impromptu midnight or 1 am discussions about whatever video game topic came to mind. Branden, our nights playing Dark Souls and Sekiro will always remain a highlight for me.

I must also thank my friends from undergrad, who have allowed me to completely disengage from research when needed and talk about, quite literally, anything else. You are all fantastic people, and I am humbled to call you all my friends. Matt Donnelly and Matteo Bolognese deserve a special mention for always being down for a chat, game, or call. Playing games with you both has been a highlight on both the good days and bad, and it truly kept me sane, no matter how pedantic the discussion. Mike and Jackie Zeimbekakis, thank you for being great friends and even better people. Visiting you has been a consistent bright spot throughout my PhD. And finally, Priyanka Ghosh, thank you for the conversations, the laughs, and the friendship; you are a wonderful friend.

Finally, I'd like to thank my family, without whom I would not have been able to complete this PhD. Thank you, Mom and Dad, for your endless love, support and advice, no matter how trivial the topic, and for allowing me to come home whenever needed to recharge. Thank you, Stephanie, for your love and for always being available to have a conversation about non-work topics (good luck at UVa!). Thank you, Grammy and Grampy, for your love, support, and ability to distract me from whatever is stressing me out at that moment. And finally, thank you Aunt Charlotte, for your love and support whenever I see you. I love you all.

I'd also like to thank my funding sources throughout my PhD – the DOE consortia FCPAD, M2FCT, H2NEW and HydroGEN – without which the work in this dissertation would not have been possible.

1. Introduction

1.1 Fuel Cells, an Energy-Conversion Technology

One of the most rapidly growing technological areas today is renewable energy, the development of which is in response to the carbon-dioxide crisis caused by the consumption of traditional fossil fuels.[1-3] The developing technologies are varied, ranging from energy generation from natural sources, such as solar cells, to methods of energy storage like more efficient batteries (*e.g.,* lithium-air batteries).[2, 4] Energy conversion is another option, converting energy between two different forms as a method of acquiring clean energy. Hydrogen-based energy-conversion devices (*e.g.*, fuel cells, electrolyzers) in particular have been recognized as a strong alternative to traditional fossil fuel-consuming devices, with support from industry as well as from the U.S. Department of Energy.[5] The Department of Energy has developed consortia specifically tied to hydrogen fuel cells (*e.g.*, Million Mile Fuel Cell Truck Consortium (M2FCT)), hydrogen production (*e.g.*, H2NEW), and materials for hydrogen devices (*e.g.*, HydroGEN), with the goal of creating a hydrogen economy to replace the fossil-fuel economy.[6-8] However, this large investment into energy-conversion technology is needed because these devices still have significant problems, primarily those of durability and cost-effectiveness compared to traditional fossil-fuel options.[6, 9]

Fuel cells, the focus of this dissertation, convert hydrogen and oxygen gas into electricity, with water as a byproduct. All low-temperature polymer-electrolyte fuel cells operate with the same basic sandwich structure at each electrode, illustrated in Figure 1.1a: gas flow fields form the exterior layer, followed by a gas-diffusion layer, the microporous layer, and the catalyst layer.[10] Electrochemical reactions occur in each catalyst layer, hydrogen oxidation (HOR) at the anode and oxygen reduction (ORR) at the cathode.[11] In most fuel cells, costly platinum (Pt) is the catalyst for the reactions. Reducing the quantity of Pt needed for efficient device performance is one of the main constraints for improving commercial viability of fuel cells.[9] The center of the fuel cell is the polymer membrane, which acts as both an electrical insulator and an ion conductor separating the two fuel-cell halves. The membrane is essential to efficient cell operation, as it completes the electrochemical circuit by allowing ions to pass from one catalyst layer to another. Electricity is extracted through an external circuit connecting the catalyst layers.

Fuel cells can be further separated into two main categories based on the type of membrane used: acidic proton-exchange-membrane fuel cells (PEMFCs) and alkaline hydroxide-exchange-membrane fuel cells (HEMFCs). A schematic of each type of fuel cell can be seen in Figure 1.1b and c. In PEMFCs, protons are the mobile ion present in the membrane, and the acidic forms of HOR and ORR, respectively, take place on platinum (Pt) nanoparticles in the catalyst layers[11]

$$H_2 \rightarrow 2H^+ + 2e^- \tag{1.1}$$

$$O_2 + 4H^+ + 4e^- \rightarrow 2H_2O \tag{1.2}$$

Potential species transport limitations already become evident: protons need free access across the membrane, oxygen and hydrogen need pathways to the Pt catalyst, and water needs pathways to

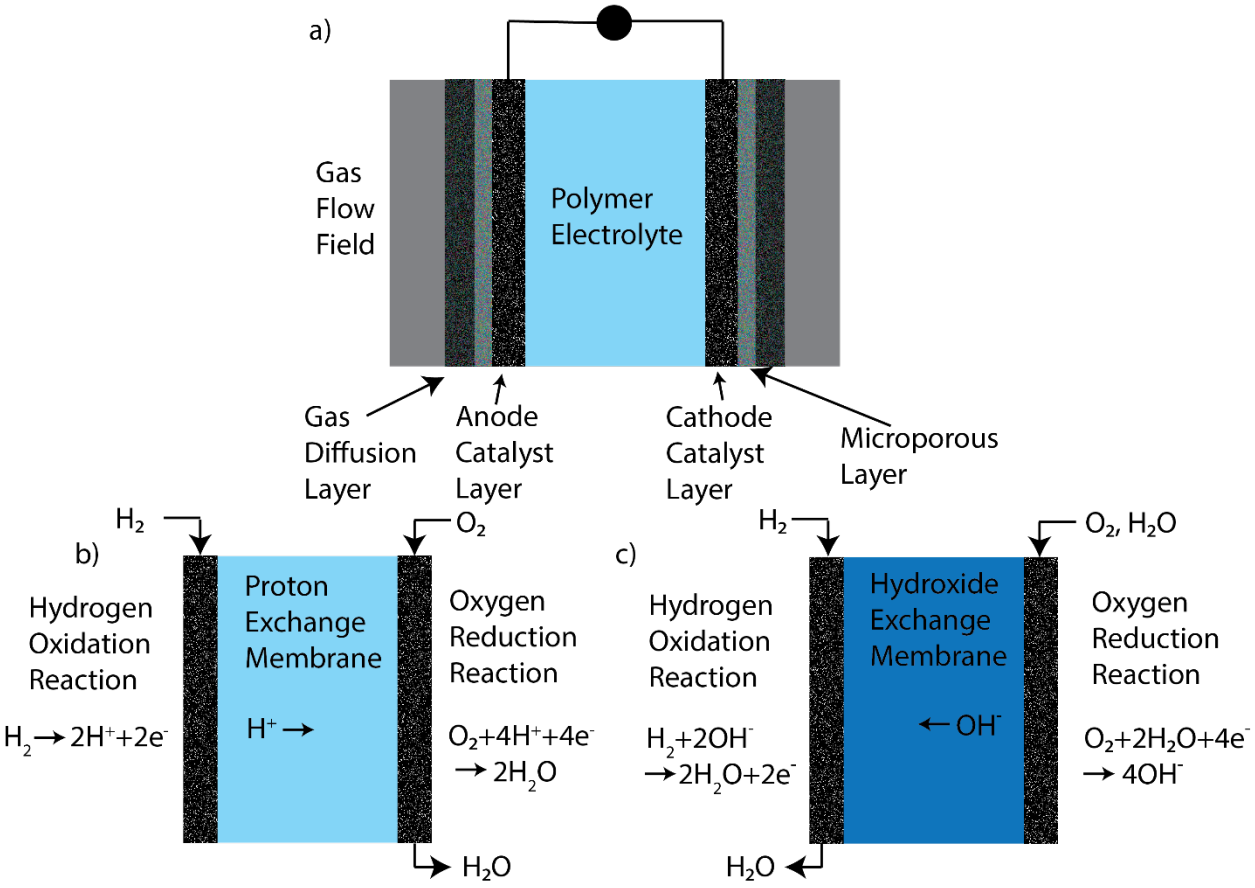

Figure 1.1: a) A general diagram of a polymer electrolyte membrane fuel cell, demonstrating the key components: gas flow field, gas-diffusion layer, microporous layer, catalyst layers, and membrane (layers not drawn to scale). b) and c) demonstrate the difference between proton- and hydroxide-exchange fuel cells with a simplified diagram.

exit the system. Catalyst layers are designed to provide these three pathways and to mitigate transport limitations.

A schematic typical catalyst layer is shown in Figure 1.2. In brief, Pt-metal catalyst particles (2-5 nm) rest on larger carbon particles (30-50 nm).[12] These carbon particles are bound together in small agglomerates (O(100 nm)) and in larger, porous aggregates by a thin binder film of ionomer.[12] This structure is critical to device performance, as it allows for all relevant species to reach and leave the Pt catalyst: reactive gas via the void space, protons via the ionomer thin film, electrons via the carbon support, and water via the ionomer thin film and void space (as diagrammed in Figure 1.2). The ionomer thin film forms a continuous ionic contact with the adjacent membrane, typically consisting of the same material as the thin film, and allowing for proton transfer between catalyst layers. However, this structure also gives rise to unique transport problems, as will be discussed in Section 1.3.

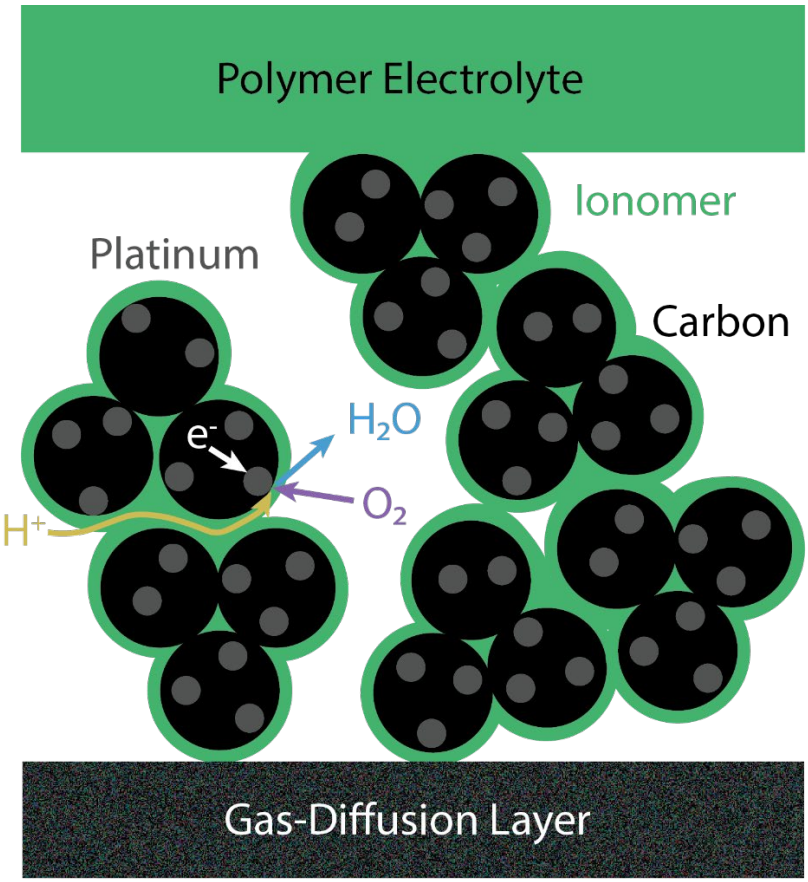

Figure 1.2: A schematic depiction of a fuel cell catalyst layer. Carbon particles (black) are covered with smaller Pt catalyst particles (gray), and the structure is bound together by an ionomer thin film (green). The polymer electrolyte is on one side of the catalyst layer and the gas-diffusion layer on the other side.

HEMFCs present an intriguing alternative to traditional PEMFCs. In HEMFCs, anions, specifically hydroxides, are the mobile ions, not protons. The system environment is therefore alkaline, not acidic, and the alkaline forms of HOR and ORR occur[11]

$$H_2 + 2OH^- \rightarrow 2H_2O + 2e^- \quad (1.3)$$

$$O_2 + 2H_2O + 4e^- \rightarrow 4OH^- \quad (1.4)$$

One of the primary advantages of using a hydroxide exchange membrane (HEM) is that it enables the use of less expensive, Pt-free catalysts (*e.g.*, iron/carbon catalyst) in the cathode catalyst layer for ORR.[13] However, myriad problems remain with HEM implementation, including low durability and low tolerance to species found in air such as carbon dioxide.[14-16]

This dissertation focuses on gas and water transport within both proton exchange membranes (PEMs) and HEMs as well as in catalyst layers, as all are relevant to modern devices and pose different challenges in study and operation. A deeper look at the polymer membranes is necessary to understand the importance of the varying modes of transport.

1.2 The Polymer Electrolyte

The industry standard PEM is Nafion®, a commercial perfluorosulfonic acid (PFSA) proton-conducting membrane.[17] Figure 1.3a demonstrates that Nafion is composed of a fluorinated carbon backbone with side appendages that terminate in sulfonic-acid groups. It has an equivalent weight, or grams of polymer per mol of ionic group, of 1100 g dry polymer/mol ionic group.[17] Nafion is known for its ability to uptake water, normally quantified by λ, or the mol of water per mol of ionic group. At sufficient water content ($\lambda > 2$), it phase separates into hydrophobic backbone regions and hydrophilic domains containing the side chains, sulfonic-acid endgroups, and water (see Figure 1.3a and 1.3b).[17-19] A large body of literature exists studying the water-uptake behavior and corresponding phase behavior of Nafion.[17, 20-25] Competing models for the structure of Nafion have been proposed by various authors, including the cluster-network model by Gierke *et al.*[26-28], the parallel cylinder model by Schimidt-Rohr and Chen[29], and a flat ribbon model by Kreuer and Gebel.[30, 31] All involve the formation of water channels within the membrane, an important structural consideration when working with Nafion.

The phase behavior of Nafion is foundational to its measured transport properties, as the hydrophilic phase typically allows for much easier movement of chemical species than does the solid-like polymer backbone. For example, proton conductivity increases significantly with hydration, and thus it is desirable to humidify gas feeds such that the membrane retains a high hydration.[32-35]

There are multiple mechanisms by which water can move through the membrane. One is diffusion due to a chemical potential gradient.[17] Another is electro-osmosis or electro-osmotic drag, where the fixed charges in the membrane and the high proton concentration require consideration of ion-water interactions, such that moving ions in the membrane carry water molecules with them.[36] This provides a method for moving water through the system beyond just diffusion and scales with current, as the movement of more ions induces the movement of more water. However, both humidified gas feeds and electro-osmosis can introduce water to other, potentially less-desirable regions of the system, such as the gas-diffusion and catalyst layers, and makes the water balance, and water transport through the membrane, critical to device performance.[37-41] Introduction of water also increases the permeability of Nafion to various gases and can amplify gas crossover, where the reactive gases move to the opposite electrode (*e.g.*, hydrogen to the cathode).[42, 43] Gas crossover generally has a deleterious effect on cell performance and durability, and thus, is desirable to minimize.[17, 44]

Alternatives to Nafion for PEMFC systems have been proposed, including Nafion variants such as Nafion XL, which include a polytetrafluoroethylene (PTFE) layer as a mechanical reinforcement and chemical modification,[45] as well as short-side-chain PFSA membranes such as Aquivion.[46-48] Other variants modify Nafion with additives such as cerium to improve membrane durability and reduce the impact of free radicals. However, cerium addition has a significant negative impact on the water uptake.[17, 49] Given the broad usage and acceptance of Nafion, it will be the primary PEM studied in this dissertation. Despite this usage, there is disagreement over the

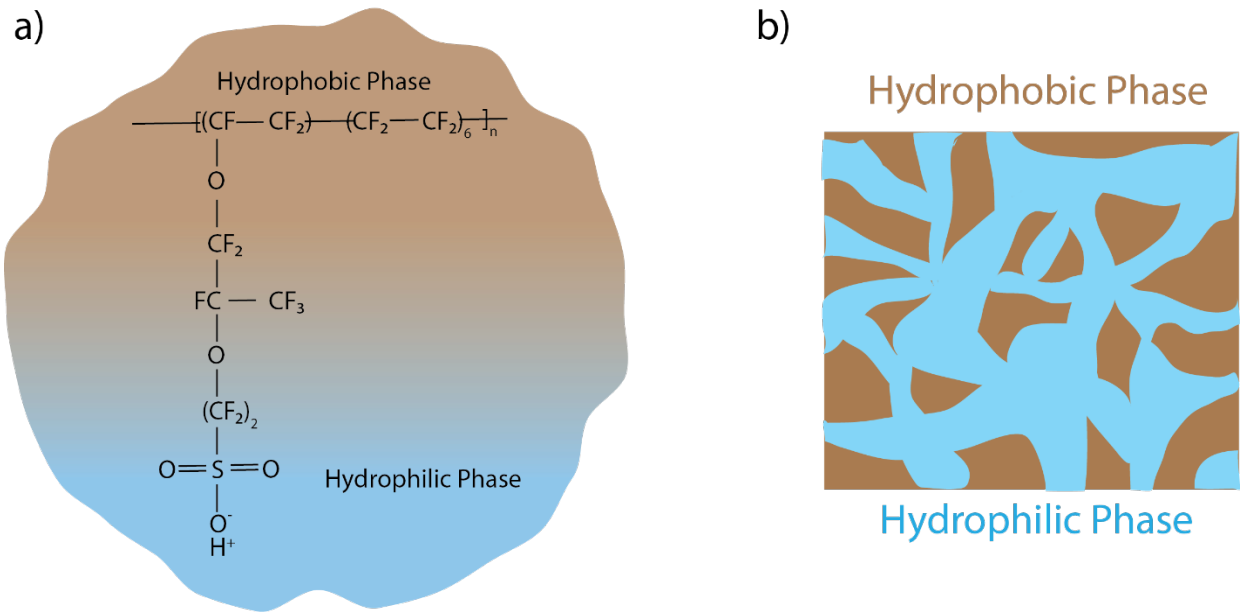

Figure 1.3: a) The relative regions of the hydrophobic and hydrophilic phases of Nafion are overlayed over the chemical structure of Nafion. b) A qualitative depiction of hydrophilic channels in-between hydrophobic backbone regions in Nafion.

gas and water transport parameters measured in Nafion, and these will be examined in this work.[17, 36, 50-52]

There are many available HEMs, including PF-AEM, Fumasep, and Versogen, to name a few.[53-55] The structures differ significantly, from fluorinated backbones similar to Nafion to benzene ring backbones and piperidinium ion side-chains.[54, 56] The equivalent weight of most HEMs is typically much lower than that of Nafion.[55, 56] Most uptake water in a similar way to Nafion, although the magnitude can vary. Fumasep, for example, uptakes somewhat less water than does Nafion, whereas Versogen is quite similar to Nafion.[55] However, unlike Nafion, there is little to no evidence to date of phase separation behavior in HEMs; instead, no definite structure is discernible.[55] Nonetheless, water content remains an important parameter for enhancing membrane conductivity, and water appears in the electrochemical reactions as both reactant and product.[55, 57] Thus, water transport is perhaps even more important in HEM systems than in PEMs.

1.3 Gas and Water Transport in Membranes and Catalyst Layers

Gas and water transport has been studied extensively in PEM fuel cells to date, using a variety of methods. Gas transport in Nafion membrane has mostly been discussed in the context of studying mass-transport resistances in the overall system. This has included both *in-situ* studies in membrane-electrode assemblies (MEAs) as well as *ex-situ* cells, such as studies using permeability cells or microelectrodes in more controlled environments.[42, 43, 50, 51, 58, 59] However, there is significant disagreement over the value of the gas-transport parameters; reliable values of

the gas-transport parameters are unclear.[43, 50, 51, 60] Gas transport in thin films in the catalyst layer is also of significant interest, as it has been reported that a large oxygen-transport resistance in Nafion thin films in the cathode catalyst layer is at least partially responsible for mass-transport potential losses seen at high current densities.[61-63] These have been studied in *ex-situ* cells and inferred from measurements in MEAs, as it is difficult to isolate the impact of the thin film in full MEAs.

Water transport in Nafion has been the subject of perhaps even more study, with multiple different methods of measuring water diffusion, including steady-state diffusion, nuclear magnetic resonance (NMR), and quasi-elastic neutron scattering (QENS).[32, 64-66] Again, measured values from these different techniques range over multiple orders of magnitude; this has been attributed to each technique measuring a different domain size within the membrane, stretching from "macroscale" values obtained from permeability studies to mesoscale local transport in QENS.[17] Electro-osmosis, or coupled water-ion transport, is also of interest, and has been less-studied than water diffusion, with much less agreement on the value of the electro-osmotic coefficient (number of water molecules carried per proton in the absence of concentration gradients).[36, 67-69] Electro-osmosis is also commonly quantified with the water transport number, or number of water molecules carried per charge of ion moved.[36] Water transport has also been measured in Nafion thin films, where the confinement effect limits water diffusion compared to membranes.[70-72]

Due to the relative newness of many of the available HEMs, there is a much smaller body of literature for modern HEMs, although studies of water transport are more common and emerging. Limited studies have been conducted demonstrating the water permeability of these materials, with a few studies focused on water diffusion and minimal attempts to examine electro-osmosis.[73-76] Gas transport is more understudied, with only a few attempts to measure the gas-transport parameters of these membranes, and no comprehensive investigation of the subject.[77] This is not surprising, given the importance of catalyst flooding to HEM fuel cells, raising the urgency of studying water transport in HEMs.[78, 79]

Both water and gas transport are coupled in the catalyst layer, where saturation of the catalyst-layer pores with water (referred to as flooding) is known to have a significant negative impact on fuel-cell performance due to limited oxygen transport to the Pt catalyst.[39] Many studies have focused on the impact of catalyst-layer saturation from both an experimental and modeling perspective.[38, 80-82] Gas transport in the layers adjacent to the catalyst layer, such as in the gas-diffusion layer, has also been studied, although gas transport in these regions is not considered limiting to the overall system in normal operation.[83-85]

1.4 Outline of Dissertation

As has been outlined, an understanding of both gas and water transport is essential to efficient fuel-cell operation. Gas transport and water transport in Nafion and, especially, in HEMs remain understudied, and thus it is necessary to accurately measure these properties to improve fuel-cell devices. This work is broken into two parts: measurement and analysis of gas and water transport

in fuel-cell polymer membranes via electrochemical techniques (Chapters 2-4), and the mathematical modeling of gas transport in catalyst layers (Chapter 5), although modeling still plays an important role in interpreting the experimental data.

The focus of Chapter 2 is two-fold: first, the use of microelectrodes to study polymer membranes is introduced, and the existing literature is reviewed, with a focus on gas-transport studies. Microelectrodes are effective for studying polymer membranes because they lend themselves well to *ex-situ* cell designs and the small electrode size minimizes the impact of the relatively high resistance of the membrane. The different available microelectrode-cell designs are presented and the pros and cons of each are discussed. Recommendations are made for proper use of microelectrode cells, including the importance of environmental factors and proper electrode cleaning. The first section concludes with a review of gas transport, primarily oxygen, using microelectrodes. The second half of the chapter discusses the flowthrough microelectrode cell, a new microelectrode-cell design that solves many of the problems with prior systems discussed in the chapter's first half. The design is evaluated, including cell equilibration time and impact of mechanical pressure. The new flowthrough cell is used in the electrochemical studies in the remaining chapters.

Chapter 3 presents an in-depth analysis of the proper technique for measuring gas transport with a microelectrode system using the flowthrough microelectrode. A numerical model is developed to compensate for shortcomings in the existing analytical solutions for determining mass-transport from current transients. Also, the importance of electrode surface roughness is considered and discussed. A two-time-regime analysis is proposed and is used to determine the oxygen and hydrogen diffusivity, Henry's constant, and permeability in Nafion 211 and Nafion XL. In addition, a two-phase parallel diffusion model accurately describes these gas transport parameters within Nafion 211 as a means of validating the measured values. The technique outlined in this chapter is broadly applicable to the study of many different types of membranes. The gas-transport parameters measured are essential to understand the impact of gas crossover and its impact on cell efficiency.

In Chapter 4, the focus turns to water transport, and specifically to the measurement of electro-osmosis within both PEMs and HEMs. A modified technique for measuring the water transport number via the microelectrode cell is detailed and validated using Nafion 211 at room temperature. The technique is then applied to measure the water transport number of different ion forms of Versogen and Sustainion over a range of temperatures. The impact of different mobile ions in water transport is interrogated by examining different ion forms of Nafion 211. Finally, a model based on the Stefan-Maxwell-Onsager framework is employed to predict the water-transport-number results as a function of water content of Nafion and to extract the water permeability of Versogen. This chapter provides a complete understanding of parameters required for studying the water balance in both PEM and HEM fuel cells and allows for more descriptive models optimizing these devices.

A mathematical modeling approach is used in Chapter 5 to examine the impact of nanodroplets of water on electrode mass-transfer limiting current. Nanodroplets form on the surface of catalyst nanoparticles in the fuel-cell catalyst layer and restrict access of oxygen to the Pt surface. Simultaneous solution of Navier-Stokes equations for water transport and Fick's law for oxygen

diffusion in conjunction with a moving mesh approach accurately captures the growth of the droplet with time and determines the impact of this growing droplet on measured current. Several variations are considered, including a pinned and advancing droplet, a droplet growing on a Nafion film, and water layer growth in a carbon nanopore. This chapter argues that small-scale water production in the catalyst layer is generally not important to device operation, and that the current is impacted only with full flooding of the catalyst layer.

The dissertation concludes with Chapter 6, which summarizes the preceding work and presents a discussion of future directions for the study of mass-transport phenomena in fuel-cell systems.

2. Microelectrode Systems to Explore Transport in Solid Polymer Electrolytes[†]

2.1 Abstract

Solid polymer electrolytes are critical in electrochemical technologies, such as fuel cells, electrolyzers, and solid-state batteries. Compared to traditional liquid electrolytes, solid polymer electrolytes provide safer, cheaper, and potentially improved device performance. However, there is a lack of standard experimental methods for studying solid-electrolyte properties outside of integrated devices. Microelectrodes have inherent benefits capable of filling this experimental gap due primarily to their integration into model electrochemical cells with solid electrolytes, which represent complex interfaces, enabling additional insight into reaction processes. In this chapter, we explore the use of microelectrodes to study solid polymer electrolytes, beginning with a brief history of the field including common experimental cell designs and their benefits and drawbacks. Methods of evaluating essential mass-transport parameters are then examined. In addition, the key studies of the past 30 years utilizing microelectrode cells and solid polymer electrolytes are summarized, with important results highlighted and compared. Finally, the microelectrode cell used in this dissertation is presented and the design is validated via multiple electrochemical tests. The design is found to be robust and effective at measuring both hydrogen oxidation and oxygen reduction. This flowthrough cell will enable more standardized, efficient, and accurate microelectrode studies in the future.

[†]Sections of this chapter were previously published as "Petrovick, J. G., Anderson, G. C., Kushner, D. I., Danilovic, N., Weber, A. Z. Method – Using Microelectrodes to Explore Solid Polymer Electrolytes. Journal of The Electrochemical Society, 2021, **168** 056517" and "Petrovick, J. G., Kushner, D. I., Tesfaye, M., Danilovic, N., Radke, C. J., Weber, A. Z. Mass-Transport Resistances of Acid and Alkaline Ionomer Layers: A Microelectrode Study Part 1 – Microelectrode Development. ECS Transactions, 2019, **92** 77". Adapted with permission from all co-authors.

2.2 Introduction

Electrochemistry is an essential field of chemistry, which is gaining prominence as it enables widespread renewable energy and deep decarbonization across numerous industrial sectors via electrical/chemical energy-conversion and -storage devices. Many of these emerging devices are solid-state systems, wherein traditional electrochemical techniques are not as readily available for exploration of the governing phenomena. In addition, it is now recognized how important the electrochemical interface plays in such technologies. For example, the reaction interface remains uninterrogated in model systems for devices that utilize polymer electrolytes, such as perfluorosulfonic membranes (PFSA, *e.g.*, Nafion®) for proton-exchange-membrane fuel cells (PEMFCs) and water electrolyzers (PEMWEs), or complex oxide ceramics for all solid-state batteries (lithium polysulfate (LPS), lithium lanthanum zirconate garnet (LLZO)). Emblematic of these issues are the exemplary and ubiquitous oxygen reduction and evolution (ORR and OER) and hydrogen oxidation and evolution (HOR and HER) reactions, shown in Figure 2.1 and Equations 1.1 and 1.2 in Chapter 1. Typical polarization curves are shown in Figure 2.1a while polarization curves and a cyclic voltammogram from *ex-situ* cells are given in Figure 2.1b. A gap exists between what can be fundamentally studied about ORR or HOR between a platinum electrode and oxygen or hydrogen-saturated aqueous acids and the behavior of ORR in a fuel cell (membrane-electrode assembly, MEA) where the ORR or HOR occurs with interaction between a Nafion ionomer, platinum electrocatalyst, and humidified reactant gas. There are both kinetic and thermodynamic implications to this gap, and it is important to have tools to study them.

The study of reaction kinetics in aqueous solutions is conventionally accomplished using the rotating disk electrode (RDE). The RDE was invented by Ivanov and Levich in 1959, utilizing the governing equations of hydrodynamics and the convective-diffusion equations.[86-89] The RDE consists of a disk electrode, typically 5-6 mm in diameter embedded in inert collets made of polytetrafluoroethylene (PTEF) or polyether ether ketone (PEEK). The disk, which represents

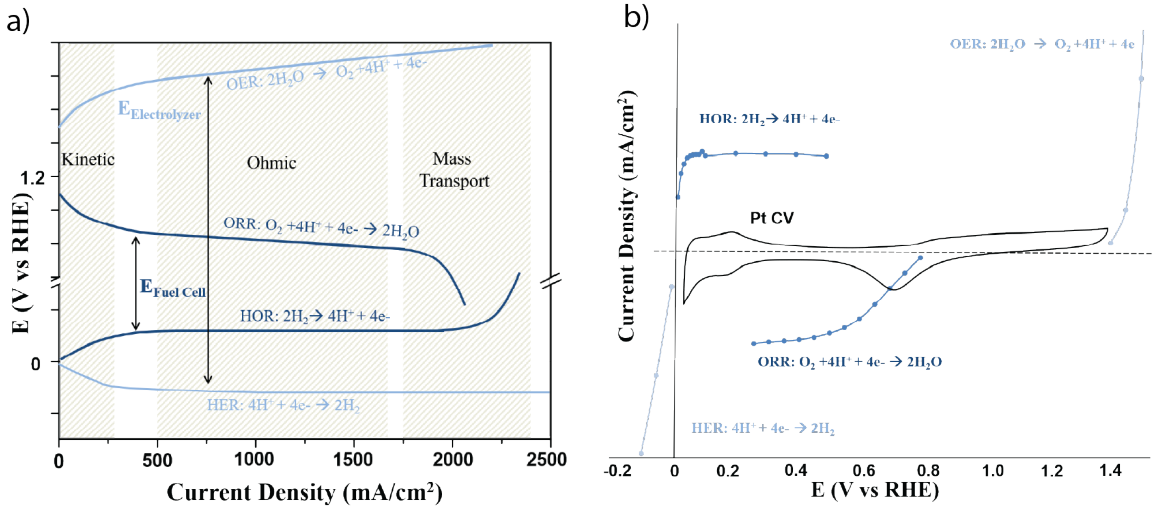

Figure 2.1. Water based, energy-conversion reactions HOR/HER and OER/ORR viewed as a) cell-level polarization curves schematically and b) Pt and Ir microelectrode measurements on Nafion solid-polymer electrolyte in humidified room temperature gases.

the working electrode, can be polycrystalline metal or oxide, single crystal (with the use of a hanging meniscus collet), glassy carbon, or other inert substrates onto which nanoparticles are drop cast. The collet is screwed into a shaft that can be rotated at a desired rotation rate. RDE equipment is largely available commercially, as well as custom-made electrode disks of various materials. The premise of the RDE is that, as it rotates, the bottom of the disk drags the solution radially away from the center in a well-controlled and defined manner. Fluid is replenished by a normal flow to the surface. Depending on the rotation rate, the diffusion-layer thickness is also changed in a prescribed manner thus allowing more reactant to be predictably presented to the working electrode disk and producing a higher limiting current. There is more uniform accessibility of reactant to the electrode surface. In other words, the mass-transport limiting current of ORR or HOR can be varied by varying the rotation rate. The RDE is an ideal method for studying ORR and HOR reaction mechanisms, catalyst activities, and stability, with the caveat being that the local environment in the RDE is aqueous and thus different than in a PEMFC MEA. This introduces multiple issues, including uncertainty regarding interfacial phenomena, reactant solubility limitations, differences in local and bulk pH, and transport limitations in different media, etc.

Performing electrochemistry in solid polymer electrolytes has largely been isolated to MEAs consisting of two heterogeneous porous electrodes that typically exhibit greater than 1-cm^2 geometric area. The electrodes are deposited on the membrane or on gas-diffusion layers and are placed on either side of the solid electrolyte, effectively sandwiching the electrolyte. Most polymer electrolytes require hydration (typically using water vapor), and a solid reproducible electrical/ionic contact must be maintained between the solid electrolyte and the working and counter electrodes to manage the electrolyte resistance. The resulting environment is much more complex and heterogeneous compared to the RDE environment in aqueous electrolyte cells. However, such a cell allows for interrogation of the solid/solid interface between the electrocatalyst and solid polymer electrolyte, in a manner similar to that in actual devices, where transport to the surface and kinetics couple to limit operation.[61] An important distinction is that MEAs are two-electrode measurements with perhaps poorly defined interfaces due to their porous, heterogeneous multicomponent catalyst layers. Also, without a specific reference electrode, although often hydrogen systems use (HOR or HER) as a pseudo reference, interpretation of the results is difficult to attribute directly to kinetic or transport limitations of either the electrode or the membrane. A third electrode can be introduced to resolve the half-cell reaction parameters in an MEA, but this procedure is not trivial and interpretation not necessarily straightforward due to interactions among the electric potential fields in the MEA.[90]

Microelectrode (ME) cells provide a pathway towards overcoming many limitations associated with MEAs and can represent controlled environments and structures, similar to RDE, that allow for in-depth interrogation of interfacial phenomena.[91, 92] MEs are distinguished as any electrode with a μm-scale diameter, while an ultramicroelectrode (UME) is classically defined as any electrode with a geometrically important dimension of 50 μm or less.[86] For example, a disk electrode with a diameter less than 50 μm is classified as an UME. The terms will be used interchangeably in the remaining text, as the same general principles apply to both cases. MEs can be formulated in several different geometries, including the aforementioned disk electrode as well as spherical, cylindrical, and band microelectrodes. However, the geometry most used in polymer-electrolyte electrochemistry is the disk electrode due to its ease of manufacture and implementation, and will be the focus of this dissertation.[93] As a result of the ME field's

association with PEMFCs, platinum (Pt) is by far the most common metal for polymer-electrolyte MEs, but other metals can be used, including gold, iridium, silver, and copper. Iridium would be most appropriate for studying OER, whereas Pt is more appropriate for HOR, HER, and ORR. For other reactions, such as CO_2 reduction or chemical conversions, other metals are more appropriate.[94]

MEs are not limited to solid-state measurements – they can also be used for *in-situ* electrochemical diagnostics. For example, in liquid electrolytes, the small size of MEs results in a very thin diffusion layer and low absolute current, reducing the impact of electrolyte resistance, which typically requires compensation in RDE. MEs are also frequently found in the adjacent field of scanning electrochemical microscopy (SECM), which allows for local probing of electrochemical reaction kinetics at a substrate surface.[95] Many of the experiments detailed later in this work, such as chronoamperometric measurements, are featured heavily in SECM studies, and thus the general principles discussed here can be applied in these systems as well.[96] MEs have also been used with limited success as sensing electrodes in operating complex devices, where they serve a similar purpose as a given reference electrode. Examples include local chemical sensing in microbial and PEMFCs.[97, 98] However, such applications are nascent and involve more complex phenomena and analysis. In-depth discussion of electrochemical diagnostics is, thus, beyond the scope of this chapter as they are a separate and more specialized use of MEs. Instead, we focus closely on the application of MEs in solid-state applications for mass-transport analysis.

MEs provide several advantages in solid-state electrochemical applications. For example, they accommodate stable reference electrodes (dynamic hydrogen electrodes) for treating half-cell electrochemical measurements of kinetics and mass transport similar to RDE half-cells. Normally, ohmic drop is a significant concern in solid electrolytes (as compared to liquid). Fortunately, the small electrode size in MEs lowers current draw such that ohmic drops are quite small. However, there are concerns as well; both MEs and RDEs present an ancillary problem in that solution impurities can have a major impact on the result. Additional pros and cons of MEs are presented in Table 2.1, many of which are discussed in more detail later in this work.

The first solid-state ME experiments were accomplished by Appleby and Srinivasan in the 1990s to study ORR using a 100 μm Pt ME and a Nafion membrane.[91, 92] These publications cover a multitude of cell-design criteria and effects found important. A handful of other groups have also developed their own unique cells. Interestingly, with only a 20-year gap between RDE and UME development, RDE and MEA testing have become significantly more widespread and common. ME apparati for studying solid electrolytes remain largely difficult for a variety of reasons, including slow equilibration times, overly complex designs, and a reliance on steady-state measurements, as discussed in depth below. In this chapter, we discuss the appropriate application of MEs including best practices and data analysis as electrochemical diagnostic tools to examine reaction interfaces using as examples the ORR/OER and HOR/HER. First, the existing cell setup and testing procedures are discussed, followed by a critical review of applications of MEs. Next, the microelectrode cell used in this dissertation is considered and tested to demonstrate its viability. Finally, the chapter is summarized and future directions noted.

Table 2.1: Pros and cons of using microelectrodes to study solid-state electrolytes.

Cell Design Features	
Pros	**Cons**
• Effective control of environmental variables, including relative humidity, potential, temperature, and gas flow • Simple, robust design that minimizes layers and interfaces with ideal geometry • Allows for product gas analysis for additional insights into reaction products	• Low currents are significantly affected by room noise, necessitating a Faraday cage • Equilibration times and experiments can be quite lengthy • Avoiding contamination is critical because low currents are easily influenced by even small amounts of contaminant
Experimental Design	
Pros	**Cons**
• A wide range of reactions are available to study, including fuel cell reactions, water splitting, and carbon dioxide reduction • Low ohmic drop ensures accurate current measurements and low overpotentials • Limiting system to one reaction simplifies both kinetics and mass transport phenomena • Allows for accurate transient analysis of current response, something that is difficult with MEA scale devices • Model system that avoids complicated interfaces	• For mass-transport measurements, no analytical solution exists, requiring the use of numerical modeling or analytical approximations • If using thin films, drop casting the films produces irregular shapes, which can impact measurements and interpretation • At high current density, thin films may peel away from the electrode surface due to repulsive forces and reactant/product consumption/generation

2.3 Microelectrode Setup and Testing

2.3.1 Microelectrode Cell Designs from Literature

The standard three-electrode experimental ME cell incorporates a working, counter, and reference electrodes, but two-electrode studies have also been performed (see Figure 2.2). In a three-electrode system, the membrane is placed between the ME and the counter electrode, where the circuit is completed using a solid polymer electrolyte that acts as an ion bridge to the

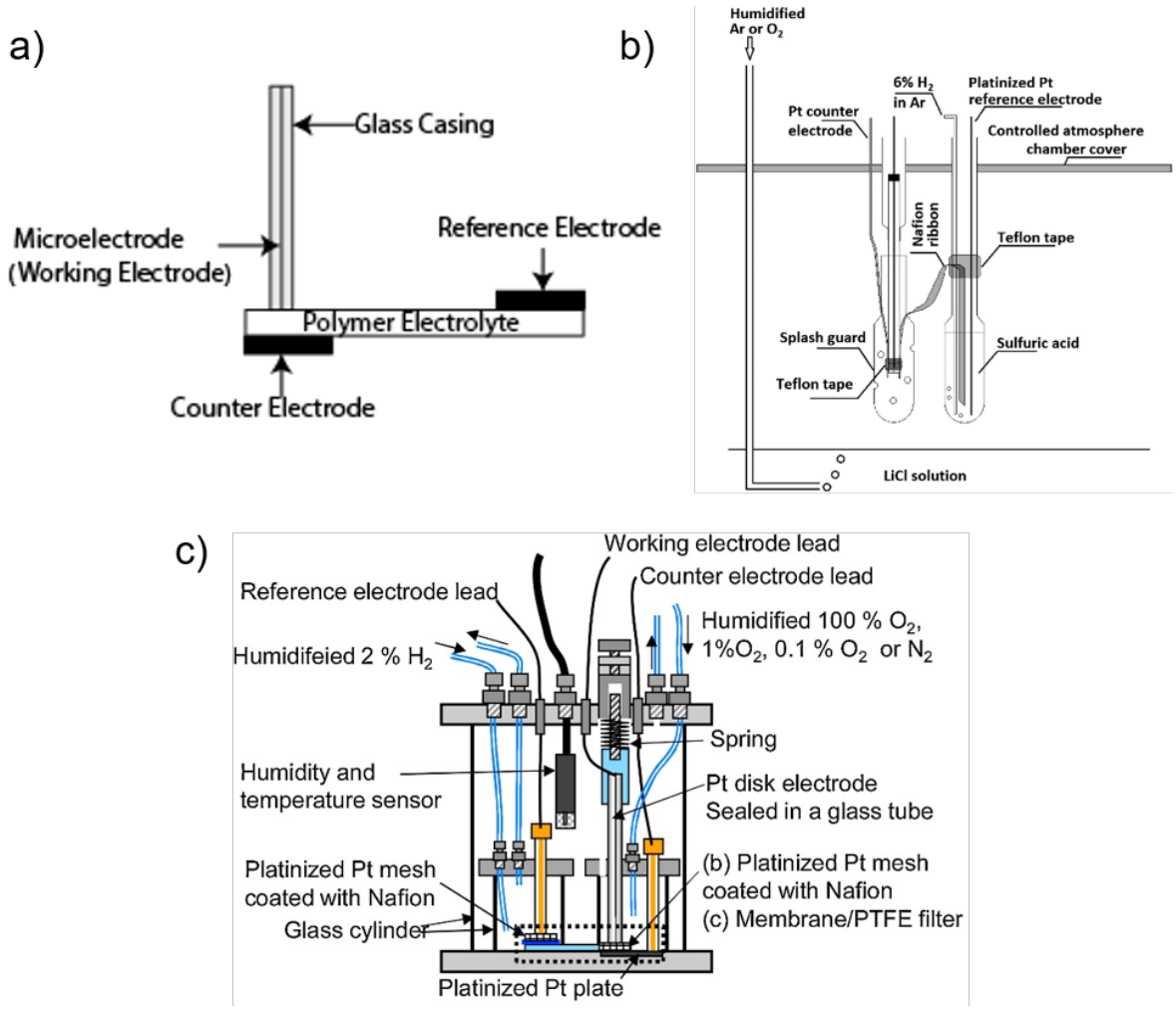

Figure 2.2: a) Simplified three-electrode circuit used for ME measurements. Complete measurement cell diagrams showing the electrode and solid polymer electrolyte placement in a b) free-standing[99] and c) force-based format.[50] This figure b) is reprinted from the Journal of Power Sources, 245, J. Chlistunoff, Oxygen permeability of cast ionomer films from chronoamperometry on microelectrodes, 203-207, Copyright (2014), with permission from Elsevier. This figure c) is reprinted from Electrochimica Acta, 209, K. Kudo, R. Jinnouchi, and Y. Morimoto, Humidity and Temperature Dependences of Oxygen Transport Resistance of Nafion Thin Film on Platinum Electrode, 682-690, Copyright (2016), with permission from Elsevier.

reference electrode. A two-electrode configuration lacks the reference electrode shown in Figure 2.2a, and the counter electrode is used as a pseudoreference due to the low currents typically measured in these experiments.[51] However, this may reduce the consistency of the measured potentials and is not universally recommended, despite the less complex cell design that is required. ME configurations can be split into two overall orientations, where the cells are assembled in the following manner: (i) casting the polymer electrolyte on the tip of the ME when the ME is free-standing or (ii) pressing the ME into a solid polymer membrane that has been prepared separately. Measurements are generally performed in environmentally controlled chambers, thereby allowing for control over gas, pressure, humidity, and temperature. Early reports by Uribe *et al.*[100] employed MEs in a free-standing configuration, allowing for full exposure of the ME tip to the environment without pressing the ME into a solid or porous surface (as seen in Figure 2.2b). Later reports using this configuration were discussed by

Chlistunoff and Sung-Dae.[99, 101] Films are cast on the tip of the ME and a counter electrode, typically comprised of a platinum wire, is bent over the cast film. A solid polymer electrolyte, typically Nafion, is also bent over the tip and adhered using a Nafion dispersion that acts as a bridge to the reference electrode. This configuration benefits from a polymer layer tightly bound to the ME surface in which external gases are unable to penetrate and react directly at the electrode. An additional benefit to a free-standing configuration is an unimpeded flow of gas to the polymer/air interface, reducing chances of an electrode blocking the pathways of the gases. However, there is difficulty in providing good connectivity between the counter electrode and cast films, as well as the reference electrode bridge acting as a weak point during hydration studies due to detachment. An additional concern involves the slow diffusion of the liquid electrolyte in the reference chamber through the bridge leading to eventual contamination of the film of interest.

The second configuration involves a reliance on the application of a constraining downforce on the ME and into the membrane, which has been more commonplace in the literature for studies involving solid polymer electrolytes (Figure 2.2c).[50, 59, 102, 103] A sandwich structure is traditional for this configuration in that the ME is pressed into the membrane that is stacked atop a porous electrode, typically a platinum mesh, or a solid electrode acting as the counter electrode. The membrane of interest generally acts as the electrolytic bridge to the reference electrode. Reference electrodes are typically composed of a platinum wire encapsulated in a glass capillary or a platinum mesh in an auxiliary chamber that is flooded with hydrogen gas, where the reference point is set by the hydrogen concentration. In this design, adequate pressure must be applied between all electrodes and the membranes to reduce gas diffusion along the electrode/polymer interface as well as provide connectivity between the electrodes and membrane. Once an appropriate pressure is applied, then the response of the ME to the testing conditions becomes pressure independent. Configurations that rely on pressure benefit from fast and simple sample changes as well as confidence in the membrane thickness when performing calculations. Both configurations suffer from high sensitivity to environmental condition changes and compromises at the electrode interface: unnecessary surface roughness and chemical contamination.

2.3.2 Factors Influencing Microelectrode Measurements

Precise environmental control plays an important factor when performing measurements, regardless of the configurations used. The most common environments explored in solid-polymer-electrolyte studies involve humidity and gas type/concentration, whereas some studies have also involved temperature and pressure. The simplest condition to change is the gas type to probe different reactions. Gases are typically supplied in a gas cylinder at specific concentrations to the environmental chamber. The next condition to probe is humidity generated at room temperature by mixing humid air at dew point with a dry air stream at different ratios to target specific relative humidity. As more variables are included in the cell design, the complexity of environmental control becomes more difficult. For instance, when temperature is involved, the control of humidity becomes increasingly difficult without proper temperature control and insulation. Humidity is generated by flowing the gas through a water vessel at a set temperature to produce air at the dew point. The difference typically seen in practice is that the vapor stream

is heated to the measurement temperature rather than mixed with a dry air stream. If any component drops below the water-vessel temperature then condensation alters the final humidity in the test cell. Lastly, although many studies involve measurements performed under atmospheric pressure, pressure can be increased to allow for humidified studies above 100°C. But, special considerations, such as back-pressure regulators and sealing, must be taken into account.

When working with MEs the small metal areas and the relation to the surface roughness of the electrode is important. The surface of the electrode may be macro- and microscopically smooth, but on the nanoscopic level there is a significant amount of surface roughness, which increases the available surface area for electrochemical reactions. This is true even for polished electrodes. For example, a smooth Pt electrode typically exhibits an electrochemically-active surface area (ECSA) that is approximately two times larger than the geometric area.[51] Actual reaction surface area is characterized by the roughness factor, which is simply the ratio of the ECSA to the geometric area,

$$Roughness\ Factor = \frac{ECSA}{Geometric\ Area} \tag{2.1}$$

It is possible to calculate the ECSA by measuring the amount of a specific species adsorbed to the electrode surface. Common species used are carbon monoxide and hydrogen. In both cases, a cyclic-voltammetry experiment is performed over a specific potential range and the current as a function of potential is measured. This current exhibits peaks at potentials where species adsorb or desorb. By integrating the area of the peak and dividing by the scan rate, the total charge of the adsorbed species can be calculated. The surface charge density of the species on the specific electrode material is measured in a separate experiment, and this value can be used to convert the total charge to an ECSA (assuming that the species adsorbs in a monolayer). This procedure is applicable to Pt electrodes but is more difficult for other metals.[104]

An example of this approach can be seen in work by Novitski *et al.,* who used a decreasing ECSA with relative humidity to correct mass-transport measurements.[51] By electroplating the ME surface, it is possible to increase the ECSA of the electrode and raise the measured current, as area and current are (in theory) directly proportional as long as the area is accessible by the electrolyte/reactant. The main benefits of this approach are that the higher current is generally more stable, less affected by background electrical noise, and easier to measure. However, this approach becomes problematic when attempting to extract mass-transport parameters from experimental data (as discussed in Chapter 3). The uncertainty introduced by the larger area relative to the geometric area greatly complicates numerical modeling, as the current measured from a plated electrode, while higher than an unplated surface, does not scale as expected with ECSA. Therefore, it is recommended to use a smooth ME if not hardware limited (lower bound current limit of potentiostat or noise of the system).

2.3.3 Microelectrode preparation including cleaning and casting

The ME requires careful handling, preparation, and usage to ensure reproducible results and to minimize the impact of contaminants either on the electrode or in the electrolyte or feeds. Due to

the small electrode size and very small currents, the threat of contaminants impacting the results is very high. It is advisable to treat the ME and cells with procedures appropriate for ultra-high purity electrochemical measurements, including periodic cleaning of the ME and hardware in strong acids and boiling in ultrapure water (18.2 MOhm) and storing all wetted components in ultrapure water.

The ME itself consists of a metal wire embedded in glass. The tip is cut and polished by the manufacturer. If using the polished ME surfaces for analysis, care must be taken to maintain the polish with a fine alumina polish and appropriate felt pad dedicated to the ME. With RDEs, one can polish and visually see the roughness level and imperfections with the naked eye. MEs, however, are too small to visualize directly and require more sophisticated tools. This becomes important if the electrode is plated or if there is an ionomer casting and/or direct compression with harder surfaces. At a minimum, the surface should be inspected by an optical microscope to ensure that no obvious pits exist. Scanning-electron microscopes (SEMs), atomic-force microscopes (AFM), or profilometers are recommended for a more detailed surface analysis. For well-studied metals like Pt, a cyclic voltammogram in a non-adsorbing liquid electrolyte (*e.g.*, perchloric) can be used to quantify the ECSA and compute a roughness factor. This procedure can be used over the life of the electrode to evaluate how worn the surface has become. After polishing, the ME must be cleaned to remove the polishing materials and prevent contamination of the electrolyte. Rinsing with an ultrasonic bath in deionized water, and a quick submersion in weak perchloric acid removes most particle contaminants and oils. The ME should also be stored in an appropriately clean vessel until it is ready to be used; deionized water is suggested.

Casting ionomers on the surface of the ME is a necessity for thin-film measurements, but it can also introduce contaminants as the ME inevitably goes through several preparation steps including perhaps annealing before the electrochemistry is performed. The most basic deposition method is drop casting, where a dilute solution of ionomer in water and solvents is deposited on the surface and allowed to dry. Drying conditions alter the structure and quality of the film and can mitigate or introduce contaminants. The cast film should be dried in a controlled gas environment and protected from particles in the air/room. Once dry, the film can be annealed in a vacuum oven, once again keeping the ME covered to prevent surface contamination. Time, temperature, and vacuum affect the structure of the ionomer film. Subsequently, the electrode is directly transferred to the ME cell. It is wise to perform an acid cleaning of the tip, with a rinse in deionized water, and a check in a dilute acid ME cell to ensure contaminants are not affecting the response of the ME. These steps may affect the structure and presence of the ionomer film. Post-testing, the ME should be carefully cleaned of the ionomer film by dipping in acid and rinsing with deionized water in an ultrasonic bath. An optical microscope is helpful to confirm that the film has been removed. Additional information surrounding ME preparation can be found in Table 2.2.

2.4 Polymer-Electrolyte Microelectrode Applications

Studies performed using ME polymer-electrolyte cells can be grouped into two main categories: mass-transport and electrochemical reaction. Because of a primary association with fuel-cell polymer membranes, oxygen and hydrogen have been the most widely studied gases, particularly

oxygen, along with the associated electrochemical HOR and ORR.[51, 59, 100, 105] However, the focus has broadened more recently to include polymers beyond Nafion, such as other PEMs and HEMs.[106-108] Thin films (<100 nm) of Nafion have also been compared to micrometer-thick membranes (such as N117 or N211, where N117 is 175-µm thick Nafion formed via extrusion and N211 is 25-µm thick Nafion formed via casting, both manufactured by

Table 2.2: Author suggestions for working with microelectrode setups.

Category	Author Recommendations
Materials/Hardware	• Ensure that the microelectrode cell has been boiled recently to remove lingering impurities. • Use a new membrane and new counter electrode (if not using a platinum mesh) for each experimental setup. • Clean (with deionized water) and dry (with nitrogen) the microelectrode tip before use.
Assembly	• Use a membrane equilibrated with ambient humidity (if working with PFSAs) to ensure drying from liquid-equilibrated conditions does not cause the membrane to lift off the electrodes. • Ensure that the membrane is cut in such a way that the reference pin touches the counter electrode, not the membrane. • Before assembly, apply a few drops (~2) of the relevant ionomer dispersion to the microelectrode tip. This will create an adhesion layer upon assembly and drying that will seal the edges of the microelectrode and not allow gas to bypass the membrane. • It is simple to confirm that the seal has worked. Upon assembly and testing, check the magnitude of the current vs. an expected current calculation. If the current is multiple orders of magnitude higher (e.g., µA vs nA) the seal has not worked, leakage is occurring, and the cell must be rebuilt.
Testing	• Due to room noise and other fluctuations, it is helpful to operate the potentiostat with a manual ground (as opposed to allowing the potentiostat to set its own ground). The ground can simply be the Faraday cage used to shield the cell. (Note: aluminum foil is an effective Faraday cage).

Chemours), allowing for an in-depth study of interface properties of thin ionomer films compared to bulk membrane properties.[50] In addition, MEs can be used to study the impact of various environmental effects in systems that mimic high-temperature PEMFCs.[109] This section examines key areas of the mass-transport literature, highlighting the most important studies. Equations used in the analysis are given here, but a detailed discussion of the advantages and disadvantages of the various analytical approaches is left for Chapter 3. The existing literature is unfortunately inconsistent on the precise definition and reporting of solubility and concentration. Unless otherwise stated, when the terminology "gas concentration" is used in the following paragraphs, it may be considered as the product of a Henry's constant and external gas pressure. Permeability, unless otherwise noted, is the product of diffusivity and this "gas concentration."

The first modern polymer-electrolyte ME cell was developed by Parthasarathy *et al*. in 1991 and subsequently used for various studes.[59, 92] This was the first paper to report the mass-transport properties of oxygen in Nafion as well as details on the kinetics of the ORR reaction in a polymer electrolyte via the ME interface. In their initial study, 175-µm thick Nafion (equivalent weight (EW) = 1100 g/mol) was used with a 100-µm diameter Pt ME under 99.9% RH, 24.5°C, and 1 atm. The authors also pioneered the analysis method used in nearly every subsequent study, where an analytical solution for the *I(t)* curve was fit over a short early-time range of the experimental data to determine mass-transport properties (see Figure 2.3).[59, 110, 111] Eq. 2.2 was used to fit the data due to its simplicity and relative accuracy:

$$I = \frac{nFAD^{\frac{1}{2}}C}{(\pi t)^{\frac{1}{2}}} + \pi nFDCR_e \tag{2.2}$$

where I is the limiting current, A is the electrode area, D is the diffusivity, C is the gas concentration in the membrane at the membrane-gas interface, F is Faraday's constant (96,485 C/mol), R_e is the electrode radius, and n is the number of electrons involved in the reaction.[59, 110, 111] Oxygen gas was shown to have a diffusion coefficient of 7.4 x 10^{-7} m^2/s and a gas concentration of 26 mM in Nafion.[59, 86] Despite the long equilibration times and laborious setup, this work showed that these parameters could be determined accurately and consistently using MEs and polymer electrolytes.[59]

In PEMFC operation, performance under reduced RH conditions is quite important and ME cells can be used to study this as well. Novitski and Holdcroft[51] applied MEs to the study of oxygen transport in Nafion with relative humidities lower than 100%. Unlike other setups, the cell design here was two-electrode and used a 5 µm Pt electrode, with Nafion 211 and deposited DE2020 Nafion dispersion as electrolytes. An identical fitting method to Parthasarathy was used, although the time domain used was significantly shorter ($0.5<\tau<1$).[51] In addition, the Shoup-Szabo equation was used,[86, 112]

$$I = \frac{4nFADC}{\pi R_e}\left[0.7854 + 0.8862\frac{1}{\sqrt{\tau}} + 0.2146e^{-0.7823\frac{1}{\sqrt{\tau}}}\right] \tag{2.3}$$

Where $\tau \equiv \frac{4Dt}{R_e^2}$. The authors found that as humidity decreased, diffusivity and permeability decreased while solubility increased (see Figure 2.4).[51] This supports previous theories that most gas transport occurs in the water phase of the membrane even though the gas is more soluble in

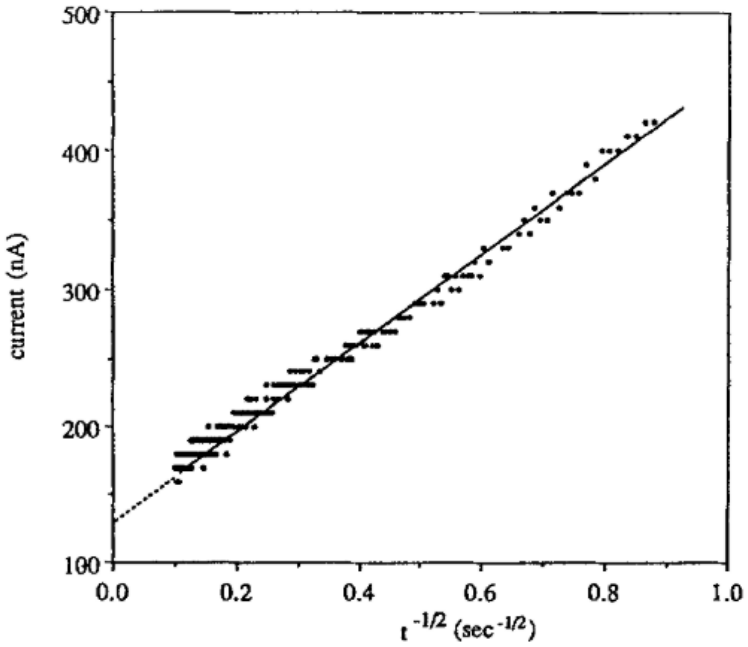

Figure 2.3: Plot of experimental current vs $t^{-1/2}$ from Parthasarathy *et al.* over a limited time range, fit using Eq. 5.[17] A. Parthasarathy, C. R. Martin and S. Srinivasan, Investigations of the O_2 Reduction Reaction at the Platinum/Nafion® Interface Using a Solid-State Electrochemical Cell. *Journal of The Electrochemical Society*, 138, (4) 916-921 (1991). DOI: 10.1149/1.2085747 © The Electrochemical Society. Reproduced by permission of IOP Publishing Ltd. All rights reserved.

the polymer phase of the membrane.[17] However, the authors also found that the results reported by the two different fitting methods differed by over an order of magnitude, casting doubt on the accuracy of the analytical fitting techniques.[51]

Due to their small size and low measured currents, MEs can also detect interface resistances of thin films. Kudo *et al*.[50] cast thin films of Nafion using 0.3-0.7 wt.% solutions, resulting in films 20 to 100 nm in thickness, and compared the results for oxygen transport with those obtained from 100-µm membranes. To determine the interfacial resistance, a linear expression for the oxygen transport resistance, R_{O_2}, was derived,

$$R_{O_2} = \frac{nFP_{O2}}{i_d} = \frac{1}{DK_H}x_0 + \frac{1}{K_H}\left(\frac{1}{k_{Pt}} + \frac{1}{k_{ion}}\right) \tag{2.4}$$

where P_{O2} is the oxygen partial pressure in the gas phase, K_H is the Henry's constant, i_d is the limiting current, x_0 is the film thickness, and k_{Pt} and k_{ion} are the overall mass-transport coefficients at the Pt/ionomer and ionomer/gas interfaces, respectively.[50] The term $\frac{1}{K_H}\left(\frac{1}{k_{Pt}} + \frac{1}{k_{ion}}\right)$ is the sum of the interfacial resistances on the Pt/ionomer and ionomer/gas sides of the film, respectively.[50] The current-time curves for the 100-µm membrane were fit by the method described by Parthasarathy *et al*. The authors concluded that for very thin films, the interfacial resistance is equivalent to adding another 30 to 70 nm of film.[50] This is important for

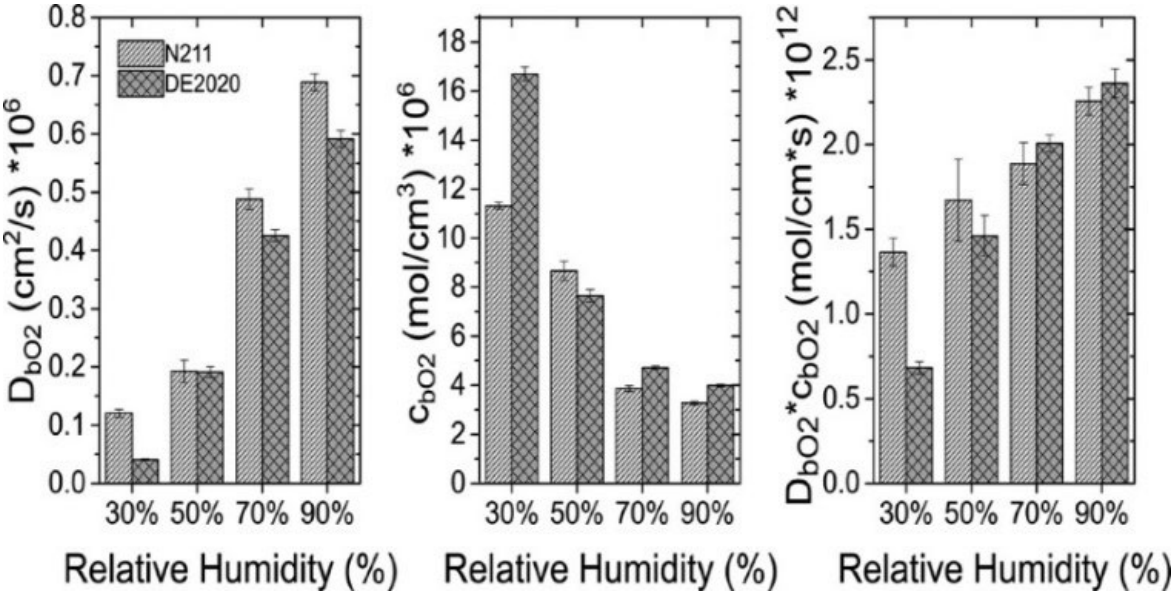

Figure 2.4: Compiled mass-transport parameters for oxygen in Nafion ionomer layers as a function of relative humidity from reference.[51] Reprinted (adapted) with permission from D. Novitski and S. Holdcroft, Determination of O_2 Mass Transport at the Pt | PFSA Ionomer Interface Under Reduced Relative Humidity. *ACS Appl Mater Interfaces*, **7**, 27314 (2015). Copyright 2015 American Chemical Society.

applications that use Nafion films of <100 nm, as this will impose a lower limit on the resistance despite reduction of film thickness below 30 nm. The study also concluded, in support of previous work, that permeability and diffusivity of oxygen gas tend to increase with increasing RH, whereas Henry's constant decreases (note that, due to the use of Henry's constant, the permeabilities reported are per unit pressure (mol/(m·s·Pa))). Similarly, interfacial resistance decreases with increasing RH.

The study of oxygen transport in polymer membranes using MEs has been extended beyond Nafion to include other polymers, including BAM3G 407 (a sulfonated trifluorostyrene copolymer) and 6F-40 (a poly(arylene ether sulfone)).[99, 102, 113] Basura *et al*.[102] compared oxygen transport in Nafion 117 and BAM3G 407 (140 μm), using a 50-μm Pt electrode in both cases at 30°C and 3 atm of O_2 as well as 100% RH. Interestingly, they concluded that although the permeabilities of the membranes were nearly identical (~55 x 10^{-12} mol/cm·s), the BAM3G 407 membrane had a diffusion coefficient about 4 times larger than that in Nafion 117, but the gas concentration of oxygen in Nafion 117 was about 4 times larger than in the BAM3G 407. This finding was attributed to the higher water content of the BAM membrane, providing additional evidence that oxygen transport occurs primarily in water but that it dissolves much easier into the polymer backbone.[17] Chlistunoff studied the mass-transport properties of oxygen in 6F-40, a membrane similar to Nafion but with a morphology that is resistant to interfacial restructuring.[99] The study was performed using 26.5-μm films of 6F-40 on a 100-μm Pt ME at 20°C and 60% RH, finding the diffusion coefficient of oxygen to be 4.5 x 10^{-8} cm^2/s and the gas concentration to be 9.8 x 10^{-6} mol/cm^3.[99] The permeability was 4.4 x 10^{-13} mol/cm·s. Data were fit using both

Eqs. 2.2 and 2.3. This study once again shows the flexibility of MEs for studying polymer membranes.

Novitski *et al*.[108] went further, abandoning the PFSA acidic-electrolyte environment entirely to test the mass-transport parameters of an alkaline membrane, hexamethyl-p-terphenyl polymethylbenzimidazoles (HMT-PMBI) and compare them to FAA-3, an alkaline membrane from FuMA-Tech GmbH. This work used a 53-μm thick membrane of HMT-PMBI and a 5-μm Pt ME, performing all tests using air at varying humidities and 60°C. Multiple films of HMT-PMBI were formulated to test different ion-exchange capacities. The Shoup-Szabo Equation (Equation 2.3) was used to fit the current-time curve to extract the diffusivity and gas concentration as well as a numerical solution. The authors found that, similar to PFSA membranes, oxygen diffusivity and permeability increase with humidity whereas gas concentration decreases for both the FAA-3 and HMT-PMBI.[108] In addition, the HMT-PMBI exhibited higher diffusivities and permeabilities at all humidities compared to FAA-3, while the FAA-3 showed higher gas concentrations at all humidities. Alternatively, membranes with lower EW (and therefore higher water content) demonstrated higher diffusivities and permeabilities but lower gas concentrations. Compared to Nafion, both alkaline membranes demonstrated higher gas transport parameters at higher humidities but lower parameters at lower humidities, leading to the conclusion that transport performance was even more water content dependent than it is in Nafion.

Only the transport parameters for oxygen have been discussed so far. However, it is possible to study other gases in MEs, such as hydrogen. Jiang and Kucernak[105] leveraged the hydrogen oxidation reaction on Pt to study the mass-transport of hydrogen in Nafion. A 50-μm Pt-plated gold electrode was used with Nafion 117 as the electrolyte membrane. Eq. 2.2 was used to fit the current-time curve over the range $0.2<\tau<100$ (see Figure 2.5).[105] The authors found that at 20°C, the diffusion coefficient of hydrogen was 7.6 x 10^{-6} cm^2/s, the gas concentration was 0.51 x 10^{-6} mol/cm^3, and the permeability was 3.9 x 10^{-12} $mol/cm \cdot s$.[105] As temperature increased, diffusivity and permeability increased, whereas gas concentration demonstrated an inconsistent trend.[105] The trends for diffusivity and permeability with temperature align with the results that have been reported for oxygen.[50, 51, 105]

The effect of polymer EW on all of the previously described mass-transport parameters can be easily studied as an extension of the prior works. Buchi *et al*.[107] examined two different types of PFSA membranes: Aciplex (a short side chain PFSA) and Nafion, to determine the impact of equivalent weight (and perhaps the side-chain length).[17] Equivalent weight varied from 880 to 1200 g/mol, with 5 different samples tested.[107] The current-time data were fit to Eq. 2.2; however, the early time data were excluded in this case due to nonlinear behavior at short times.[107] This behavior was attributed to surface-oxide reduction, but the actual cause is unclear. The authors conclude that oxygen diffusivity decreases with increasing equivalent weight, while gas concentration increases over the same range. Permeability exhibited no definitive trend other than Aciplex having a much higher permeability than Nafion, likely due to differences in membrane structure leading to improved oxygen diffusion in the Aciplex membranes.[107] Basura *et al*.[106] performed a similar study with BAM and DAIS polymer membranes. BAM is a sulfonated α,β,β -trifluorostyrene-co-substituted- α,β,β-trifluorostyrene, while the DAIS polymers are sulfonated styrene-(ethylene-butylene)-styrene copolymers. Experiments were performed in a similar manner as other studies, using a 50-μm Pt ME and fit with Eq. 2.2 over a

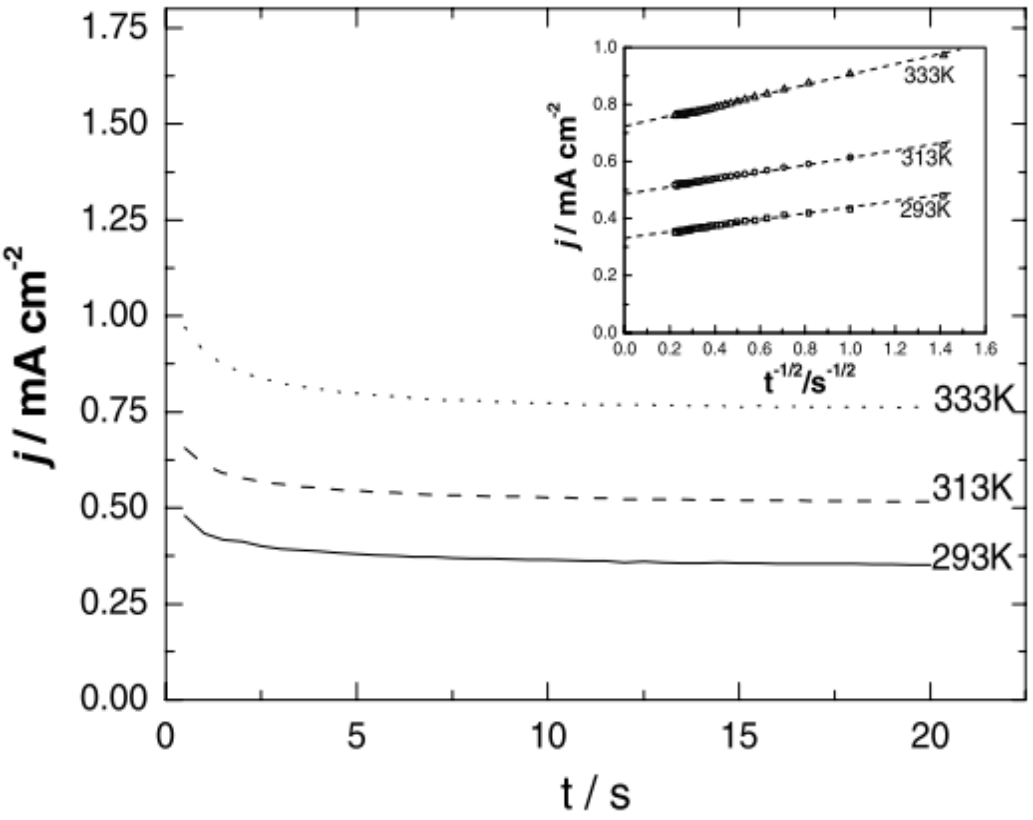

Figure 2.5: Current density-time curves for the HOR at a Pt electrode (inset: current density vs $t^{-1/2}$). Results are quite similar in trend as for oxygen, and the linearity of the plot in the inset is quite clear.[105] Reprinted from the Journal of Electroanalytical Chemistry, 567, J. Jiang and A. Kucernak, Investigations of fuel cell reactions at the composite microelectrode|solid polymer electrolyte interface. I. Hydrogen oxidation at the nanostructured Pt|Nafion® membrane interface, 123-137, Copyright (2004), with permission from Elsevier.

limited, early-time window.[106] Similar to Buchi *et al*., the authors found that oxygen diffusivity decreases with increasing equivalent weight, whereas gas concentration increases. Contrary to the previous works, permeability decreased with increasing equivalent weight, as the drop in diffusivity was higher than the increase in solubility. Taken together, both studies show that the aqueous phase, which increases as equivalent weight decreases, has a large role in the diffusion pathways of oxygen through polymer membranes. In addition, the solubility is much more dependent on the polymer backbone than on the water phase. Examination of these properties was relatively straightforward as a simple extension of previous work and highlights the flexibility of polymer-electrolyte ME cells for studying a wide variety of experimental conditions.

2.5 Flow-through Microelectrode Cell Design

To address the shortcomings of existing microelectrode-cell designs described in sections 2.3 and 2.4, we present an improved design that allows probing and mitigation of poor equilibration

times and contaminants. Basic experimental procedures are performed, showing the redesigned cell's effectiveness for both HOR and ORR. In addition, the effect of applied pressure on electrochemically active surface area (ECSA) and ORR is studied, as well as the effect of gas flowrate, equilibration times, and IR drop.

2.5.1 Experimental Setup

The microelectrode cell is designed using Solidworks CAD software and fabricated from co-polyester, using a 3D printer (Ultimaker, Netherlands) for rapid prototyping purposes. The working electrode (WE) is a 50-µm platinum ultramicroelectrode (UME, Bioanalytical Systems, Inc, West Lafayette, IN, USA), the counter electrode (CE) is a platinum mesh (Alfa Aesar, Ward Hill, MA, USA) coated with Nafion,[50] while the reference electrode (RE) is a commercial dynamic hydrogen electrode (DHE, Gaskatel, Germany). Nafion 211 (Ion Power, New Castle, DE, USA) is the solid-state electrolyte pretreated by boiling and acid exchange.[17] Mechanical pressure is monitored using a piezoresistive force sensor (Tekscan, South Boston, MA, USA) interfaced with an Arduino readout. Placement and spacing of the WE, CE, and RE minimize the distance between the WE/CE and RE and allow for gas flow through the CE while also isolating the WE/CE and RE compartments.

Measurements in liquid electrolyte were performed with the commercial DHE, Pt microelectrode, and a Pt wire immersed in 0.5 M sulfuric acid. The microelectrode was plated with Pt prior to use, using a solution of chloroplatinic acid, hydrochloric acid, and deionized water. The WE was placed in the plating solution, along with a 35.6 x 5.7 mm Pt mesh CE, and 2 V was applied for ~1 min to plate the electrode. All glassware was acid cleaned, and measurements were taken to control UME cleanliness throughout plating, handling, and storage.

2.5.2 Electrochemical Measurements

All electrochemical measurements were performed with an SP-150 potentiostat with a low-current card (Bio-Logic, France) at room temperature. Gases were fed by a mass-flow controller (MKS, Andover, MA, USA) either dry or through a humidifier (Fuel Cell Technologies, Albuquerque, NM, USA) before entering the microelectrode cell. Gas flow was maintained throughout the entirety of the experiments. For ECSA measurements, cyclic voltammetry (CV) was performed under humidified argon from 0 to 1.4 V vs DHE at a scan rate of 50 mV/s. ECSA was calculated by integrating under the hydrogen desorption peak (in the range of ~0-0.43 V vs DHE) after subtracting the capacitive background current to find the total surface charge, then normalizing by a standard hydrogen monolayer charge of 210 µC/cm^2.[51] For HOR and ORR kinetic measurements, cyclic voltammetry was performed using 2% H_2 in Ar and 4% O_2 in nitrogen, respectively, from 0 to 1 V vs DHE at a scan rate of 20 mV/s. All chronoamperometric

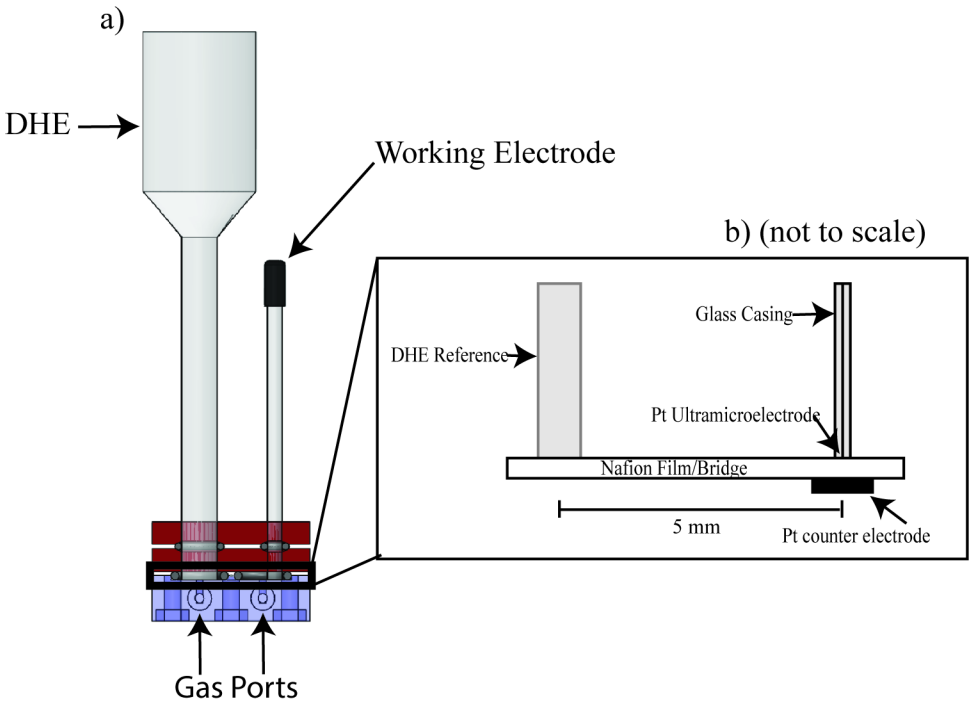

Figure 2.6. Schematic of microelectrode cell design. a) shows a cross-section from the side. The front and back of the UME cell each have a gas port for each chamber providing an inlet and outlet. b) shows a detailed layout of the components that make the cell circuit.

holds were performed at 0.5 V vs DHE and held for 5 min. The current for these holds was determined by averaging the last 100 s of the hold. Electrochemical impedance spectroscopy was performed at 0.5 V vs DHE from 100 mHz to 1 MHz at a perturbration amplitude of 10 mV.

2.5.3 Microelectrode Cell Design

A CAD rendered image of the microelectrode cell is shown in Figure 2.6. Briefly, the design consists of two separate chambers, one for the working and counter electrodes, and one for the reference electrode with a small path between the two chambers for the reference bridge to pass and make ionic contact (Figure 2.6a). The counter electrode is placed on the bottom of the larger chamber, and the reference bridge (Nafion 211) is placed on top, with its other end placed in the reference electrode chamber. Two Viton O-rings seal the chambers and prevent gas leakage. Gas enters and exits each chamber through gas inlet/outlet ports at the chamber edges; gas tubes can be attached to larger ports on the side of the overall cell. Each chamber has its own set of channels, allowing for different gases to be fed in each one. When using the commercial DHE the reference flow ports are closed.

A two-piece lid, shown as red in Figure 2.6a, guides and compresses the WE and RE to the base using screws while also sealing the cell against gas leakage. A two-piece cell top compartment is used because the screws and both electrodes pass through O-rings in the lid to provide additional protection against gas leakage. Both the working electrode and DHE pass through this top

compartment and press directly into the reference bridge, completing the cell (Figure 2.6b). Nafion acts both as an electrolyte bridge and as the ionomer interface with the Pt UME. Contact is made with the CE by a wire fed out through the gas outlet port. Pressure is applied to the WE and RE using high precision screws to maintain consistent electrode contact using an external frame structure, not shown. Pressure on the WE is measured *in situ* by placing the piezoresistive force sensor between the microelectrode and high precision screw.

2.5.4 Design Feasibility

After plating the UME, we perform cyclic voltammetry at a scan rate of 50 mV/s in a liquid electrolyte cell under argon and compare to the same conditions in the microelectrode cell. The gases are humidified at ~95% and 1.38 MPa (200 psi) is applied to the working electrode in the solid-state cell. Cyclic voltammetry results are seen in Figure 2.7. There is good agreement between the CVs in sulfuric acid and the Nafion in the UME cell. In argon, these currents are primarily derived from hydrogen adsorption/desorption and oxide formation/reduction.[86] A small (~20 mV) reference shift is also seen when using the solid-state cell compared to the aqueous electrolyte. This is likely a result of a mixed-junction potential in the reference chamber caused by the membrane. When 2% hydrogen gas is used in the UME cell, a positive shift in current in the CV is seen compared to under Ar. This likely comes from the positive contribution of the hydrogen oxidation current. An apparent reduction in OH adsorption occurs during HOR, seen in

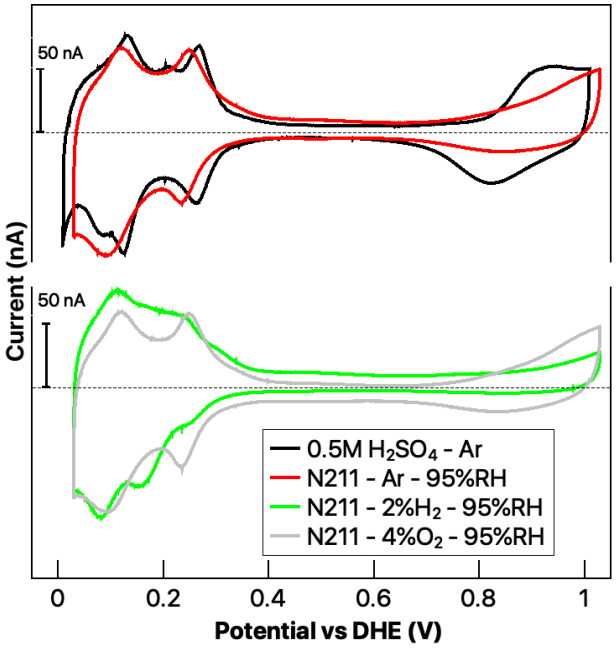

Figure 2.7: CV scans at 50 mV/s at various operating conditions. The applied mechanical pressure was 1.38 MPa (200 psi) when Nafion 211 was used. Solid-state cell was humidified at ~95% for measurements.

the smaller area contained in the CV near 1 V vs DHE compared to ORR or under Ar, but the reason for this is unknown. Similarly, when 4% oxygen gas is used, a negative shift in the CV is observed, likely caused by the negative contribution of the ORR current.

2.5.5 Effect of Mechanical Pressure on Roughness Factor and ORR

ECSA was measured as described in section 2.5.2. The ECSA was then divided by the geometric area (GA) to obtain the roughness factor (RF). The roughness at different mechanical pressures is reported in Figure 2.8. RF remained relatively unchanged with increasing pressure, fluctuating around a value of 145 cm^2/cm^2. The slight variation in values is likely a result of measurement error. Below 0.34 MPa (50 psi), RF values were inconsistent and inaccurate and were omitted from this work. For comparison, the RF of the electrode in liquid was ~192 cm^2/cm^2. One potential reason for this difference is that the microelectrode is plated, which induces sub-micrometer features. In the aqueous cell, the liquid electrolyte can contact all of these features, increasing the area for adsorption/desorption and the measured current. However, in the solid-state cell, Nafion electrolyte is restricted to contact a more limited area of the electrode (the "peaks"), which results in a lower ECSA.

The change in the ORR current, measured using chronoamperometry, was also examined. Similarly, no significant trend was observed with applied pressure, with currents varying from ~5.17 to 5.31 nA across the 2.76 MPa (400 psi) range. These results demonstrate the mechanical

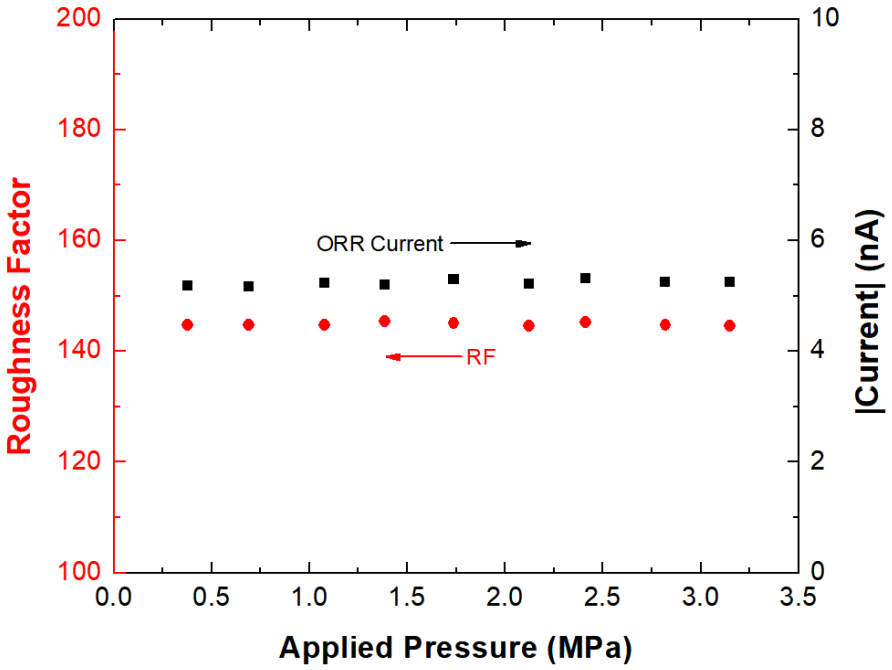

Figure 2.8: Effect of mechanical pressure on both roughness factor and ORR current. In both cases, no discernible trend is observed, with little absolute change in values across the 2.76 MPa (400 psi) range.

robustness of our microelectrode cell. Even if the pressure varies slightly, electrode contact remains sufficient to produce consistent results. 1.38 MPa (200 psi) was chosen as the mechanical pressure to carry out all subsequent experiments.

2.5.6 Effect of Gas Flowrate on ORR Current

To examine further the robustness of the experimental design, the 4% oxygen gas flowrate was varied, and the resulting ORR currents were measured via chronoamperometry (Figure 2.9). No significant trend was observed across a flowrate range as wide as 50 to 500 cm^3/min. Three things then become apparent. One, gas-phase convection is not important in the system. Measured currents are ionomer diffusion-controlled, as expected. Two, the system is not oxygen limited, allowing for mass-transfer-limited currents to be determined. Three, changing the flowrate of the gas does not change the hydration of the membrane. Additionally, small fluctuations in flowrate as a result of mass-flow-controller error or other causes should have minimal impact on results.

2.5.7 Equilibration Time

One of the advantages of a flow-through UME cell compared with previous UME designs is smaller equilibration times. For standard UME designs, equilibration times often are greater than

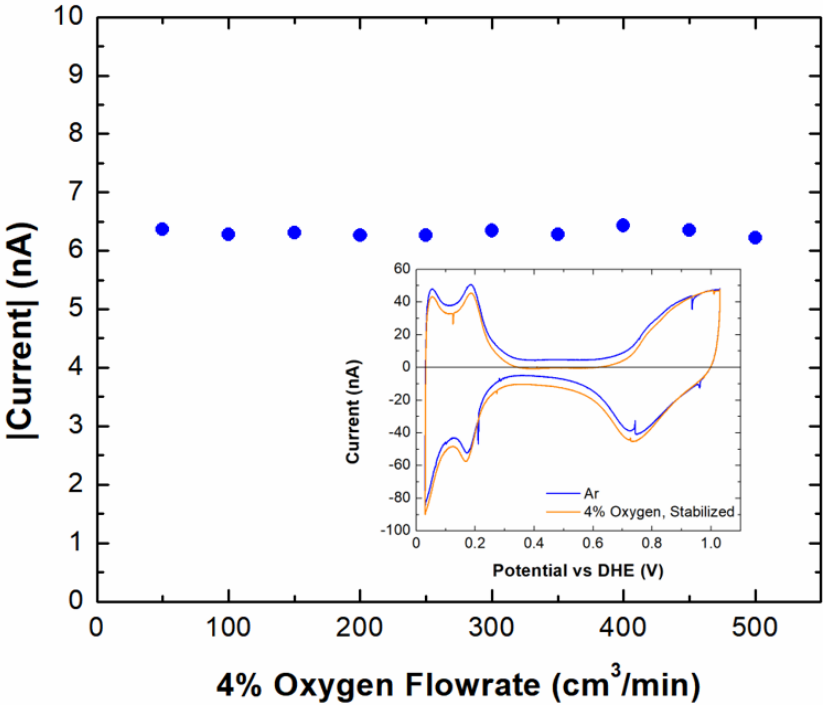

Figure 2.9 : Plot of absolute value of ORR current versus oxygen gas flowrate. There is no discernible trend as flowrate increases. Inset plot shows CVs before and after switching from Ar to 4% O_2 gas. The O_2 gas CV stabilized after 7 cycles, approximately 12 min after the switch.

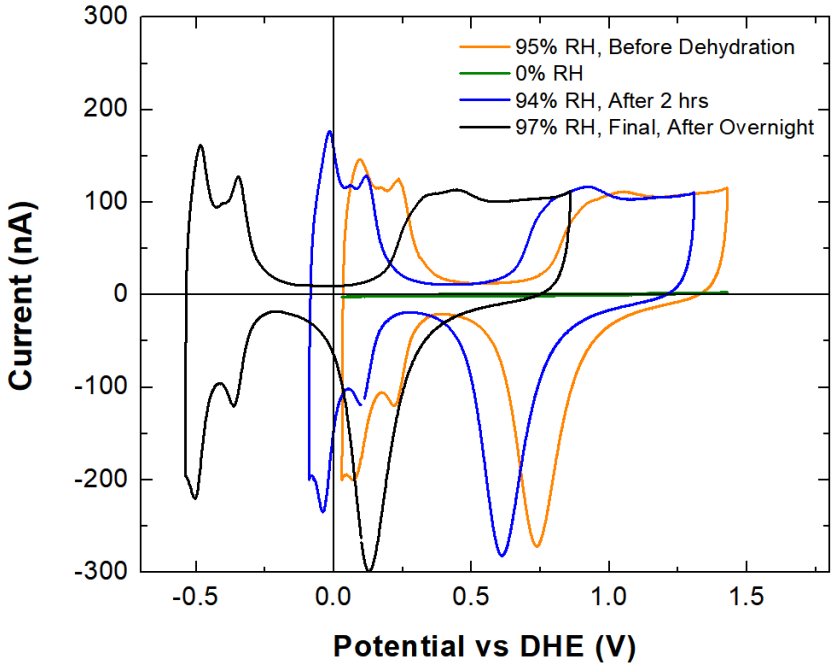

Figure 2.10: CVs taken both before and after dehydration of Nafion membrane. Scans are performed at 50 mV/s (0% RH line lies on the x-axis).

12 h.[51, 114] One of the proposed benefits of the present cell design is that the small volume and gas flow into the working electrode chamber dramatically reduces the time needed for the membrane to equilibrate. To test this hypothesis, a CV was taken at ~95% relative humidity followed by drying the cell with 0% RH argon. The cell was then rehydrated, and additional CVs were performed. Results are shown in Figure 2.10. They demonstrate two major points. First, the system is highly responsive to changes in RH, as the CV taken at 0% RH has a very small magnitude and is highly resistive. Second, the membrane recovered quite quickly, with peaks reaching their previous level of magnitude after about 2 hours. It may have equilibrated faster if not limited by the humidifier. However, there was a significant shift in the reference electrode. After 2 hours, the reference shifted −110 mV, and after the overnight equilibration nearly −600 mV. This shift did not impact peak height or shape. It is unknown what caused this shift, but one possible solution is to humidify and control the gas flowing into the reference chamber, as this was not done in this experiment.

A second test was performed to ascertain equilibration of the system when switching from one gas to another (e.g., Ar to 4% O_2). To accomplish this, a CV scan at 20 mV/s was started under Ar at 95% humidity (see inset in Figure 2.9). During the scan, the gas was changed to 4% O_2, also at 95% humidity. The CV scan stabilized after just 7 cycles, which took about 12 min. Further work is needed to confirm the accuracy of these measurements and to determine what effect, if any, the CV experiment has on the time for equilibration.

2.5.8 IR-Drop Measurements

Electrochemical-impedance spectroscopy measured the IR drop in the microelectrode apparatus between the working and counter electrodes. From a plot of the imaginary part versus the real part of the resistance, the x-intercept was calculated by interpolation, resulting in an area-normalized resistance of 0.133 Ω-cm^2, which is expected for hydrated N211.[115] This resulted in an IR drop of -7.34×10^{-10} V, which is negligible in practice.

2.6 Conclusions

Studying polymer electrolytes and the ionomer/electrode interface with microelectrodes is an underdeveloped, yet important aspect of modern electrochemistry. Progress has been slow and disjointed; it is only recently that the available body of research has expanded to include basic studies such as numerical modeling of transport in the membrane. However, in the last few years significant progress has been made with the developments by several groups on new types of membranes and thin films. Care must be taken in both the data acquisition and the data analysis, especially in terms of understanding mass transport (as discussed in Chapter 3) and the impact of contaminants.

One significant area of future growth is in the standardization and improvement of ME studies. On the hardware side, even with recent improvements, many ME cells lack efficiency (*e.g.*, long equilibration times) and/or features to improve accuracy, such as using a dedicated reference electrode. As these designs mature, it will become easier to study other aspects of membrane performance, such as with non-Nafion thin films and membranes, doped ionomers, and other reactions and electrode materials. The flowthrough-cell design described in this chapter is one step toward this goal. During testing of the flowthrough cell, both ORR and HOR behavior was observed, and this behavior did not change with mechanical pressure or gas flowrate. In addition, equilibration time was very small, potentially as low as 12 min when switching Ar to 4% O_2, although further work is needed to confirm this result, correcting one of the major issues with previous ME cells. Finally, the measured IR drop in the cell was very small. These results demonstrate that the new microelectrode-cell design is robust. Applications of the flowthrough cell are explored in subsequent chapters.

2.7 Symbols

Roman

A: electrode area

C: gas concentration in the membrane

D: gas diffusivity

ECSA: electrochemical surface area

F: Faraday's constant

I: limiting current

i_d: limiting current

K_H: Henry's constant

k_{Pt}: overall mass-transport coefficient at the Pt/ionomer interface

k_{ion}: overall mass-transport coefficient at the ionomer/gas interface

n: number of electrons

P_{O_2}: oxygen partial pressure

R_e: electrode radius

R_{O_2}: oxygen transport resistance

t: time

Greek

π: the constant Pi

τ: dimensionless time

3. Gas Mass-Transport Coefficients in Polymer Membranes Using a Microelectrode[†]

3.1 Abstract

Gas permeability, the product of gas diffusivity and the Henry gas-absorption constant, of ionomer membranes is an important transport parameter in fuel-cell and electrolyzer research, as it governs gas crossover between electrodes and perhaps in the catalyst layers as well. During transient operation, it is important to divide the gas permeability into its constituent properties as they are individually important. Although transient microelectrode measurements have been used previously to separate the gas permeability into these two parameters, inconsistencies remain in the interpretation of the experimental techniques. In this work, a new interpretation methodology is introduced for determining independently diffusivity and Henry's constant of hydrogen and oxygen gases in ionomer membranes (Nafion 211 and Nafion XL) as a function of relative humidity using microelectrodes. Two time regimes are accounted for. At long times, gas permeability is determined from a 2D numerical model that calculates the solubilized-gas concentration profiles at steady state. At short times, permeability is deconvoluted into diffusivity and Henry's constant by analyzing transient data with an extended Cottrell equation that corrects for actual electrode surface area. Gas permeability and diffusivity increase as relative humidity increases for both gases in both membranes, whereas Henry constants for both gases decrease with relative humidity. In addition, results for Nafion 211 membranes are compared to a simple phase-separated parallel-diffusion transport theory with good agreement. The two-time-regime analysis and the experimental methodology can be applied to other electrochemical systems to enable greater precision in the calculation of transport parameters and to further understand gas transport in fuel cells and electrolyzers.

[†]This chapter was originally published as "Petrovick, J. G., Radke, C. J., Weber, A. Z. Gas Mass-Transport Coefficients in Ionomer Membranes Using a Microelectrode. ACS Measurement Science Au, 2022, 2, 3, 208-218". Portions of this chapter were published as "Petrovick, J. G., Anderson, G. C., Kushner, D. I., Danilovic, N., Weber, A. Z. Method – Using Microelectrodes to Explore Solid Polymer Electrolytes. Journal of The Electrochemical Society, 2021, **168** 056517". Adapted with permission from all co-authors.

3.2 Introduction

Proton-exchange-membrane fuel cells (PEMFCs) are a critical next-generation renewable energy technology due to their potential to replace traditional internal combustion engines in both light- and heavy-duty transportation. PEMFCs operate through the conversion of hydrogen and oxygen gases to water vapor via hydrogen-oxidation (HOR) and oxygen-reduction (ORR) reactions. These reactions occur at the anode and cathode catalyst layers, respectively, and are separated by an ion-conducting polymer (ionomer). As a result, crossover of gases, specifically hydrogen and oxygen, through the ionomer membrane is deleterious and a significant contributor to PEMFC inefficiencies as the movement of hydrogen and/or oxygen to opposing electrodes can result in Pt degradation and mixed potentials.[17, 44] Ionomer thin films also act as a binder and ion conductor in the catalyst layers to hold together agglomerates of platinum (Pt) catalyst supported on carbon particles; it has been shown that oxygen transport through these films can limit fuel-cell performance.[12, 61] The gas permeability of the membrane or thin film captures gas transport under steady-state conditions.[116] However, fuel cells do not solely operate at steady state. In applications such as heavy-duty trucks, power loads vary due to both normal operation and fuel cell degradation.[6, 117, 118] Thus, the individual parameters permeability, diffusivity, and Henry's constant are necessary to capture fully the transient fuel-cell performance.[116]

The most common PEMFC ionomer is Nafion, a perfluorosulfonic acid (PFSA) polymer. It consists of a hydrophobic fluorinated polyethylene backbone with ether-fluorocarbon side chains that terminate in hydrophilic sulfonic-acid groups.[17] PFSA ionomers are phase-separated with discrete polymer- and water-filled domains, and are typically categorized by their equivalent weight (EW), or grams of dry polymer per mole of ionic group.[17] Several different models for the microstructural phase separation in Nafion have been proposed; see Chapter 1.2 for more detail.[17, 18, 26, 30] However, for the present analysis, a simple phase-separated parallel-channel model captures the impact of water content on the effective gas transport properties, as discussed below. The atomistic microstructure can also be influenced by the surface Nafion is coated on, including the presence of lamellae as discussed in the literature,[119-122] although such nanoscopic details are averaged over in our analysis as part of the membrane and catalyst system.

The diffusivity, Henry's constant, and permeability of oxygen gas in Nafion membranes is well-studied.[42, 43, 50, 51, 59, 123, 124] Conversely, hydrogen gas is less well-studied, with a primary focus on permeability in-lieu of individual diffusivity and Henry's constant (see Chapter 1.3 for more detail on previous gas transport studies).[43, 58, 60, 125] There are several methods to interrogate gas-transport properties, including gas cross-over, electrochemical monitoring, and permeation experiments.[42, 58, 123, 126] The apparatus discussed here is a microelectrode, traditionally defined as an electrode smaller than 100 μm in lateral dimension.[86] Microelectrodes have several advantages, including a well-defined working-electrode area, extremely low current draw, and an apparatus that acts as a mimic for the environment found in a PEMFC; see Chapter 2 for more detail on the benefits of microelectrodes.[127]

A typical microelectrode assemblage features a microelectrode pressed into contact with an ionomer membrane with the entire chamber exposed to humidified reactant gases (see Chapter 2.3.1). Here, the electrostatic potential difference is adjusted to attain the limiting-current regime. Once limiting-current conditions are met, current decay is recorded as a function of time. Current history is then fit by mathematical expressions, such as those of Cottrell or Shoup-Szabo

(Equations 2.2 and 2.3), to determine diffusivity and Henry's constant.[51] The governing mathematical expressions have been rigorously studied for aqueous electrolytes (equivalent to infinitely thick membranes in our microelectrode), notably by the work of Zoski and Oldham.[128] However, our membranes are of finite thickness, requiring a more detailed analysis, as discussed below.

Despite the large effort invested, questions linger about quantitative gas-transport values obtained.[42, 43, 50, 51, 59, 106-108, 115, 123, 126, 129] Most works follow the same general experimental procedure, discussed in the previous paragraph, involving chronoamperometry performed at limiting-current conditions. Disagreements arise with the analysis of the data, including what equations to use and where to apply them. First, there is disagreement over the interpretation methodology. The original work by Parthasarathy *et al.* advocated the Cottrell equation, whereas Chlistunoff *et al.* used the Shoup-Szabo equation, and Novitski *et al*. recommended using only a numerical model, discarding analytical solutions entirely.[59, 99, 108] In the latter case, deviations of up to approximately 30% between the analytical and numerical models are reported.[108] Second, the time range utilized for fitting the adopted equations to experimental data varies widely. Parthasarathy *et al*. used a large time range of up to ~20 s, whereas Novitski *et al*. fit a linear section in the ms regime and Chlistunoff concluded that no longer than ~10 s should be exercised. Although general trends remain similar between these analysis techniques, the values of oxygen mass-transport parameters can vary by over an order of magnitude among various studies, even for very similar experimental systems and membranes.[50, 51, 59] Finally, some studies report anomalous deviations from expected currents at very short time scales.[107]

In this work, an improved interpretation method is developed for interpreting the current-time curves at mass-transport limiting current. The procedure ensures high precision by analyzing short-time and long-time current asymptotes, rather than relying only on short-time measurements. A rigorous 2D diffusion model describes the long-time steady behavior in a finite-thickness membrane, while a surface-roughness-extended Cottrell expression accounts for short times. Our proposed analysis method is applied to ionomer membranes of Nafion 211 and Nafion XL, a polytetrafluoroethylene-reinforced variant of Nafion. The gas diffusivity, Henry's constant, and permeability are presented for both hydrogen and oxygen gases as functions of relative humidity. Finally, a simple phase-separated parallel-diffusion model explores the experimental results for Nafion 211, allowing for greater insight into the physical transport processes occurring within PFSA ionomers.

3.3 Experimental Methods

3.3.1 Microelectrode Cell Design

The experimental microelectrode cell has been described previously (see Chapter 2.5).[103] A schematic is provided in Figure 3.1. In brief, the cell is a two-chambered, flow-through design

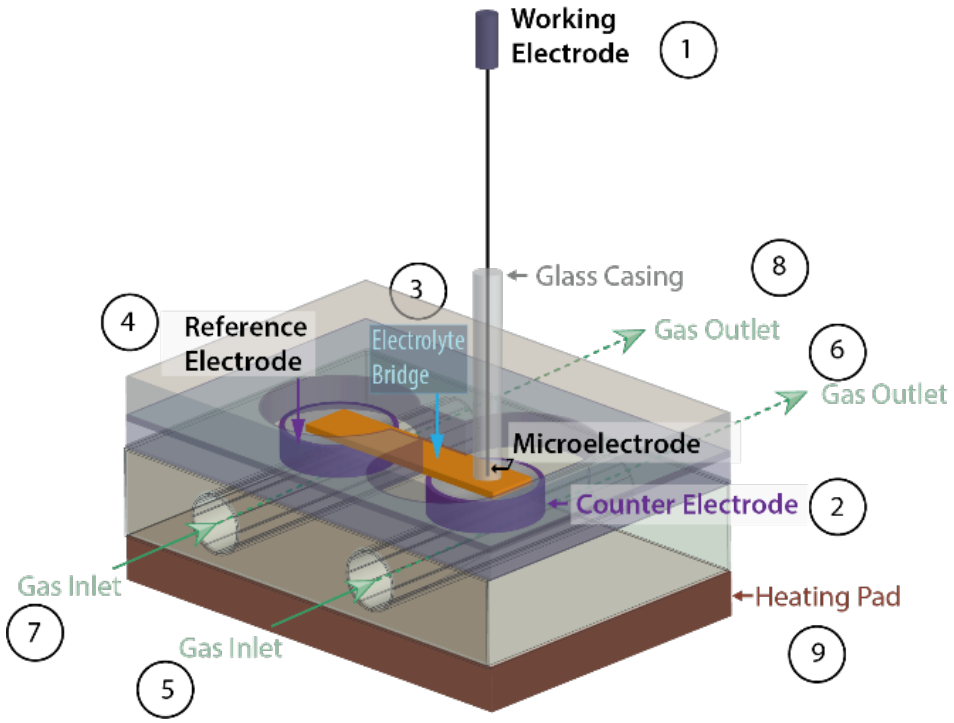

Figure 3.1: Schematic of microelectrode cell. Electrodes are labeled (1), (2), and (4), while the electrolyte resides near (3). Gas enters through the inlets (5) and (7) and exits through the outlets (6) and (8). A heating pad (9) sits beneath the cell but is unused in this chapter.

with one chamber containing the working (micro-) and counter electrodes and one for a reversible hydrogen (RHE) reference electrode. The two chambers are sealed but are connected by a salt bridge of the ionomer of interest (*e.g.*, Nafion 211), which also serves as the electrolyte separating the working and counter electrodes. Gas is humidified before entering the cell and each chamber's gas flow is controlled independently. To ensure good contact between the working electrode and the membrane, a fine-threaded screw applies mechanical force to the top of the working electrode, as measured by a resistive pressure sensor. To prevent leakage of reactive gases directly to the electrode surface (thereby bypassing the membrane), a Nafion adhesion layer is first dropcast on the microelectrode prior to cell construction by placing a single drop of D2021 Nafion dispersion (Ion Power, Delaware, USA) on the microelectrode tip. The cell is wrapped in a Faraday cage of aluminum foil to limit electrical noise.

3.3.2 Materials

The microelectrode cell is fabricated from inert polyether ether ketone (PEEK) (McMaster-Carr, Illinois, USA). A 50-µm Pt microelectrode (BASi, Inc., Indiana, USA, polished sequentially using 15-µm diamond, 3-µm diamond, 1-µm alumina, and 0.05-µm alumina powder, rinsed with deionized water to remove contaminants, and dried under an N2 stream) is the primary working electrode, whereas the counter and reference electrodes are Pt-coated gas-diffusion electrodes (GDE) (Sigracet 25BC, 0.5 mg/cm^2 Pt, SGL Carbon, Wiesbaden, Germany). The two membrane types used were Nafion 211 (25 µm, 1100 EW, preboiled,[17] Ion Power, Delaware, USA) and

Nafion XL (~28 μm, 1100 EW, as-received, Ion Power, Delaware, USA). Both are proton-exchange membranes. In addition, Nafion XL is reinforced with an ~3-μm polytetrafluoroethylene layer for additional mechanical stability.[45] Water uptake and swelling profiles account for the change of membrane thickness with humidity.[17, 45] Gases used were argon (Praxair, Connecticut, USA), hydrogen (Praxair, Connecticut, USA, 2% in argon), and oxygen (Airgas, Pennsylvania, USA, 4% in nitrogen).

Atomic force microscopy (AFM) was performed on a bare Pt microelectrode with a Bruker (Massachusetts, USA) AFM probe over a scanning window of 10 μm x 10 μm. The open-source Gwyddion software package (Czech Metrology Institute, Czech Republic) performed post-processing and analyzed the AFM images.

3.3.3 Electrochemical Surface Area

Cyclic voltammetry (CV) ascertained the electrochemical surface area (ECSA) of the microelectrode surface by evaluating the area of the hydrogen underpotential-deposition region.[127] In this method, the peaks appearing in the approximate range of 0 to 0.4 V on the CV scan represent hydrogen desorption and adsorption depending on whether the current is positive or negative, respectively.[86] By integrating the area under the desorption peak, subtracting the double-layer capacitance region, and dividing by the scan rate, the total adsorbed charge from this process can be determined. By assuming that the hydrogen adsorbs in a monolayer with a surface charge density of 210 μC/cm^2,[86] the electrochemical surface area is calculated by[51]

$$ECSA = \frac{A_{UC}}{\nu \rho_s} \tag{3.1}$$

where *ECSA* is the electrochemical surface area, A_{UC} is the area under the curve [A·V], ν is the scan rate [V/s], and ρ_s is the surface charge density [C/cm^2]. The roughness factor, R_F, is then defined as the *ECSA* divided by the geometric area. Details are given in Section 3.8.2. CV curves were recorded under argon gas at room temperature and 90% relative humidity (RH) at a scan rate of 50 mV/s. Three CVs were recorded with high reproducibility, with the surface area calculated from either cycle 2 or 3, depending on feature clarity. Prior to the recorded CVs, 50 sequential CVs were performed at a scan rate of 500 mV/s to clean the surface. A typical CV scan is given in Figure S3.1 with the pertinent integrated area highlighted. R_F values varied depending on the specific electrode in use but ranged from 4.3 to 14.8.

3.3.4 Electrochemical Techniques

Chronoamperometry was used to determine the mass-transport coefficients of oxygen and hydrogen in the ionomer membranes.[86] Prior to measurement, the microelectrode cell was held at open-circuit voltage (OCV) for 10 min, until no significant change in OCV with time was observed. The potential was then set to 0.5 V versus OCV and –0.7 V versus OCV for hydrogen and oxygen, respectively, where the specific values were predetermined from identifying the

mass-transport limit in obtained polarization curves (see Figure S3.2a and S3.2b for ORR and HOR, respectively, in Section 3.8.3 of SI). Potentials were held at those values for 5 min with the transient current recorded every 100 ms using an SP-300 potentiostat (Bio-Logic, Seyssinet-Pariset, France) equipped with an ultra-low current precision channel. The humidity of each chamber was controlled either by external humidifiers (Humidification System, Fuel Cell Technologies, New Mexico, USA) or by a custom wet/dry gas mixing bubbler and varied depending on the particular membrane under study to capture an effective range of relative humidities. Nafion 211 was tested at 25, 60, 75, 85, and 95% RH. Nafion XL was tested at 30, 60, 75, 85, and 90% RH. All measurements were performed at room temperature, approximately 20°C.

3.4 Theory

3.4.1 2D Numerical Solution for Transient Current

Gas diffusion to the surface of the microelectrode through the ionomer membrane is the subject of several previous studies.[50, 51, 59, 106, 107] In most works, however, a modified Cottrell equation fits the current transient to extract gas diffusivity and Henry's constant.[127] The modified Cottrell equation describes the mass-transport limiting-current density at a planar electrode in a semi-infinite electrolyte as a function of time.[59, 110, 111] A typical form for use with disk electrodes of radius R_e is[59]

$$I = \frac{\left(nF\pi^{\frac{1}{2}}R_e^2 D^{\frac{1}{2}} H P_{g,\infty}\right)}{\sqrt{\mathrm{t}}} + \pi nFDHP_{g,\infty}R_e \tag{3.2}$$

where I is current, n is the number of electrons transferred, F is Faraday's constant (96485 C/mol), D is the effective membrane gas diffusivity, $P_{g,\infty}$ is the set external gas partial pressure, H is the effective Henry's constant, and t is time.[59] The first term on the right of Equation 3.2 corresponds to transient growth of a diffusion boundary layer in a stagnant infinite medium, while the second term is empirically added to describe the steady-state current to a finite radius disk in an infinite electrolyte. Other solutions do exist, with varying degrees of accuracy and complexity. A more accurate solution was provided by Aoki and Osteryoung[130, 131]:

$$I = \frac{4nFADC}{\pi R_e}\left[0.88623\tau^{-\frac{1}{2}} + 0.78540 + 0.094\tau^{\frac{1}{2}}\right], \tau_I < 1$$

$$I = \frac{4nFADC}{\pi R_e}\left[1 + 0.71835\tau^{-\frac{1}{2}} + 0.05626\tau^{-\frac{3}{2}} - 0.00646\tau^{-\frac{5}{2}} + \cdots\right], \tau_I > 1 \tag{3.3}$$

where

$$\tau_I = \frac{4Dt}{R_e^2} \tag{3.4}$$

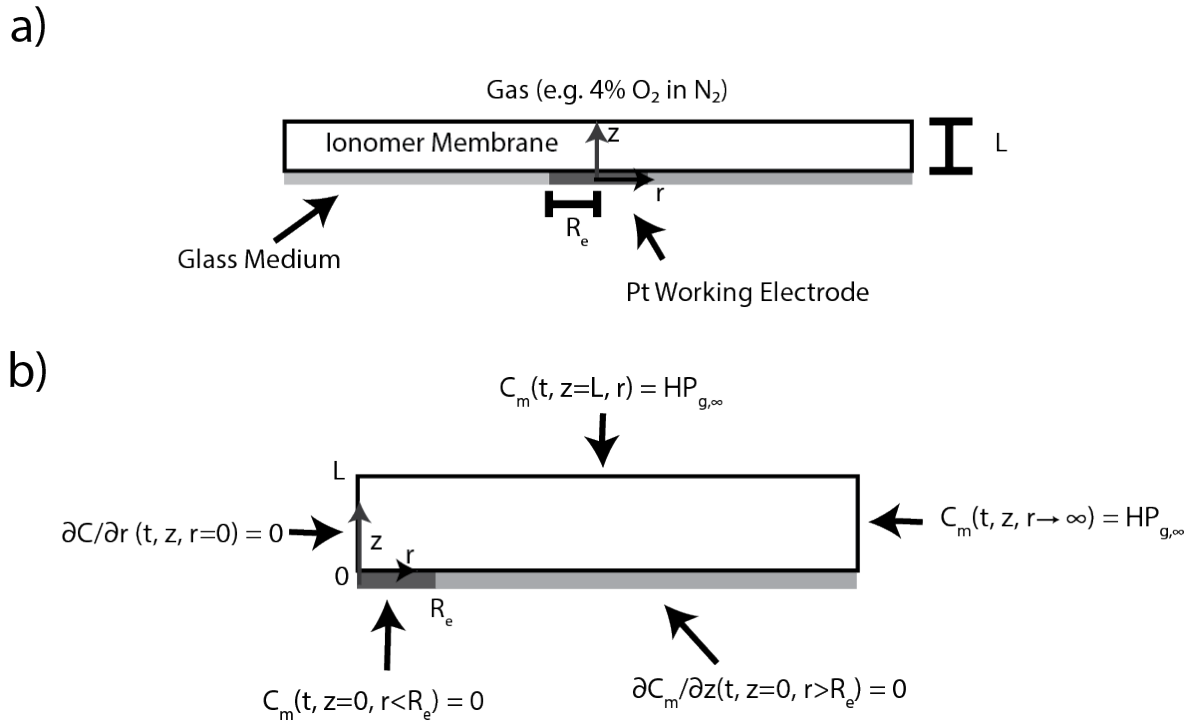

Figure 3.2: a) Schematic of electrode geometry in the microelectrode. b) Schematic of the calculation domain labeling the boundary conditions for the microelectrode, except for the initial condition $C_m(0, z, r) = HP_{g,\infty}$.

A is the electrode area, and C is the concentration of gas within the membrane at the gas-membrane interface.[86] This solution is separated into two regimes for short and long times, with the division at $\tau_I = 1$.[86] An alternative, empirical solution has been formulated by Shoup and Szabo[112]:

$$I = \frac{4nFADC}{\pi R_e}\left[0.7854 + 0.8862\tau^{-\frac{1}{2}} + 0.2146e^{-0.7823\tau^{-\frac{1}{2}}}\right] \tag{3.5}$$

which is within 0.6% of the solution given by a variation of Eq. 3.2 at all times (the factor of π is replaced by 4, in this case).[86] More exact solutions do exist, but they are not typically necessary, as experimental error usually exceeds the additional accuracy provided.[132]

However, an infinite thickness membrane is not achievable in a microelectrode cell where the membrane thickness is on the same order as the electrode size, rendering the accuracy of the steady-state term questionable. In addition, the first term on the right side of Equation 3.2 is restricted to short times only, where the boundary of the diffusion field has not reached the thickness of the membrane; it is not clear at what precise time this condition is met.

To alleviate the finite-membrane-thickness approximation in Equation 3.2, a 2D numerical model was implemented based on molecular diffusion through the membrane. Figure 3.2a illustrates the system geometry. A finite-radius flat-disk electrode of radius R_e is embedded in an impermeable substrate that extends infinitely in the r dimension. The infinite-radius ionomer membrane rests on this surface and extends in the z direction to a distance L, the thickness of the

membrane. The system is symmetric in the azimuthal coordinate. This geometry demands 2D transient diffusion in cylindrical coordinates:

$$\frac{\partial C_m}{\partial t} = D\left[\frac{1}{r}\frac{\partial}{\partial r}\left(r\frac{\partial C_m}{dr}\right) + \frac{\partial^2 C_m}{\partial z^2}\right] \tag{3.6}$$

where r is the radial coordinate, z is the axial coordinate, and C_m is the gas concentration per unit volume of membrane. To solve this equation, four boundary conditions and one initial condition are required:

$$[C_m\,(t, r < R_e, z\ =\ 0) =\ 0;\ \frac{\partial C_m}{\partial z}(t, r > R_e, z = 0) = 0]$$

$$\frac{\partial C_m}{\partial r}(t, r = 0, z) = 0; C_m(t, r = \infty, z) = HP_{g,\infty} \tag{3.7}$$

$$C_m(t, r, z = L) = HP_{g,\infty};\ C_m(t = 0, r, z) = HP_{g,\infty}$$

In order, the boundary conditions correspond to zero surface concentration at the electrode due to limiting current and zero surface flux in the surrounding impermeable glass medium (a piecewise boundary condition at $z = 0$), symmetry at the membrane center, constant equilibrium membrane concentration as r approaches infinity, constant equilibrium membrane concentration at the membrane finite-thickness boundary, and constant equilibrium concentration prior to the application of an electric potential. The fourth and fifth expressions state that the membrane exterior is in equilibrium with the external gas supply. Figure 3.2b delineates the boundary conditions.

At the surface of the electrode, the mass-transport-limited current is calculated from the expression:

$$I(t) = -2\pi nFD\int_0^{R_e}\left[\frac{\partial C_m}{\partial z}(t, r, z = 0)\right] r dr \tag{3.8}$$

Upon nondimensionalizing C_m by $HP_{g,\infty}$, r by R_e, and z by L, Equation 3.8 reduces at steady state to

$$I\ (t = \infty) = -\pi nFDHP_{g,\infty}R_e\left[\frac{2R_e}{L}\int_0^1 \frac{\partial \widetilde{C_m}}{\partial \tilde{z}}(\infty, \tilde{r}, 0)\tilde{r}d\tilde{r}\right] \tag{3.9}$$

where the over-squiggle symbol reflects nondimensional variables. The bracketed term on the right of Equation 3.9 is a function only of the geometry. Accordingly, the steady finite-thickness current is not equivalent to the steady infinite-thickness current in Equation 3.2. As in Equation 3.2, however, only the product HD, or gas permeability, P, appears in Equation 3.9. Thus, P is readily calculated by fitting Equation 3.9 to the measured steady-state current. Once permeability is known, the measured transient current can then be fit to the transient solution of Equation 3.8 to determine D (or H). Equations 3.6 and 3.7 (and thus the gradient in Equation 3.8) are solved numerically in a finite-element multiphysics model, COMSOL 5.6. Numerical details (*e.g.*, mesh density, etc.) can be found in Section 3.8.4.

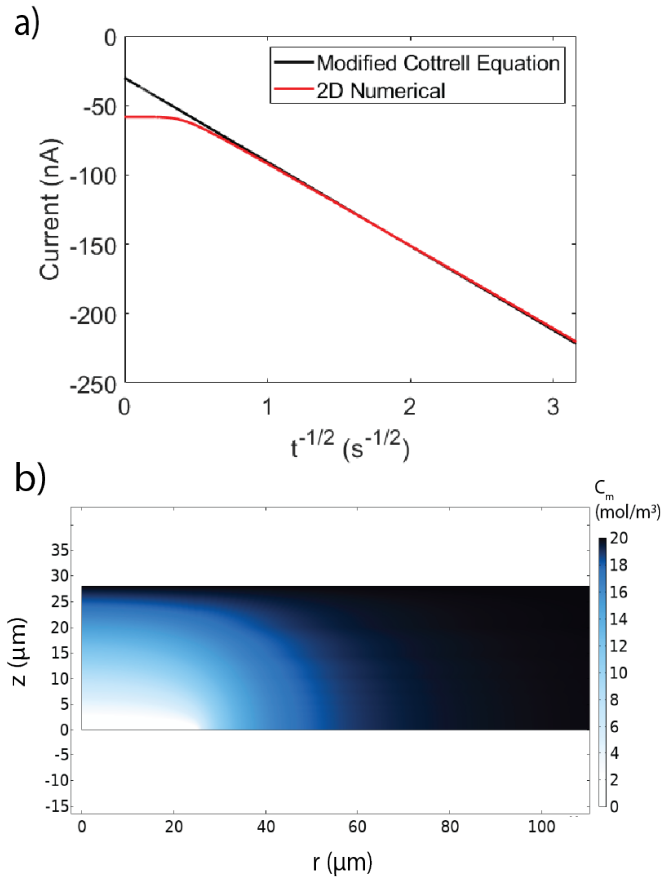

Figure 3.3: a) Plot of current versus inverse square root of time comparing the modified Cottrell equation and the COMSOL solution using D= 5 x 10^{-11} m^2/s, H= 20 $mol/m^3 \cdot bar$, L=25 µm, and $P_{g,\infty}$=1 bar. b) Concentration profile of oxygen gas in the system at steady-state, as calculated in COMSOL using $P_{g,\infty}$ = 1 bar and H = 20 $mol/m^3 \cdot bar$.

Either Equation 3.2 or Equation 3.8 can be used to determine D, H, and P. Unfortunately, and not surprisingly, Equations 3.2 and 3.8 give disparate results for the same parameter values, as illustrated in Figure 3.3a. We find that the modified Cottrell equation (Equation 3.2) deviates strongly from the finite thickness numerical solution (Equation 3.8) at long times and takes much longer to approach steady state. Both are consequences of a finite-thickness membrane in the numerical model compared to the infinite-thickness membrane in the modified Cottrell expression. A typical calculated steady-state profile from Equation 3.8 is seen in Figure 3.3b. It is a flattened hemisphere due to the finite z boundary. The steady-state gas-concentration profile is clearly not one dimensional.

Figure 3.4 illustrates application of Equation 3.8 to typical experimental data for ORR from our microelectrode apparatus. Here, the permeability was fit using steady-state data and the 2D analysis in Equations 3.6 and 3.8 to 1.08 x 10^{-9} $mol/(m \cdot bar \cdot s)$ and diffusivity was varied to fit the data. Adjustment of the oxygen-gas permeability allows Equation 3.8 to demonstrate good agreement with experiment at long times, as expected, but no matter the value chosen for diffusivity, theory does not match the experimental short-time slope, as highlighted in Figure 3.4. A typical explanation for the deviation of Equation 3.8 from theory is double-layer charging, but based on electrode size and Nafion's RC (resistance-capacitance) constant,[129] charging effects

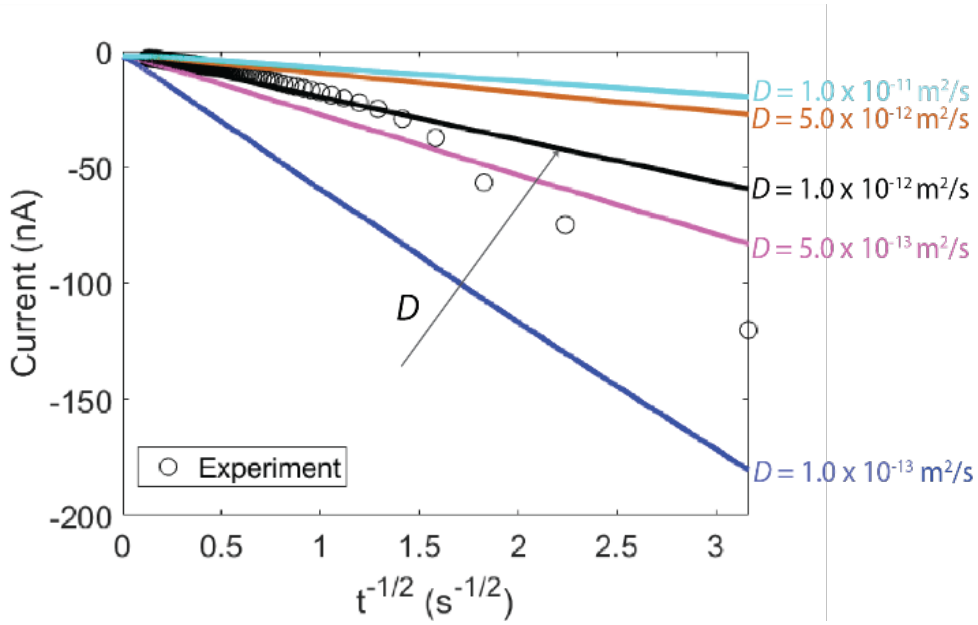

Figure 3.4: Comparison of Equation 3.8 to typical ORR microelectrode experimental data. At low $t^{-1/2}$ in Figure 3.4, the currents approach steady-state values of approximately –1 to –2 nA.

should dissipate in the µs regime, whereas deviations from Equation 3.8 clearly persist for up to 1 s ($t^{-1/2} > 1$) in Figure 3.4.

3.4.2 Rough Electrode Surface

An implicit assumption in Equation 3.8 is that the electrode-reaction area is equal to the geometric area. However, even a polished Pt surface is not perfectly smooth.[51] We posit that the surface roughness of the Pt electrode should be accounted for (especially at short times) as it increases the initial available reactive area. A qualitative depiction of the hypothesized impact of surface roughness on current is illustrated in Figure 3.5a and 3.5b. At very short times, high concentrations of dissolved gas molecules in the previously equilibrated membrane reside directly in the rough Pt-electrode crevices. Because the diffusion boundary layer is initially infinitesimally thin, the rough surfaces appear planar thereby increasing the electrode effective area (and therefore the current) compared to the flat geometric area used in the numerical model. As time increases, however, the diffusion layer grows, and gas molecules must travel from farther away in the membrane to reach the reactant surface. Here, the nanometer-size crevices of the electrode no longer contribute as much to the diffusion flux (atomic-force micrograph of the microelectrode surface can be found in Figure S3.3). Thus, the electrode-reaction area diminishes in time, approaching the physical geometric area. Changing area at short time is important when considering how to evaluate Equation 3.8.

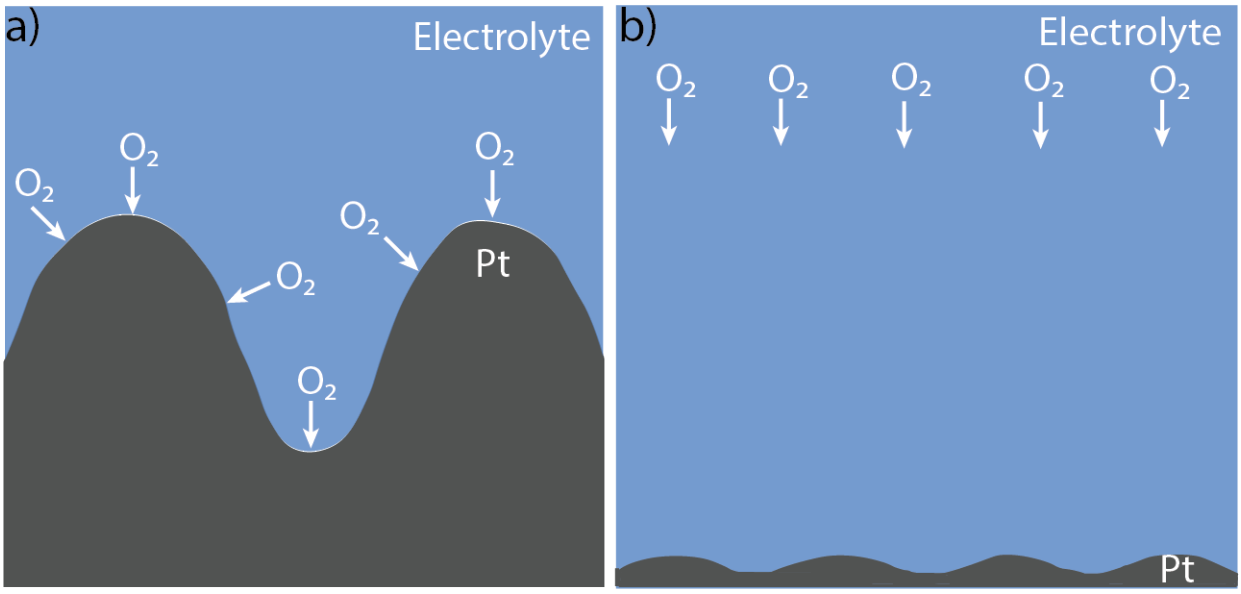

Figure 3.5: Accessible surface area for oxygen to react on the Pt surface at a) very short time and b) long time, respectively.

3.4.3 Chronoamperometric Data Interpretation

To provide meaningful estimates of membrane-gas diffusivities and Henry's constants, a two-time-regime analysis is proposed. First, Equation 3.9 is applied to calculate the gas permeability from the measured steady-state current and the geometric electrode area. Second, the short-time Cottrell equation is extended to account for surface roughness by the expression

$$I = \frac{nF\pi^{0.5}PR_e^2P_{g,\infty}R_F}{D^{0.5}t^{0.5}} \tag{3.10}$$

with gas permeability defined by

$$P = HD \tag{3.11}$$

where again R_F is the *ECSA*-determined roughness factor. All other variables are as defined previously.

Given the fitted experimental short-time slope, Equation 3.10 permits assessment of the diffusion coefficient since permeability is known from fitting to Equation 3.9. Henry's constant can then be determined from the definition of permeability in Equation 3.11. The advantage of this approach is that both steady-state and short-time information is used. Steady-state measurements yield accurate permeabilities, while roughness-corrected short-time data give meaningful diffusivities. It is assumed in the analysis that for each measurement, water gradients are not present because measured currents are low and humidified gases are flowing. Thus, diffusivity and Henry's constant are taken to be constant for a given measurement and humidity. Discussion of the applicability of this analysis technique to experimental data can be found in Section 3.5.1.

3.4.4 Phase-Separated Parallel-Diffusion Model

It is common to describe PFSA ionomers as composed of two distinct phases when hydrated: a hydrophilic aqueous phase, consisting of tortuous water channels in the ionomer, and a hydrophobic polymer phase, consisting primarily of the polymer backbone (see Chapter 1.2, Figure 1.3).[17, 133] Thus, to ascertain whether the suggested analysis procedure gives physically reasonable values for *D*, *H*, and *P*, a simple model was developed based on the assumption of phase separation of polymer and aqueous phases in the membrane. It is meant as a first-order rationalization of the results, described later, and is not intended to be a rigorous characterization of phase separation in Nafion membranes. This model is applied only to Nafion 211, as the addition of PTFE reinforcement in Nafion XL introduces multiple uncharacterized gas-transport pathways.[45] We assume further that diffusion is the only mode of mass transport. A mass balance of the diffusing gas in the membrane is

$$\varphi \frac{\partial c}{\partial t} + (1-\varphi)\frac{\partial n}{\partial t} = \varphi D_a \nabla^2 c + (1-\varphi) D_p \nabla^2 n_p \tag{3.12}$$

where c is the volume concentration of gas in the aqueous phase, n_p is the volume concentration of gas in the polymer phase, D_a is the diffusivity of the gas in the aqueous phase, D_p is the diffusivity of the gas in the polymer phase, and φ is the water volume fraction within the hydrated ionomer. Gas adsorption is neglected at the polymer/aqueous interface. By defining $C_m = \varphi c + (1-\varphi) n_p$ (where C_m is the total gas concentration per volume of membrane) and assuming local equilibrium, such that the partition coefficient $K = n_p/c$, Equation 3.12 can be rewritten as

$$\frac{\partial C_m}{\partial t} = D_{eff} \nabla^2 C_m \tag{3.13}$$

where

$$D_{eff} = \frac{D_a + D_p K(1-\varphi)/\varphi}{1 + K(1-\varphi)/\varphi} \tag{3.14}$$

Both aqueous and polymer phases are considered to have tortuous paths and so the diffusivities are modified from their bulk values,[134-136]

$$D_a = D_a^{\infty}/\tau_a^2 \tag{3.15}$$

with

$$\tau_a^2 = e^{\frac{k}{2}\left(\frac{1}{\varphi}-1\right)} \tag{3.16}$$

and

$$D_p = D_p^{\infty}/\tau_p^2 \tag{3.17}$$

with

$$\tau_p^2 = e^{\frac{k}{2}\left(\frac{1}{1-\varphi}-1\right)} \tag{3.18}$$

where τ_a^2 and τ_p^2 are the tortuosities of the aqueous and polymer phases, respectively, and D_a^∞ and D_p^∞ are the diffusivities in bulk water and polymer, respectively. The porosity dependence of tortuosity follows from Yasuda *et al.* where k is a fitting parameter with a value of 0.93 (determined by Crothers *et al.*) for Nafion.[134, 135] Similarly, the effective Henry constant for the total membrane is a volume-average linear combination of the Henry constants of each phase:

$$H_{eff} = \varphi H_a + (1-\varphi)H_p \tag{3.19}$$

where H_a represents the Henry constant for the aqueous phase, H_p is the Henry constant of the polymer phase, and $K \equiv H_p/H_a$. The product of Equations 3.14 and 3.19 is the gas permeability, P, of the ionomer membrane[50]:

$$P \equiv D_{eff}H_{eff} \tag{3.20}$$

The phase-separation model predicts membrane diffusivity, Henry's constant, and permeability based on the diffusivity and Henry constant of the gases in each of the individual phases and the overall membrane water content (volume fraction). By comparing the effective predicted values to the experimentally measured ones, physical insight can be made into the transport processes in the ionomer.

3.5 Results and Discussion

3.5.1 Nafion 211

We argue that the proposed methodology is more precise than directly using Equation 3.2. To illustrate this assertion, comparison of the proposed method to Equation 3.2 (dashed line) is plotted in Figure 3.6 with an example data set for oxygen diffusion in Nafion 211 at 95% RH (open circles). The short-time solution was obtained using linear regression and Equation 3.10 (blue line) on the first linear short-time region, whereas Equation 3.9 (red line) was used to calculate the long-time solution. Clearly, the long-time solution fits quite well at long times (>10 s), whereas the short-time solution is only valid for the first four data points (up to ~0.5 s). The diffusivity and Henry's constant calculated from this approach for the data in Figure 3.6 are quite reasonable, 2.23 x 10^{-12} m^2/s and 208 $mol/(m^3 \cdot bar)$, respectively, and the permeability is 4.64 x 10^{-10} $mol/(m \cdot bar \cdot s)$. The standard deviation for the gas permeability is about 5% across multiple samples, while the standard deviations for diffusivity and Henry's constant are approximately 25 to 30%. This latter error is likely a result of differences in Nafion-membrane samples. Run-to-run variation is less than 5%.

Figure 3.6 emphasizes the differences between Equation 3.2 and Equations 3.9 and 3.10 at long times. The steady-state current calculated using Equation 3.2 fit to the experimental data is positive, which is clearly aphysical for a reduction reaction, further highlighting the importance

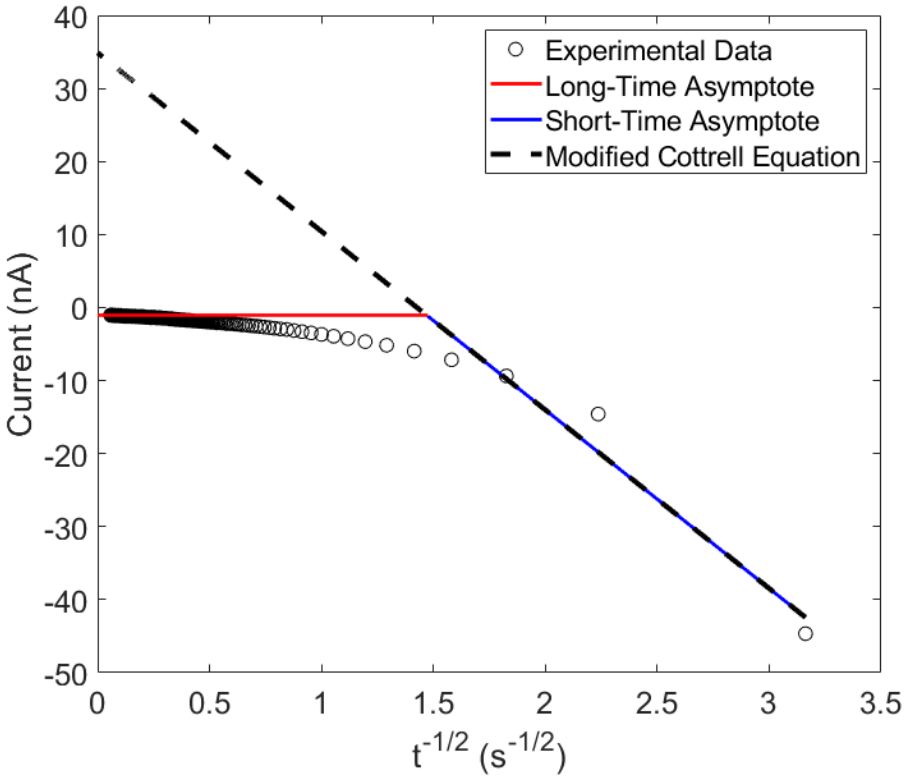

Figure 3.6: Current versus inverse square root of time with both the short- (blue line) and 2D long-time (red line) asymptotes compared to experimental results (open circles). The modified Cottrell equation (Equation 3.2) is shown as a black dashed line superimposed on the short-time asymptote.

of Equation 3.9 in fitting the steady-state data. The difference in D, H, and P values that result from the same data set of ORR currents as a function of RH, calculated using both Equation 3.2 and Equation 3.9 and 3.10, is given in Section 3.8.6 and Figure S3.4. We find that compared to Equation 3.10, Equation 3.2 produces a diffusivity that is three orders of magnitude higher, whereas Henry constants are one order of magnitude lower and permeability two orders of magnitude higher. These variations are extreme, demonstrating the need for an improved analysis method, as described herein, and they reinforce the need for careful data analysis.

Oxygen diffusivity, Henry's constant, and permeability determined from the two-time-regime technique are compared with the results from other studies in Figure 3.7a-c, which highlight the wide variability in previously reported works. Differences in temperature (20 versus 40 versus 70°C) account for some of this variation, but the data from Kudo *et al*. exhibit higher diffusivity than those of Novitski *et al.* at a lower temperature. The impact of different membrane processing methods (*e.g.*, Nafion 117 vs 211) on these results is also unclear and may be an additional source of variation in parameter values. In Figure 3.7, Novitski (1) data show the results determined by Novitski *et al.* using the modified Cottrell equation, whereas Novitski (2) data are the results determined from the Shoup-Szabo equation.[51] These two diffusivities differ by over an order of magnitude depending on the analysis method, further highlighting the importance of an accurate analysis technique. In contrast, Novitski *et al*. report similar Henry's

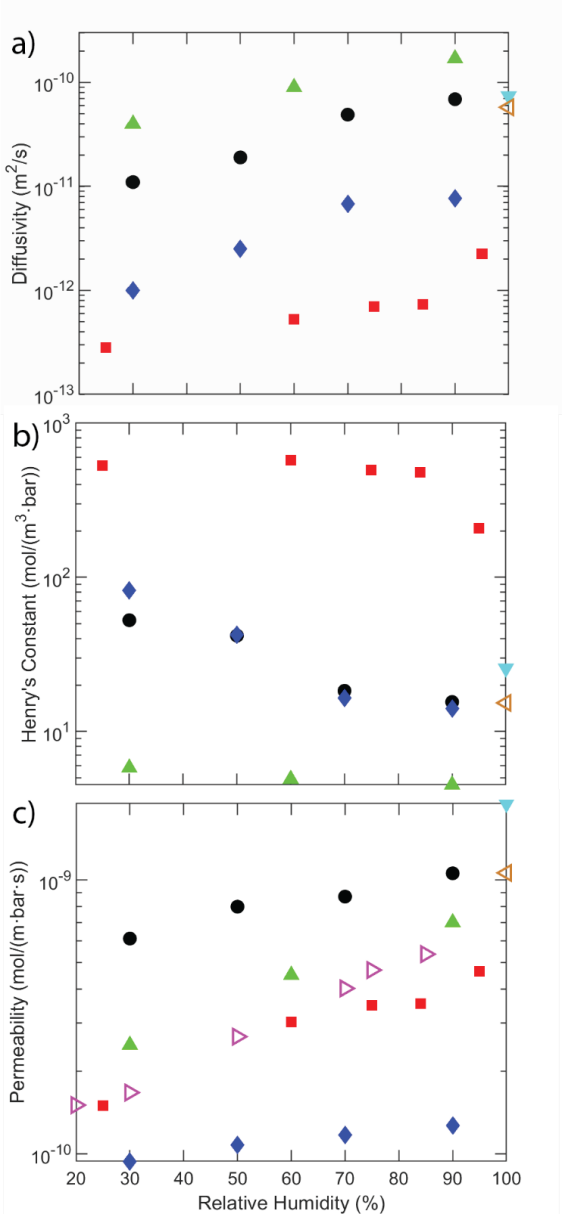

Figure 3.7: a) Oxygen diffusivities as a function of relative humidity (red squares) compared with microelectrode literature results [Novitski (1), Nafion 211 (filled black circles), Novitski (2), Nafion 211 (filled blue diamonds), Kudo, 100 µm Nafion, (filled green triangles), Parthasarathy, Nafion 117, (filled cyan inverted triangles)] and non-microelectrode studies [Baschetti, Nafion 117, (open magenta right triangles), Sethuraman Nafion 117, (open brown left triangles)]. b) Oxygen Henry constants compared with literature values determined from microelectrode measurements. c) Oxygen permeabilities compared with literature determined from microelectrode measurements.[42, 50, 51, 59, 123]

constants irrespective of analysis method, thus calculating permeabilities that differ by over an order of magnitude. Results from the work herein fall between the minimum and maximum reported values for gas permeability but exhibit the lowest diffusivity and highest Henry-constant values. This is likely the result of two factors. Temperature plays a contributing role, as diffusivity typically increases and Henry's constant decreases at higher temperatures. This study measured at the lowest reported temperature. In addition, the new proposed analysis technique

Table 3.1: Pure-phase transport parameters for hydrogen and oxygen gas

	Water[137, 138]		Dry Nafion[124]	
Gas	Diffusivity (m^2/s)	Henry Constant ($mol/m^3 \cdot bar$)	Diffusivity (m^2/s)	Henry Constant ($mol/m^3 \cdot bar$)
Oxygen	2.4×10^{-9}	1.3	5.9×10^{-12}	5.7
Hydrogen	6.3×10^{-9}	0.7	1.0×10^{-10}	2.3
Oxygen, Effective	-	-	4.0×10^{-13}	500
Hydrogen, Effective	-	-	3.0×10^{-11}	20

has a significant impact on reported parameter values compared to the oft-used Equation 3.2, as discussed previously.[17, 139, 140]

Unlike oxygen, there is a scarcity of data for hydrogen. Measured diffusivity, Henry's constant, and permeability for hydrogen and oxygen are given in Figure 3.8a-c. For oxygen, diffusivity and permeability increase as a function of RH, whereas the Henry constant decreases. This is likely due to the increased size of the aqueous-phase domains at high RH. Oxygen has a higher diffusivity in water than it does in the polymer backbone, but its Henry constant is lower, as it dissolves more readily in the polymer phase due to interactions with the ether groups in the polymer.[17] Permeability increases because diffusivity increases faster with RH than the Henry constant decreases. These trends are consistent with previous studies of oxygen transport in Nafion membranes, including those not using microelectrodes.[42, 50, 51, 133] Similarly, hydrogen diffusivity increases as the RH increases, whereas hydrogen Henry constant decreases. This result indicates that hydrogen moves more rapidly through the aqueous phase than through the polymer phase and again dissolves more readily in the polymer phase than in the aqueous phase. Hydrogen permeability, however, still increases overall as RH increases due to the faster increase in diffusivity.

Further insight into the membrane gas-transport processes can be obtained by comparison of the data to the predictions of the parallel phase-separated transport model (Equations 3.14, 3.17, and 3.20), plotted as dashed lines in Figure 3.8a-c. Water volume fraction was estimated based on tabulated data collected at 25°C.[17] The values of D and H for hydrogen and oxygen in water were used for the aqueous phase, while dry Nafion was initially used for the polymer phase.[124, 137, 138] Table 3.1 lists the parameters used. However, use of dry Nafion values overestimates the diffusivity and underestimates the Henry's constant (with a net underestimation of permeability) by about an order of magnitude (two orders of magnitude for oxygen Henry constant). There are a few potential reasons for these discrepancies. It is possible that the membrane is more tortuous than the model accounts for, which results in a higher predicted diffusivity than is witnessed experimentally. For Henry's constant, the values measured for dry Nafion are likely lower than

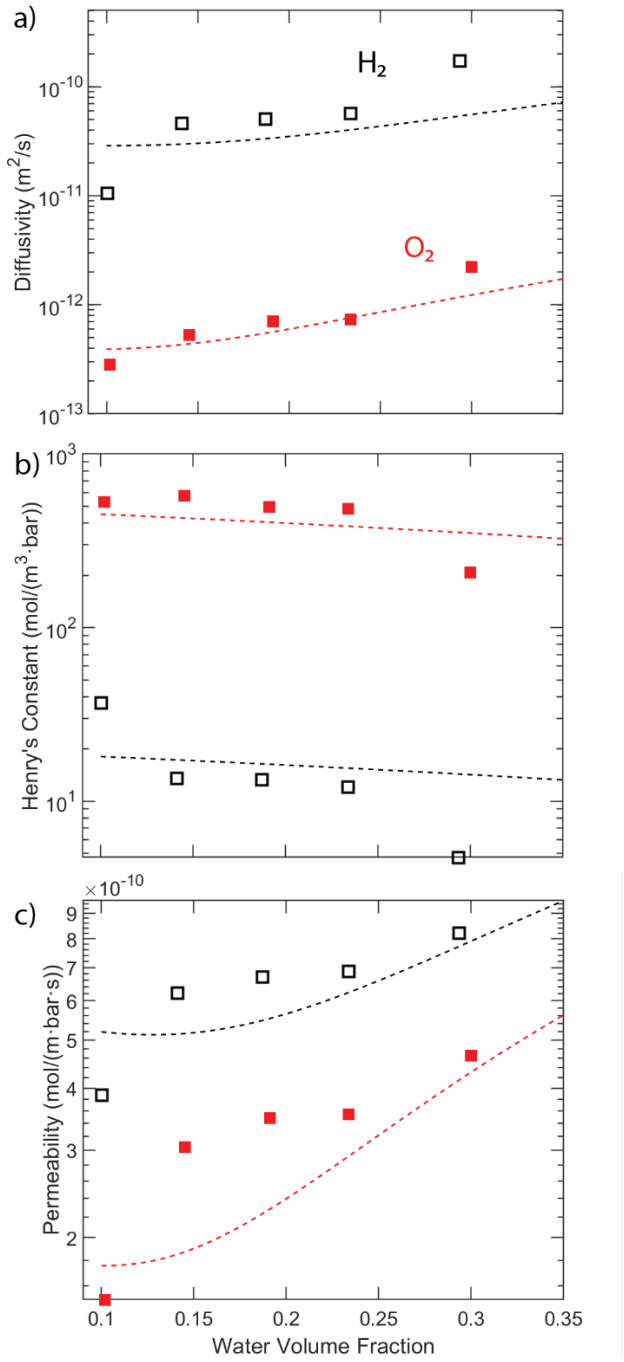

Figure 3.8: a)-c) Diffusivity, Henry's constant, and permeability, respectively, for hydrogen (open squares) and oxygen (filled squares) in Nafion 211. Dashed lines show the theory-predicted values calculated as a function of water volume fraction using the effective phase-separated parallel-diffusion model.

the real values due to some water uptake. It is also difficult to measure gas uptake in a completely dry membrane due to the small Henry's constant. Finally, assumptions used in the model derivation may not strictly hold, such as local equilibrium between the phases, and this contributes to the discrepancy.

To account for potential inaccuracies, effective polymer-phase parameters were used to improve the model fit (effective values found in Table 3.1). With the effective parameters, the phase-separated model is successful at capturing the nonlinearity of the diffusivity, Henry's constant, and permeability as functions of water volume fraction for both gases, captured by Figure 3.8. Corresponding plots using the pure polymer-phase parameters can be found in Section 3.8.7 and Figure S3.5. The results demonstrate that treating the aqueous and polymer domains as separate, parallel channels results in qualitative trends consistent with the obtained experimental data, indicating that gas transport occurs predominately through the aqueous phase. However, the lack of quantitative agreement when using the pure polymer-phase parameters likely suggests that the model oversimplifies gas-phase interactions, particularly in the calculation of the Henry's constant, as the pure polymer-phase Henry's constant had to be adjusted up to two orders of magnitude to achieve a reasonable fit of the experimental data.

3.5.2 Nafion XL

Figure 3.9a-c illustrates the gas mass-transport parameters for Nafion XL. Oxygen diffusivity and permeability increase with increasing RH, whereas the Henry's constant decreases, similar to Nafion 211. Also, hydrogen diffusivity and permeability increase with increasing RH, whereas Henry's constant decreases, again similar to Nafion 211. These trends occur for the same reasons they do in Nafion 211, given similarities in their membrane structures. However, diffusivity is generally higher and Henry's constant generally lower for both gases in Nafion XL in contrast to Nafion 211, although their product, permeability, is similar in value. This may be a result of the unique structure of Nafion XL, which can be compared to a sandwich – two layers of Nafion, with a polytetrafluoroethylene (PTFE) layer between them.[45] The PTFE layer is highly porous and approximately 2.5-μm thick in an overall membrane thickness of 27.5 μm, with the pores containing additional Nafion ionomer. The added PTFE may produce confinement in the Nafion layers, with chain alignment along the PTFE such that the tortuous water channels are aligned more in the through-plane direction than is found in Nafion 211. This alignment along the PTFE would enhance the through-plane gas diffusivity, the primary diffusivity of interest in this work. Nafion XL is also further modified by the addition of proprietary additives, including possibly silica and cerium, to improve the chemical stability of the membrane.[45, 49, 141] It is possible that these additives are responsible for some of the differences in diffusivity and solubility seen between Nafion 211 and Nafion XL. Ce is larger than the protons normally found in Nafion and may have widened the water channels in the Nafion such that gas diffusivity is enhanced. In addition, the added concentrations of Ce and silica may have occupied sites where gas would normally dissolve into the membrane, reducing gas dissolution and resulting in the lower observed Henry's constants.

3.6 Conclusions

A new method is developed for extracting diffusivity, Henry's constant, and permeability of gases from transient chronoamperometry measurements taken using Pt microelectrodes. A transient 2D numerical model of the microelectrode is implemented. The modified Cottrell

equation for data interpretation is supplanted by a two-time-regime analysis: a 2D numerical result at long time and a roughness-corrected Cottrell equation for short time. The new data-interpretation methodology is applied to two membranes, Nafion 211 and Nafion XL, to determine the diffusivity, Henry's constant, and permeability of oxygen and hydrogen gases in these membranes as a function of relative humidity. Permeability and diffusivity uniformly increase for all membranes as humidity increases, whereas the Henry constant generally decreases as a function of humidity. The trends in permeability, diffusivity, and Henry's constant for oxygen in Nafion 211 match quite closely with

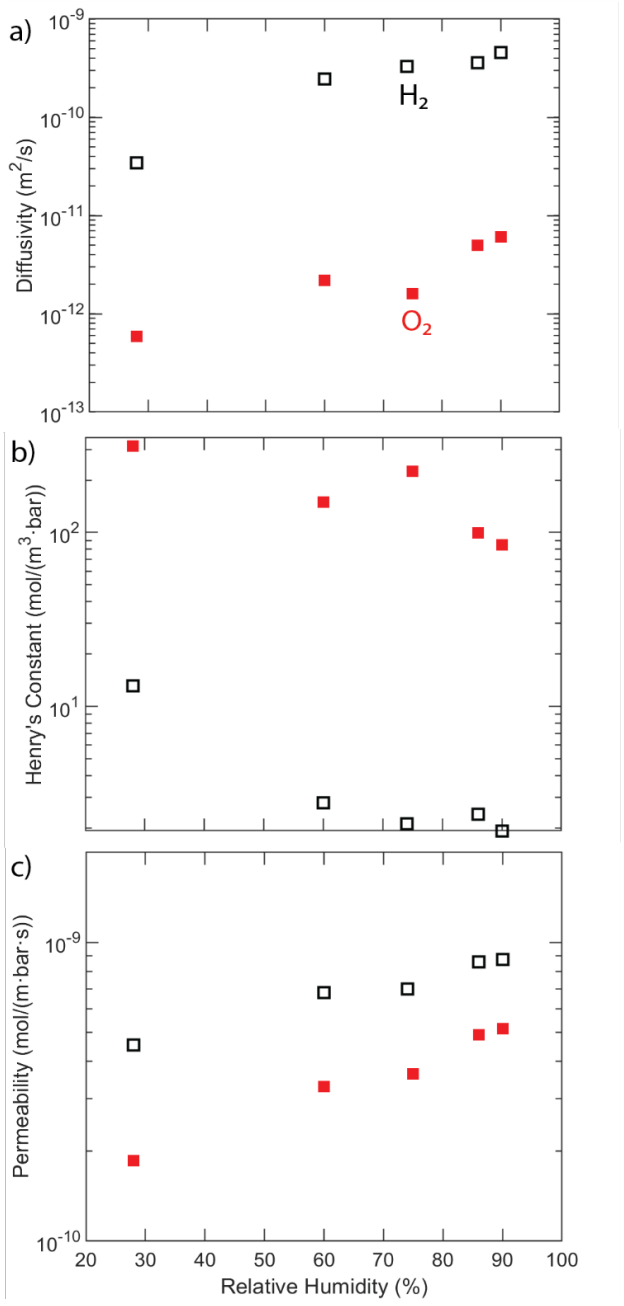

Figure 3.9: a)-c) Diffusivity, Henry's constant, and permeability, respectively, for hydrogen (open squares) and oxygen (filled squares) in Nafion XL.

existing literature but differ quantitatively due to the more rigorous interpretation method applied here, thus highlighting the need to analyze all data time regimes consistently and holistically and account for such effects as surface roughness. Nafion XL exhibited higher diffusivities, lower Henry's constants, and similar permeabilities for both gases in contrast to Nafion 211. A phase-separated parallel-diffusion theoretical model also predicts the trends in diffusivity, Henry's constant, and permeability of both hydrogen and oxygen gases in Nafion 211 well when effective polymer-phase properties are used; a more rigorous model may be needed to fit the experimental data quantitatively. Overall, the presented data and methodology suggests that the proposed two-time-regime analysis yields physically reasonable parameters and trends. These findings are important for applications such as determining fuel-cell operating conditions, where there is a tradeoff between proton conductivity and gas crossover at high RHs, and precise measurements of gas transport parameters are needed to calculate gas crossover rates. In addition, this study highlights how to use and interpret solid-state microelectrodes effectively and rigorously for mass-transport interrogations.

3.7 Symbols

Roman

A_{UC}: Area under the curve

A: electrode area

C: concentration of gas within the membrane at the gas-membrane interface

c: volume concentration of gas in the aqueous phase

C_m: gas concentration per unit volume of membrane

$\tilde{C}_m$: dimensionless concentration

D: gas diffusivity

D_a: diffusivity of gas in the aqueous phase

D_p: diffusivity of gas in the polymer phase

D_{eff}: effective diffusivity

D_a^{∞}: diffusivity of gas in bulk water

D_p^{∞}: diffusivity of gas in bulk polymer

$ECSA$: Electrochemical Surface Area

F: Faraday's constant

H: Henry's constant

H_{eff}: effective Henry's constant

H_a: Henry's constant in the aqueous phase

H_p: Henry's constant in the polymer phase

I: current

K: partition coefficient

k: tortuosity expression fitting parameter

n: number of electrons

n_p: volume concentration of gas in the polymer phase

$P_{g,\infty}$: external gas partial pressure

P: gas permeability

r: radial coordinate

R_e: electrode radius

R_F: roughness factor

t: time

z: axial coordinate

$\tilde{z}$: dimensionless z coordinate

Greek

ν: scan rate

φ: water volume fraction

ρ_s: surface charge density

π: the constant Pi

τ_1: dimensionless time

τ_a^2: tortuosity in the aqueous phase

τ_p^2: tortuosity in the polymer phase

3.8 Supplemental Information

3.8.1 Example CV scan used to Calculate ECSA

Figure S3.1 is an example CV scan captured on the Pt electrode using Nafion 211 at 50 mV/s. The area under the curve used in Equation 3.1 is shown highlighted in yellow, which is the hydrogen deposition region with the double-layer capacitance region removed. Hydrogen deposition is chosen to avoid any impact from HER current increasing the area of the hydrogen adsorption region. Double-layer capacitance is removed by subtracting the double-layer current from the hydrogen desorption peak (double-layer current marked by blue line). The area in yellow is evaluated numerically for use in Equation 3.1 of the text.

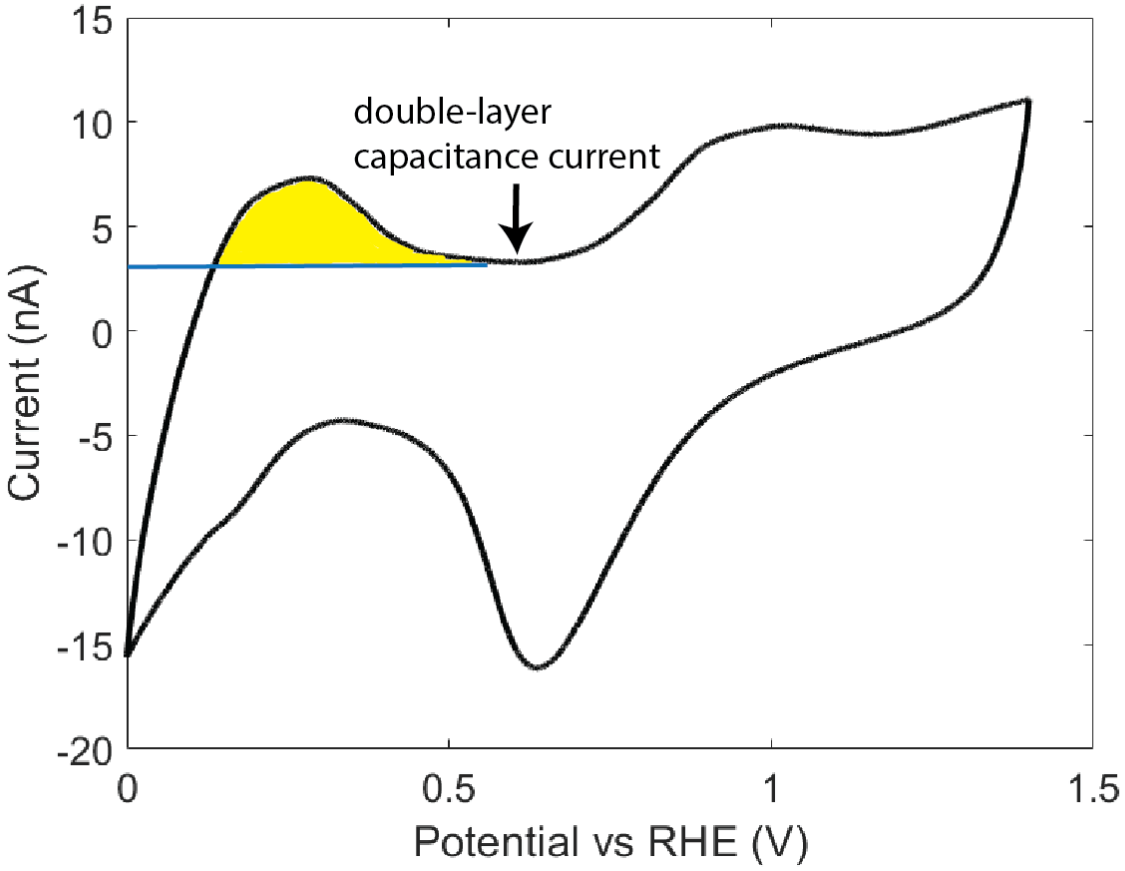

Figure S3.1: Example of a CV curve captured under argon gas (humidified, 90% RH) at a scan rate of 50 mV/s. The electrolyte is Nafion 211. The hydrogen under-deposition region is highlighted in yellow.

3.8.2 Polarization Curves

Figure S3.2 shows polarization curves for both oxygen a) and hydrogen b) gas as a function of relative humidity. Current clearly increases as a function of relative humidity, and the mass-transport plateaus are clearly denoted – around –0.7 V for oxygen and 0.5 V for hydrogen.

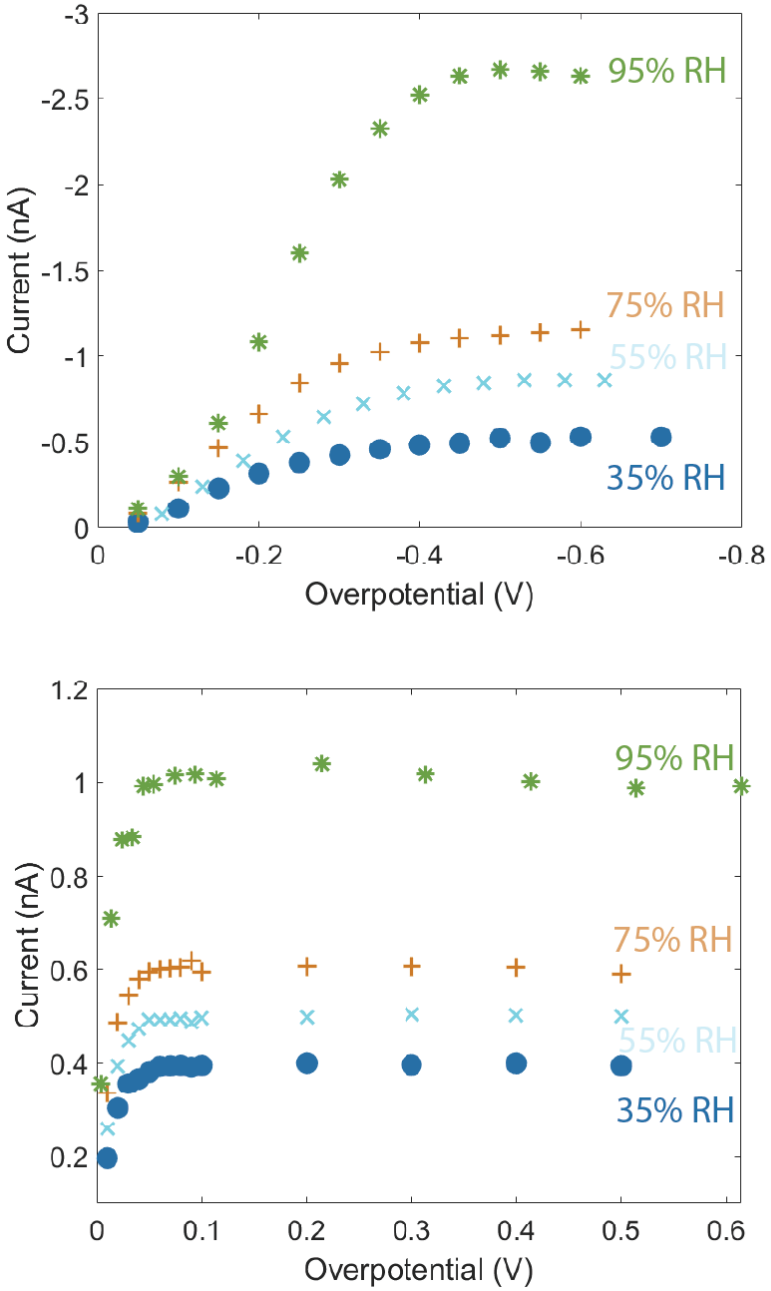

Figure S3.2: a) Polarization curves for the oxygen reduction reaction, plotted as current versus overpotential at four different humidities. b) Polarization curves for the hydrogen-oxidation reaction plotted as current versus overpotential at four different humidities. The mass-transport limited region is clearly indicated in both figures where the polarization curve becomes constant with increasing overpotential.

3.8.3 Model Numerics

Equations 3.6-3.8 were solved using COMSOL 5.6. The mesh consists of 3400 four-sided elements spread across the membrane domain for the appropriate membrane thickness (based on membrane type and humidity). To capture the semi-infinite nature of the system, a radius of 300 μm proves adequate. The mesh-element distribution is skewed such that a higher number of elements are focused on the electrode/glass boundary (found at r = 25 μm).

3.8.4 Rough Microelectrode Surface

To verify the existence of surface roughness, atomic force microscopy (AFM) images were captured of the dry microelectrode surface (see Figure S3.3a and S3.3b). The images clearly display nanoscopic features on the surface of the Pt, with a calculated root-mean-square roughness of about 55 nm, and a calculated surface area about 9 times larger than the geometric one. This value is similar to the roughness value of R_F = 14.8 estimated by measuring the *ECSA* for this electrode, suggesting that *ECSA* is a relatively accurate method of determining the actual reaction surface area.

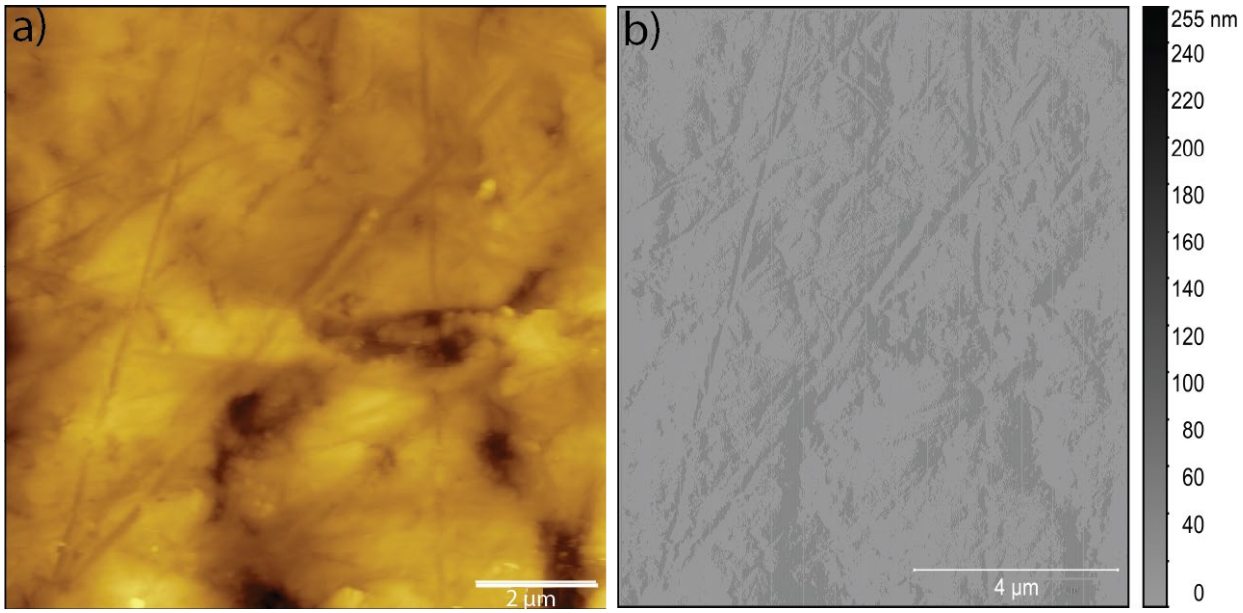

Figure S3.3: (a) A 10 x 10 μm AFM image of the Pt microelectrode surface demonstrating the nanoscale surface features of the electrode. The RMS value is 55 nm. (b) Colorized image of the Pt microelectrode surface that shows surface roughness; darker color indicates a higher feature.

3.8.5 Difference Between Modified Cottrell Equation and This Work

The difference in best-fit gas parameter values between the modified Cottrell equation (Equation 3.2) and a combination of Equations 3.8 and 3.10 is quite large (see Figure 3.5 for an example of the difference in fits between these two methods). The difference is largest for diffusivity, at three orders of magnitude, but is still a one order of magnitude discrepancy for the Henry constant and two orders of magnitude for permeability, as seen in Figure S3.4. In addition, the trends are quite different, with D appearing to be approximately constant with RH, while H and P increase using the modified Cottrell equation. Conversely, using Equations 3.8 and 3.10, D increases, H decreases, and P increases with increasing RH. These differences are a result of two main factors: first, the use of a 2D steady-state term calculated for the membrane assembly geometry, as opposed to the pseudo-1D geometry of the modified Cottrell equation, and second, the addition of a roughness factor to the short-time analysis in Equation 3.10. Our results emphasize the importance of using the proposed interpretation methodology, as each method paints a different picture of transport inside the membrane. The modified Cottrell equation indicates that oxygen moves much more quickly through Nafion 211 than is actually occurring, while underestimating Henry's constant. The modified Cottrell equation also severely overestimates the permeability (see Figure 3.6), which could lead to overestimates of such phenomena as gas crossover when these parameters are used in other works and models.

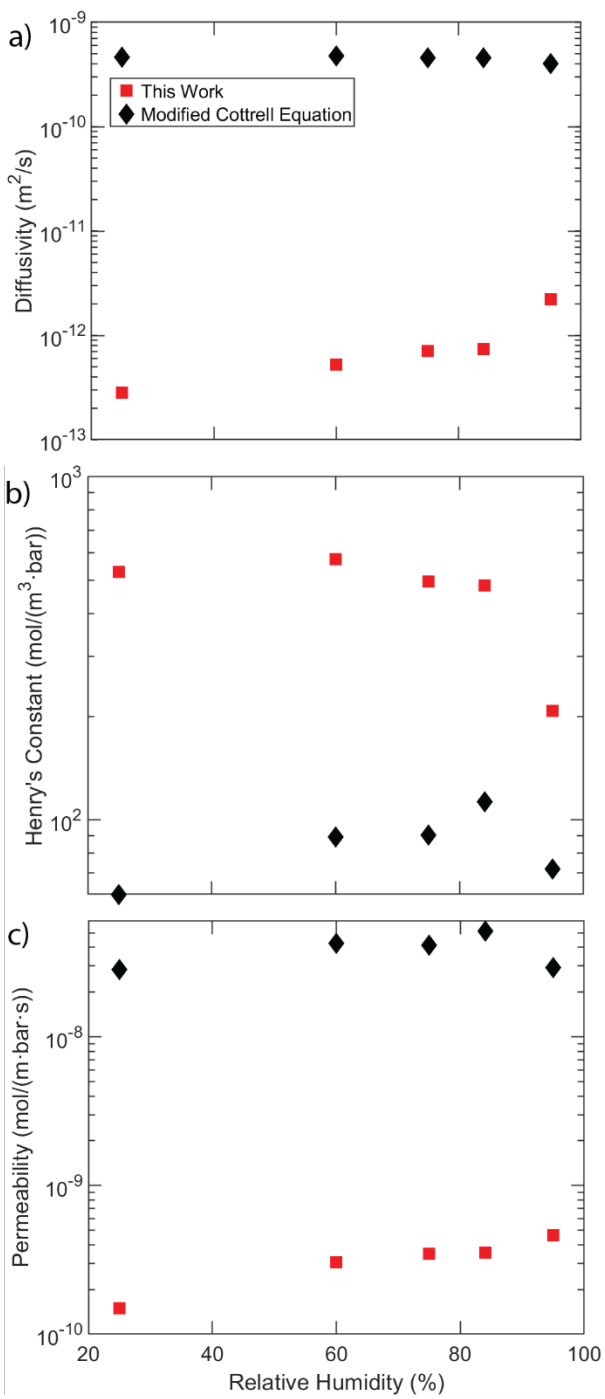

Figure S3.4: Plots showing the difference in diffusivity, Henry's constant, and permeability between using the Cottrell equation and the new analysis technique found in this work for oxygen gas in Nafion 211.

3.8.6 Phase-Separated Parallel Diffusion Model with Pure Polymer-Phase Parameters

Figure S3.5 compares the phase-separated parallel diffusion model using the pure polymer-phase parameters to the measured diffusivities, Henry's constants, and permeabilities for hydrogen and oxygen gas. The unadjusted model overestimates the measured diffusivities and underestimates the Henry's constants for both gases, resulting in a slight underestimation of permeability due to the more-severe underestimation of the Henry's constant. Even without adjustment, however, the trends determined from the phase-separated parallel diffusion model approximately match the experimental trends.

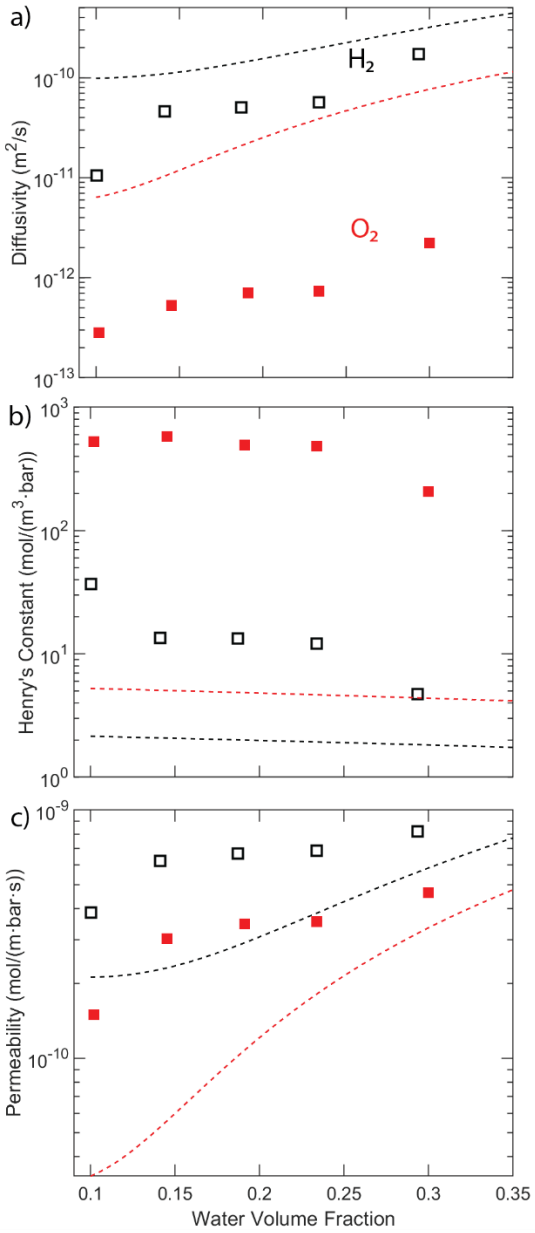

Figure S3.5: a)-c) Diffusivity, Henry's constant, and permeability, respectively, for hydrogen (open squares) and oxygen (filled squares) in Nafion 211. Dashed lines show the theory-predicted values calculated as a function of water volume fraction using the phase-separated parallel-diffusion model using the pure polymer-phase parameters.

3.8.7 Error Bar Analysis

Figure S3.6 adds error bars to the oxygen diffusivity, Henry's constant, and permeability results from Figure 3.7 and 3.8. Representative error bars, each the length of one standard deviation, are added to the highest and lowest humidity points.

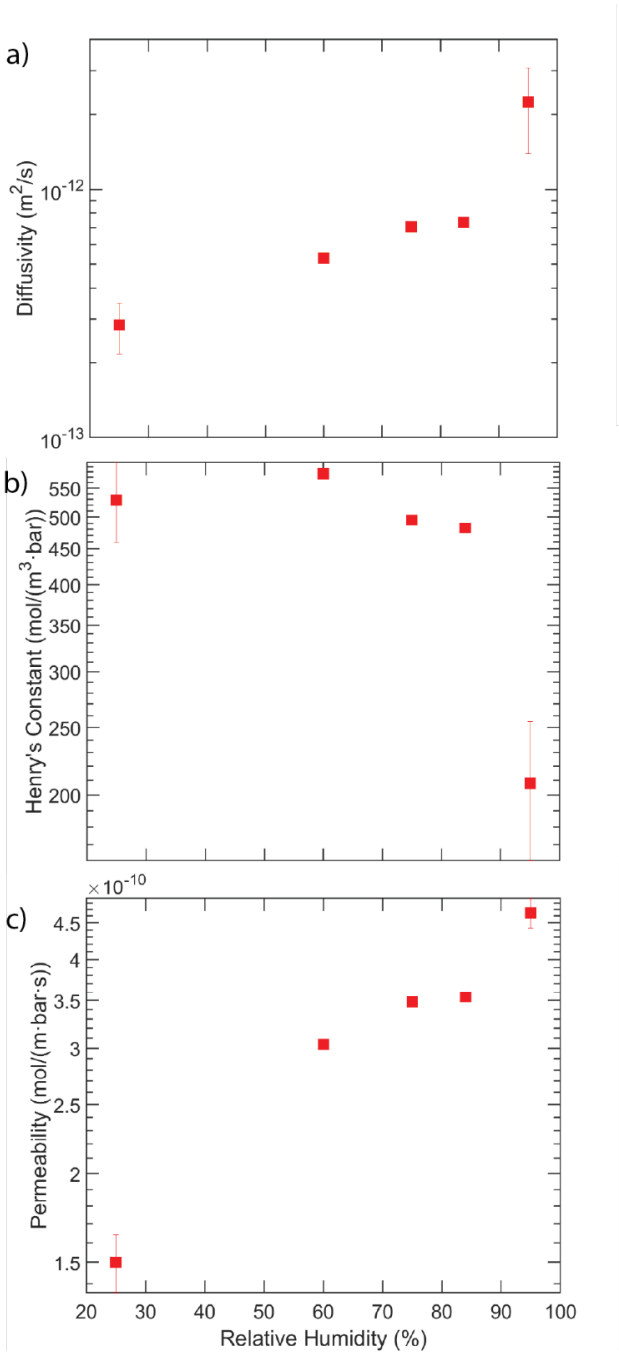

Figure S3.6: a)-c) Diffusivity, Henry's constant, and permeability, respectively, for oxygen (filled squares) in Nafion 211. Error bars representing one standard deviation are provided for the highest and lowest humidity points.

4. Electrochemical Measurement of the Electro-osmotic Coefficient in Anion-Exchange Membranes

4.1 Abstract

Anion-exchange membranes (AEMs) are a possible replacement for traditional perfluorosulfonic acid membranes in energy-conversion devices, primarily due to the hydroxide mobile ion allowing the devices to operate in alkaline conditions (instead of acidic), thus enabling use of less expensive electrocatalysts. However, the transport properties of AEMs remain understudied, with little work performed examining the effect of electro-osmosis in the membranes, a key factor in the overall- system water balance. In this chapter, an electrochemical technique that measures the open-circuit potential of an electrochemical cell containing the membrane and two gas chambers at different relative humidities is used to determine the water transport number of various ionomers including Nafion proton exchange membrane (PEM) and Versogen and Sustainion AEMs as a function of water content and at different temperatures. In addition, the PEM and AEMs are examined in differing single-ion forms, specifically proton and sodium (PEM) and hydroxide and carbonate (AEM). Finally, a multicomponent transport model based on the Stefan-Maxwell-Onsager framework of binary interactions via friction coefficients is used to examine the water transport numbers, developing a link to water-transport properties and extracting a range for the unmeasured membrane water permeability of Versogen as a function of water content. Together, determination of the water transport number and the link to water permeability present a more complete description of water transport in ionomers and, therefore, more accurate water balances in fuel cells and electrolyzers.

4.2 Introduction

Use of hydrogen-based energy-conversion technologies continues to grow in importance especially for fossil-fuel-free energy sources. In fuel cells, hydrogen and oxygen gas are fed to the anode and cathode, where they react in the hydrogen oxidation (HOR, Equation 1.1) and oxygen reduction (ORR, Equation 1.2) reactions, respectively, to produce electricity and water. In electrolyzers, water is fed to the anode, where the oxygen evolution reaction (OER, Figure 2.1) occurs. Hydrogen evolution (HER, Figure 2.1) occurs at the cathode. In both cases, the anode and cathode are separated by an ion-conducting polymer-electrolyte membrane. The standard membrane is Nafion®, a perfluorinated sulfonic-acid proton-exchange membrane (PEM), that conducts protons as the mobile ion (see Figure 1.3).[17] However, mainly due to catalyst cost, hydroxide-exchange membranes (HEMs), where hydroxide is the mobile ion, are being explored for different technologies.[16, 54, 142-144] Popular HEMs include Versogen® and Sustainion®, both of which use variations of styrene-ring backbones. Versogen HEM has piperidine active side groups, whereas Sustainion HEM uses imidazole-ring active side groups (see Figure 4.1).[54, 145] HEMs are also utilized in CO_2 electrolyzers,[146] where the hydroxide ion converts to a mix of carbonate and bicarbonate ions spontaneously upon exposure to carbon dioxide,[147]

$$CO_2 + OH^- \leftrightarrow HCO_3^- \qquad (K_1 = 4.27 \times 10^7) \qquad (4.1)$$

$$CO_2 + 2OH^- \leftrightarrow H_2O + CO_3^{2-} \qquad (K_2 = 1.96 \times 10^{11}) \qquad (4.2)$$

thus rendering the HEM a more general anion-exchange membrane (AEM). Both reactions have large equilibrium constants.[147] These reactions are useful for systems that rely on the carbonate ion (*e.g.*, molten carbonate fuel cells) but can be detrimental in fuel cells and CO_2 electrolyzers where air is often used as a reactant and hydroxide is the desired mobile ion due to the lower conductivity of carbonate-exchanged AEMs compared to HEMs.[55, 148]

Water management is critical in fuel cells and electrolyzers, wherein much work has been invested.[40, 41, 149-152] Water enhances membrane ion conductivity significantly compared to a dry membrane and may also be a reactant (see Equations 1.3 and 1.4).[17, 142] In Nafion, water uptake develops a phase-separated structure, with hydrophobic regions of polymer backbone and hydrophilic water channels that are responsible for the majority of the proton conduction (see Figure 1.3).[17] Versogen and Sustainion uptake water similarly to Nafion, yielding significant conductivity benefits, but their microstructures are not clear.[55, 56, 153] Nevertheless, excess water in the system can be detrimental. For example, PEM and AEM fuel-cell catalyst layers can flood with water due to excess water invading gas-filled channels, leading to additional mass-transport limitations and poor cell performance (as will be explored in Chapter 5).[13, 38, 39, 79-82, 154] As a result, proper management of water balance is necessary to maintain adequate ion conductivity without flooding.

There are multiple methods by which water can move through an AEM. A classical mechanism is by viscous flow due to an applied pressure difference. A second mechanism is movement along a chemical-potential gradient, *e.g.,* by exposing each side of the membrane to a different relative humidity (RH). Yet another mechanism is application of an electrical field (*i.e.*, electro-osmosis) in which mobile ions carry water in their solvation shells as they move from one side of the

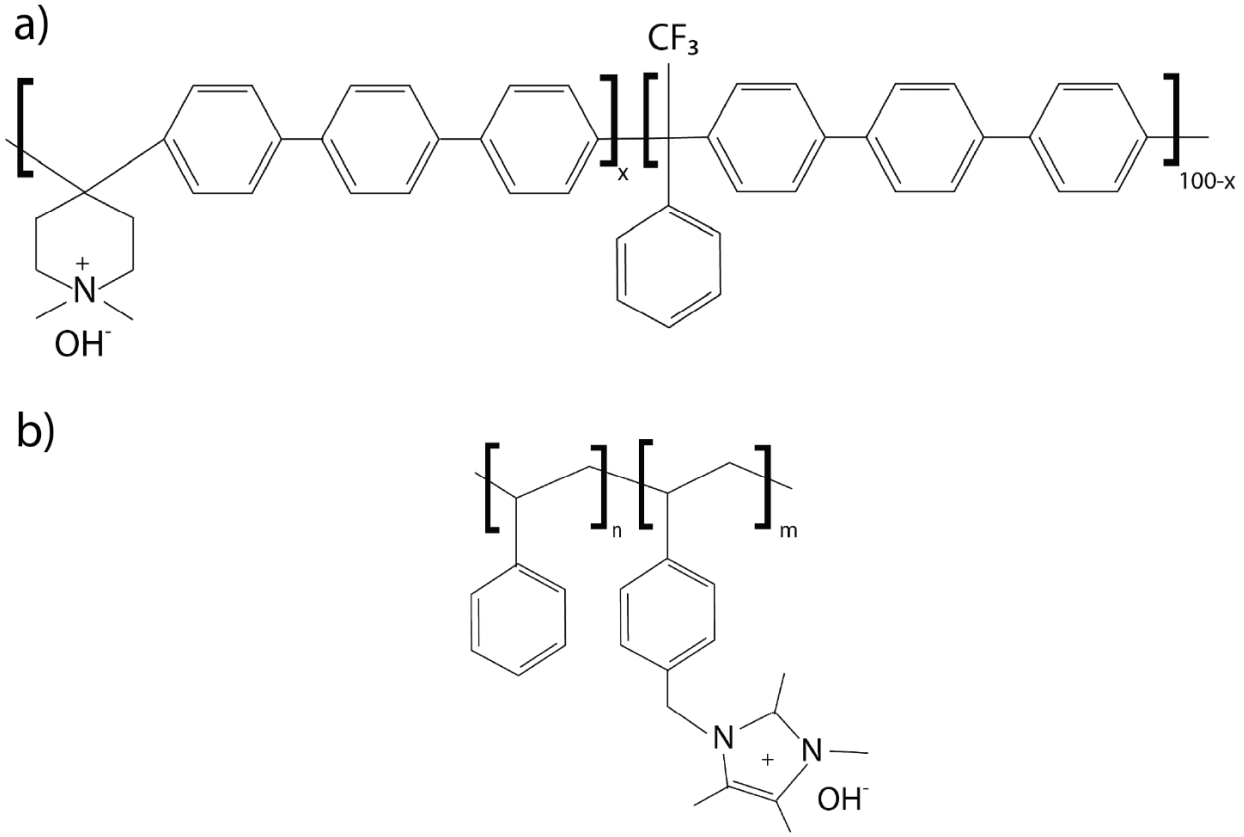

Figure 4.1: a) Molecular structure of Versogen polymer and b) Sustainion polymer.[54, 145]

membrane to the other.[17] The number of water molecules transported per mobile-counterion charge is defined as the ion-water transport number,

$$\mathrm{T}_i = \frac{N_0}{|z_i|N_i} \tag{4.3}$$

where N_i is electro-osmotic flux of mobile ion species i, N_0 is flux of water, and z_i is the counterion valence.[36] We refer to T_i below simply as the water transport number. It is related to the more familiar electro-osmotic coefficient by the relation

$$\xi_i = |z_i|\mathrm{T}_i \tag{4.4}$$

where the electro-osmotic coefficient is defined as the amount of water moved per mobile counterion, not to the mobile counterion charge. When the ion valence is unity, the electro-osmotic coefficient and the water transport number are identical. Due to the possible presence of multivalent counterions in AEMs, we utilize the water transport number exclusively in this chapter. Depending on the magnitude of the water transport number, the effect of counterion valence can be significant in the water balance, especially at high current densities due to the single-ion electro-osmotic flux scaling with current density, i, by the relationship

$$N_0 = T_i \frac{i}{\mathrm{F}} \tag{4.5}$$

where *F* is Faraday's constant. The water transport number of hydronium ions in Nafion is well-studied, using a variety of techniques, including electrochemical measurements,[36, 67, 68] various types of membrane-electrode assemblies,[52, 155-158] and electrophoretic nuclear magnetic resonance.[69, 159] At room temperature, proton T_{H^+} values in the range of 1.0 to 1.4 are common in vapor-equilibrated membranes, with higher values near 2.5 to 3 for liquid-equilibrated membranes.[17, 21, 36, 69, 157] Unfortunately, the water transport numbers of AEMs are largely unknown, with no comprehensive study. Two prior efforts focus on the Tokuyama A201® AEM, with both reporting water transport numbers for hydroxide as a function of water content[160, 161] and with Roy[161] also reporting the water transport number for bicarbonate-exchanged as a function of water content. However, the reported values differ significantly (~ 0.6[160] versus up to 8.2[161]) depending on the specific ion and water content, and do not agree on the water transport number for the hydroxide-form AEM. Multiple temperatures are not considered, and minimal physical explanation is provided. Thus, there is a need for further study of water transport numbers in AEMs, especially when multivalent mobile counterions are present.

One method to determine T_i is the electrochemical technique developed by Fuller and Newman, in which an exchange membrane is placed between two separate abutting chambers.[17, 36] Water-vapor activity on the membrane upstream side is varied while holding the downstream-side water activity constant, and the open-circuit potential (OCV) is measured as a function of water activity. By imposing a water chemical-potential gradient across the membrane, water transports downstream, carrying ions with it due to the coupled nature of multicomponent diffusion. Ions carried downstream by water diffusion must then migrate back upstream to maintain zero net current (i.e., counter electro-osmosis). Back osmosis is driven by a generated open-circuit voltage difference (OCV). The magnitude of the OCV quantifies the water transport number, as illuminated below.

The microelectrode assembly developed in Chapter 2 may be easily adapted to use the technique developed by Fuller and Newman.[36] This assembly measures the water transport number of Nafion PEM, and Versogen and Sustainion AEMs, as a function of water vapor activity, and, accordingly, as a function of membrane water content. The gas flow-through design of the microelectrode cell enables much faster equilibration, and, thus, enhances experimental throughput and ease of use. Cell data interpretation builds on that developed by Fuller and Newman[36], with important modifications to adapt to the materials used here. Multiple transporting counterions are explored, including the proton and sodium-exchange forms of Nafion and hydroxide, carbonate, and bicarbonate-exchange forms of the AEMs. The impact of temperature is also explored in the Versogen AEM for both hydroxide and carbonate counterions at low and high membrane water contents. Finally, a theoretical framework is developed to describe the measured water transport numbers in Nafion and Versogen. We then predict the water transport number as a function of water content of Nafion using literature[32] to extract membrane tortuosity and use the measured water transport number to predict the range of the water permeability of Versogen.

4.3 Experimental Methods

4.3.1 Materials

The microelectrode working electrode (WE) was Pt, 50 μm in diameter (Metrohm, Florida, USA), and the counter (CE) and reference electrodes (RE) were gas-diffusion electrodes (GDE), again Pt. For acid-based experiments, commercial GDEs were used (Sigracet 25BC, 0.5 mg/cm^2 Pt, SGL Carbon, Wiesbaden, Germany); for alkaline-based experiments, custom GDEs were fabricated (AVCarb 370, AVCarb Material Solutions, MA, USA, MPL loading 0.5 mg/cm^2, Pt loading 0.5 mg/cm^2) using Versogen as the ionomer (PiperION-A (PAP-TP-85), 5 wt% in ethanol, Versogen, Delaware, USA).[162] Additional fabrication details are available elsewhere.[162]

The cation-exchange membranes used were Nafion 211 (25 μm, 1100 EW, used pre-boiled[17] and as-received, Ion Power, Delaware, USA) and sulfonated polystyrene cast from solution (poly(4-styrenesulfonic acid) solution, 18 wt% in water, 100 g, Sigma-Aldrich, Massachusetts, USA). Nafion 211 was also exchanged to sodium form by submersion in 0.5M Na_2SO_4 solution (Sodium sulfate, 1 kg, ACS reagent, ≥ 99.0%, Sigma-Aldrich, Massachusetts, USA). AEMs studied were Versogen (20 and 80 μm, ~425 EW, Versogen, Delaware, USA) and Sustainion (X37-50, 50 μm, ~900 EW, Fuel Cell Store, Colorado, USA).[55, 153] 1M ion solutions determined the membrane ion-exchange form. Potassium carbonate (500 g, ACS reagent, ≥ 99.0%, Sigma-Aldrich, Massachusetts, USA), potassium bicarbonate (500 g, ACS reagent, 99.7%, Sigma-Aldrich, Massachusetts, USA), and potassium hydroxide (3 kg, Certified ACS pellets, Thermo Fisher Scientific, Massachusetts, USA) were used for carbonate, bicarbonate, and hydroxide AEM ion-exchanged forms, respectively. Before use, membranes were placed in three successive reverse-osmosis water baths to rinse excess ions, for at least 4 hours, overnight, and 30 minutes, respectively. In the case of hydroxide-form membranes, the water was degassed with nitrogen to prevent conversion to carbonate form due to dissolved carbon dioxide.

4.3.2 Water-Uptake Measurements

Membrane water uptake as a function of RH were from previous studies at 25°C for Nafion in the proton form, for Sustainion in the hydroxide form, and for Sustainion and Versogen in the carbonate and bicarbonate forms.[17, 55, 153] Water content was assumed invariant with temperature, as the impact of temperature on water content for Nafion in the studied range is inconclusive.[17] The water uptake of hydroxide-form Versogen was measured using a dynamic-vapor sorption (DVS) system (Surface Measurement Systems, UK) with the chamber flushed with dry nitrogen gas to remove residual CO_2. The sample was placed directly in the sample holder from a degassed water reservoir to minimize carbonate formation and held at 25°C and 70% RH for 3 hrs to equilibrate the membrane. Next, the humidity was increased to 98% RH to begin equilibration for the water-uptake measurements. The 98% RH step was followed by 95% RH and 90% RH before the humidity set points were reduced in intervals of 10% RH down to 0% RH and then ramped back to 98% RH in a mirrored manner. All humidity set points were held for 60 min. The second, increasing-humidity sorption curve was used to analyze the water uptake. Dry weight was obtained by weighing the membrane in a 0% RH environment in the DVS for 1 hour. Additional details are found in prior studies.[45, 55]

4.3.3 Electrochemical Experiments

The microelectrode cell used was as described previously.[103, 163] Hydrogen gas (2 or 4 vol % in Ar, Linde Gas, or 100%, H2PEM-510 H_2 generator, Parker Hannifin, Ohio, USA) was humidified via external humidifiers (Humidification System, Fuel Cell Technologies, New Mexico, USA) or a custom wet/dry gas mixing bubbler before entering the cell. Cell temperature was controlled by a heating pad below the cell and custom proportional-integral-derivative (PID) control system (Red Lion, Pennsylvania, USA). Gas lines entering the cell were held at 80 or 90°C for the 40/50 and 70°C trials, respectively, to minimize water-droplet formation. A syringe tube heater (New Era Pump Systems, New York, USA) maintained temperature between the humidifier and the microelectrode cell. Electrochemical measurements were performed with a VSP-300 potentiostat and ultra-low current card (Bio-Logic, Seyssinet-Pariset, France).

4.3.4 OCV Measurements

OCV was measured between the working and reference electrodes**.** OCV was held for 30 min or until a stable reading was achieved at each tested humidity. An OCV was considered stable if there was a less than 2 mV continuous increase or decrease in at least a 5-10 min period as a baseline, or if the OCV was fluctuating in a ± 5-mV range in the same time period. For the hydroxide-form AEMs, a 15-hour potential hold at 0.5 V was performed to remove trace carbon dioxide before the OCV measurements. A hydrogen reference electrode was used in all cases.

All membranes and counterion-exchange forms were tested by fixing the reference electrode (RE) at a constant RH and varying the WE/CE side in 5% RH intervals ± 10% from each of these setpoints, *e.g.*, when the RE was held constant at 50% RH, the WE/CE side was varied in increments at 40, 45, 50, 55, and 60% RH. A table of all test conditions may be found in Table 4.1. The standard test for AEMs held the RE at 50, 70, and 90% RH while the WE/CE side was varied accordingly. 100% RH was not used when the RE was held at 90% RH due to water-droplet formation. Temperatures tested include 30, 40, 50, and 70°C. At the non-50°C temperatures, only 50% RH RE (30, 70°C) or 90% RH RE (30, 40°C) were tested. Experiments involving Nafion 211 used the standard procedure at 50°C, but at 20°C, the RE was held at 39, 57, 79, and 89% RH, and the WE/CE varied. At 20°C, experimental error sometimes resulted in RH differences between the WE and RE of up to 14% instead of 10%. Raw OCV versus RH data can be found in Tables S4.2-S4.9 in Section 4.8.6.

Table 4.1: Table indicating the combinations of membrane ion form, temperature, and reference RH setpoints. An "X" in the reference RH columns indicates that measurement was performed and a "-" indicates the measurement was not performed.

Membrane, Ion Form	Temperature (°C)	Reference Relative Humidity (%)						
-	-	39	50	57	70	79	89	90
Nafion, H	20	X	-	X	-	X	X	-
Nafion, H	50	-	X	-	X	-	-	X
Nafion, Na	50	-	X	-	X	-	-	X
PSS, H	50	-	X	-	X	-	-	-
Versogen, OH	30	-	X	-	-	-	-	X
Versogen, OH	40	-	-	-	-	-	-	X
Versogen, OH	50	-	X	-	X	-	-	X
Versogen, OH	70	-	X	-	-	-	-	-
Versogen, CO_3	30	-	X	-	-	-	-	X
Versogen, CO_3	40	-	-	-	-	-	-	X
Versogen, CO_3	50	-	X	-	X	-	-	X
Versogen, CO_3	70	-	X	-	-	-	-	-
Sustainion, OH	50	-	X	-	X	-	-	X
Sustainion, CO_3	50	-	X	-	X	-	-	X

4.4 Data Interpretation

4.4.1 PEM

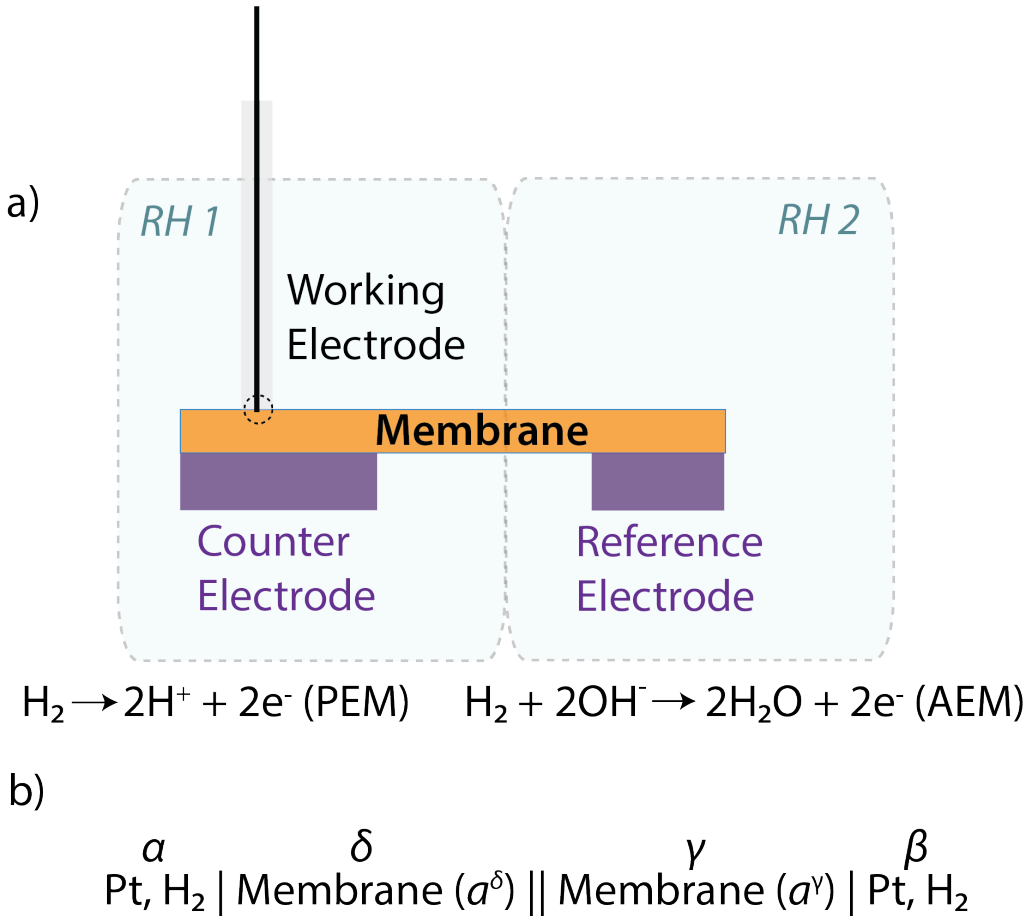

Figure 4.2: a) Schematic of the microelectrode cell. b) Thermodynamic phase diagram used in the analysis of the OCV. Single vertical bars indicate a phase boundary and a vertical double bar indicates where the water activity changes in the membrane.

OCV, the open circuit or equilibrium potential, U, is a thermodynamic property of the system, *i.e.,* electrical current is net zero. Conversely, the counter-ion water transport number, T_i, is a transport property relating the flow of ions to the flow of water in the membrane. To relate these two properties, both system thermodynamics and species fluxes must be considered. We follow closely the development for hydronium ions in Nafion by Fuller and Newman.[36]

The electrochemical cell consists of two Pt electrodes (RE and WE/CE) separated by a PEM (or AEM), with the membrane enclosed in two regions each with a different water activity (as set by the RH). The Pt electrode and membrane enclosed on the "left" side are arbitrarily denoted as phases α and δ, respectively, and the electrode and membrane enclosed on the "right" side as β and γ. A cell schematic is given in Figure 4.2a, and a corresponding thermodynamic phase diagram is depicted in Figure 4.2b. The cell analysis of Fuller and Newman[36] for the water transport number of hydrogen ions in a PEM reduces to

$$\mathrm{T}_{\mathrm{H}^+} = \frac{F}{RT}\frac{dU}{dln\left(\frac{a_0^{\delta}}{a_0^{\gamma}}\right)} \tag{4.6}$$

where F is Faraday's constant, U is the OCV, R is the ideal-gas constant, T is the absolute temperature, and phases δ and γ are as defined in Figure 4.2.[36] a_0^i is the water activity in phase i controlled by exposure to water vapor of known RH. Equality of water activity is imposed between the membrane phase and water vapor on each side. For an isothermal membrane, the ratio of upstream and downstream water activities is given by the ratio of the corresponding RHs. Thus, the hydronium-counterion water transport number, and those to follow, are ascertained by measuring the OCV as a function of the water-vapor RH ratio between the working and reference electrodes. We note that these correspond to in-plane transport numbers.[17, 164]

Equation 4.6 demands isothermal cell operation with condensation of water on the upstream membrane side and vaporization on the downstream membrane side. Gas convection and small counter-electro-osmotic water flows justify this assumption. The membrane is also assumed homogeneous with membrane charge and neutralizing counterions uniformly distributed spatially. In addition, the membrane must be a single-neutralizing ion-exchange form. Hydrogen partial pressures on each side of the membrane do not appear in Equation 4.6 because equal composition of hydrogen gas is supplied to both the working and reference electrode chambers. Partial pressure differences caused by different humidities are not significant, as calculated from the Nernst equation.

4.4.2 Sodium-Form Nafion

Transport numbers of single cations other than hydronium can likewise be quantified by Equation 4.6 even in the absence of electrode reactions (*e.g.*, sodium ions). In this situation, the completely polarized electrodes sense the electric potentials enforced at the boundary between the electrode surface and the membrane. We report results below for the water transport number of sodium ions in Nafion 211. Implicit is the assumption that sodium will not react at the electrode surface.

4.4.3 HEM

When an AEM is in the single hydroxide-exchanged form, *i.e.*, HEM, the hydrogen oxidation reaction[144] is

$$\mathrm{H_2} + 2\mathrm{OH^-} \leftrightarrow 2\mathrm{H_2O} + 2\mathrm{e^-} \tag{4.7}$$

and thus different than that for a PEM (see Equation 1.1). This reaction necessitates a different expression for the OCV than that used in the hydrogen-ion PEM case. We extend the framework of Fuller and Newman[36] to arrive at

$$FU = \int_{x_\gamma}^{x_\delta} \nabla\mu_{\mathrm{OH^-}} dx - \int_{x_\gamma}^{x_\delta} \nabla\mu_0 dx \tag{4.8}$$

where x is the coordinate parallel to the membrane between the two electrodes with subscript phases defined in Figure 4.2, and μ_i is the electrochemical potential of species *i.* Water is given the subscript 0. The last term on the right involving the water gradient arises from the alkaline reaction equilibrium in Equation 4.7.

Zero current[36] of hydroxide ion demands that

$$\nabla\mu_{OH^-} = -|z_{\mathrm{OH^-}}|\mathrm{T}_{\mathrm{OH^-}}\nabla\mu_0 \tag{4.9}$$

where $\mathrm{T}_{\mathrm{OH^-}}$ is the transport number of water in a HEM and $z_{\mathrm{OH^-}}$ is the valence of hydroxide ion. Substitution of Equation 4.9 into Equation 4.8 and differentiation results in the desired expression for the hydroxide-ion water transport number

$$\mathrm{T}_{\mathrm{OH^-}} = -\frac{F}{RT}\frac{dU}{dln\left(\frac{a_0^\delta}{a_0^\gamma}\right)} - 1 \tag{4.10}$$

This result has previously been derived by Wang *et al.*[160] and Roy.[161]

4.4.4 Carbonate and Bicarbonate-Form AEMs

In the presence of atmospheric carbon dioxide, alkaline AEMs can transform into multi ion-exchange forms of hydroxide, bicarbonate, and carbonate counter ions. Accordingly, we desire the water transport numbers of bicarbonate and carbonate ions in addition to that of hydroxide ion. However, the general multi-ion case is highly involved.[165] To simplify the analysis, we ion exchange the AEMs into predominately bicarbonate or carbonate forms where each counter ion is present singly. By analogy to Equation 4.9, we write for bicarbonate and carbonate ions, respectively, that

$$\nabla\mu_{\mathrm{HCO_3^-}} = -\left|z_{\mathrm{HCO_3^-}}\right|\mathrm{T}_{\mathrm{HCO_3^-}}\nabla\mu_0 \tag{4.11}$$

and

$$\nabla\mu_{\mathrm{CO_3^{2-}}} = -\left|z_{\mathrm{CO_3^{2-}}}\right|\mathrm{T}_{\mathrm{CO_3^{2-}}}\nabla\mu_0 \tag{4.12}$$

When AEMs are either in the carbonate or bicarbonate forms, the reaction at the electrode remains the same as Equation 4.7, as the system is still alkaline, and thus Equation 4.8 still holds. However, the primary mobile ion is no longer hydroxide but is either bicarbonate or carbonate. From Equations 4.1 and 4.2, respectively, the hydroxide electrochemical potential in Equation

4.7 is replaced by either that of bicarbonate or carbonate species. Upon neglect of the small quantity of dissolved carbon dioxide, one finds that

$$\nabla\mu_{\mathrm{OH^-}} = \nabla\mu_{\mathrm{HCO_3^-}} \tag{4.13}$$

or

$$\nabla\mu_{\mathrm{OH^-}} = \frac{1}{2}\nabla\mu_0 + \frac{1}{2}\nabla\mu_{\mathrm{CO_3^{2-}}} \tag{4.14}$$

for bicarbonate and carbonate ions, respectively. Following the development above for HEM, Equations 4.13 and 4.14 are sequentially substituted into Equation 4.8 and the result differentiated to yield

$$\mathrm{T}_{HCO_3^-} = -\frac{F}{RT}\frac{dU}{dln\left(\frac{a_0^\delta}{a_0^\gamma}\right)} - 1 \tag{4.15}$$

and

$$\mathrm{T}_{CO_3^{2-}} = -\frac{F}{RT}\frac{dU}{dln\left(\frac{a_0^\delta}{a_0^\gamma}\right)} - \frac{1}{2} \tag{4.16}$$

for bicarbonate and carbonate water transport numbers, respectively.

To evaluate the various water transport numbers as a function of water content, a differential approach is used with Equations 4.6, 4.10, 4.15, or 4.16. In previous studies, an integral method was used to evaluate the water transport number, *i.e.*, the reference side was held at one RH and the working side varied over the entire tested range of RHs.[36] The water transport number was then evaluated from the slope of the data over the entire range of water contents. Herein, differential measurements were used as described above, where the reference-side RH was held at discrete points and the working-side RH was varied in a small range around this value. To quantify the water transport number as a function of water activity, measured OCV data were plotted versus the natural logarithm of RH (*i.e.,* water activity) and the local slopes calculated. Figure S4.1 in Section 4.8.1 illustrates the procedure. Differential data analysis better accounts for the variation of the water transport number with water content as it minimizes the magnitude of the water diffusion gradient and error caused by overly large gradients, especially with properties dependent on membrane water content, and also better represents a true water transport number. However, this approach also results in inherently more data scatter and error, as the smaller amount of data around each reference RH datum results in more variability in slope (due to intrinsic variability in RH measurement), as documented in Figure S4.1. Figure S4.2 reports typical error bars in water transport numbers for counterions in AEMs; similar data scatter was witnessed for Nafion.

4.5 Results and Discussion

4.5.1 Verification of Experimental Technique

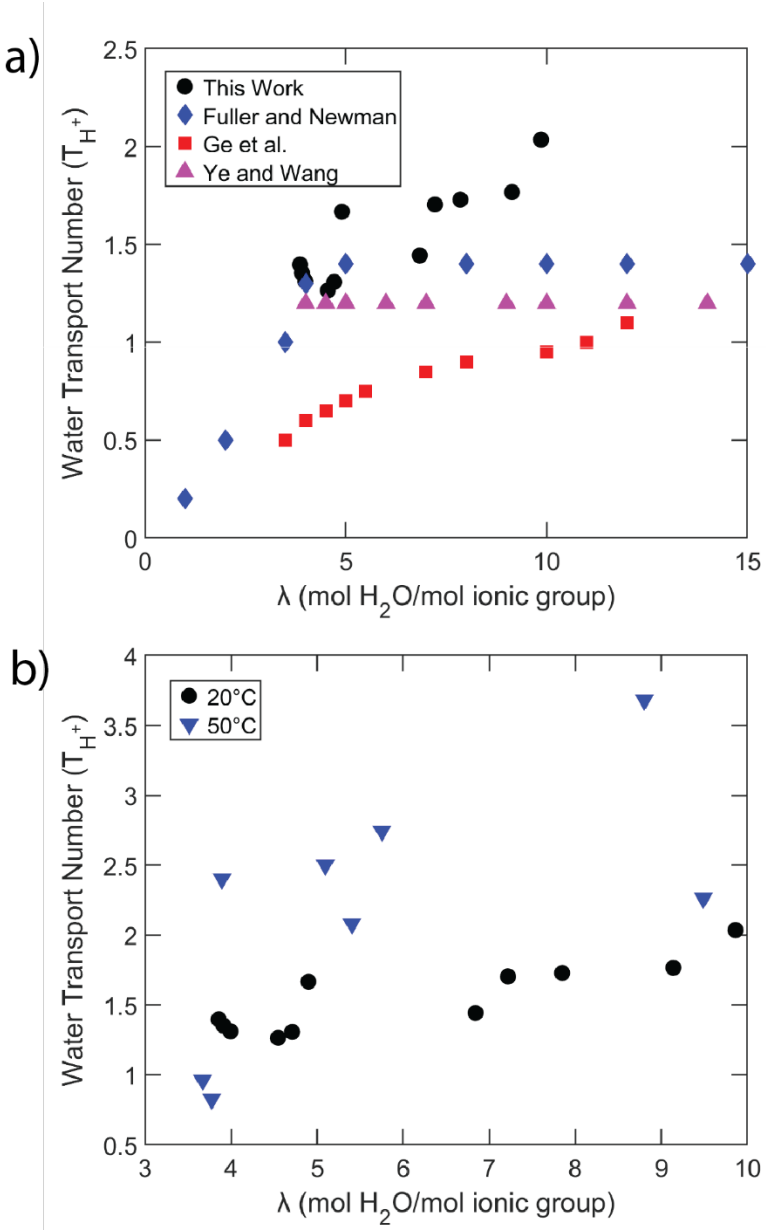

Figure 4.3: a) Measured water transport number of hydronium ion in Nafion 211 at 20°C (black circles) compared to literature sources (colored symbols) as a function of membrane water content.[36, 52, 156] b) Measured water transport number of hydronium ion in Nafion 211 at 20°C and 50°C as a function of membrane water content.[17] Values reported at 50°C are the average of three trials.

To validate the microelectrode experimental apparatus and interpretation scheme, measurements were performed with hydronium ion in Nafion 211 at 20°C. Results are shown as filled circles in Figure 4.3a compared with existing literature (remaining symbols).[36, 52, 156] All reported water contents in Figure 4.3 and in subsequent figures are the average between the working and

reference electrodes. Measured water transport numbers increase from approximately 1.3 at low membrane water contents to nearly 2 at high water contents, or 1.3 to 2 water molecules moving per proton migrated. An increase is expected as higher water contents raise the availability of free water in the membrane,[17] which then migrates with the counterion via electro-osmosis. With less free water, the solvation shell of the protons may not be fully filled, resulting in the lower measured water transport numbers. Our measured values are somewhat higher than previously reported, with a previous Nafion-211 maximum in water vapor reported as ~1.4.[17, 36] Membranes were pretreated in both cases.[36] It is possible that error introduced from the flow cell design used here is partially responsible for this difference as well.

The proton water transport number of Nafion 211 at 50°C is compared to that at 20°C in Figure 4.3b. There is a modest increase in the water transport number from a high of 2 at 20°C to approximately 3 at 50°C. This result is somewhat higher than expected based on prior studies of the water transport numbers for Nafion.[69, 157, 158] In those studies over the same temperature range, the water transport numbers increased ~ 20% for liquid-equilibrated Nafion. It has been shown that the primary solvation shell of aqueous ions does not change significantly in this temperature regime.[166, 167] As a result, it is likely that only the secondary solvation shell (*i.e.,* long-range interactions) is impacted by the increasing temperature. We suggest that at higher temperature, local water viscosity in the secondary shell around each ion is relatively lower than that at lower temperature leading to lessened viscous forces on the primary shell and more water transporting with the migrating ion. Additional analysis of temperature effects in the AEMs is addressed below.

4.5.2 Water Transport Number of AEMs

Understanding water uptake of the different ion-exchange forms of Versogen is requisite to describe fully how the water transport number changes with RH. The water uptake of Nafion as a function of RH is well-studied.[17, 20, 21, 168] Likewise, water uptake in hydroxide and carbonate forms of Sustainion is available.[153] Figure 4.4 shows our measurement of water uptake of hydroxide-form Versogen (solid line) as a function of RH, compared to available literature data for carbonate and bicarbonate forms (dashed and dotted lines).[55] The water uptake for the hydroxide counterion is slightly lower than that of carbonate and bicarbonate counterions, which, in turn, are almost identical.[55] It should be noted that water uptake is defined here as per fixed endgroup – if defined per transport ion, the water uptake values for carbonate will be half that displayed in Figure 4.4.

Figure 4.5a demonstrates the water transport number for hydroxide and carbonate ion-exchange forms of Versogen as a function of membrane water content at 50°C (Figure 4.5a can be found as a function of RH in Figure S4.3). Carbonate-form Versogen has the highest water transport number at all water contents, ranging from ~3 to ~11, with the difference more pronounced at higher water contents. Hydroxide form consistently has the lowest water transport number, ranging from ~0.5 to ~6, with bicarbonate-ion form bracketed between carbonate- and hydroxide-form values. The values for all ions are similar to that of protons in Nafion at low water content and exceed that of protons at high water content. A similar trend is seen for Sustainion in Figure 4.5b, with the water transport number for the carbonate species clearly

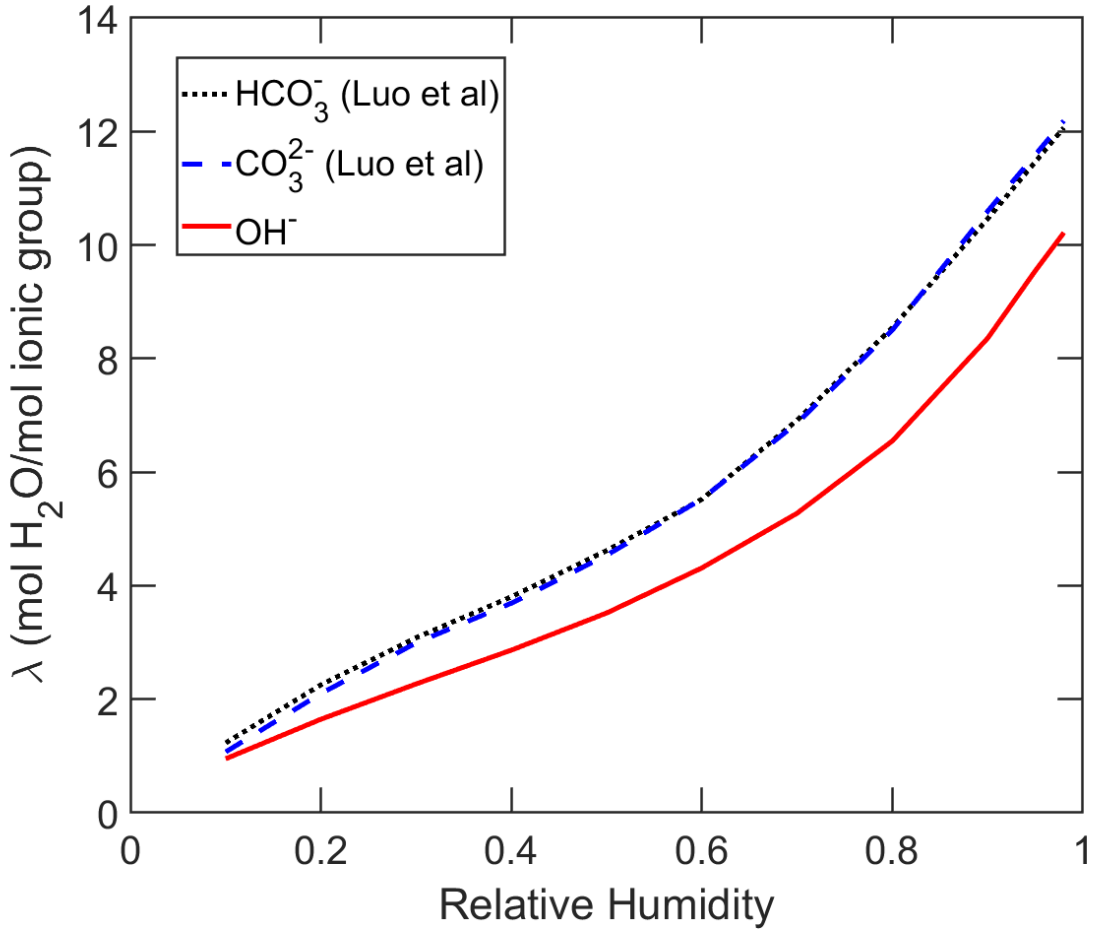

Figure 4.4: Water content of the different ion-exchanged forms of Versogen as a function of RH at 25°C. Carbonate and bicarbonate results (blue dashed and black dotted lines) are from Luo et al.[55]

higher than the hydroxide counterion, particularly at high water content. The carbonate and hydroxide forms of Versogen are given with error bars in Figure S4.2. These error bars are somewhat large, particularly at high water content, and are likely due to two primary factors. The first is the nature of small interval slope measurements, as mentioned previously, which gives rise to larger error bars. The second is water-droplet formation at high water content (RH). Water droplets result in significant variation in the OCV as a function of time, making it difficult to discern the true OCV at a given RH. Even very small quantities of liquid water disturb the measurement.

The origin of the differences in water transport number between specific ion forms is likely related to the solvation shells of the different ions. One interpretation of water transport number is that the amount of water dragged by an ion as it migrates is at least partially related to the water complexed around the ion in its solvation shells.[17] In this case, the transported solvation shell of protons is 2 or 4 waters, hydroxide ion is 4 or 5 waters, bicarbonate is 6.9 waters, and carbonate is 8.7 waters, as depicted in Figure 4.6.[169-172] With this framework, the origin of the trend with ion type becomes clear: the larger is the number of water molecules solvated around

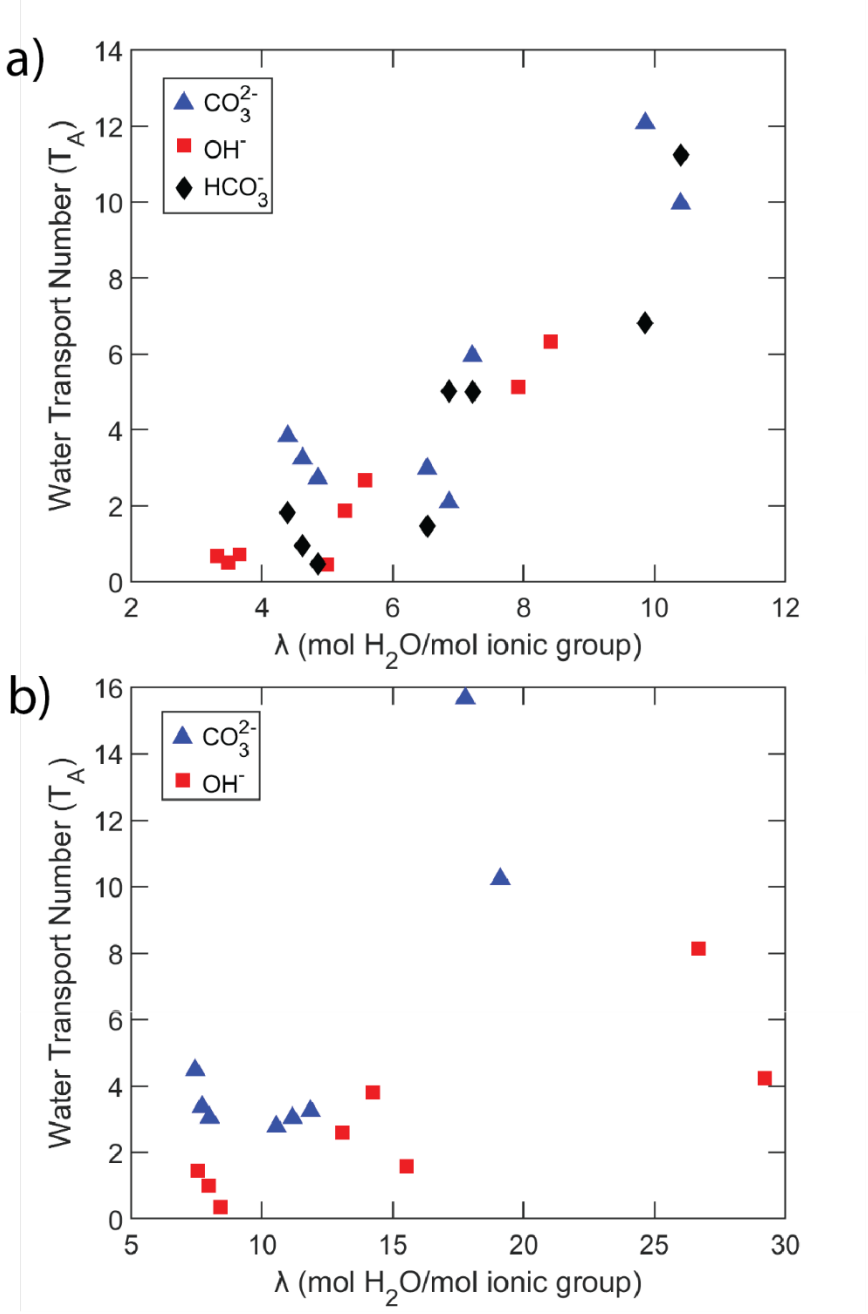

Figure 4.5: a) Water transport numbers for hydroxide (red squares), carbonate (blue triangles), and bicarbonate (black diamonds) forms of Versogen as a function of water content at 50°C. Subscript A represents a generic anion. b) Water transport numbers of hydroxide (red squares) and carbonate (blue triangles) forms of Sustainion versus water content at 50°C.

an ion, the larger is the amount of water transported via electro-osmosis. The results indicate that the ion water transport numbers exceed the hydration number of the first solvation shell at high water content. Likely, this is due to the impact of secondary solvation shells and the presence of more free water at high water uptake.[17] The solvation shells listed above are primary solvation shells only, and do not consider long-range interactions, such as water outside the primary solvation shell transporting with the moving shell due to viscous effects, which would increase

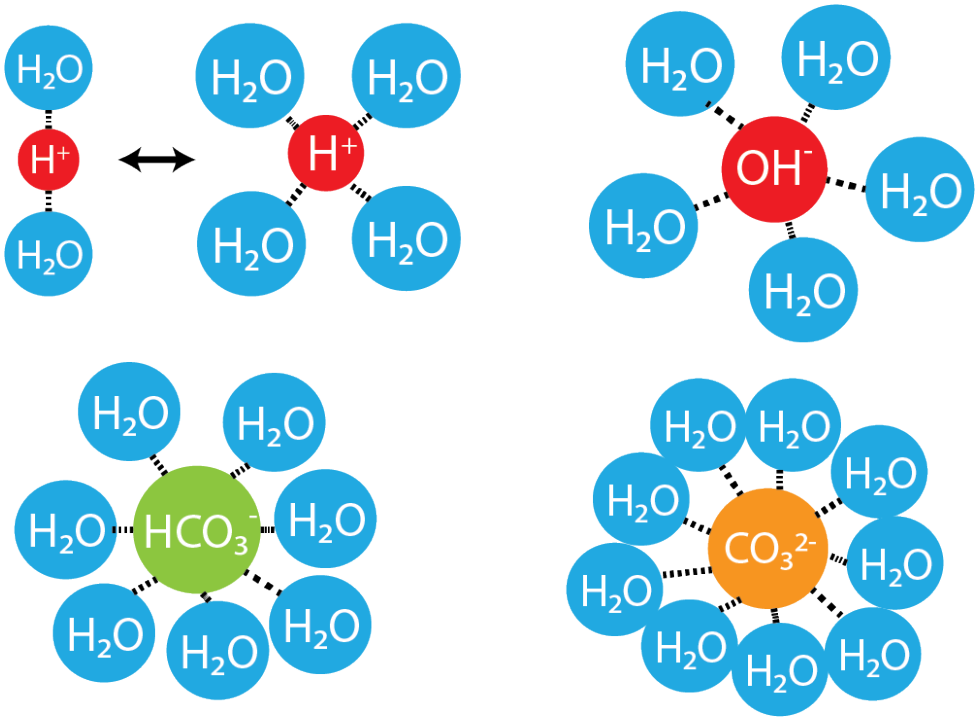

Figure 4.6: Schematic of the primary solvation shells of protons, hydroxide, bicarbonate, and carbonate ions

the measured water transport number. The carbonate ion, in particular, appears to transport water in amounts far exceeding that of its first solvation shell (multiplying the values in Figure 4.5a and 4.5b by the valence obtains a water transported per carbonate ion value of 20 to 24 in Versogen, for example). Although this result is somewhat surprising, it is known that carbonate ions have a longer range impact than only in the primary solvation shell.[171] In addition, divalent ions (*e.g.*, Ni^{2+}, Cu^{2+}) have similarly high electro-osmotic coefficients in Nafion, and thus transport similar large quantities of water.[173, 174] Our results for the divalent carbonate ion in AEMs are roughly in line with those for divalent ions in Nafion.[173, 174]

To verify that the origin of differences in water transport number between Nafion and the AEMs is primarily related to solvation shells, and not membrane microstructure, the water transport number of proton-form Nafion is compared in Figure 4.7 with sodium-form Nafion and proton-form sulfonated polystyrene (PSS) (a non-phase-separated PEM) as a function of RH at 50°C.[56] Proton PSS exhibits a water transport number equal to or slightly less than that of proton Nafion 211 at all RHs; transport numbers for PSS at high humidity are not shown due to membrane dissolution under those conditions. In contrast, sodium-form Nafion exhibits a water transport number of up to 8 at high humidity, greatly exceeding that of proton-form Nafion. Sodium ions display a solvation shell of 6 waters, again larger than that of a proton.[175] The only ion/membrane combination that transports less water than its ion solvation shell at high water content is protons in PEMs. This is likely due to Grotthuss hopping that protons undergo at high membrane water contents.[176] Any proton that moves via hopping does not transport water with it, reducing the measured transport number compared to that of an ion that only moves vehicularly. Taken together, ion solvation shells are the primary driver of differences in water transport numbers between membranes, as the impact of membrane microstructure appears smaller, with

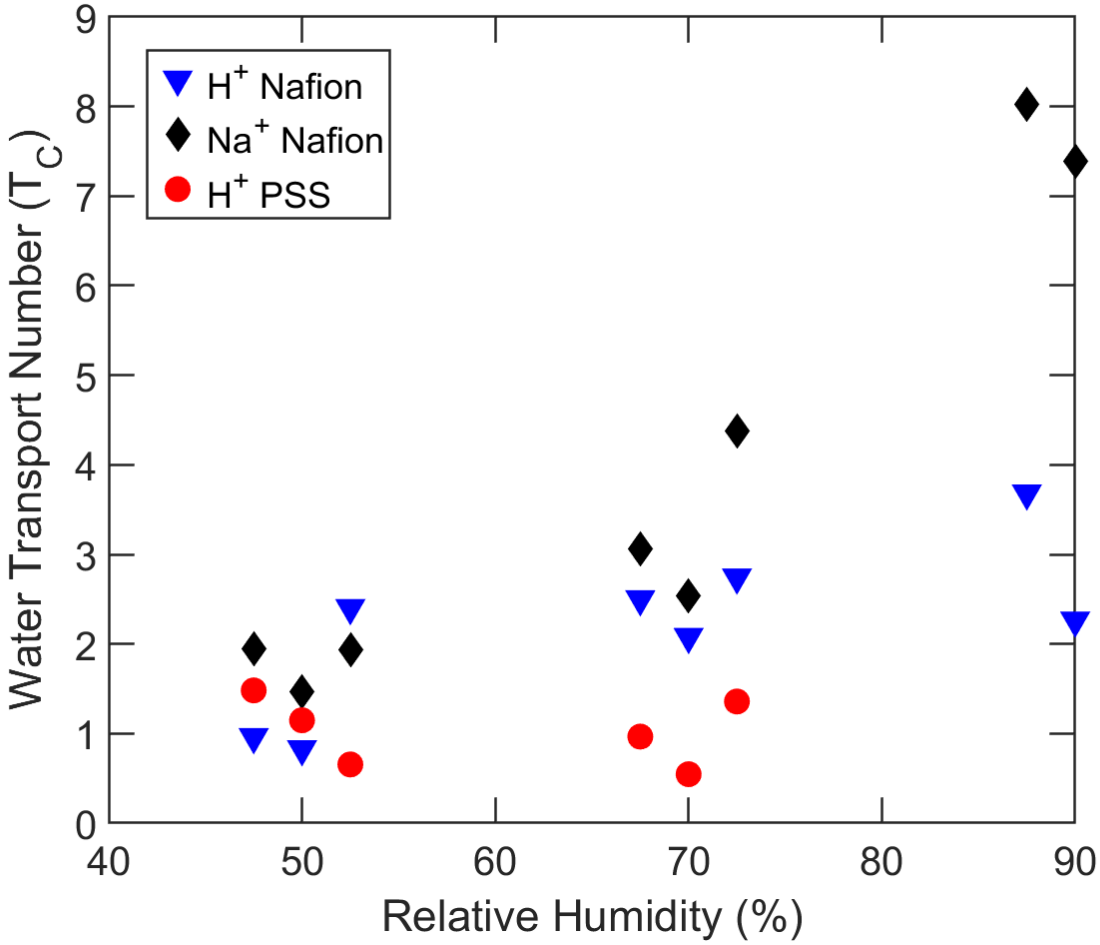

Figure 4.7: Water transport numbers of sodium-form Nafion (black diamonds), proton-form Nafion (inverted blue triangles), and proton-form sulfonated polystyrene (red circles) as a function of RH at 50°C. PSS coefficients are omitted at high RH due to membrane dissolution. Subscript C denotes a generic cation.

the lack of phase separation appearing to dampen slightly the transport number, in agreement with prior studies examining the water transport numbers in hydrocarbon-based membranes that similarly lack phase separation.[177, 178]

4.5.3 Impact of Temperature on the Water Transport Number in AEMs

Most electrochemical devices do not run solely at 50°C. Accordingly, it is of interest to determine how the water transport number varies with temperature. Figure 4.8a and 4.8b report the influence of temperature on water transport numbers for both the carbonate and hydroxide forms of Versogen as a function of RH. There appears to be a weak but inconsistent increase in water transport number with temperature, suggesting that the impact of temperature is limited at best. This assertion is supported by examining the activation energies of the transport number: 5 J/mol and –166 J/mol for carbonate form at low and high water contents, respectively, and 153

J/mol and 705 J/mol for hydroxide form at low and high water content, respectivley. Three of the four activation energies indicate weak increases with temperature, whereas the activation energy of electro-osmosis in high water content carbonate form actually demonstrates a weak decrease with temperature; the large amount of scatter in the data prevents drawing definitive physical conclusions.

4.5.4 Modeling of Water-Transport Parameters

To correlate different transport properties, especially for cases where there is a lack of experimental data, a model is developed for the water transport number. The Stefan-Maxwell-Onsager framework of frictional interactions between chemical species in a membrane is pertinent for electro-osmotic phenomena.[179, 180] A detailed description of the model can be found in Section 4.8.3, where we expand upon the specific adaptation of Crothers *et al*.[180, 181] In the Stefan-Maxwell framework of multicomponent diffusion, the water transport number is defined as[36, 181]

$$\mathrm{T}_i = \frac{L_{i0}}{|z_i| L_{ii}} \tag{4.17}$$

where L_{ij} is the binary interaction parameter between species i and species j. As outlined in Section 4.8.3, we estimate L_{i0} and L_{ii} by calculation of binary species friction coefficients.[181] In this approach, the ion-water friction coefficient is determined by scaling the microscale friction coefficient obtained from a Stokes-Einstein estimate of the ion-water binary diffusion coefficient to account for temperature and viscosity.[180, 181] The water-membrane and ion-membrane friction coefficients are determined from Darcy's law for porous-media flow following the work of Crothers *et al*.[180, 181] All experimental results used in this section correspond to 50°C. In all cases, calculated curves are not smoothed over the discrete datum points.

Two unknown parameters assess the water transport number using the Stefan-Maxwell formulation in Equation 4.17: the Darcy absolute permeability of water (k) in the membrane as a function of water content (see Equation S4.5, $v_z = -\frac{k}{\eta}\frac{dP}{dz}$, where η is the water viscosity, v_z the mass-average water velocity in the z direction, and P is the water pressure)[116, 182] and the power-law parameter χ in Archie's law for membrane tortuosity (see Equation S4.9, $\tau = \phi^{-\chi}$, where τ is the membrane tortuosity and ϕ is the water volume fraction).[183] Because there is one permeability for each experimental water-content datum, plus an unknown tortuosity power-law index, additional information is needed to quantify the transport numbers. For Nafion membranes, literature water transport coefficients, representing water flow in response to a chemical potential gradient, are available and are converted to a Darcy permeability and inserted into the model.[17, 32, 184] The χ parameter was varied over a physically acceptable range to arrive at a value of approximately 2. The solid line in Figure 4.9a compares the water transport number calculated via this approach with the experimental data from Nafion 211. An excellent fit is achieved for the proton water transport number over the range of water contents examined. Figure 4.9b shows the resulting tortuosity as a function of water content, which decreases as expected, although is somewhat high compared to models in previous literature.[134, 180, 181]

Nevertheless, the Archie law power index of 2 is well within the physical range determined for other porous media.[185] Furthermore, the tortuosity of liquid-equilibrated Nafion (λ=22) is approximately 5.5 when using $\chi = 2$ (determined from Archie's law), which is quite reasonable.[180, 181, 185] Figure 4.9 is re-plotted as a function of water volume fraction in Figure S4.5, and the corresponding water transport coefficient and Darcy permeability are likewise presented in Figure S4.4.

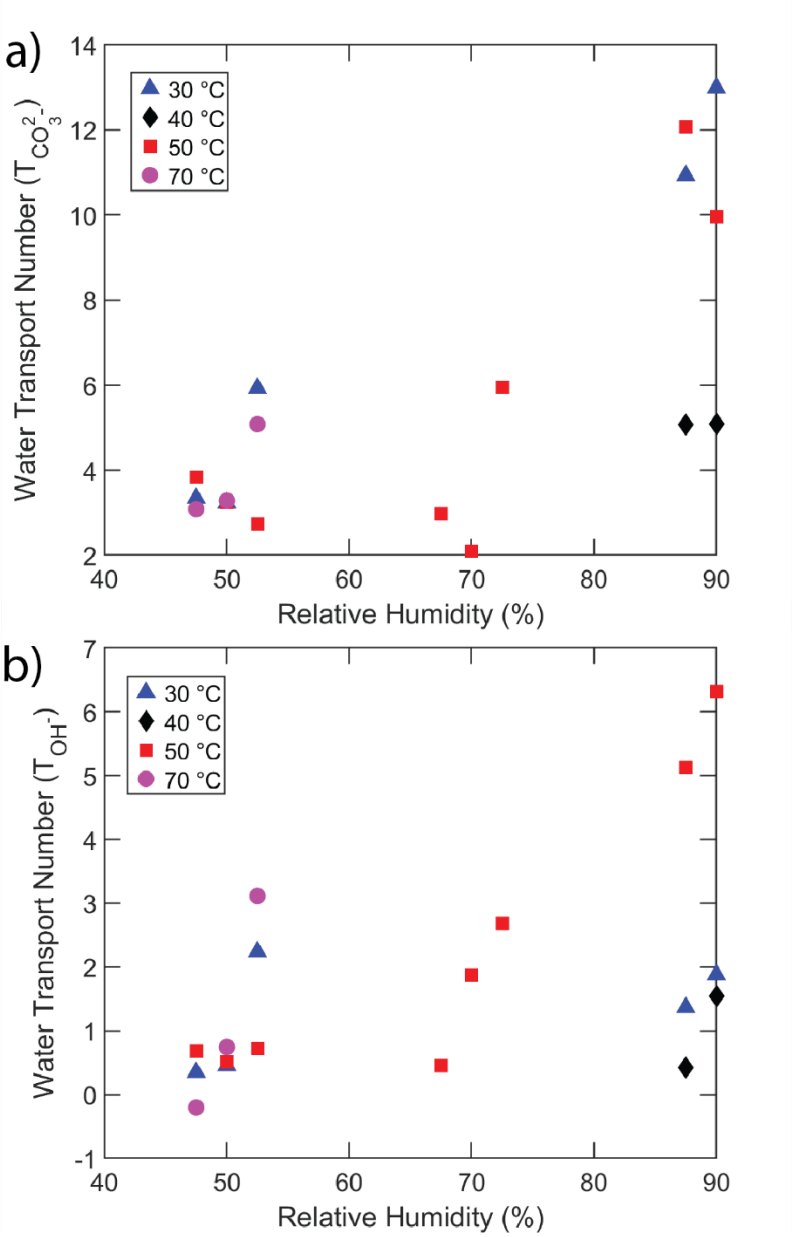

Figure 4.8: Water transport numbers in the a) carbonate and b) hydroxide forms of Versogen, respectively, as a function of RH and temperature (blue triangles, black diamonds, red squares, and magenta circles are 30, 40, 50, and 70°C, respectively).

The good-quality fit of the water transport number and the magnitude of the tortuosity for Nafion PEM suggest that the proposed model may be accurately applied for Versogen AEMs. Literature water transport coefficients are not available for Versogen. We thus adopt a different approach. To determine Versogen tortuosity, a reasonable range of χ parameters is considered, with that used for Nafion ($\chi = 2$) as the maximum and the value calculated from the tortuosity of a liquid-equilibrated hydrogel with similar water uptake as Versogen as the minimum ($\chi = 1.3$).[186] The latter value is reasonable because Versogen has an interpreted morphology similar to a hydrogel, as demonstrated by Figure S4.7.[55, 187, 188] A total of 5 different χ values are chosen in the 1.3 to 2

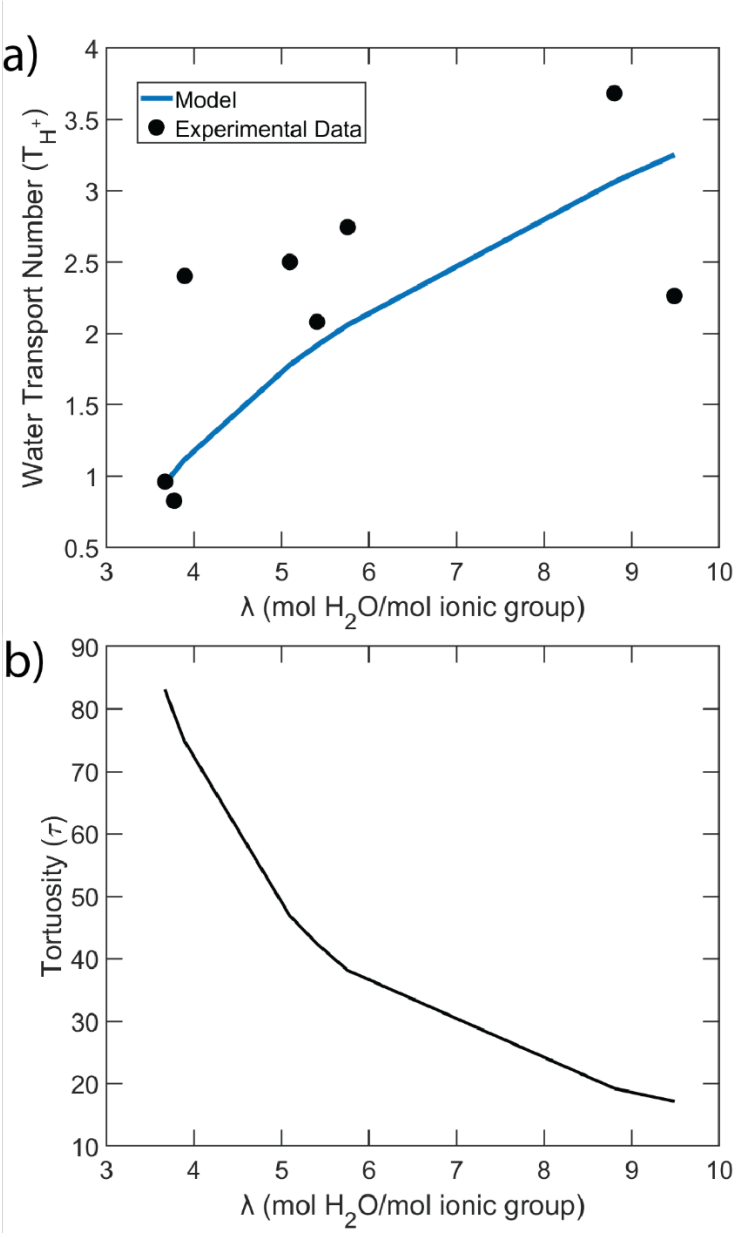

Figure 4.9: a) Water transport number for Nafion 211 as calculated from the friction coefficient model at 50 °C. The solid line represents the model prediction (blue) compared to experimental data (black circles). b) Calculated tortuosity of the Nafion 211 as a function of water content with $\chi = 2$.

range. The water transport number is then fit by nonlinear least-squares to extract the Darcy permeability as a function of water content.

Figure 4.10a-c give the water transport number, Darcy permeability (k), and tortuosity for hydroxide-form Versogen, respectively, as a function of water content. Each curve represents one χ parameter. The fit in Figure 4.10a is quite good and is independent of the χ-value chosen. Corresponding Darcy permeability and tortuosity increase and decrease, respectively, with water content in all cases. Figure 4.10b and 4.10c also reveal that permeability and tortuosity are inversely proportional: more tortuous transport pathways result in less water transport. The permeability of Versogen appears to be higher than that of Nafion with the vapor-equilibrated Versogen permeability at high water content approximately equivalent to that of liquid-equilibrated Nafion.[189] This finding is likely caused by the fact that Versogen has a higher water volume fraction (calculated assuming additive molar volumes) than does Nafion at the same water content due to the significantly lower equivalent weight and dry density of Versogen.[17, 55] A higher water volume fraction lowers tortuosity and increases permeability. It is also likely that

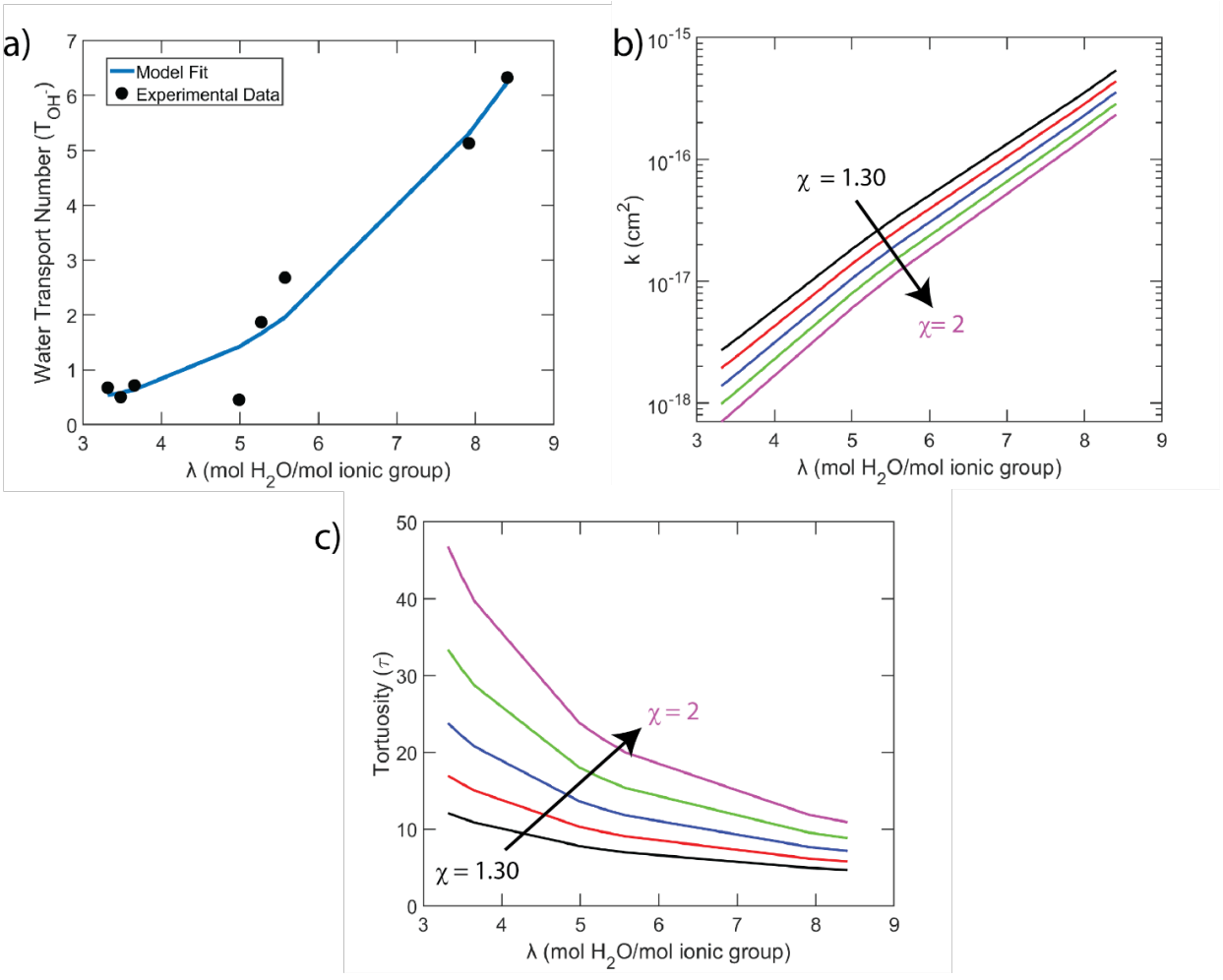

Figure 4.10: a) The model fit of the water transport number of hydroxide-form Versogen (blue line) compared to experimental data (black circles) as a function of water content at 50°C. b) Darcy permeability for hydroxide-form Versogen as a function of water content at 50 °C. c) Calculated tortuosity of the Versogen membrane as a function of water content. Values of χ are, in order, 1.30, 1.4, 1.65, 1.82, and 2.

the more hydrogel-like structure enables faster water movement than in the phase-separated Nafion. Figure 4.10 is shown as a function of water volume fraction in Figure S4.6, in addition to the calculated water transport coefficients.

Actual Versogen tortuosity and Darcy permeability lie between the two extremes in Figure 4.10, highlighting the importance of independent verification of either Darcy permeability or tortuosity. Nevertheless, the values of the permeability across the investigated range of tortuosities are within an order of magnitude of each other at high water content (the most likely condition for device operation), and thus useful as an initial estimate of the water transport parameters in the absence of data. These values can be used to determine more accurate water balances in AEM fuel-cell and electrolyzer models,[190, 191] thereby improving predictions of device performance.

4.6 Conclusions

Water transport numbers of Versogen and Sustainion AEMs in three single-ion exchange forms are measured using an extension of the Fuller-Newman electrochemical technique[36] and correlated to water content via measured water uptake at different relative humidities (RHs). In general, carbonate counterion has the highest transport number (ranging from ~3 to ~11 in Versogen) and hydroxide the lowest (~0.5 to ~ 6), over an RH range of 50 to 90%. This finding is likely due to differences in solvation-shell size between these two ions, as confirmed by examination of the Na-form of Nafion and H-form of PSS exchange membranes. Temperature does not have a significant impact on the measured water transport number in the range studied. A range of the Darcy permeability of Versogen were obtained from a Stefan-Maxwell-Onsager friction-coefficient framework. Membrane permeability is higher in non-phase-separated gelatinous Versogen than in phase-separated Nafion, likely due to the higher water volume fraction of Versogen at similar water content (reducing tortuosity and increasing permeability) and more hydrogel-like structure of Versogen. Ion-water transport numbers and Darcy permeabilities obtained in this study are useful for predicting more accurate water balances in AEM-based fuel cells and electrolyzers.

4.7 Symbols

Roman

a_0^x: water activity in phase x

a_i: ion radius

A: lumped parameter in Darcy's law

c_i: interstitial concentration of species i

$\tilde{c}_i$: macroscopic concentration of species i

D_{ij}: modified binary diffusion coefficient

D_{ij}^{∞}: bulk binary diffusion coefficient

EW_i : equivalent weight of membrane *i*

F: Faraday's constant

k: membrane permeability

$\widetilde{K}_{ij}$: macroscopic friction coefficient between species *i* and *j*

K_{ij}: microscopic friction coefficient between species *i* and *j*

k_B: Boltzmann's constant

L_{ij}: Interaction parameter between species *i* and *j*

M_i: molar mass of species *i*

N_i: flux of species *i*

P: pressure

q: scattering vector

R: gas constant

T: temperature

U: open circuit voltage

$\bar{V}_i$: molar viscous volume of the solvation shell of species *i*

v_0: molar volume of water

v_z: macroscopic mass-average velocity

$\boldsymbol{v_i}$: mole-average velocity of species *i*

w_i: mass fraction of species *i*

x: spatial coordinate parallel to the membrane between two electrodes

z_i: valence of species *i*

z: spatial coordinate parallel to flow

Greek

α: water transport coefficient

λ: water content

χ: power index in Archie's law, $\tau = \phi^{-\chi}$ [183]

μ_i: chemical potential of species *i*

η: effective water viscosity

η_∞: bulk water viscosity

ϕ: water volume fraction

ρ_i: dry density of membrane *i*

τ: tortuosity

T_i: water transport number in membrane of counterion-form *i*

ξ_i: electro-osmotic coefficient in membrane of counterion-form *i*

4.8 Supplemental Information

4.8.1 Error Analysis of the Water Transport Number in Versogen

To illustrate the amount of data scatter due to differential assessment of the reported water transport numbers, Figure S4.1 reports an example graph of FU/RT versus the natural logarithm of the ratio of the RHs. The data shown are for Nafion at 50°C with a reference RH of 70%.

According to definition, the water transport number is the local slope on this graph. Over the relatively narrow range of relative humidities reported in Figure S4.1, the slope is not constant, meaning that near RH = 70% the water transport number is subject to experimental error. To minimize this error, we evaluate three slopes using three sequential clustered data. The three slopes extracted (*i.e.,* the three water transport numbers) are listed in the figure. Differences in local slopes even near a set RH reveal the inherent scatter produced from the differential-analysis approach. For proton-form Nafion, hydroxide-form Versogen, and carbonate-form Versogen at 50ºC and at each reference RH, three repeat experiments were performed, and Figure S4.1 was reconstructed. Corresponding slopes at each incremented RH (± 10 %) were averaged and the

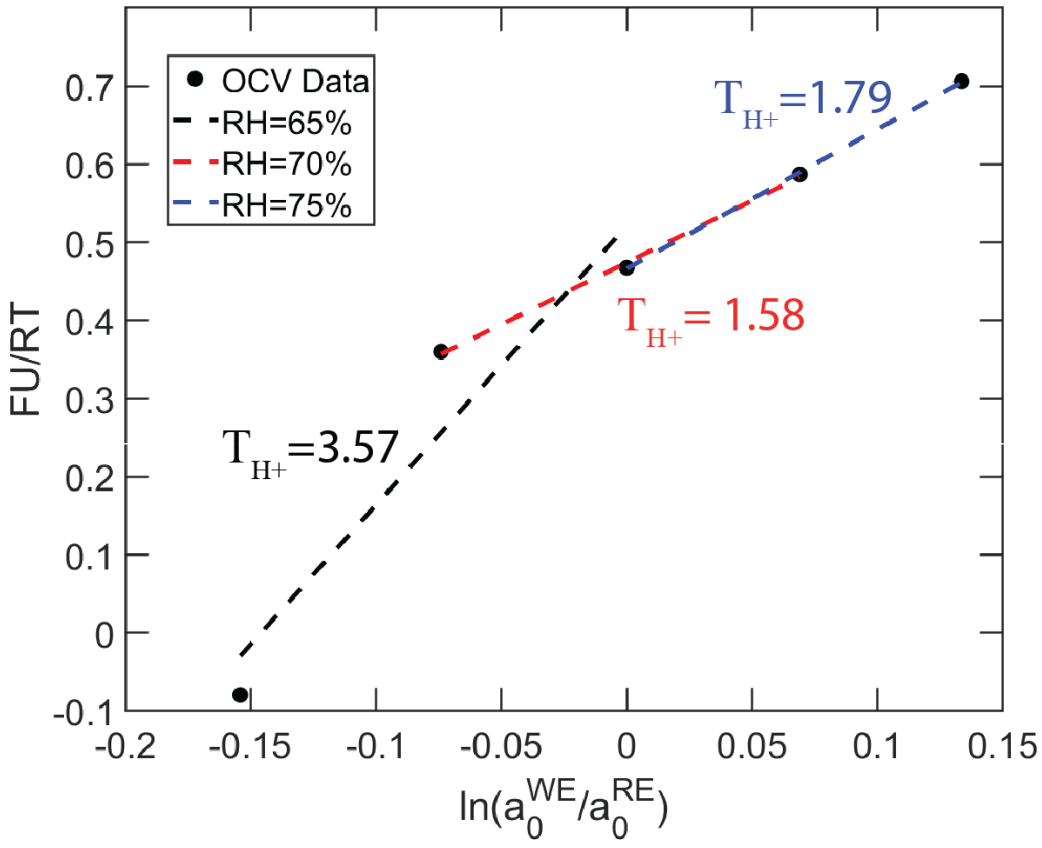

Figure S4.1: OCV data plotted as FU/RT versus the natural logarithm of the ratio of the water activities. The three transport numbers extracted from this data set are shown on the plot with the accompanying straight lines used. The RH values chosen in the legend are the WE RH at the middle of the three points used to create the line.

standard error evaluated. An example is shown in Figure S4.2 for the hydroxide and carbonate exchange forms of Versogen at 50°C. Error bars represent one standard deviation. Error is small at low water content and increases at high water content, likely because of condensation caused by high RH conditions.

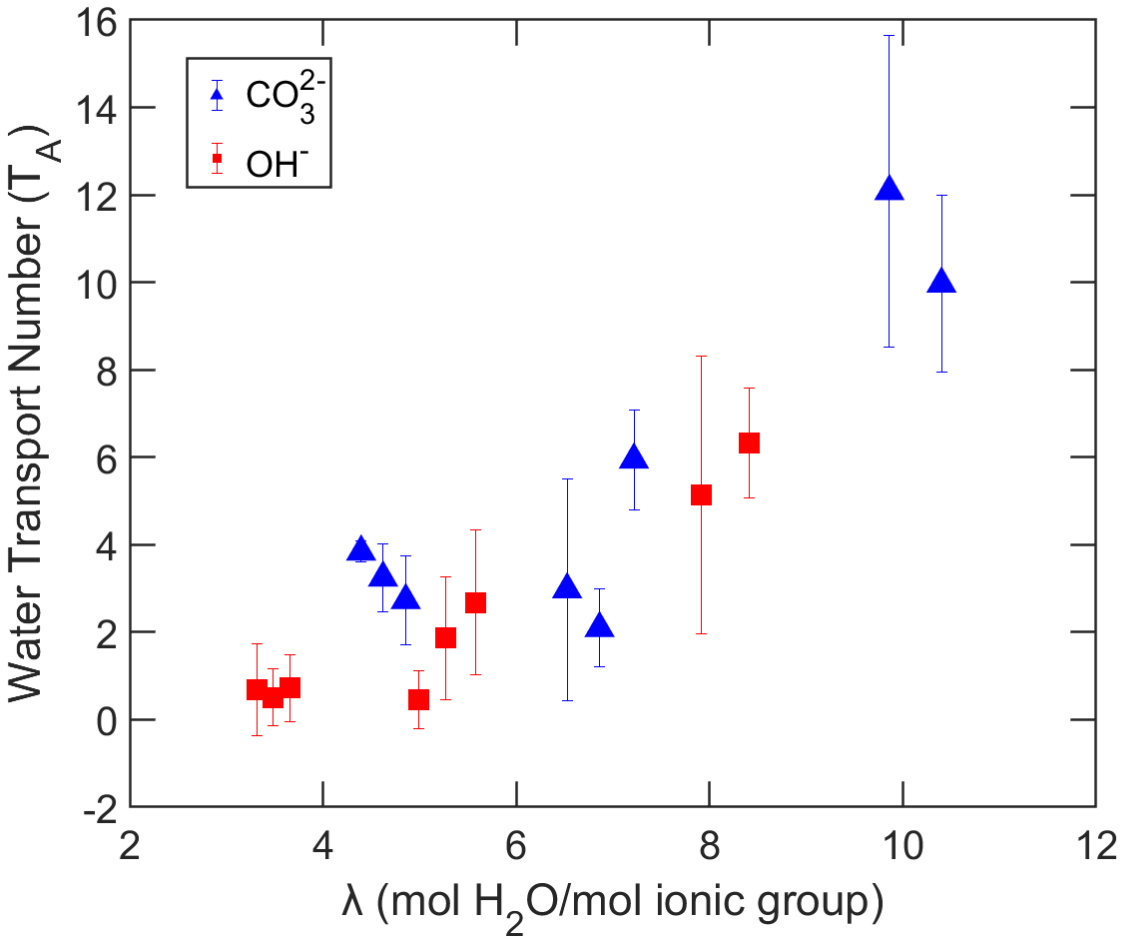

Figure S4.2: The carbonate and hydroxide trials for Versogen at 50°C from Figure 4.5a are replotted versus water content with error bars (1 standard deviation) to demonstrate repeatability. Subscript A denotes a generic anion.

4.8.2 Water Transport Number versus Relative Humidity

Water transport numbers for Versogen and Sustainion are replotted as a function of RH instead of water content as in Figure S4.3.

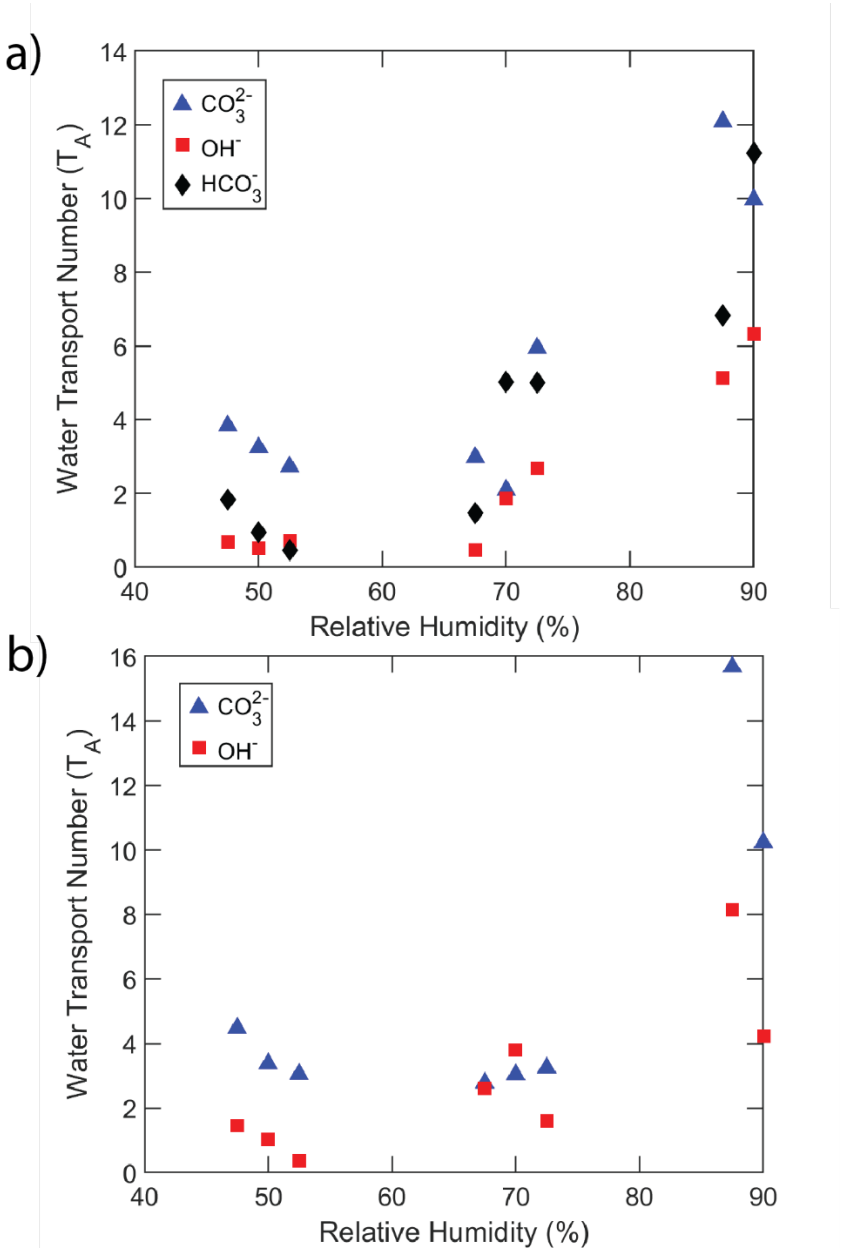

Figure S4.3: a) The water transport number of carbonate (blue triangles), hydroxide (inverted red triangles), and bicarbonate (black triangles) forms of Versogen as a function of RH. b) The water transport number of carbonate (blue square) and hydroxide (red circle) forms of Sustainion as a function of RH. Subscript A denotes a generic anion.

4.8.3 Friction Coefficient Model of Electro-Osmosis

We model water transport numbers in terms of a Stefan-Maxwell-Onsager framework that explicitly relies on binary interaction parameters calculated from the system friction coefficients.[116, 165, 180, 181, 192] Such an approach has been used with success for Nafion previously with micro-, meso- (network), and macroscale models.[179-181] Due to the lack of information available about the structure of AEMs, the macroscopic Darcy law determines the membrane-species friction coefficients, a difference from previous theory developed for Nafion.[193] The model is presented generally for any membrane/ion combination.

We define the water transport number, as in Equation 4.17, as[36, 181]

$$\mathrm{T_i} = \frac{L_{i0}}{|z_i| L_{ii}} \tag{S4.1}$$

where z_i is the charge of ion *i* and the L_{ij}'s are the binary interaction parameters between ion *i* and species *j*. A more complete description of the origin of this formulation can be found elsewhere.[36, 181] Both *L*'s must be determined to obtain the water transport number. The overall approach treats the membrane as a homogeneous porous medium, with polymer domains as impermeable regions and the imbibed water as the regions inside the "pores" or domains where transport occurs. Therefore, properties are determined on the microscale, inside the "pores", and upscaled to the macroscale when necessary. The *L*'s are defined as a function of binary-interaction friction coefficients as[179, 181]

$$L_{i0} = \tilde{c}_i \tilde{c}_0 \frac{\widetilde{K}_{i0}}{\widetilde{K}_{0M}\widetilde{K}_{iM} + \widetilde{K}_{i0}\left(\widetilde{K}_{0M} + \widetilde{K}_{iM}\right)} \tag{S4.2}$$

and

$$L_{ii} = \tilde{c}_i^2 \frac{\widetilde{K}_{i0} + \widetilde{K}_{0M}}{\widetilde{K}_{0M}\widetilde{K}_{iM} + \widetilde{K}_{i0}\left(\widetilde{K}_{0M} + \widetilde{K}_{iM}\right)} \tag{S4.3}$$

Where $\widetilde{K}_{ij}$ is the macroscale friction coefficient between species *i* and *j* and $\tilde{c}_i$ is the macroscale concentration of species *i* averaged across the entire membrane (*i.e.*, a superficial quantity). Here species 0 represents water, and species *M* labels the immobile membrane. The macroscale concentration is obtained from the expression

$$\tilde{c}_i = \phi c_i \tag{S4.4}$$

where ϕ is the water volume fraction and c_i is the interstitial concentration in the pores. The concentrations for the water and ion are determined from the molar volume of water and the equivalent weight of the membrane, respectively, assuming total ion dissociation and additive molar volumes.[17, 55, 194]

The next step requires the macroscale friction coefficients. Starting with the ion-water friction coefficient[116, 180, 181, 183, 192, 195, 196]

$$\widetilde{K}_{i0} = K_{i0}\left(\frac{\tau}{\phi}\right) = \frac{RTc_0c_i}{(c_i + c_0)D_{i0}}\left(\frac{\tau}{\phi}\right) \tag{S4.5}$$

with

$$D_{i0} = \frac{\eta_\infty}{\eta} D_{i0}^\infty \tag{S4.6}$$

$$\eta = \eta_\infty \frac{\left(1 + \frac{c_i\bar{V}_i}{2}\right)}{(1 - c_i\bar{V}_i)^2} \tag{S4.7}$$

$$D_{i0}^\infty = \frac{k_B T}{6\pi\eta_\infty a_i} \tag{S4.8}$$

and

$$\tau = \phi^{-\chi} \tag{S4.9}$$

where K_{i0} is the microscale friction coefficient, τ is the tortuosity, χ is the power index in Archie's law, η_∞ is the bulk water viscosity, η is the water viscosity accounting for dissolved ions, D_{i0} is the modified ion-water diffusivity, D_{i0}^∞ is the Stokes-Einstein bulk ion-water diffusivity, $\bar{V}_i$ is the molar viscous volume of the solvation shell of the ion, k_B is Boltzmann's constant, a_i is the ion radius, and all other variables are as defined previously. All physical parameters in the preceding equations are listed in Table S4.1. Equation S4.5 determines the microscale friction coefficient and scales it to the macroscale domain, Equations S4.6-S4.8 determine the diffusion coefficient as a function of the effective viscosity and the Stokes-Einstein diffusion coefficient, and Equation S4.9 is Archie's Law, determining tortuosity as a function of water volume fraction and a fitting parameter.[116, 180, 181, 183, 192, 195, 196] The term $\left(\frac{\tau}{\phi}\right)$ allows for conversion from the microscale to macroscale domain.[180]

The ion-membrane and water-membrane friction coefficients can be determined by starting from Darcy's law, which is inherently macroscopic in nature.[182] Darcy's law reads[116, 182]

$$v_z = -\frac{k}{\eta}\frac{dP}{dz} \tag{S4.10}$$

where v_z is the mass-average velocity in the z direction, k is the Darcy permeability of the membrane, and P is the water pressure. Following Crothers,[180] the pressure gradient is converted to a chemical potential gradient via the isothermal Gibbs-Duhem relation,[197] resulting in

$$v_z = -\sum_{i \neq M} \frac{c_i}{A}\frac{\partial \mu_i}{\partial z} \tag{S4.11}$$

with

Table S4.1: Physical Constants and Parameters

Symbol	Value	Definition
z_{H^+}	1	Proton Charge
z_{OH^-}	-1	Hydroxide Charge
F	96485 C/mol e^-	Faraday's Constant
v_0	18.01 cm^3/mol [194]	Molar volume of water
EW_{Naf}	1100 g/mol [17]	Nafion Equivalent Weight
EW_{Vers,OH^-}	426 g/mol [55]	Versogen Equivalent Weight, Hydroxide Form
ρ_{Naf}	2.05 g/cm^3 [17]	Nafion Dry Density
ρ_{Vers,OH^-}	1.22 g/cm^3 [55]	Versogen Dry Density, Hydroxide Form
M_w	18.02 g/mol	Molar Mass of Water
M_{H^+}	1.01 g/mol	Molar Mass of Proton
M_{OH^-}	17.01 g/mol	Molar Mass of Hydroxide
R	8.314 J/mol*K	Gas constant
T	323.15 K	Temperature
η_∞	0.00055 Pa*s [194]	Viscosity of Water
k_B	1.381 x 10^{-23} J/K	Boltzmann's Constant
a_{H^+}	0.28 Å [198]	Stoke's Radius of proton
a_{OH^-}	0.46 Å [198]	Stoke's Radius of hydroxide
$\bar{V}_{H^+}$	56.6 cm^3/mol [198]	Molar volume of proton solvation shell
$\bar{V}_{OH^-}$	68.1 cm^3/mol [198]	Molar volume of hydroxide solvation shell

$$A = \frac{\eta}{k} \tag{S4.12}$$

where A is a lumped parameter.[180] The electrochemical potential gradient can also be related to species velocity by[165, 179, 181, 192]

$$c_i \nabla \mu_i = \widetilde{K}_{iM}(-\boldsymbol{v}_i) + \sum_{j \neq i,M} \widetilde{K}_{ij}(\boldsymbol{v}_j - \boldsymbol{v}_i) \tag{S4.13}$$

where $\boldsymbol{v}_i$ is the species velocity of species i and all other variables are as stated previously, assuming no other external forces in the system. Simultaneous solution of Equations S4.11 and S4.13 gives[180]

$$\widetilde{K}_{iM} = A\mathrm{w_i} = \frac{\eta}{k} w_i \tag{S4.14}$$

where w_i is the mass fraction of i. Equation S4.14 is the result of algebraic substitution and simplification.[180]

The remaining unknowns are the Darcy permeability (from Equation S4.10) as a function of water content and the tortuosity (Equation S4.9), or equivalently the power index χ in Equation S4.9 since the water volume fraction is known. There are one too many unknowns to fit the experimental data via a least-squared error method (N permeability values and χ, compared to only N datum points) To circumvent the underspecification, additional water transport-coefficient data from literature for Nafion are used to determine the Darcy permeability as a function of water volume fraction.[32] The water transport coefficients are obtained from diffusion coefficients by the method of Weber and Newman.[32, 184] Permeability is obtained from water transport coefficient by

$$k = \alpha v_0^2 \eta_\infty \tag{S4.15}$$

where α is the water transport coefficient and v_0 is the molar volume of water.[17] The experimental data (diffusivity versus water volume fraction) are fit to a line above $\phi = 0.1$ before conversion to water transport coefficients to allow for selection of permeabilities at the necessary water volume fractions (this also requires a small extrapolation of the data above $\phi = 0.2$).[32, 184] The water transport coefficient and Darcy permeability used are plotted in Figure S4.4a and S4.4b, respectively, along with the experimental data. By selecting a reasonable χ value, we calculate directly the water transport number of proton-form Nafion as a function of water content, as seen in Figure 4.9a.

Similar experimental data are not available for Versogen. Instead, reasonable χ values are chosen and the water transport number is then fit with a non-linear least-square-error method to extract the Darcy permeability. The data is smoothed to a curve before fitting. The minimum and maximum χ parameters selected are based on those used for Nafion (maximum) and hydrogels with a similar wt % of water when fully hydrated (minimum).[55, 186] The comparison to a hydrogel is valid based on the apparent structure of Versogen. Structure information for Versogen is in

Section 4.8.5. Results for this approach applied to hydroxide-form Versogen are graphed in Figure 4.10 in the main text.

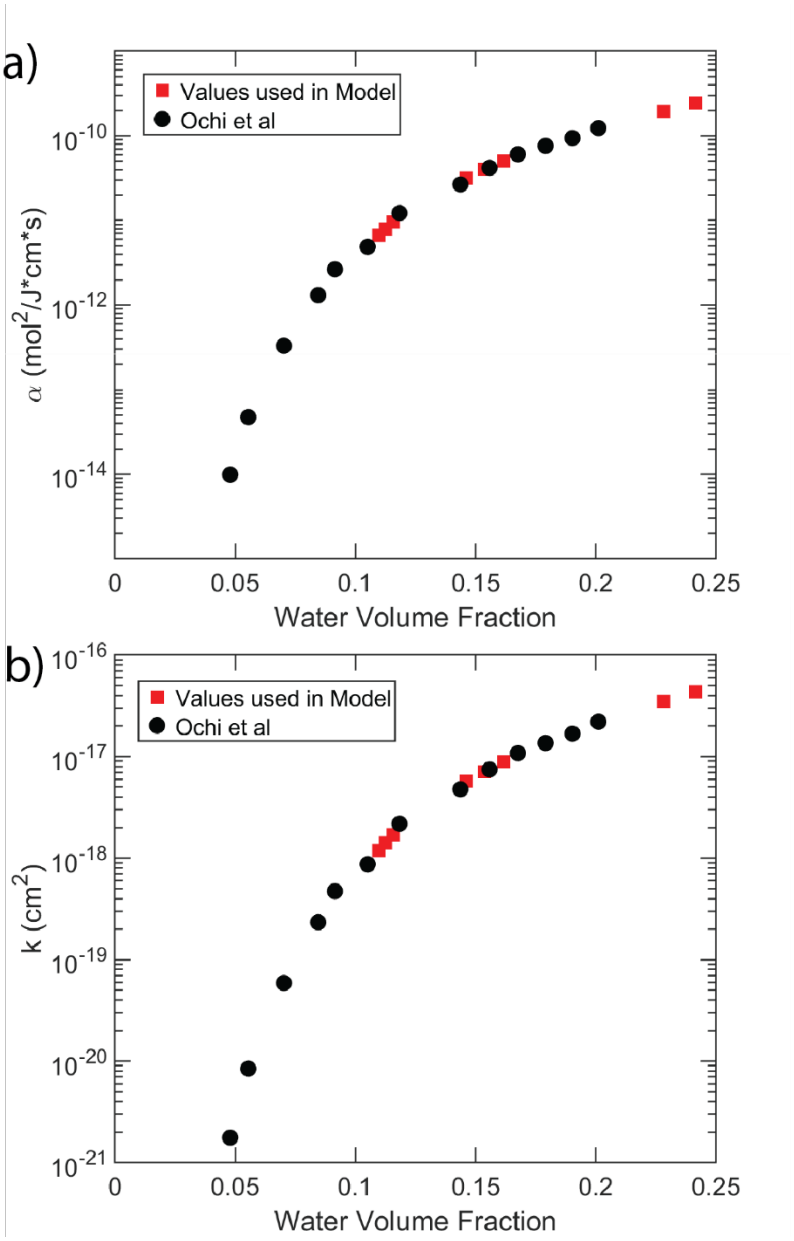

Figure S4.4: a) Water transport coefficient as a function of water volume fraction calculated from Ochi et al.[32] (black circles) and the values used in the model (red squares). b) Darcy permeability coefficient as a function of water volume fraction as calculated from Ochi et al.[32] (black circles) and the values used in the model (red squares).

4.8.4 Water Transport Parameters as a Function of Water Volume Fraction

Both Figure 4.9 and 4.10 are shown here as functions of the water volume fraction instead of the water content. Figure S4.6 additionally shows the water transport coefficient as a function of water volume fraction as calculated from the Darcy permeability using Equation S4.15.

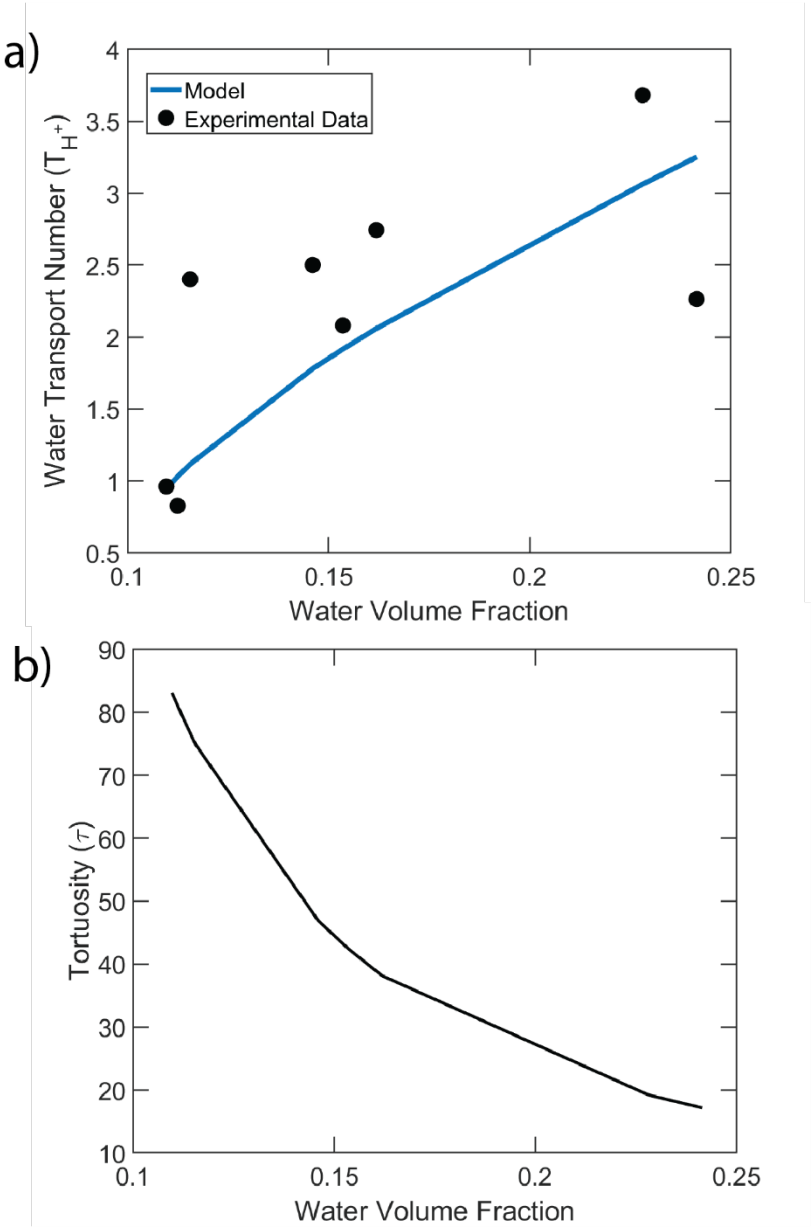

Figure S4.5: a) Water transport number for Nafion 211 as a function of water volume fraction calculated from the friction coefficient model at 50°C. Solid line represents the model prediction (blue) compared to experimental data (black circles). b) Calculated tortuosity of the Nafion 211 as a function of water volume fraction with $\chi = 2$.

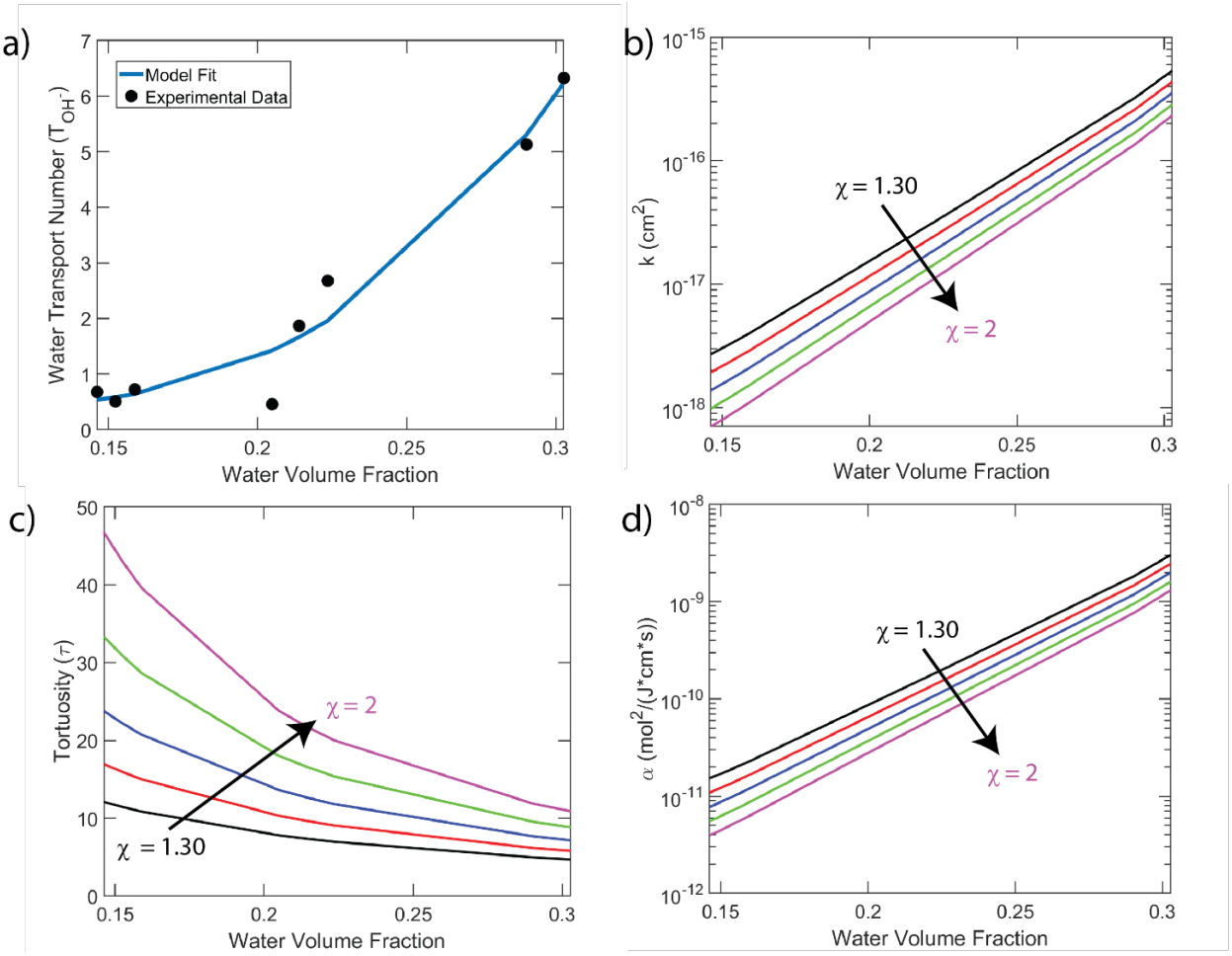

Figure S4.6: a) The model fit of the water transport number of hydroxide-form Versogen (blue line) is compared to the experimental data (black circles) as a function of water volume fraction at 50°C. b) Darcy's permeability for hydroxide-form Versogen as a function of water volume fraction at 50°C. c) Calculated tortuosity of the Versogen membrane as a function of water volume fraction. d) Calculated water transport coefficient as a function of water volume fraction. Values of χ are, in order, 1.3, 1.4, 1.65, 1.82, and 2.

4.8.5 Structure of Versogen Compared to Nafion via SAXS

The molecular structure of Versogen is necessary to model the water transport number (*i.e.,* whether Versogen is phase-separated or not). To verify the structure of Versogen, small angle X-ray scattering (SAXS) was performed at the 7.3.3 beamline at Lawrence Berkeley National Laboratory. The results can be seen in Figure S4.7. Unlike Nafion (dotted lines), both 20 and 80-μm thick Versogen showed no clearly defined scattering peaks over the range measured. Both wet and dry Nafion showed two single peaks, indicating some level of phase-separated structure.[55, 187] Lack of such peaks in Versogen demonstrates that it is relatively unstructured and exhibits a homogeneous structure throughout similar to a hydrogel.[55, 188] Based on this finding, a hydrogel-based model is used in Section 4.8.3 to model the water transport number and water permeability of Versogen.

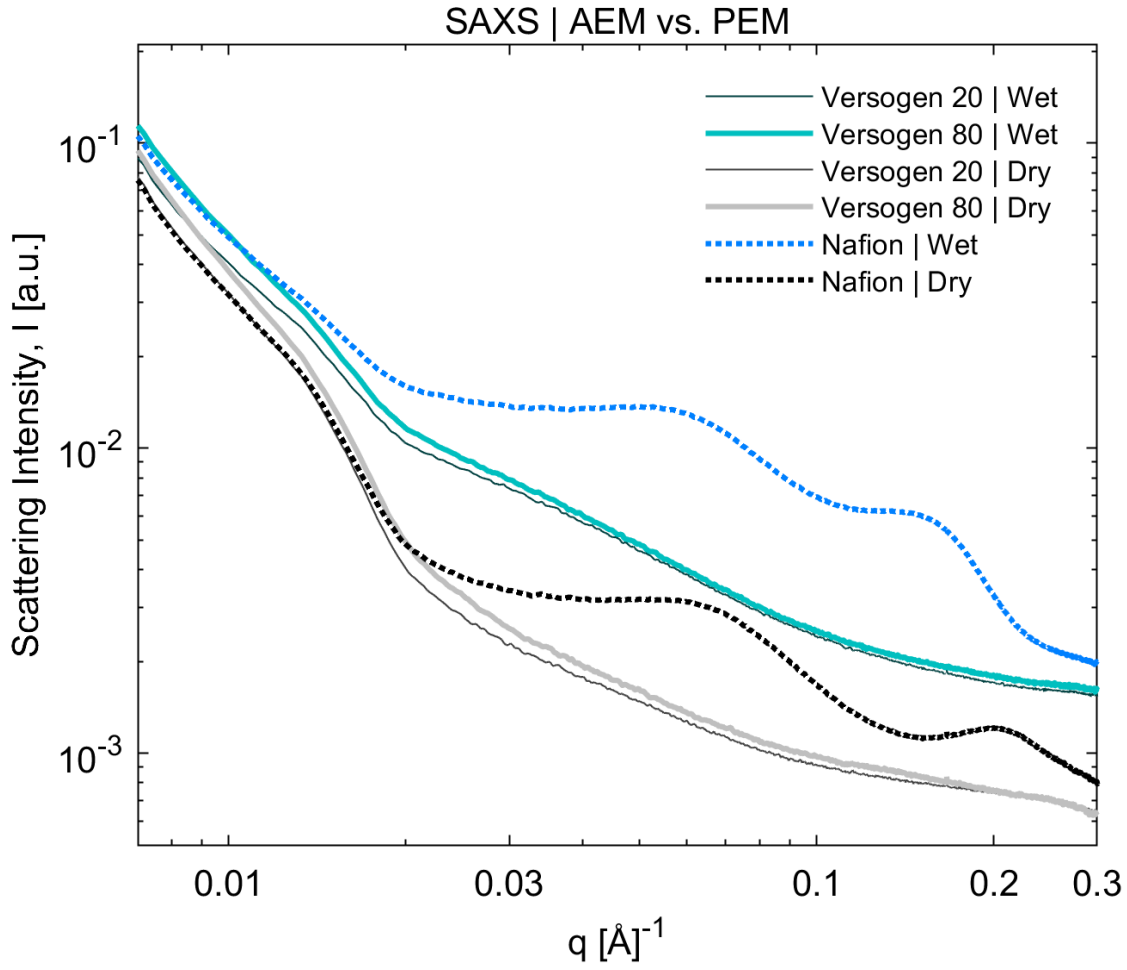

Figure S4.7: Small-angle x-ray scattering for Nafion and different thicknesses of Versogen (20 and 80 μm) as scattering intensity versus scattering vector (q).

4.8.6 OCV Data versus RH

Tables S4.2-S4.9 contain the raw OCV versus RH data for all trials in this chapter.

Table S4.2: Proton-form Nafion OCV versus RH data.

Membrane/Ion	Trial	Temperature (°C)	WE RH	RE RH	OCV (V)
Nafion/H^+	1	20	0.32	0.39	-0.0121
			0.37	0.39	-0.0063
			0.4	0.39	0.0012
			0.45	0.39	0.0016
			0.5	0.39	0.0055
			0.47	0.58	-0.0071
			0.52	0.57	-0.0039
			0.57	0.57	-0.0009
			0.62	0.57	0.002
			0.67	0.57	0.0052
			0.67	0.79	-0.0049
			0.71	0.79	-0.003
			0.75	0.79	-0.0008
			0.81	0.79	0.0026
			0.85	0.79	0.0047
			0.75	0.89	-0.0055
			0.81	0.89	-0.0024
			0.86	0.89	0.0007
			0.95	0.88	0.0064
Nafion/H^+	1	50	0.4	0.5	-0.0100

			0.45	0.5	-0.0008
			0.5	0.5	-0.0067
			0.55	0.5	-0.0019
			0.6	0.5	0.0154
			0.6	0.7	-0.0034
			0.65	0.7	0.0013
			0.7	0.7	0.0077
			0.75	0.7	0.0126
			0.8	0.7	0.0172
			0.8	0.9	0.0017
			0.85	0.9	0.0054
			0.9	0.9	0.0129
			0.95	0.9	0.0139
Nafion/H^+	2	50	0.4	0.5	-0.0156
			0.45	0.5	-0.0119
			0.5	0.5	-0.0066
			0.55	0.5	-0.0027
			0.6	0.5	0.0020
			0.6	0.7	-0.0125
			0.65	0.7	-0.0106
			0.7	0.7	-0.0067
			0.75	0.7	-0.0034
			0.8	0.7	0.0079
			0.8	0.9	-0.0374

			0.85	0.9	-0.0267
			0.9	0.9	-0.0265
			0.95	0.9	-0.0164
Nafion/H^+	3	50	0.4	0.5	0.0069
			0.45	0.5	0.0091
			0.5	0.5	0.0121
			0.55	0.5	0.0150
			0.6	0.5	0.0182
			0.6	0.7	-0.0022
			0.65	0.7	0.0100
			0.7	0.7	0.0130
			0.75	0.7	0.0163
			0.8	0.7	0.0197
			0.8	0.9	0.0036
			0.85	0.9	0.0156
			0.9	0.9	0.0176
			0.95	0.9	0.0177

Table S4.3: Sodium-form Nafion OCV versus RH data.

Membrane/Ion	Temperature (°C)	WE RH	RE RH	OCV (V)
Nafion/Na^+	50	0.4	0.5	-0.0176
		0.45	0.5	-0.0089
		0.5	0.5	-0.0056
		0.55	0.5	-0.0007

		0.6	0.5	0.0042
		0.6	0.7	-0.0004
		0.65	0.7	0.0087
		0.7	0.7	0.0127
		0.75	0.7	0.0189
		0.8	0.7	0.0290
		0.8	0.9	-0.0393
		0.85	0.9	-0.0220
		0.9	0.9	-0.0131
		0.95	0.9	0.0009

Table S4.4: Proton-form PSS OCV versus RH data.

Membrane/Ion	Temperature (°C)	WE RH	RE RH	OCV (V)
PSS/H^+	50	0.4	0.5	-0.0069
		0.45	0.5	-0.0007
		0.5	0.5	0.0022
		0.55	0.5	0.0058
		0.6	0.5	0.0055
		0.6	0.7	-0.0071
		0.65	0.7	-0.0041
		0.7	0.7	-0.0029
		0.75	0.7	-0.0020
		0.8	0.7	0.0021

Table S4.5: Hydroxide-form Versogen OCV versus RH data.

Membrane/Ion	Trial	Temperature (°C)	WE RH	RE RH	OCV (V)
Versogen/OH^-	1	50	0.4	0.5	0.0400
			0.45	0.5	0.0306
			0.5	0.5	0.0220
			0.55	0.5	0.0182
			0.6	0.5	0.0088
			0.6	0.7	0.1011
			0.65	0.7	0.0985
			0.7	0.7	0.0917
			0.75	0.7	0.0818
			0.8	0.7	0.0764
			0.8	0.9	0.0971
			0.85	0.9	0.0809
			0.9	0.9	0.0563
			0.95	0.9	0.0544
Versogen/OH^-	2	50	0.4	0.5	0.0084
			0.45	0.5	0.0048
			0.5	0.5	0.0016
			0.55	0.5	-0.0021
			0.6	0.5	-0.0057
			0.6	0.7	0.0050
			0.65	0.7	0.0031
			0.7	0.7	0.0013

			0.75	0.7	-0.0091
			0.8	0.7	-0.0175
			0.8	0.9	0.0085
			0.85	0.9	0.0006
			0.9	0.9	-0.0019
			0.95	0.9	-0.0223
Versogen/OH^-	3	50	0.4	0.5	0.0073
			0.45	0.5	0.0038
			0.5	0.5	0.0008
			0.55	0.5	-0.0021
			0.6	0.5	-0.0049
			0.6	0.7	0.0072
			0.65	0.7	0.0046
			0.7	0.7	0.0014
			0.75	0.7	-0.0009
			0.8	0.7	-0.0054
			0.8	0.9	0.0219
			0.85	0.9	0.0192
			0.9	0.9	0.0030
			0.95	0.9	0.0006
Versogen/OH^-	1	30	0.4	0.5	0.0210
			0.45	0.5	0.0128
			0.5	0.5	0.0088
			0.55	0.5	0.0045

			0.6	0.5	0.0060
			0.8	0.9	0.1099
			0.85	0.9	0.0920
			0.9	0.9	0.0712
			0.95	0.9	0.0685
Versogen/OH^-	1	40	0.8	0.9	0.0033
			0.85	0.9	0.0016
			0.9	0.9	-0.0012
			0.95	0.9	-0.0060
Versogen/OH^-	1	70	0.4	0.5	0.0248
			0.45	0.5	0.0221
			0.5	0.5	0.0195
			0.55	0.5	0.0117
			0.6	0.5	-0.0027

Table S4.6: Bicarbonate-form Versogen OCV versus RH data.

Membrane/Ion	Temperature (°C)	WE RH	RE RH	OCV (V)
Versogen/HCO_3^-	50	0.4	0.5	-0.1354
		0.45	0.5	-0.1476
		0.5	0.5	-0.1528
		0.55	0.5	-0.1585
		0.6	0.5	-0.1602
		0.6	0.7	-0.0500
		0.65	0.7	-0.0548

		0.7	0.7	-0.0606
		0.75	0.7	-0.0790
		0.8	0.7	-0.0828
		0.8	0.9	-0.0124
		0.85	0.9	-0.0231
		0.9	0.9	-0.0381
		0.95	0.9	-0.0610

Table S4.7: Carbonate-form Versogen OCV versus RH data.

Membrane/Ion	Ion Form	Temperature (°C)	WE RH	RE RH	OCV (V)
Versogen/CO_3^{2-}	1	50	0.4	0.5	0.0145
			0.45	0.5	-0.0006
			0.5	0.5	-0.0108
			0.55	0.5	-0.0167
			0.6	0.5	-0.0225
			0.6	0.7	-0.0109
			0.65	0.7	-0.0147
			0.7	0.7	-0.0173
			0.75	0.7	-0.0289
			0.8	0.7	-0.0420
			0.8	0.9	-0.0176
			0.85	0.9	-0.0300
			0.9	0.9	-0.0479
			0.95	0.9	-0.0569

Versogen/CO_3^{2-}	2	50	0.4	0.5	0.0244
			0.45	0.5	0.0100
			0.5	0.5	-0.0039
			0.55	0.5	-0.0146
			0.6	0.5	-0.0258
			0.6	0.7	-0.0190
			0.65	0.7	-0.0278
			0.7	0.7	-0.0301
			0.75	0.7	-0.0347
			0.8	0.7	-0.0581
			0.8	0.9	0.0463
			0.85	0.9	0.0127
			0.9	0.9	0.0065
			0.95	0.9	-0.0268
Versogen/CO_3^{2-}	3	50	0.4	0.5	0.0140
			0.45	0.5	0.0004
			0.5	0.5	-0.0132
			0.55	0.5	-0.0215
			0.6	0.5	-0.0288
			0.6	0.7	-0.0217
			0.65	0.7	-0.0477
			0.7	0.7	-0.0486
			0.75	0.7	-0.0578
			0.8	0.7	-0.0681

			0.8	0.9	0.0285
			0.85	0.9	-0.0179
			0.9	0.9	-0.0246
			0.95	0.9	-0.0490
Versogen/CO_3^{2-}	1	30	0.4	0.5	0.0689
			0.45	0.5	0.0516
			0.5	0.5	0.0468
			0.55	0.5	0.0319
			0.6	0.5	0.0161
			0.8	0.9	0.0335
			0.85	0.9	0.0149
			0.9	0.9	-0.0017
			0.95	0.9	-0.0243
Versogen/CO_3^{2-}	1	40	0.8	0.9	0.0298
			0.85	0.9	0.0195
			0.9	0.9	0.0104
			0.95	0.9	0.0011
Versogen/CO_3^{2-}	1	70	0.4	0.5	0.0368
			0.45	0.5	0.0283
			0.5	0.5	0.0130
			0.55	0.5	0.0059
			0.6	0.5	-0.0174

Table S4.8: Hydroxide-form Sustainion OCV versus RH data.

Membrane/Ion	Temperature (°C)	WE RH	RE RH	OCV (V)
Sustainion/OH^-	50	0.4	0.5	-0.0168
		0.45	0.5	-0.0253
		0.5	0.5	-0.0320
		0.55	0.5	-0.0365
		0.6	0.5	-0.0389
		0.6	0.7	0.0146
		0.65	0.7	0.0127
		0.7	0.7	-0.0010
		0.75	0.7	-0.0064
		0.8	0.7	-0.0106
		0.8	0.9	0.0563
		0.85	0.9	0.0363
		0.9	0.9	0.0264
		0.95	0.9	0.0202

Table S4.9: Carbonate-form Sustainion OCV versus RH data.

Membrane/Ion	Temperature (°C)	WE RH	RE RH	OCV (V)
Sustainion/CO_3^{2-}	50	0.4	0.5	0.0132
		0.45	0.5	-0.0045
		0.5	0.5	-0.0177
		0.55	0.5	-0.0261

		0.6	0.5	-0.0358
		0.6	0.7	0.0083
		0.65	0.7	-0.0019
		0.7	0.7	-0.0057
		0.75	0.7	-0.0161
		0.8	0.7	-0.0196
		0.8	0.9	0.0720
		0.85	0.9	0.0327
		0.9	0.9	0.0192
		0.95	0.9	-0.0006

5. Effect of Water Droplet Growth Dynamics on Electrode Limiting Current in Fuel-Cell Catalyst Layers[†]

5.1 Abstract

Fuel cells are a promising next-generation energy-conversion technology designed to replace internal combustion engines in cars, trucks, and larger vehicles. However, much work remains to optimize fuel-cell systems and to enhance their commercial viability. Water droplets have been observed exiting gas-diffusion layers and in flow fields of fuel cells due to the high humidity environment needed for operation. Within catalyst layers, liquid water can block reactive gases from reaching electrode surfaces. Also of interest is the direct formation of water droplets on Pt catalyst particles during oxygen reduction, potentially impeding reactant arrival to the reactive electrode. In this work, four different cases of water droplet growth in fuel-cell catalyst layers are considered: pinned and advancing droplets on a bare Pt surface, advancing droplets on a Nafion film, and water-layer growth in carbon nanopores. Transient drop growth is accurately captured with a combination of mass, species mass, and momentum balances. Electrode limiting current is determined via oxygen diffusion and Tafel kinetics.

Water droplets are found not to be mass-transfer limiting in the catalyst layer, as the large, exposed surface area of the growing liquid-gas interface relative to the Pt nanoparticle ensures that a Pt nanoparticle has sufficient supply of oxygen gas, independent of droplet size. Mass-transfer-limited behavior is calculated in carbon nanopores, but only at pore sizes larger than is typically found in current high-surface-area carbon supports. As a result, the impact of both water droplets and catalyst-layer flooding may be significantly less than is typically assumed.

[†]This chapter was originally published as "Petrovick, J. G., Radke, C. J., Weber, A. Z. Effect of Water Droplet Growth Dynamics on Electrode Limiting Current in Fuel-Cell Catalyst Layers, *In Press*." Adapted with permission from all co-authors.

5.2 Introduction

Fuel cells have gradually grown in importance as clean energy-conversion devices. Their relative scalability compared to lithium-ion batteries makes them preferable in many heavy-duty applications, such as in trucks and buses.[6] The standard proton-exchange-membrane fuel cell (PEMFC) operates using the hydrogen-oxidation (HOR) and oxygen-reduction (ORR) reactions, which consume hydrogen and oxygen, respectively, to produce electricity and water as a byproduct. These reactions occur in sequence at the anode and cathode catalyst layers (CLs). The two CLs are separated by an ion-conducting membrane that carries protons from the anode to the cathode; the industry standard is Nafion, a perfluorosulfonic acid membrane (see Chapter 1, Figure 1.3).[17]

PEMFC CLs are complex, heterogeneous structures,[61, 199-201] typically consisting of nm-size platinum (Pt) particles supported on larger carbon particles (see Chapter 1, Figure 1.2). The carbon-support particles aggregate into agglomerates that are covered by a thin layer of Nafion (~1-5 nm thick).[12] Solvent drying of the Pt-activated carbon agglomerates into a porous structure forms the CL, typically ten micrometers thick, with pores ranging from twenty nanometers within agglomerates to up to 100 nm between agglomerates.[12, 61, 202, 203] Further complexity is added by using carbon particles with varying degrees of internal porosity, such as Vulcan XC-72 (lower porosity) and Ketjen Black (higher porosity).[12, 202] The final structure of the CL is critical to device performance because electrons, protons, and reactive gases must have transport pathways to reach the Pt-catalyst surfaces. Carbon acts as an electrical conductor, Nafion is both a proton conductor and a structural support, and non-water occupied interparticle void pace allows transport of gases. If reactive gases cannot reach active Pt sites, device performance is severely limited.

PEMFC performance is normally evaluated by examining potential losses in polarization curves, or graphs of potential versus current density. Potential losses are typically classified as one of three types: kinetic, ohmic, and mass transport.[5] The mass-transport losses, which are of interest here, are typically attributed to ORR because of oxygen diffusion resistance in the Nafion thin film of the cathode CL (losses on the hydrogen side are negligible due to the facile nature of the HOR), but other sources are possible.[61, 204, 205] For example, operating at high relative humidity (RH) maximizes the proton conductivity of the ionomer membrane and limits ohmic losses.[17] However, water condensation in a high RH environment along with ORR water droplet production partially saturate both the CL and the adjacent gas-diffusion layer (GDL). Significant evidence exists pointing to this phenomenon in GDLs and to the resulting formation of droplets on the exterior surface of the GDL where water exits the GDL.[37, 206-211] Complete aqueous flooding, where gas transport is limited to diffusion through the water-filled pores, can severely restrict gas transport to the CL. Thus, CL flooding is of particular interest given the importance of the catalyst in driving device performance.[38, 39, 80, 81] In general, water management in PEFCs is critical to their overall performance.[40, 41, 149, 150, 212, 213]

Nevertheless, few works examine the formation of water droplets in the CL before two-phase flow commences and cell performance degrades, including nanoscale models of oxygen transport in the CL.[214] ORR produces water as a reaction by-product at the Pt particles in the cathode CL leading to the generation of water droplets in the catalyst layer.[215] Produced droplets subsequently coalesce into two-phase channel flow that restricts oxygen gas from accessing Pt in

the CL and reduces performance. This effect has been previously modeled by assuming Pt sites that are covered by water reduce active surface area.[149] With minimal experimental evidence of droplet formation and correlation to performance or a transient model simulating droplet growth, it is difficult to know the precise impact that CL-generated water droplets have on cell performance.

Water-droplet formation models (and analogously, bubble-production models for electrolyzers) are well-studied in a wide variety of applications ranging from condensation nucleation to fully-formed droplets adhering to a solid surface to coalescence of emulsified water or oil droplets in fluid-fluid systems.[216-222] A key aspect in these models is that droplets form from an external source. With a few exceptions, it is uncommon to grow a droplet from a liquid-producing electrochemical reaction.[223] However, in PEMFCs, water droplets appear because of the water-production reaction (see Equation 1.2) at the catalyst surface inside the droplet. Large droplet sizes might limit oxygen supply both by covering reaction area and by restricting transport through the droplet.

In this work, a computational-fluid-dynamics model is developed for droplet growth in a cathode CL. Figure 5.1 illustrates the four variants considered: pinned or advancing drops on a bare Pt surface, growth of an advancing droplet on a Nafion-covered Pt surface, and growth of a water layer on a Pt surface buried at the base of a carbon nanopore. Growth is driven by reactive production of water at the Pt surface and is captured using a moving-mesh framework. Internal droplet convection is described by the Navier-Stokes equation. Fick's second law captures the transient oxygen diffusion. In all cases, droplet height and current density are evaluated as a function of time for given applied potentials. Finally, the origin and magnitude of system-performance losses, or lack thereof, are addressed.

5.3 Model Development

5.3.1 Droplet Growth

There are two major contributions to water-droplet growth in a fuel-cell CL: growth hydrodynamics and oxygen transport in the growing droplet to the reactive surface. We start with droplet-growth dynamics. A hemispherical water droplet rests on a flat Pt electrode that, in turn, is embedded in an impermeable carbon surface. Initial drop size is characterized by estimating the remnant drop volume remaining after a previous drop release. The 2D axisymmetric droplet initially extends to the Pt periphery and is surrounded by air at ambient temperature and pressure. As the drop grows due to the ORR, it may either remain pinned at the Pt periphery, as illustrated in Figure 5.1a, or advance onto the carbon support, as pictured in Figure 5.1b. Each case is considered separately.

Overall droplet size is controlled by overall mass balance

$$\frac{dm_w}{dt} = \dot{m}_{w,in} = \frac{2M_w}{nF}\int_0^{R_e} i(t,r)2\pi r dr \tag{5.1}$$

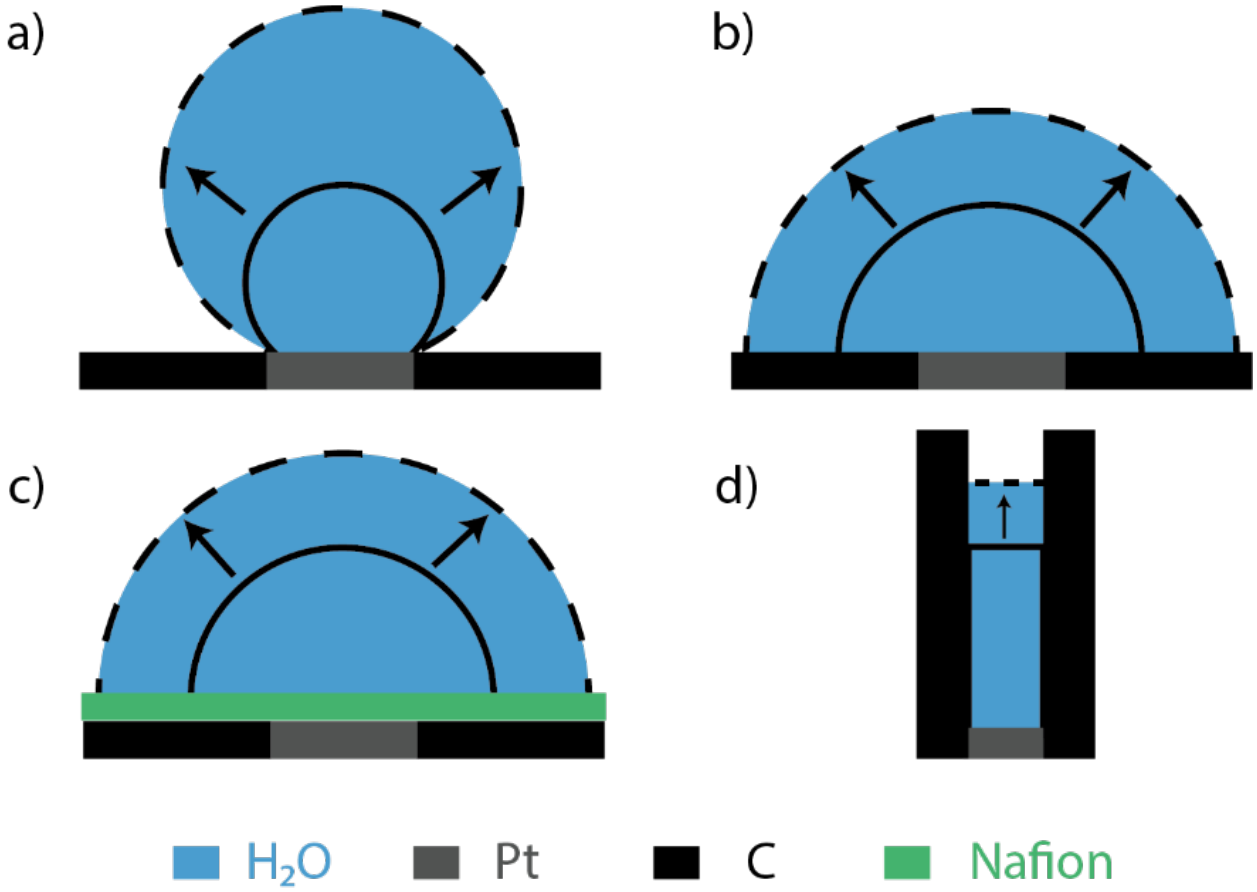

Figure 5.1: Schematic of the four cases of droplet growth: a) pinned b) advancing c) advancing over Nafion layer and d) internal carbon pore.

where m_w is water mass, t is time in seconds, $\dot{m}_{w,in}$ is reaction-produced water mass flowrate, M_w is water molar mass, n is the number of electrons transferred (n = 4 for ORR), F is Faraday's constant, i is ORR current density at the Pt surface, R_e is electrode radius, and r is the radial coordinate directed along the abscissa in Figure 5.2a-c. Dissolved oxygen in the droplet is assumed negligible in the growth hydrodynamics. Current density depends on oxygen arrival to the Pt-catalyst surface, as discussed below. The factor of 2 in the numerator of the far right of Equation 5.1 arises from the water to oxygen stoichiometric ratio in the ORR reaction (see Equation 1.2). Evaporation of water into the gas phase is not considered as the gas is assumed fully humidified. Inclusion of evaporation, although more accurate, reduces droplet size.

Both momentum and force balances are needed to locate precisely the expanding interface. Momentum balances are imposed for the liquid droplet and the air outside the droplet along with equality of gas and liquid interface velocities:[216]

$$\rho_w \frac{D\boldsymbol{u_w}}{Dt} = -\nabla P_d + \mu_w \nabla^2 \boldsymbol{u_w} \tag{5.2}$$

$$\rho_g \frac{D\boldsymbol{u_g}}{Dt} = -\nabla P_g + \mu_g \nabla^2 \boldsymbol{u_g} \tag{5.3}$$

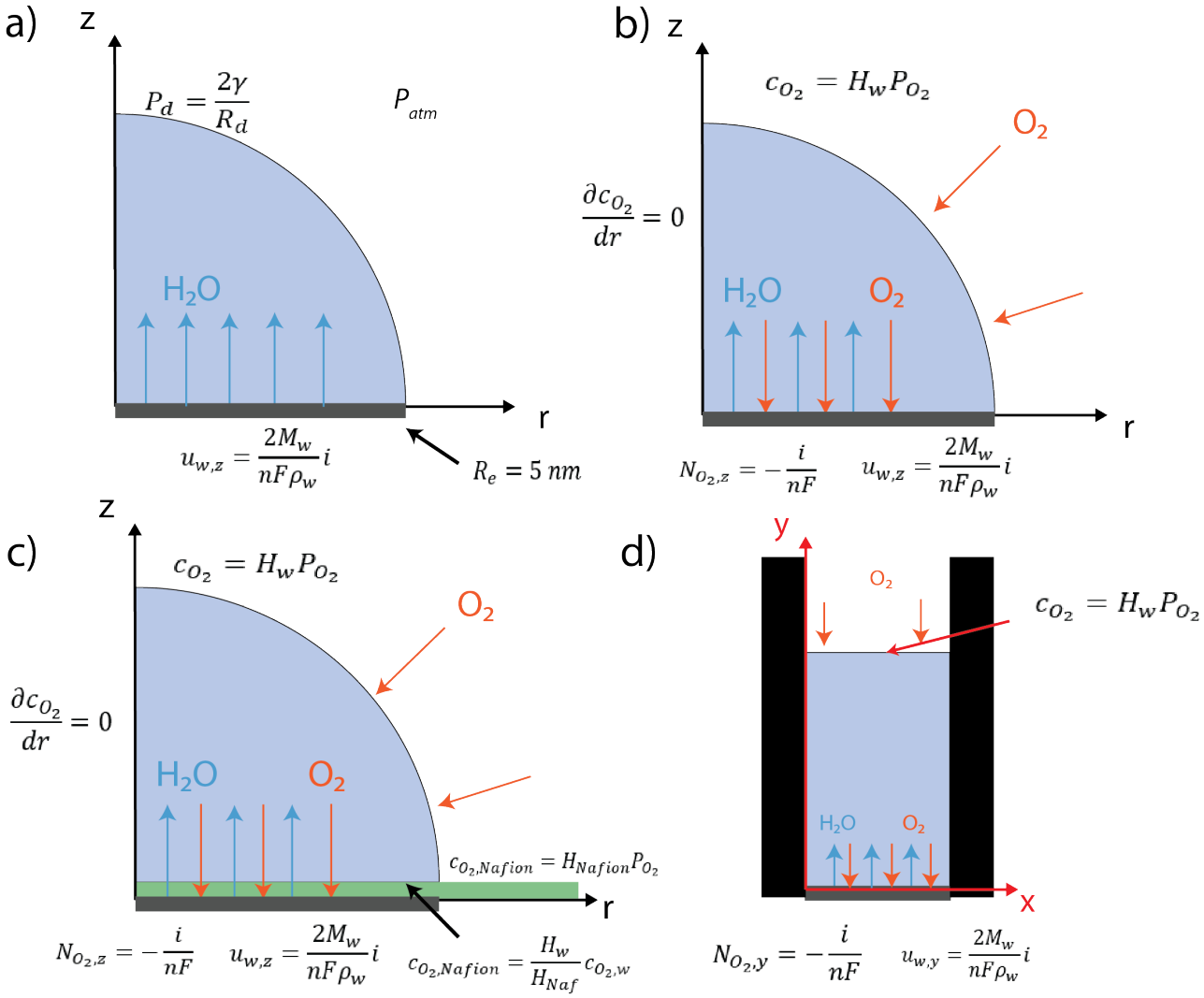

Figure 5.2: Schematic of boundary conditions for droplet growth. a) diagrams the growth conditions, b-d) oxygen-transport boundary conditions for the bare electrode, Nafion-covered electrode, and internal carbon pore, respectively.

$$\boldsymbol{u_w}|_{interface} = \boldsymbol{u_g}|_{interface} \tag{5.4}$$

where ρ_w and ρ_g are the mass density of liquid water and air, μ_w and μ_g are the Newtonian viscosity of liquid water and air, P_d and P_g are the pressure in the liquid water and air, and $\boldsymbol{u_w}$ and $\boldsymbol{u_g}$ are the velocity vectors of water and air in each phase, respectively.[116] Equations 5.2 and 5.3 are momentum balances on the water and gas phases, respectively, whereas Equation 5.4 is the no-slip boundary condition at the interface. The gas phase is stagnant with no external convective flow (*i.e.*, no gas flow occurs over the droplet surface). Symmetry is imposed in the axisymmetric direction. Continuity of total stress is enforced at the interface by

$$\boldsymbol{n} \cdot \underline{\boldsymbol{\tau_g}} = \boldsymbol{n} \cdot \underline{\boldsymbol{\tau_w}} + \gamma(\nabla_s \cdot \boldsymbol{n})\boldsymbol{n} \tag{5.5}$$

where $\underline{\boldsymbol{\tau_w}}$ and $\underline{\boldsymbol{\tau_g}}$ are the stress tensors in the water and gas phases, respectively, $\boldsymbol{n}$ is the outward unit-normal vector, γ is the surface tension coefficient, and ∇_s is the gradient operator on the droplet surface.

For the pinned drop in Figure 5.1a, boundary conditions are

$$\frac{\partial \boldsymbol{u_w}}{\partial r}\Big|_{r=0} = 0$$

$$u_{w,z}(t, r \le R_e, z = 0) = \frac{2M_w}{nF\rho_w} i(t, r) \tag{5.6}$$

$$u_{w,z}(t, r > R_e, z = 0) = 0$$

$$\boldsymbol{u_w}(t, r, z = droplet\ edge) \cdot \boldsymbol{n} = 0$$

$$P(t, r, z \to \infty) = P_{atm}$$

where z is the ordinate coordinate from the electrode surface as shown in Figure 5.2a-b. In order, the boundary conditions represent: symmetry at the center axis, water flowrate into the droplet due to chemical reaction at the Pt surface, no reaction at the carbon surface outside the electrode, a water-impermeable liquid-gas interface (*i.e.,* the normal velocity is zero relative to the interface velocity), and a fixed gas pressure equal to atmospheric. In addition, no-slip is imposed inside (liquid) and outside (gas) the droplet on the electrode and carbon surfaces, respectively.

For the initial condition, liquid velocities are zero everywhere, and pressure far away remains atmospheric. The initial droplet radius is set to either that of the reactive surface (R_e = 5 nm) for the pinned droplet case or to double that of the reactive surface (R_e = 10 nm) for the sliding droplet case. These initial conditions are meant to represent the droplet left behind after a previous drop detaches. A precise remnant drop volume is not needed, as we focus on drop limiting current at later growth times. For the advancing droplet, boundary conditions in Equation 5.6 remain the same, except that slip is allowed. With slip, the droplet advances unhindered along the carbon surface at the initial 90º contact angle in accordance with the overall mass balance.

Boundary conditions in Equation 5.6 require specification of the current density at the Pt surface. We utilize a kinetically controlled Tafel expression at the electrode surface, where the current depends on the local concentration of oxygen, $c_{O_2}(t, r, z = 0)$:

$$i(t, r) = -i_0 \frac{c_{O_2}(t, r, z = 0)}{c_{O_2,ref}} \exp\left(-\frac{\alpha F}{RT}\eta\right) \tag{5.7}$$

where i_0 is the exchange current density, $c_{O_2,ref}$ is the oxygen reference, α is the symmetry factor, R is the ideal-gas constant, T is the absolute temperature, and η is the overpotential.[224] Table 5.1 lists values of the parameters. The Tafel equation is accurate over the high overpotentials explored herein. Equation 5.7 demands calculation of the surface oxygen concentration, and thus the transient oxygen profiles, during droplet growth.

5.3.2 Oxygen Transport

Oxygen transport is captured by liquid-phase convection and molecular diffusion

$$\frac{\partial c_{O_2}}{\partial t} + \boldsymbol{u_w} \cdot \nabla c_{O_2} = D_{O_2} \nabla^2 c_{O_2} \tag{5.8}$$

where c_{O_2} is the molar concentration of oxygen in the droplet, D_{O_2} is the diffusivity of oxygen in water, and all other symbols are as defined previously.[116] The water velocity, $\boldsymbol{u_w}$_ is determined by Equation 5.2. It is reasonable to use Fick's law because of the low concentration of oxygen in the water droplet. Boundary conditions for Equation 5.8 are listed on the droplet schematic in Figure 5.2b

$$\frac{\partial c_{O_2}(t, z, r = 0)}{\partial r} = 0$$

$$c_{O_2}(t, r, z = interface) = H_w P_{O_2} \tag{5.9}$$

$$N_{O_2,z}(t, r \leq R_e)|_{z=0} = \frac{i(t, r)}{nF}$$

$$N_{O_2,z}(t, r > R_e)|_{z=0} = 0$$

where H_w is the Henry's constant for oxygen dissolved in water, $N_{O_2,z}$ is the flux of oxygen in the z direction, and i is local current density. The boundary conditions are symmetry at the center axis, constant concentration at the liquid/gas interface, kinetically controlled current density at the electrode surface from Equations 5.7 and 5.9, and zero oxygen flux outside the electrode surface, respectively.

For the Nafion-covered electrode in Figure 5.2c, all above equations apply, but an additional equation must be added to capture transport of oxygen through the Nafion layer. Fick's second law is again used, but without a convection term:

$$\frac{\partial c_{O_2}}{\partial t} = D_{O_2,Nafion} \nabla^2 c_{O_2} \tag{5.10}$$

where c_{O_2} is now the oxygen concentration in the Nafion coating per unit film volume and $D_{O_{2,Nafion}}$ is the diffusivity of oxygen in the Nafion film. All boundary conditions remain the same, but two additional constraints are requisite: one for the water/Nafion interface and a second for the gas/Nafion interface beyond the liquid droplet, as illustrated in Figure 5.2c.

$$c_{O_2,Nafion}(t, r \geq R_e, z = L) = H_{Nafion} P_{O_2}$$

$$c_{O_2,Nafion}(t, r \leq R_e, z = L) = \frac{H_w}{H_{Nafion}} c_{O_2,w} \tag{5.11}$$

where H_{Nafion} is Henry's constant for oxygen partitioning in the Nafion phase, L is the thickness of the Nafion layer, and all other variables are as defined previously. To remove the effect of differing solubilities in the water and Nafion phases on measured performance, the same solubility was used for both the water and Nafion phases (see Table 5.1). The initial condition

Table 5.1: Physical Constants

Symbol	**Value**	**Definition**
F	96485 C/mol	Faraday's Constant
n	4	Number of electrons for ORR
M_w	18.02 g/mol	Water Molar Mass
ρ_w	1000 kg/m^3	Water Density
μ_w	1 mPa*s	Water Viscosity
ρ_g	1.2 kg/m^3	Gas density
μ_g	1.7 x 10^{-5} Pa*s	Gas viscosity
γ	72.3 mN/m	Surface tension
P_{atm}	1 atm	Atmospheric Pressure
D_{O_2}	2.42 x 10^{-9} m^2/s [137]	Oxygen Diffusivity in Water
$D_{O_2,Nafion}$	1.04 x 10^{-10} m^2/s [115]	Oxygen Diffusivity in Nafion
H_w	1.3 mol/m^3*bar [138]	Henry's Constant of Oxygen in Water
H_{Nafion}	1.3 mol/m^3*bar	Henry's Constant of Oxygen in Nafion
i_0	0.0166 A/m^2	Exchange Current Density
$c_{O_2,ref}$	0.85 mol/m^3 [224]	Reference Oxygen Concentration
α	0.479 [224]	Transfer Coefficient
R	8.314 J/mol*K	Universal Gas Constant
T	293.15 K	Absolute Temperature

demands phase equilibrium between both the external gas phase and the liquid droplet, and the external gas phase and the Nafion layer, *i.e.*

$$c_{O_2}(t = 0, r, z) = H_w P_{O_2} \tag{5.12}$$

5.3.3 Droplet Simulation Description

Equations 5.1-5.6 provide accurate description and tracking of the mass of water in the droplet, the interface location and shape, and the internal drop pressure. Equations 5.7-5.12 determine the current density as a function of the oxygen transport within the droplet. All equations are solved simultaneously in COMSOL Multiphysics software via finite elements to produce droplet-growth histories for varying overpotentials. A moving mesh tracks droplet size and interface location. The number of mesh vertices to reach independent solutions depended on the case studied, with 13062 mesh points for the pinned drop, increasing to 18169 mesh points for the advancing drop, and 48663 mesh points for the advancing drop on Nafion. The ~5-nm initial droplet starts with a very dense mesh that is subsequently stretched at each time step based on the solution to the governing equations. Consequently, mesh density decreases with time; longer simulations require increasingly denser initial meshes, restricting the length of performed simulations while obtaining accurate results. This limits the practical size to which we can grow the droplet. Therefore, we limited most simulations to 5 s. Select longer simulations were performed, however; conclusions did not meaningfully differ. Once the dynamic drop radius is established, the Young-Laplace equation determines the pressure in the spherical droplet[218]

$$P_d(t) = \frac{2\gamma}{R_d(t)} + P_{atm} \tag{5.13}$$

where P_d is the time-dependent pressure in the droplet and R_d is the expanding-drop radius. Gravity does not affect drop shape because Bond numbers are small. All physical constants used in the simulations are listed in Table 5.1. For illustration purposes, initial and advancing-drop contact angle is fixed at 90°. Preliminary studies indicate sensitivity of results to contact angle is weak.

5.3.4 Internal Carbon Pore

A schematic for the internal-carbon-pore case is pictured in Figure 5.2d. A 5-nm radius Pt electrode rests at the bottom of the pore with initially a thin water layer above it. The walls are impermeable, non-reactive carbon. All equations used in the preceding section for the non-Nafion cases apply (Equations 5.1-5.9), except 2D Cartesian coordinates, y and x, are used. Boundary conditions needed are

$$u_{w,y}(t, x, y = 0) = \frac{2}{nFc_w} i(t, x)$$

$$\boldsymbol{u_w}(t, x, y = interface) \cdot \boldsymbol{n} = 0$$

$$P(t, x, y \to \infty) = P_{atm} \tag{5.14}$$

$$c_{O_2}(t, x, y = interface) = H_w P_{O_2}$$

$$N_{O_2,y}(t, x)|_{y=0} = \frac{i(t, x)}{nF}$$

where c_w is the molar concentration of pure water. The first three boundary conditions in Equation 5.14 are hydrodynamic: water inlet velocity from the electrochemical reaction, velocity at the extending *y*-interface, and gas pressure far away. The latter two boundary conditions are those for oxygen: concentration of oxygen at the growing liquid-gas interface and oxygen flux at the electrode surface. For the initial condition, velocities are assumed to be zero, and the initial 1-nm water layer is equilibrated with the external gas phase, as in Equation 5.12. The mesh used consisted of 940 mesh points in this simple 2D geometry. Most simulations were restricted to 1 s due to extremely rapid growth of the water layer in the pore; the only exception involved the determination of the height at which mass-transport limitations occurred (Figure 5.6d), as described below. In addition, the contact angle was held at 90° for illustration purposes.

5.4 Results and Discussion

5.4.1 Bare Pt Electrode

The dissolved oxygen concentration profile is reported in Figure 5.3a for a pinned droplet growing on a bare Pt electrode after 5 s with $\eta = -0.8\,V$. Oxygen depletion is nearly constant across the electrode except for an increase close to the contact line. Pinning of the droplet to the edge of the electrode surface is clearly demonstrated by examination of the three-phase contact line, which remains at the initial droplet radius of 5 nm and with a contact angle significantly larger (>150°) than the initially pinned 90°. The droplet apex height at $r = 0$ increases quite rapidly, especially at high overpotential (–0.7 V and higher), as demonstrated by Figure 5.3b. This dependence is expected due to the use of Tafel kinetics (Equation 5.7), which has an exponential dependence on overpotential. Figure 5.3c shows the effectiveness factor as a function of time and overpotential (and therefore droplet size, implicitly). Here, current density (per unit Pt area) is normalized by that calculated from the maximum possible concentration of oxygen dissolved in water (*i.e.*, the boundary condition at the drop exterior). These results are unexpected, as the current density does not appear to decay with time. After the initial decline, a time-independent oxygen boundary layer forms at the droplet base. In other words, current density does not depend on droplet size and mass transport in the droplet is not limiting. By pinning the droplet to the electrode, the shortest diffusion path at the three-phase contact line is maintained throughout the entire simulation, as seen in Figure 5.3d and e. This place is where most of the oxygen enters the drop, as well as where the local current density is highest; the supply majority does not change during the simulation.

The pinned-drop corner is eliminated in Figure 5.4 by allowing the drop contact line to slide over the carbon-support surface. Accordingly, the water droplet should be more limiting to current-density performance. A sliding-droplet oxygen profile at 5 s with $\eta = -0.8\,V$ is exhibited in

Figure 5.4a. The droplet radius in Figure 5.4b increases much more slowly compared to the pinned case, as growth is uniform in all directions, although a high overpotential (reaction rate) is still critical to significant growth. Nevertheless, effectiveness factor transients again indicate little change with time following an initial decline. The sliding drop does, however, lower current density from 83% to 75% effectiveness compared to a hinged contact angle but is unchanged as

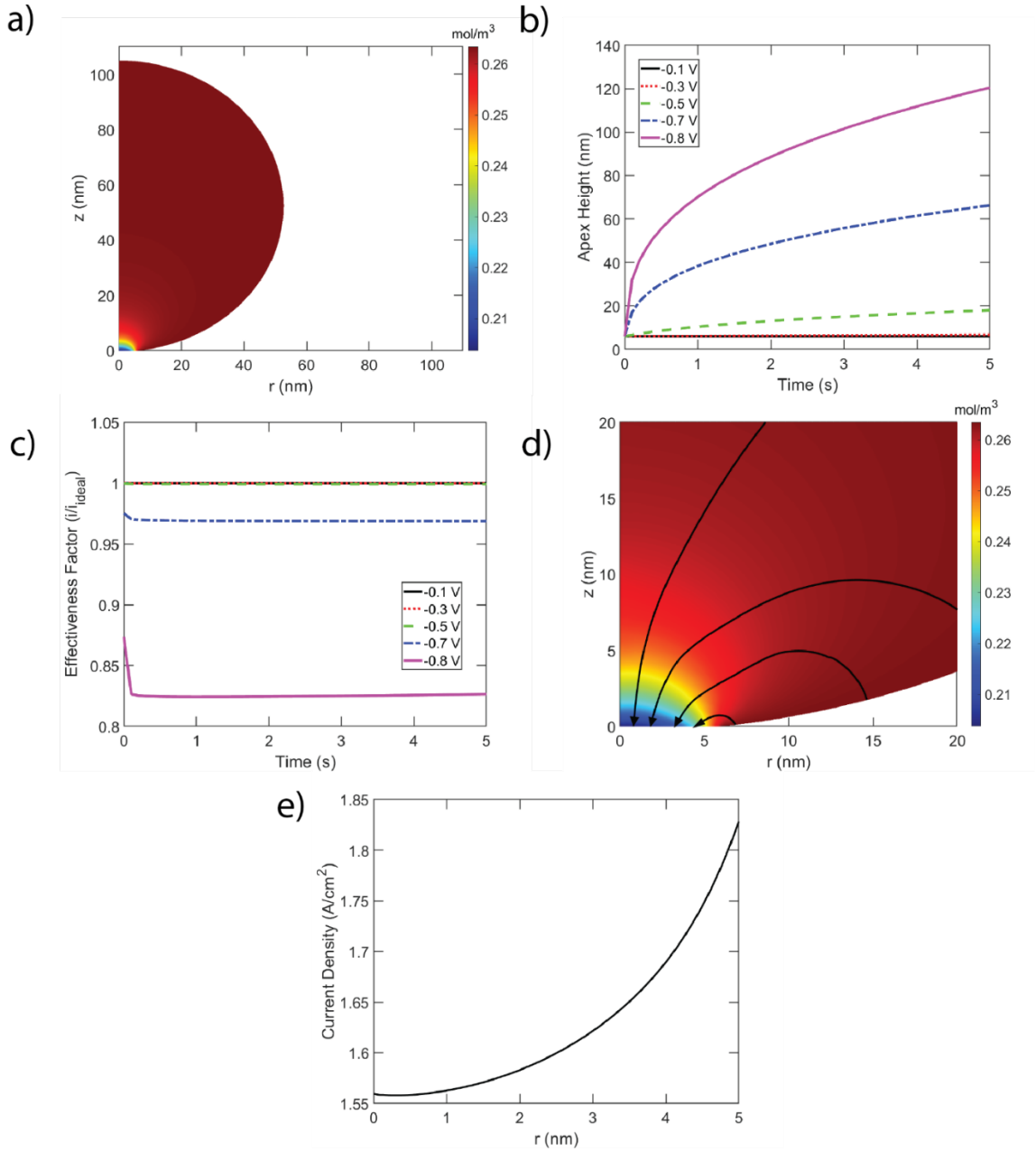

Figure 5.3: a) Concentration profile of oxygen gas dissolved in the droplet at t = 5 s and an overpotential of –0.8V for a pinned drop, b) droplet height as a function of time at increasing overpotential, c) effectiveness factor as a function of time and overpotential, d) a concentration profile with streamlines near the electrode surface for the drop in panel a, and e) current distribution along the droplet base for t = 5 s and an overpotential of –0.8V.

the drop grows. This result remains true even in the most severe limiting case, where in Figure 5.4d, the oxygen concentration in the surrounding gas phase is reduced to as low as 1%. As with the pinned drop, current density is still largest near the electrode radius, as illustrated in Figure 5.4e. Current density is lower than the pinned case, as expected, due to the lower surface oxygen concentration.

The lack of mass-transfer limitations was unexpected in both the pinned and sliding-drop cases for two reasons. First, we anticipated that produced water welling up from the surface of the electrode would hinder counter oxygen diffusion. The calculations presented in Figure S5.1 and Figure S5.2 in Section 5.7.1, however, disclose that water velocity is near zero and that pressure is pseudo steady and constant throughout the drop. Section 5.7.1 establishes that the pertinent Reynolds and Capillary numbers are both very small. Simple scaling then shows that the drop is pseudo steady with both convected and viscous momentum terms negligible (*i.e.*, $\nabla P_d = 0$). The small Capillary numbers maintain a spherical drop shape undistorted by flow. Thus, the momentum equation describes a spherical drop growing at uniform Laplace equilibrium pressure. Essentially, the flux of water produced at the electrode surface is too small to generate significant pressure-driven flow.

The second reason that mass-transport resistance was expected is the lengthening of the diffusion path due to droplet growth and a concomitant reduction in diffusive-reactant supply to the electrode. However, Section 5.7.2 establishes that the expanding surface area of the growing drop funnels oxygen to a thin boundary layer adjacent to the electrode. Beyond the boundary layer, oxygen concentration is in equilibrium with the gas, as shown in Figure 5.3 and Figure 5.4. Because the boundary-layer Peclét number is small and because the drop growth rate considerably slows, especially at later time, the convection-diffusion equation in the boundary layer is pseudo steady with $\nabla^2 c_{O_2} = 0$. This observation explains the constant concentration boundary layer observed in Figure 5.3 and Figure 5.4. Essentially, the surface area of the droplet interface greatly exceeds that of the Pt electrode and funnels oxygen to a point (the electrode). This effect gains in importance as the droplet grows, negating the longer diffusion lengths in a large droplet. As a result, mass-transfer of oxygen is never limiting in these systems. This effect is explored further in the internal carbon nanopore discussion below.

5.4.2 Nafion-Covered Electrode

For perhaps the more fuel-cell realistic case of droplet growth on top of an additional resistive Nafion layer covering the Pt electrode, contact-line pinning is not likely on the homogeneous, somewhat hydrophilic Nafion surface.[225, 226] Furthermore, water generated at the Pt electrode is assumed to pass directly through the thin Nafion layer with minimal resistance.[17, 64] Values for the diffusivity of oxygen in the droplet and Nafion phases are given in Table 5.1. The value used for Nafion is that of liquid-water equilibrated Nafion, about one order of magnitude lower than that in liquid water.[115]

Figure 5.5a shows an oxygen concentration profile in a droplet growing over a Nafion-covered electrode at time equals 5 s and at $\eta = -0.8\,V$. Droplet radius is portrayed in Figure 5.5b as a function of time and overpotential. A time-independent diffusion boundary layer forms in the

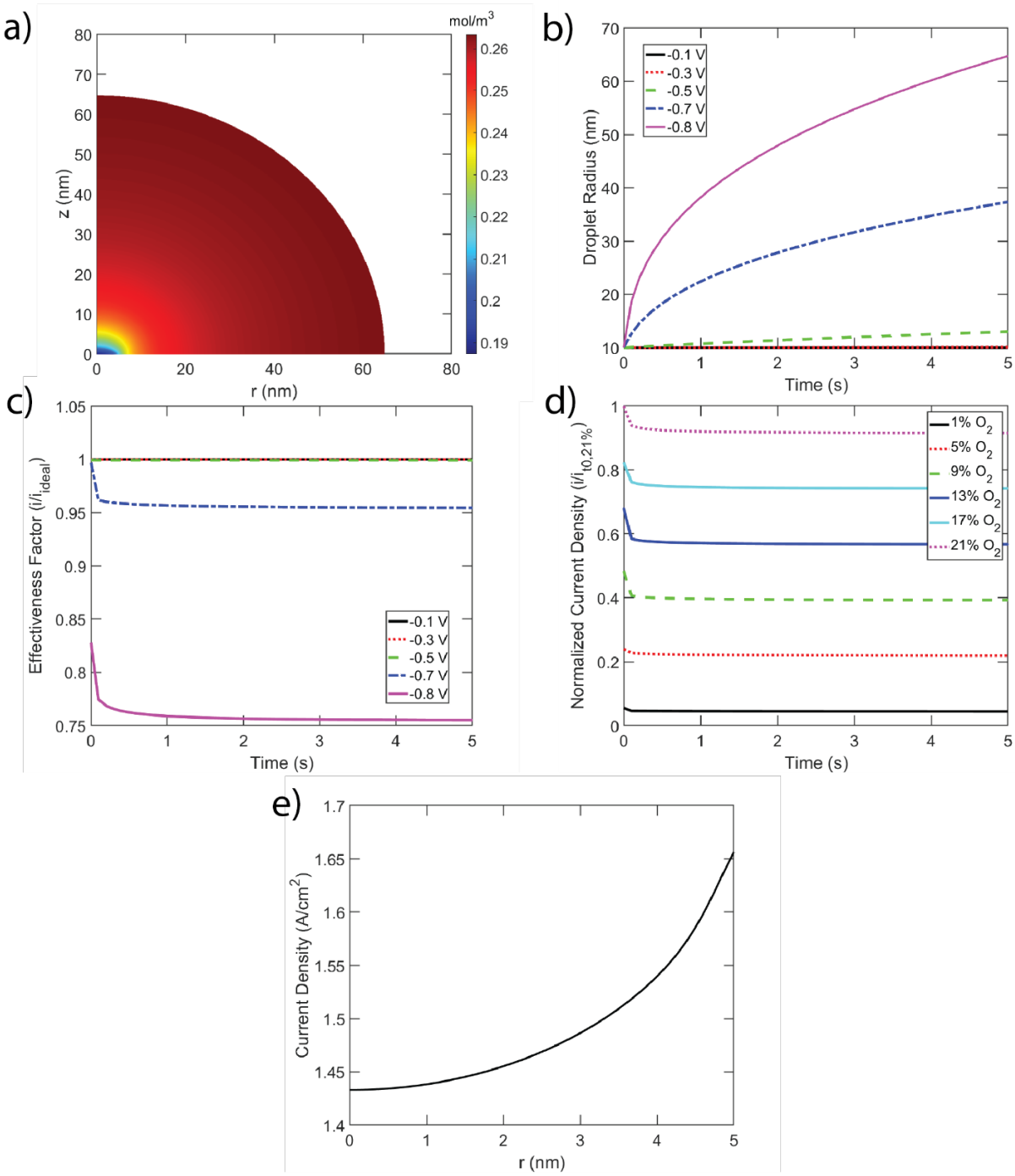

Figure 5.4: a) Concentration profile of oxygen gas dissolved in the droplet at t = 5 s and an overpotential of –0.8V for an advancing drop, b) droplet height as a function of time at increasing overpotential, c) effectiveness factor as a function of time and overpotential, d) normalized transient current densities for drops exposed to various gas mole percentages relative to 21% oxygen and 1 atm air, and e) current distribution along the droplet base at 5 s and an overpotential of –0.8V.

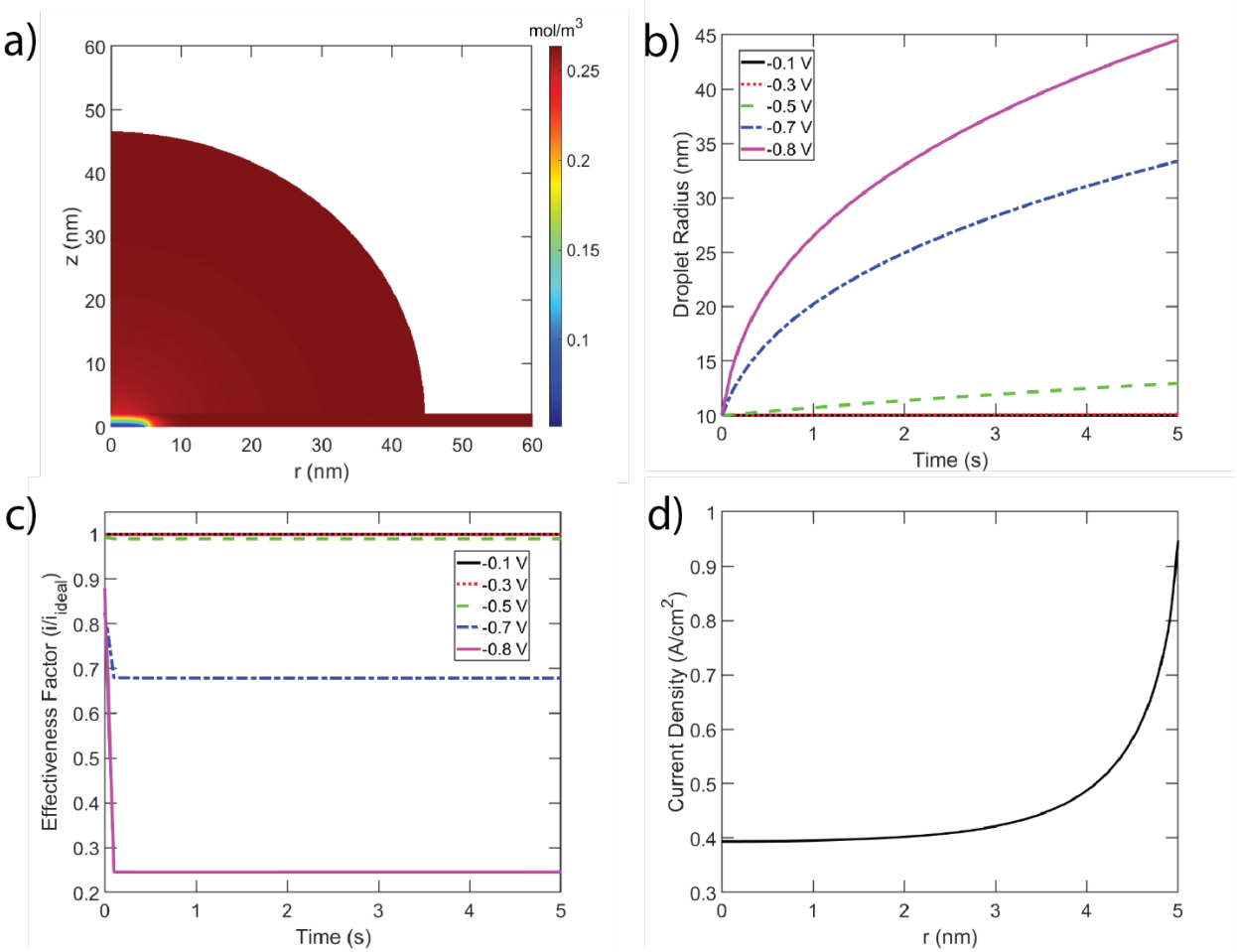

Figure 5.5: a) Concentration profile of oxygen gas dissolved in the droplet and Nafion layer at t = 5 s and an overpotential of –0.8 V, b) droplet height as a function of time at increasing overpotential, c) effectiveness factor as a function of time and overpotential, and d) current distribution along the droplet base at 5 s and an overpotential of –0.8 V.

Nafion layer fed by oxygen funneling similar to the bare Pt electrode in Figure 5.4. Outside of the boundary layer, the oxygen concentration is uniform and in equilibrium with the gas phase, similar to Figure 5.4. However, now the boundary-layer thickness is that of the Nafion coating. Section 5.7.3 shows that this is due to the order-of-magnitude lower diffusivity of oxygen in Nafion compared to in water; the transient effectiveness factor in Figure 5.5c confirms this finding. The initial drop in current is sharper because of the steeper oxygen gradient forming in the Nafion layer, indicating worse performance compared to the ideal case. However, current, once again, is invariant with time. The current distribution at the electrode, displayed in Figure 5.5d, exhibits a much steeper increase toward the edge of the electrode than either of the Nafion-free cases. This indicates, as expected, that it is more difficult for oxygen to travel to the electrode surface due to the lower diffusivity of oxygen in Nafion, also reflected in the lower normalized current density compared to both preceding cases. Taken together, droplet growth has little impact on electrode performance when a Nafion layer is included as it is never truly limiting.

5.4.3 Internal Carbon Nanopore

The final case is growth of a water layer in an internal carbon nanopore (typically 2-10 nm in diameter), which is functionally water filling a slit.[227] Water height as a function of time and overpotential are shown in Figure 5.6a. As in the droplet cases, high overpotential is required to sustain a significant growth rate. However, unlike previous drop-height transients, here high overpotential cases exhibit very similar linear slopes in the height versus time plots following the initial increase. This result implies a similar water production rate (*i.e.*, current density) under mass-transfer control, as change in height is controlled by current density. Examination of the normalized current density profiles in Figure 5.6b-c reveals a decrease in effectiveness factor with time, confirming that growth of the water column impacts current density. This too suggests mass-transfer limiting behavior, unlike with growing water droplets.

Mass-transfer limitation is also confirmed in Figure 5.6d where current density is plotted versus water height for two high overpotentials. At $h \sim 300$ nm, current density becomes potential-

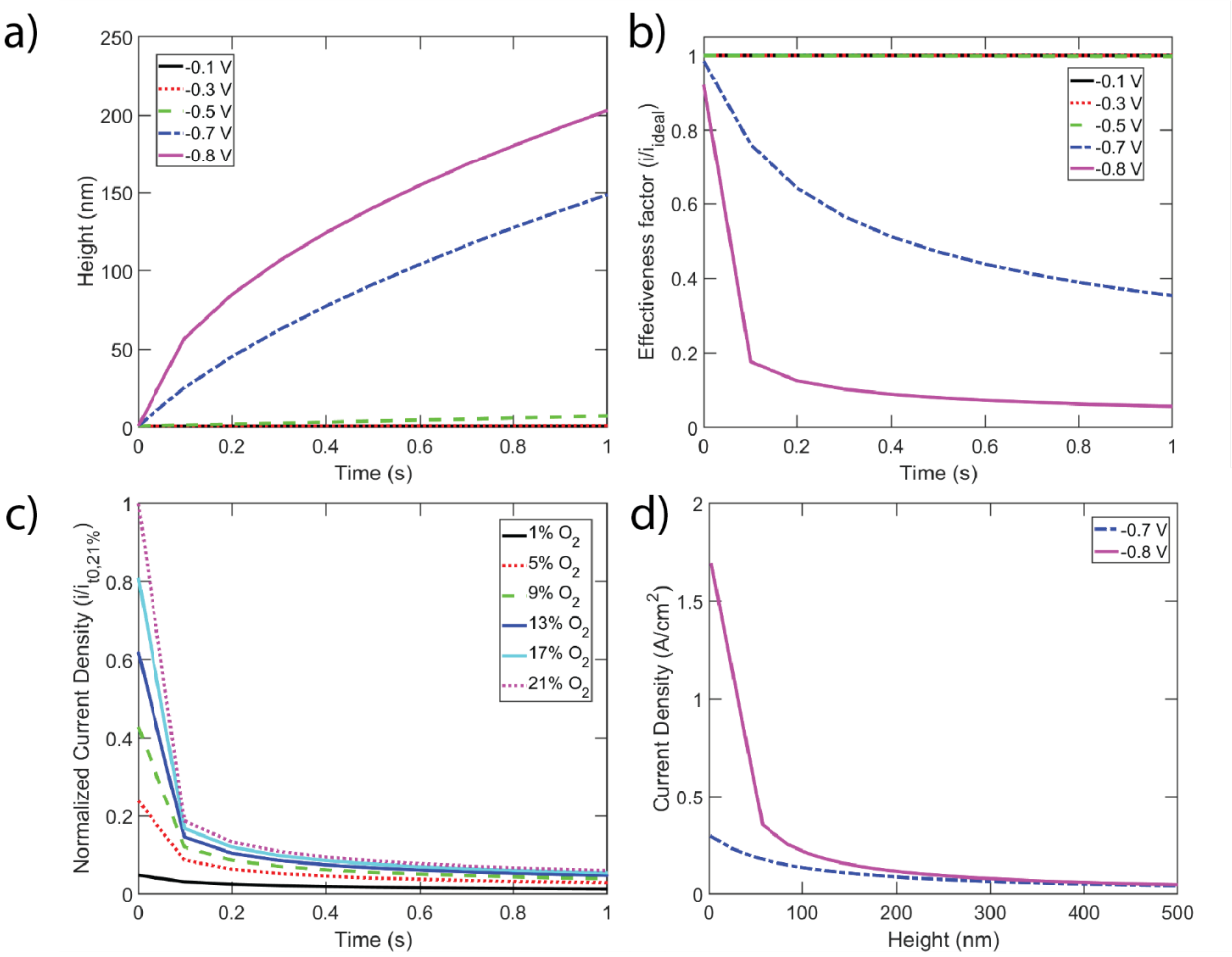

Figure 5.6: Water-column growth for the internal carbon nanopore. a) and b) height and effectiveness factor, respectively, as a function of time and overpotential, c) normalized current density as a function of oxygen concentration and time at $\eta = -0.8$, and d) cross-correlation curve indicating the water column height at which the current density curves overlap at high overpotential.

independent indicating that oxygen mass transport through the water column is fully limiting. It is unlikely, however, that actual carbon nanopores extend over such length-scales.[12] Accordingly, flooding of actual carbon nanopores with water is unlikely to impact measured current densities beyond an initial drop.

To confirm that oxygen funneling is the reason that nanopores experience mass-transfer limitations at larger filling heights whereas droplets do not, the example nanopore was widened while keeping the reactive Pt area the same size, *i.e.*, by adding non-reactive carbon surfaces outside the Pt surface at the bottom of the pore. Figure 5.7a displays a schematic of the widened nanopore. Current density as a function of time for the different pore widths (see the inset) is captured in Figure 5.7b. Tripling of the column width leads to a nearly three times higher current density for a given time. To eliminate the impact of different water heights at different times, oxygen concentration at the surface is plotted against water height in Figure 5.7c for the different column widths. At the same height, a three-fold increase in width causes a two-fold increase in concentration, which leads directly to the higher current densities seen in Figure 5.7b. A substantial increase in current commences for a relatively small change in pore width. We ascribe this increase to the funneling effect: the large surface area at the liquid-gas interface directs all the oxygen to a smaller reactive Pt area, which in turn leads to a higher local oxygen concentration and therefore a higher current.[214]

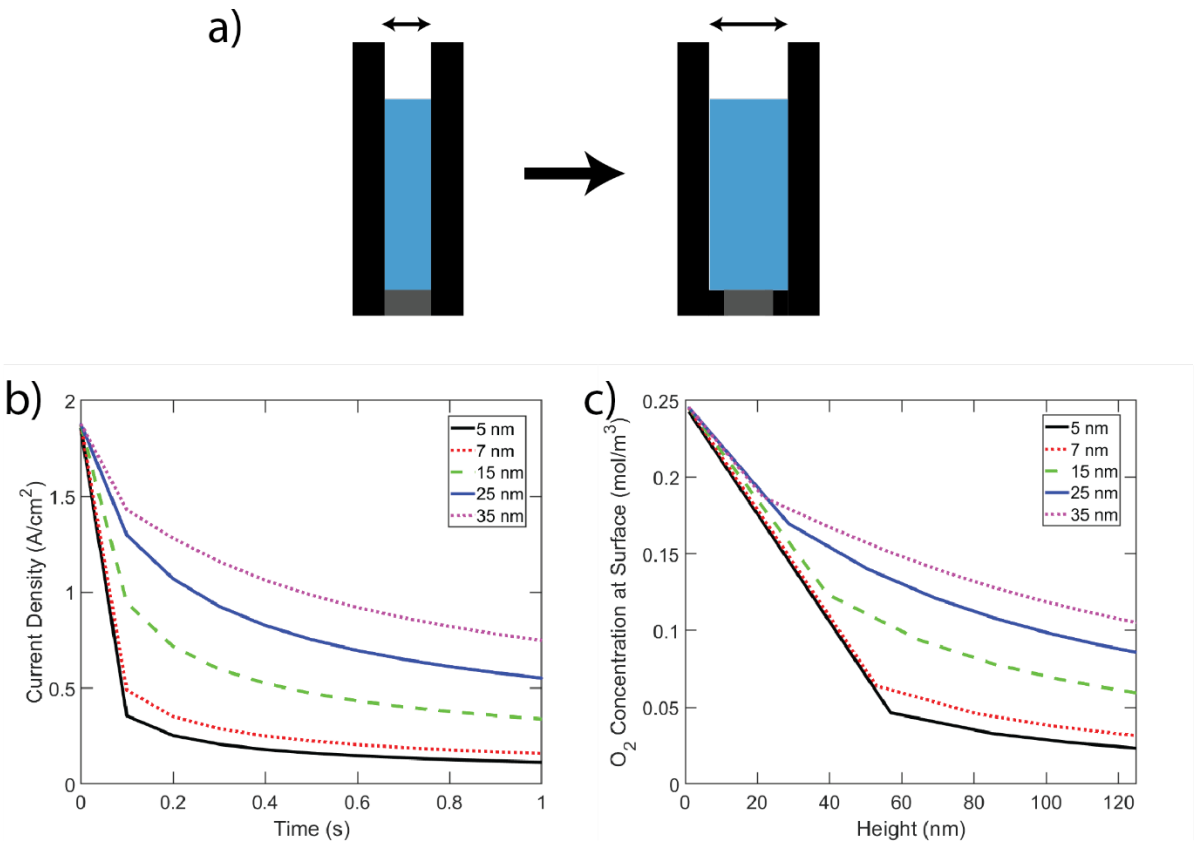

Figure 5.7: a) Schematic of widening of the nanopore. b) Current density as a function of time and pore width. c) Oxygen concentration at the electrode surface as a function of water column height for several different pore widths.

Reactant funneling is the same reason why droplets do not exhibit transport limiting behavior, as reflected in Figure 5.3 and Figure 5.4 (see Section 5.7.2). It is, therefore, unlikely that local water-droplet formation is mass-transfer limiting in current catalyst-layer designs. However, we do not address droplet coalescence here or higher length-scale effects. Coalescence into continuous water channels does impede gas flow by occupying pore space that otherwise would be gas occupied. Thus, although not considered here, some lowering of system efficiency is possible. It is noteworthy that Sabharwal *et al.* argue that catalyst-layer flooding, although commonly believed to cause large performance losses, is not as limiting as originally assumed.[38]

5.5 Conclusions

Four cases of water droplet growth in fuel-cell CLs were examined for possible mass-transfer limitations including: bare Pt electrodes with and without droplet slip, Nafion-covered electrodes, and internal carbon pores. Transient mass and momentum balances were solved simultaneously with oxygen species transport in an axisymmetric geometry by finite elements. We find that growth of water droplets is never transport limiting in traditional fuel-cell CLs. For droplet growth on Pt electrodes, the expanding liquid/gas interface funnels oxygen diffusion to the smaller ORR surface overcoming drop-volume growth. Oxygen supply is large enough that the reacting electrode cannot consume the oxygen inflow leading to lack of mass-transport limitations. For the case of internal carbon pores, mass-transport limitations exist, but only at pore lengths larger than the size of the pores typically found in fuel-cell particles. Lack of drop-growth mass-transfer limitations is an important result for fuel-cell optimization, as design changes performed to minimize droplet growth and flooding may not be necessary or more strategic placement of catalyst can be used.

5.6 Symbols

Roman

A: area

A_e: electrode area

c_{O_2}: oxygen concentration

c_w: liquid water concentration

c_e: equilibrium oxygen concentration

$c_{O_2,ref}$: oxygen reference concentration

$Ca = \mu_w u_{char}/2\gamma$: Capillary number

D_{O_2}: oxygen diffusivity in water

$D_{O_2,Nafion}$: oxygen diffusivity in Nafion

F: Faraday's constant

F_f: frictional forces term

H: pore column height

H_w: Henry's constant for oxygen in water

H_{Nafion}: Henry's constant for oxygen in Nafion

i: current density

i_0: exchange current density

L: Nafion thickness

m_w: mass of water

$\dot{m}_{w,in}$: water flowrate in

M_w: water molar mass

n: number of electrons

$\boldsymbol{n}$: normal vector

$N_{O_2,z}$: oxygen flux in z direction

N_w: Water flux

P_{atm}: atmospheric pressure

P_{char}: characteristic pressure

P_d: droplet pressure

$Pe = \frac{\delta u_{char}}{D_{O_2}}$: Peclet number

$Re = \frac{\rho_w u_{char} R_e}{\mu_w}$: Reynolds number

R: universal gas constant

R_d: droplet radius

R_e: electrode radius

R_w: oxygen resistance in water phase

R_{Naf}: oxygen resistance in Nafion phase

r: radial coordinate

S: droplet surface area

t: time

t_{char}: characteristic time

t_{diff}: characteristic time, diffusion

t_{grow}: characteristic time, droplet growth

T: temperature

$\boldsymbol{u_w}$: water velocity vector

$\boldsymbol{u_g}$: gas velocity vector

u_{char}: characteristic velocity

V: droplet volume

z: axial coordinate

Greek

α: transfer coefficient

β: coefficient defined in Equation S3

γ: surface tension

δ: mass-transfer boundary-layer thickness

ρ_w: water density

μ_w: water viscosity

μ_g: gas viscosity

$\underline{\boldsymbol{\tau_g}}$: stress tensor, gas phase

$\underline{\boldsymbol{\tau_w}}$: stress tensor, water phase

∇: gradient operator

∇_S: surface gradient operator

η: overpotential

5.7 Supplemental Information

5.7.1 Scaling Analysis

To determine the origin of the near-zero velocity profile and the constant pressure profile (verified in Figure S5.1 and Figure S5.2), we scale the Navier-Stokes equation,

$$\rho_w \frac{D\boldsymbol{u_w}}{Dt} = -\nabla P_d + \mu_w \nabla^2 \boldsymbol{u_w} \tag{S5.1}$$

Each term in Equation S5.1 is scaled by a characteristic dimension, R_e, a characteristic pressure, $P_{char} = 2\gamma/R_e$, a characteristic time, and a characteristic velocity. We first garner the characteristic time from Equations 5.1 and 5.7:

$$t_{char} = \frac{\rho_w R_e}{6 M_w \beta c_e} \tag{S5.2}$$

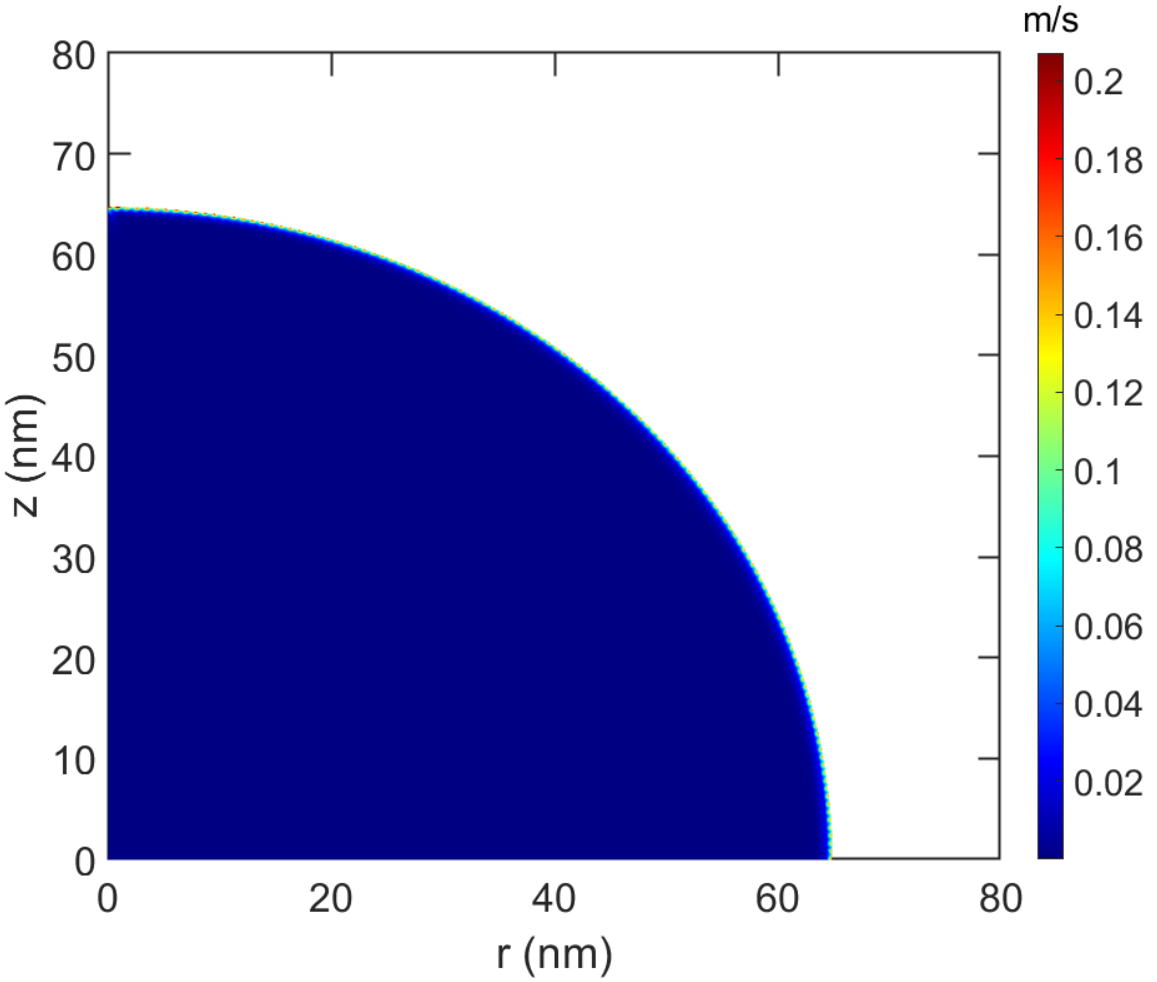

Figure S5.1: Velocity profile in the advancing droplet at 5 s and –0.8 V of overpotential.

where c_e is the equilibrium oxygen concentration in the drop and

$$\beta = \frac{i_0}{nF c_{O2,ref}} \exp\left(-\frac{\alpha F}{RT}\eta\right) \tag{S5.3}$$

The characteristic drop velocity then follows by definition: $u_{char} = R_e/t_{char}$, or

$$u_{char} = \frac{M_w}{\rho_w} 6\beta c_e \tag{S5.4}$$

where Equation S5.4 specifies the characteristic early-on growth rate of the drop. Now, by utilizing the above-defined characteristic quantities, Equation S5.1 reads in nondimensional form:

$$\frac{\rho_w u_{char} R_e}{\mu_w} \frac{D\widetilde{\boldsymbol{u_w}}}{D\tilde{t}} = -\frac{2\gamma}{\mu_w u_{char}} \nabla\widetilde{P_d} + \nabla^2\widetilde{\boldsymbol{u_w}} \tag{S5.5}$$

where over-tildes indicate non-dimensional variables. The parameter multiplying the substantial derivative is the Reynold's number. From Equations S5.3 and S5.4 and the parameters in Table

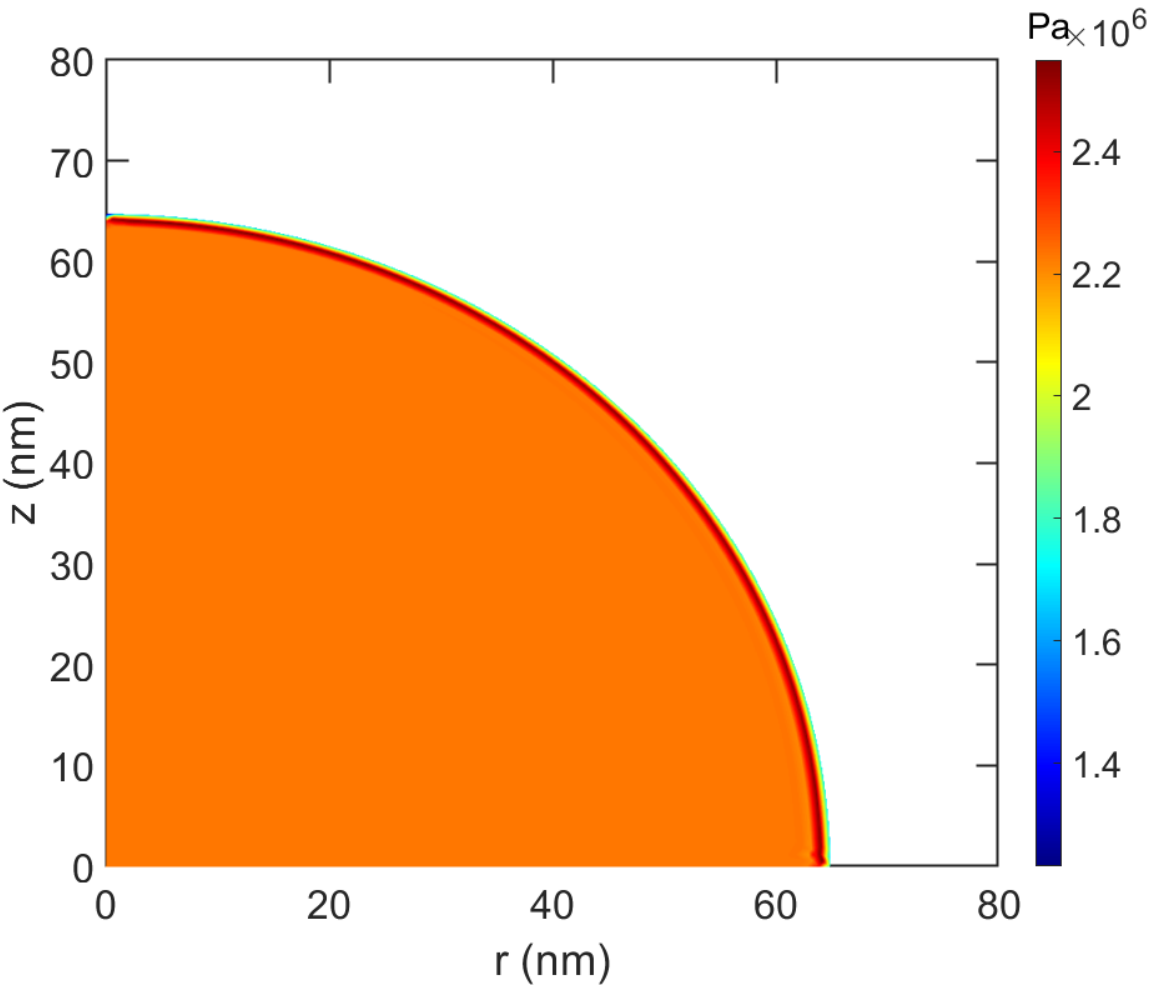

Figure S5.2: Pressure profile in the advancing droplet at 5 s and –0.8 V of overpotential.

5.1, we find that u_{char} ~ O(10^{-6}) m/s**.** Because R_e is on the order of a nm, the Reynolds number is much less than unity, thus eliminating the material derivative and reducing the hydrodynamics to pseudo steady state. Given the characteristic velocity, we also find that the characteristic Capillary number, $Ca = \mu_w u_{char}/2\gamma$, is ~ 10^{-8} << 1. Consequently, the viscous term also drops out of the momentum equation. We are left with the result of

$$\nabla P_d = 0 \qquad \text{(S5.6)}$$

as the governing momentum balance, also implying that the pressure is essentially constant, and the velocity profile is ~ 0. We confirm these results by examining the velocity and pressure profiles in a rigorous simulation. Shown in Figure S5.1 and Figure S5.2 are the velocity and pressure profiles, respectively, for an advancing drop on a bare Pt surface for an overpotential of –0.8 V at 5 s. Clearly, the velocity is near zero everywhere and the pressure is constant throughout the droplet except for a thin layer at the droplet edge, where mass balance forces a non-zero velocity (and thus, a change in pressure) to allow the drop to move. However, in the region relevant for oxygen diffusion (near the electrode), pressure is constant, and velocity is near-zero. Further, the small Capillary number enforces a spherical shape for the growing drop. Before scaling the convection-diffusion equation for dissolved oxygen transport, we address the funneling effect in a growing drop.

5.7.2 Diffusion Funneling in a Growing Drop

As the droplet grows, its radius increases providing more surface area to gather and funnel oxygen from the gas phase to the bare Pt surface. Thus, examination of the funneling effect in oxygen transport equation is paramount. Again, Equation 5.1 of the text yields a characteristic time when the increasing drop radius, R_d is larger than the Pt surface radius, R_e:

$$t_{grow} = \frac{\rho_w R_e}{6 M_w \beta c_e} \left(\frac{R_d}{R_e}\right)^3 \tag{S5.7}$$

The ratio of droplet radius to electrode radius to the third power represents the strong funneling effect. Thus, large drops both slow droplet growth and collect oxygen from larger areas of gas exposure. Because of the surface-area funneling effect, the concentration of oxygen is nearly uniform in the drop except in a boundary layer near the electrode surface. The boundary layer thickness, δ, is found from the flux boundary condition,

$$-D_{O_2} \frac{\partial c_{O_2}}{\partial z} = \beta c_{O_2} \tag{S5.8}$$

Scaling Equation S5.8 by the diffusion boundary-layer thickness gives

$$\delta = \frac{D_{O_2}}{\beta} \tag{S5.9}$$

in agreement with Figure 5.3-5.5 except immediately near the electrode edge.

With this information, we scale the convection-diffusion equation for oxygen using the boundary-layer thickness as characteristic length, the characteristic equilibrium oxygen concentration, $c_{e,}$, and the characteristic diffusion time, $t_{diff} = \delta^2 / D_{O_2}$, giving

$$\frac{\partial \tilde{c}_{O_2}}{\partial \tilde{t}_{diff}} + \left(\frac{u_{char}\delta}{D_{O_2}}\right) \tilde{\boldsymbol{u}}_{\boldsymbol{w}} \cdot \tilde{\nabla} \tilde{c}_{O_2} = \tilde{\nabla}^2 \tilde{c}_{O_2} \tag{S5.10}$$

where the Peclét number, $Pe = \frac{\delta u_{char}}{D_{O_2}}$, is quite small

$$Pe = \frac{\delta u_{char}}{D_{O_2}} = \frac{10^{-8}\, m * 10^{-6} \frac{m}{s}}{10^{-9} \frac{m^2}{s}} \ll 1 \tag{S5.11}$$

Thus, convection plays a minor role and molecular diffusion dominates oxygen transport to the electrode, despite water convecting oxygen away from the reacting surface; Fick's second law holds. Finally, we note from Equation S5.7 that the expanding-drop growth characteristic time is always much larger than the diffusion-boundary-layer time constant:

$$t_{grow} = \frac{\rho_w R_e}{6 M_w \beta c_e} \left(\frac{R_d}{R_e}\right)^3 \gg t_{diff} = \frac{\delta^2}{D_{O_2}} = \frac{D_{O_2}}{\beta^2} \tag{S5.12}$$

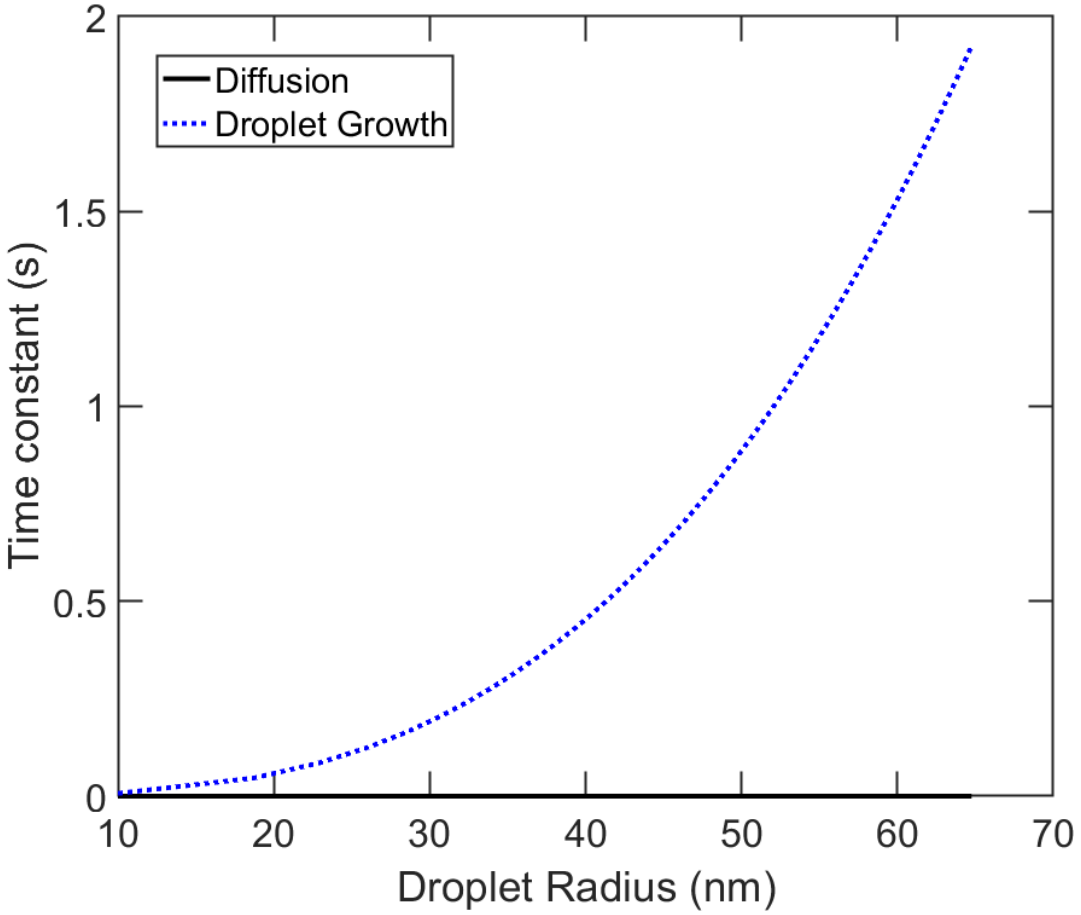

Figure S5.3: Comparison of the two different time constants for the sliding droplet – droplet growth (blue dotted line) and oxygen diffusion (black solid line).

This result reduces Fick's second law to pseudo-steady molecular diffusion across a boundary layer (i.e., $\nabla^2 c_{O_2} = 0$), and sets the boundary-layer thickness constant, as confirmed in Figure 5.3 and Figure 5.4. More importantly, it also prevents bulk droplet diffusion from becoming the limiting process despite larger growing drop sizes.

When we examine Equations 5.1 and 5.7 for the nanopore system, we obtain

$$t_{grow,nano} = \frac{\rho_w H}{2\beta c_e M_w}\left(\frac{w}{R_e}\right) \tag{S5.13}$$

where H is the height of water in the pore and w is the width of the pore. The funneling effect is also present in the ratio of the width to the electrode radius, although it is less significant here as it lacks the cubic exponent found in the growing droplet time constant. When $w = R_e$, there is no funneling effect, and the characteristic time is small. As w is increased, the characteristic time becomes larger, lessening the importance of diffusion and revealing the impact of funneling. Funneling is clearly demonstrated in Figure 5.7 by the increased current densities as the pore widens.

5.7.3 Validation of Resistance in Series of Droplet Growth on a Nafion-Covered Electrode

We validate the claim of minimal droplet diffusion resistance on system performance by approximating the resistance of each phase to oxygen transport and then summing the resistances in series to identify the main contribution to the total resistance. Reasonable approximations for the resistances are

$$R_w = \frac{V/S}{D_{O_2}} \tag{S5.14}$$

and

$$R_{Naf} = \frac{L}{D_{O_2,Nafion}} \tag{S5.15}$$

where R_w is oxygen resistance in the water droplet, R_{Naf} is the resistance in the Nafion, V/S is the ratio of drop volume to surface area, and L is the thickness of the Nafion film. The remaining variables are defined previously (see Section 5.6). Equations S5.14 and S5.15 as well as the sum of the two resistances, are reflected in Figure S5.4. At small droplet sizes, the droplet contribution is less than 5% of the total resistance, rising to approximately 20% at larger droplet sizes. This is somewhat higher than expected, but Equation S5.15 likely underestimates the Nafion resistance as it assumes a purely 1D problem, whereas the actual system in the model is 2D. These estimates are supported by examining the concentration profile at the center of the droplet as a function of the z axis, as in Figure S5.5. A slight drop in oxygen concentration occurs in the droplet, accounting for ~10% of the total loss, whereas the other 90% is due to the Nafion, supporting the conclusion that droplet diffusion resistance is largely unimportant when a Nafion layer is included.

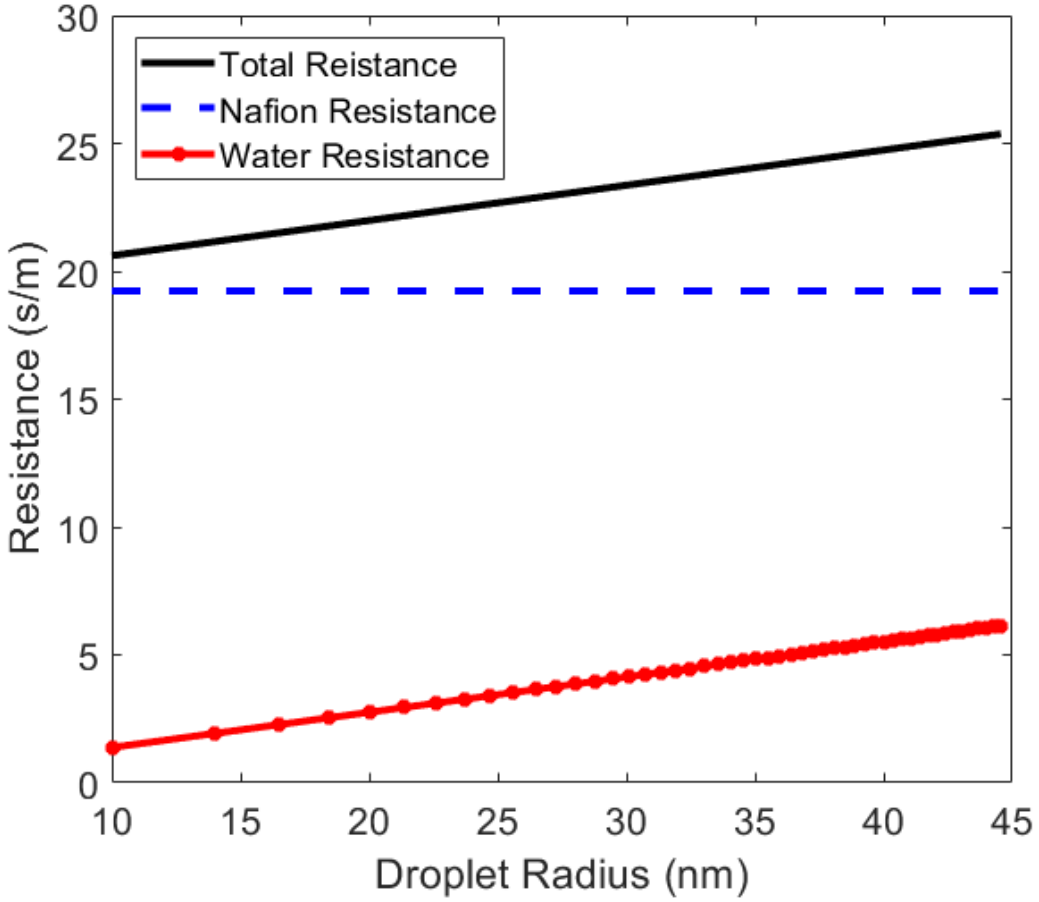

Figure S5.4: Resistance to oxygen transport in each phase (blue dash and red dotted line), as well as the total resistance (solid black), as a function of droplet radius.

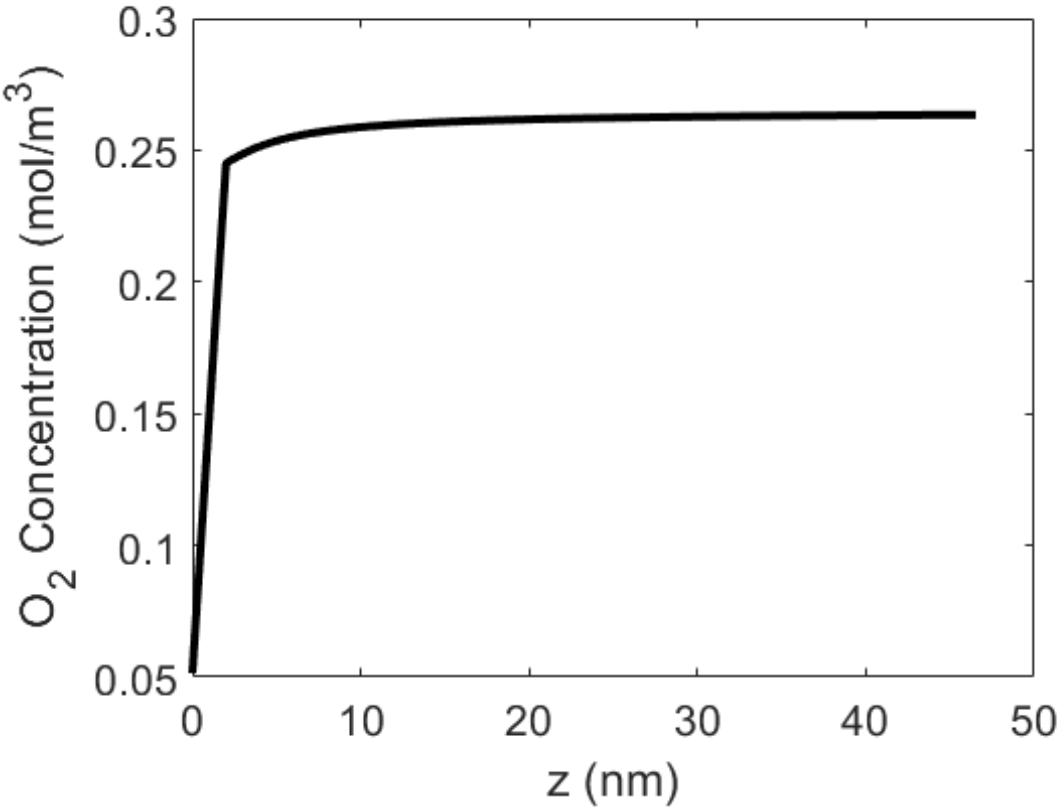

Figure S5.5: Oxygen concentration at the center of the droplet (r = 0) along the z-axis. The Nafion layer is 2-nm thick, which can be seen in the change in slope at z = 2 nm. The remaining ~ 45 nm reflects the water-droplet oxygen concentration.

6. Conclusions and Future Directions

6.1 Summary and Conclusions

In this dissertation, the gas and water transport properties of ion-conducting polymers (ionomers) including proton- and hydroxide-exchange membranes (PEMs and HEMs, respectively) and oxygen transport inside low-temperature polymer-electrolyte fuel-cell catalyst layers have been studied using electrochemical techniques and mathematical modeling. In Chapter 2, a flowthrough microelectrode cell was developed to address problems with previous designs and to study the transport properties of ionomer membranes. Chapters 3 and 4 described modified experimental techniques aimed at studying gas transport in PEMs and electro-osmosis in PEMs and HEMs. Experimental results in both chapters were supported by simple models aimed at capturing the fundamental physics of gas transport and electro-osmosis in these membranes. In Chapter 5, a more complex continuum model was developed to study the impact of droplets within the catalyst layer on oxygen transport, using the same fundamental principles used to study gas transport in Chapter 3. Every chapter provides context for where transport losses may or may not be occurring in the overall fuel-cell system.

Only specific membranes and one type of catalyst layer were examined in this work; they were chosen to reflect what is being used broadly in the field today. However, the methods described could be applied to any new membrane materials or catalyst-layer structure that would be developed in the future. Chapters 2 and 3 may be considered a manual for how to study gas transport accurately in polymer electrolytes using microelectrodes, the most common application of the device. Although detailed conclusions are accentuated in these three preceding chapters, it is possible to draw broad conclusions based on an overall view of the dissertation:

(1) *Microelectrode systems are a flexible foundation from which to design experiments for studying the properties of polymer electrolytes.* This dissertation examines mass transport in polymer electrolytes using microelectrodes in two different ways: gas transport in Chapter 3 and water transport in Chapter 4. In both cases, the techniques employed are not that different, but in fact study different phenomena. It is feasible to consider other methods of using microelectrodes, including investigation of ion transport (conductivity), water transport more directly via diffusion, and other materials unrelated to fuel cells, such as those used in carbon-dioxide electrolyzers or bipolar membranes. It is also possible to study electrochemical kinetics using the same system. This dissertation establishes microelectrodes as a solid-state analog to rotating disk electrochemistry.

(2) *System geometry can become extremely relevant, perhaps even controlling, when working with microscale and smaller systems.* In Chapter 3, the importance of considering the specific system geometry of a finite thickness, micrometer-thick membrane abutting a micrometer-sized microelectrode is described and its impact on the measured gas transport properties is discussed. In Chapter 5, a water droplet 100 nm in diameter is no more limiting than one 20 nm in diameter due to the geometry funneling a vast amount of incoming dissolved oxygen to a 5-nm active Pt site. In both cases, the geometry plays a large role in the result; assuming an infinite thickness membrane and applying the analytical solution, even over a short time range, is inaccurate. The unique conditions of

an unconstrained growing droplet prevent it from becoming limiting to oxygen transport when a nanopore of a similar length is limiting. This is an important finding that should influence the design of further studies examining mass transport in membranes and catalyst layers.

(3) *Water content is the most important parameter controlling mass transport within polymer electrolytes.* The Introduction (Chapter 1) detailed how important the presence of water in the membrane is for ion conduction. This significance extends to gas transport and electro-osmosis, as well. In Chapter 3, the largest changes in gas diffusivity and permeability occur when water content is varied, much larger than the difference between gases studied or between Nafion 211 and Nafion XL. In Chapter 4, the water content again played a controlling role, particularly for HEMs, with significantly lower water transport numbers measured at low water contents compared to the difference between ion types at the same water content. The role of temperature was also found to be relatively insignificant in this case. This result only emphasizes the importance of designing the overall-system water balance such that the optimal ratio of conductivity, gas permeance, and electro-osmosis is obtained to maximize fuel-cell performance. It also highlights the need for a microelectrode cell where environment can be controlled and that does not rely on liquid studies.

Clearly, microelectrodes are a powerful tool for studying polymer electrolytes, but geometry-specific concerns must be taken into account when using them. Water content is also more relevant than expected for transport parameters beyond conductivity. As future directions are discussed below, it is important to keep these conclusions in mind.

Throughout this work, the focus was placed on understanding transport in membranes and catalyst layers within the fuel cell, with no attention paid to the impact on the overall fuel cell. This was necessary to develop a fundamental understanding of the materials, but also makes it difficult to contextualize fully some of the results presented without additional information (*e.g.*, what is the impact of the measured HEM water transport number on the necessary humidity of the gas inlet feeds). However, such attention is beyond the scope of this dissertation.

6.2 Future Directions

Species transport in the polymer membrane and catalyst layer remain critically important to the performance of fuel-cell devices; it is important to design and choose the proper materials to optimize performance based on transport properties. There are many directions in which the methodology presented in this dissertation may be extended to elucidate further gas, ion, and water transport. Those listed below are simply a selection and should not be construed as the only options for future research.

(1) *Gas transport in HEMs and other membranes*. Perhaps one of the clearest extensions of this work, gas transport and crossover within HEM systems is an unexplored avenue, at least for modern HEMs in *ex-situ* cells. Gas crossover remains important in HEM fuel cells as it impacts performance in a similar manner to PEM systems and thus is a

necessary parameter to study. It is also possible to study gas transport in other, related systems, such as in carbon dioxide electrolyzers.

(2) *Transport in novel membrane chemistries*. This dissertation focused primarily on the most common commercial membranes, but there are many other variants, particularly of PEMs, that change various aspects of the membrane chemistry, such as equivalent weight/side-chain spacing and side-chain length.[48] Complicating this study is the impact that changing these parameters has on water uptake, which is also critical to measured transport parameters. Microelectrodes are an excellent system to deconvolute the impact of water uptake and membrane chemistry and/or structure on the transport properties. This system could also allow for better delineation of structure/transport property relationships if other techniques, such as small-angle scattering or infrared spectroscopy, are coupled with microelectrode studies, thus aiding in the design of better materials.

(3) *Exploration of bipolar membranes*. Bipolar membranes are another class of membranes that combine aspects of both PEMs and HEMs into one composite membrane, and as a result can be difficult to study.[147] The techniques presented in Chapters 3 and 4 could be modified to account for the water dissociation reaction such that gas and water transport could be effectively measured in these materials.[228] Microelectrodes would allow for probing of each side of the interface independently.

(4) *Gas and water transport in thin films*. Gas transport within the thin films in the catalyst layer is known to be more resistive than transport within the bulk membrane.[61] It is possible that this is due to structural changes and water uptake differences between thin films and bulk membranes. However, no comprehensive study has been performed studying this effect.[229] Electro-osmosis in the thin film remains entirely unexplored. It is feasible to restructure the microelectrode cell based on the design principles discussed in Chapter 2 to enable application of the techniques from Chapters 3 and 4 to the study of thin films that are present in catalyst layers.

(5) *Water diffusion in bulk membranes*. Water diffusion within membranes is often difficult to study, with indirect methods such as NMR and quasi-electric neutron scattering being popular as well as direct steady-state diffusion measurements.[32, 64, 66] Control of environmental parameters is sufficient in the microelectrode cell such that it may be possible to devise an experiment to measure in-plane water diffusion in the membrane. This would provide another alternative to the experimental techniques mentioned above for studying water diffusion. The microelectrode cell also allows for an investigation of interfacial resistances via dynamic, fast-time experiments, something that is particularly relevant for water uptake and transport.[17]

(6) *Exploring the impact of bubble growth on catalyst surfaces in electrolyzers*. In an analogous manner to the droplets discussed in Chapter 5, gas bubbles may form on catalyst particles in the catalyst layers in electrolyzers.[218] However, two key differences differentiate this case from that of droplets: ions are typically unable to move through the gas bubble covering the catalyst particle, and water is consumed at the catalyst surface such that local drying may influence transport of species near the catalyst surface. It is possible that both of these differences have a sufficient impact to make bubbles more limiting than the analogous droplet case in fuel cells.

7. References

1. Archer, D.; Eby, M.; Brovkin, V.; Ridgwell, A.; Cao, L.; Mikolajewicz, U.; Caldeira, K.; Matsumoto, K.; Munhoven, G.; Montenegro, A.; Tokos, K., Atmospheric Lifetime of Fossil Fuel Carbon Dioxide. *Annual Review of Earth and Planetary Sciences* **2009,** *37* (1), 117-134.
2. Ellabban, O.; Abu-Rub, H.; Blaabjerg, F., Renewable energy resources: Current status, future prospects and their enabling technology. *Renewable and Sustainable Energy Reviews* **2014,** *39*, 748-764.
3. Li, L.; Lin, J.; Wu, N.; Xie, S.; Meng, C.; Zheng, Y.; Wang, X.; Zhao, Y., Review and outlook on the international renewable energy development. *Energy and Built Environment* **2022,** *3* (2), 139-157.
4. Koohi-Fayegh, S.; Rosen, M. A., A review of energy storage types, applications and recent developments. *Journal of Energy Storage* **2020,** *27*.
5. Gerhardt, M. R.; Pant, L. M.; Bui, J. C.; Crothers, A. R.; Ehlinger, V. M.; Fornaciari, J. C.; Liu, J.; Weber, A. Z., Method—Practices and Pitfalls in Voltage Breakdown Analysis of Electrochemical Energy-Conversion Systems. *Journal of The Electrochemical Society* **2021,** *168* (7).
6. Cullen, D. A.; Neyerlin, K. C.; Ahluwalia, R. K.; Mukundan, R.; More, K. L.; Borup, R. L.; Weber, A. Z.; Myers, D. J.; Kusoglu, A., New roads and challenges for fuel cells in heavy-duty transportation. *Nature Energy* **2021,** *6* (5), 462-474.
7. Pivovar, B.; Rustagi, N.; Satyapal, S., Hydrogen at Scale (H2@Scale): Key to a Clean, Economic, and Sustainable Energy System. *The Electrochemical Society Interface* **2018,** *27* (1), 47-52.
8. Pivovar, B. S.; Ruth, M. F.; Myers, D. J.; Dinh, H. N., Hydrogen: Targeting $1/kg in 1 Decade. *The Electrochemical Society Interface* **2021,** *30* (4), 61-66.
9. Guerrero Moreno, N.; Cisneros Molina, M.; Gervasio, D.; Pérez Robles, J. F., Approaches to polymer electrolyte membrane fuel cells (PEMFCs) and their cost. *Renewable and Sustainable Energy Reviews* **2015,** *52*, 897-906.
10. Sazali, N.; Wan Salleh, W. N.; Jamaludin, A. S.; Mhd Razali, M. N., New Perspectives on Fuel Cell Technology: A Brief Review. *Membranes (Basel)* **2020,** *10* (5).
11. Lucia, U., Overview on fuel cells. *Renewable and Sustainable Energy Reviews* **2014,** *30*, 164-169.
12. Holdcroft, S., Fuel Cell Catalyst Layers: A Polymer Science Perspective. *Chemistry of Materials* **2013,** *26* (1), 381-393.
13. Zhang, J.; Zhu, W.; Huang, T.; Zheng, C.; Pei, Y.; Shen, G.; Nie, Z.; Xiao, D.; Yin, Y.; Guiver, M. D., Recent Insights on Catalyst Layers for Anion Exchange Membrane Fuel Cells. *Adv Sci (Weinh)* **2021,** *8* (15), e2100284.
14. Zhegur-Khais, A.; Kubannek, F.; Krewer, U.; Dekel, D. R., Measuring the true hydroxide conductivity of anion exchange membranes. *Journal of Membrane Science* **2020,** *612*.
15. Ziv, N.; Dekel, D. R., A practical method for measuring the true hydroxide conductivity of anion exchange membranes. *Electrochemistry Communications* **2018,** *88*, 109-113.
16. Lindquist, G. A.; Oener, S. Z.; Krivina, R.; Motz, A. R.; Keane, A.; Capuano, C.; Ayers, K. E.; Boettcher, S. W., Performance and Durability of Pure-Water-Fed Anion

Exchange Membrane Electrolyzers Using Baseline Materials and Operation. *ACS Appl Mater Interfaces* **2021**.
17. Kusoglu, A.; Weber, A. Z., New Insights into Perfluorinated Sulfonic-Acid Ionomers. *Chem Rev* **2017,** *117* (3), 987-1104.
18. Mauritz, K. A.; Moore, R. B., State of understanding of nafion. *Chem Rev* **2004,** *104* (10), 4535-85.
19. Allen, F. I.; Comolli, L. R.; Kusoglu, A.; Modestino, M. A.; Minor, A. M.; Weber, A. Z., Morphology of Hydrated As-Cast Nafion Revealed through Cryo Electron Tomography. *ACS Macro Lett* **2015,** *4* (1), 1-5.
20. Zawodzinski, T. A.; Springer, T. E.; Davey, J.; Jestel, R.; Lopez, C.; Valerio, J.; Gottesfeld, S., A Comparative-Study of Water-Uptake by and Transport through Ionomeric Fuel-Cell Membranes. *Journal of the Electrochemical Society* **1993,** *140* (7), 1981-1985.
21. Zawodzinski, T. A.; Derouin, C.; Radzinski, S.; Sherman, R. J.; Smith, V. T.; Springer, T. E.; Gottesfeld, S., Water-Uptake by and Transport through Nafion(R) 117 Membranes. *Journal of the Electrochemical Society* **1993,** *140* (4), 1041-1047.
22. Mauritz, K. A.; Rogers, C. E., A Water Sorption Isotherm Model for Ionomer Membranes with Cluster Morphologies. *Macromolecules* **1985,** *18* (3), 483-491.
23. Kusoglu, A.; Modestino, M. A.; Hexemer, A.; Segalman, R. A.; Weber, A. Z., Subsecond Morphological Changes in Nafion during Water Uptake Detected by Small-Angle X-ray Scattering. *ACS Macro Lett* **2012,** *1* (1), 33-36.
24. Takata, H.; Mizuno, N.; Nishikawa, M.; Fukada, S.; Yoshitake, M., Adsorption properties of water vapor on sulfonated perfluoropolymer membranes. *International Journal of Hydrogen Energy* **2007,** *32* (3), 371-379.
25. Shi, S.; Weber, A. Z.; Kusoglu, A., Structure-Transport Relationship of Perfluorosulfonic-Acid Membranes in Different Cationic Forms. *Electrochimica Acta* **2016,** *220*, 517-528.
26. Gierke, T. D.; Hsu, W. Y., The Cluster-Network Model of Ion Clustering in Perfluorosulfonated Membranes. *Acs Sym Ser* **1982,** *180*, 283-307.
27. Gierke, T. D.; Munn, G. E.; Wilson, F. C., The Morphology in Nafion Perfluorinated Membrane Products, as Determined by Wide-Angle and Small-Angle X-Ray Studies. *J Polym Sci Pol Phys* **1981,** *19* (11), 1687-1704.
28. Hsu, W. Y.; Gierke, T. D., Ion transport and clustering in nafion perfluorinated membranes. *Journal of Membrane Science* **1983,** *13* (3), 307-326.
29. Schmidt-Rohr, K.; Chen, Q., Parallel cylindrical water nanochannels in Nafion fuel-cell membranes. *Nat Mater* **2008,** *7* (1), 75-83.
30. Kreuer, K.-D.; Portale, G., A Critical Revision of the Nano-Morphology of Proton Conducting Ionomers and Polyelectrolytes for Fuel Cell Applications. *Advanced Functional Materials* **2013,** *23* (43), 5390-5397.
31. Berrod, Q.; Lyonnard, S.; Guillermo, A.; Ollivier, J.; Frick, B.; Manseri, A.; Améduri, B.; Gébel, G., Nanostructure and Transport Properties of Proton Conducting Self-Assembled Perfluorinated Surfactants: A Bottom-Up Approach toward PFSA Fuel Cell Membranes. *Macromolecules* **2015,** *48* (17), 6166-6176.
32. Ochi, S.; Kamishima, O.; Mizusaki, J.; Kawamura, J., Investigation of proton diffusion in Nafion®117 membrane by electrical conductivity and NMR. *Solid State Ionics* **2009,** *180* (6-8), 580-584.

33. Zawodzinskijr, T.; Springer, T.; Uribe, F.; Gottesfeld, S., Characterization of polymer electrolytes for fuel cell applications. *Solid State Ionics* **1993,** *60* (1-3), 199-211.
34. Sone, Y.; Ekdunge, P.; Simonsson, D., Proton conductivity of Nafion 117 as measured by a four-electrode AC impedance method. *Journal of the Electrochemical Society* **1996,** *143* (4), 1254-1259.
35. Choi, P.; Jalani, N. H.; Datta, R., Thermodynamics and proton transport in Nafion - II. Proton diffusion mechanisms and conductivity. *Journal of the Electrochemical Society* **2005,** *152* (3), E123-E130.
36. Fuller, T. F.; Newman, J., Experimental-Determination of the Transport Number of Water in Nafion-117 Membrane. *Journal of the Electrochemical Society* **1992,** *139* (5), 1332-1337.
37. Wang, Y.; Wang, X.; Wang, X.; Liu, T.; Zhu, T.; Liu, S.; Qin, Y., Droplet dynamic characteristics on PEM fuel cell cathode gas diffusion layer with gradient pore size distribution. *Renewable Energy* **2021,** *178*, 864-874.
38. Sabharwal, M.; Secanell, M., Understanding the effect of porosity and pore size distribution on low loading catalyst layers. *Electrochimica Acta* **2022,** *419*.
39. Li, H.; Tang, Y.; Wang, Z.; Shi, Z.; Wu, S.; Song, D.; Zhang, J.; Fatih, K.; Zhang, J.; Wang, H.; Liu, Z.; Abouatallah, R.; Mazza, A., A review of water flooding issues in the proton exchange membrane fuel cell. *Journal of Power Sources* **2008,** *178* (1), 103-117.
40. Weber, A. Z.; Newman, J., Coupled thermal and water management in polymer electrolyte fuel cells. *Journal of the Electrochemical Society* **2006,** *153* (12), A2205-A2214.
41. Andersson, M.; Beale, S. B.; Espinoza, M.; Wu, Z.; Lehnert, W., A review of cell-scale multiphase flow modeling, including water management, in polymer electrolyte fuel cells. *Applied Energy* **2016,** *180*, 757-778.
42. Giacinti Baschetti, M.; Minelli, M.; Catalano, J.; Sarti, G. C., Gas permeation in perflurosulfonated membranes: Influence of temperature and relative humidity. *International Journal of Hydrogen Energy* **2013,** *38* (27), 11973-11982.
43. Broka, K.; Ekdunge, P., Oxygen and hydrogen permeation properties and water uptake of Nafion(R) 117 membrane and recast film for PEM fuel cell. *J Appl Electrochem* **1997,** *27* (2), 117-123.
44. Rodgers, M. P.; Bonville, L. J.; Kunz, H. R.; Slattery, D. K.; Fenton, J. M., Fuel cell perfluorinated sulfonic acid membrane degradation correlating accelerated stress testing and lifetime. *Chem Rev* **2012,** *112* (11), 6075-103.
45. Shi, S.; Weber, A. Z.; Kusoglu, A., Structure/property relationship of Nafion XL composite membranes. *Journal of Membrane Science* **2016,** *516*, 123-134.
46. D'Urso, C.; Oldani, C.; Baglio, V.; Merlo, L.; Aricò, A. S., Towards fuel cell membranes with improved lifetime: Aquivion® Perfluorosulfonic Acid membranes containing immobilized radical scavengers. *Journal of Power Sources* **2014,** *272*, 753-758.
47. Gatto, I.; Carbone, A.; Saccà, A.; Passalacqua, E.; Oldani, C.; Merlo, L.; Sebastián, D.; Aricò, A. S.; Baglio, V., Increasing the stability of membrane-electrode assemblies based on Aquivion® membranes under automotive fuel cell conditions by using proper catalysts and ionomers. *Journal of Electroanalytical Chemistry* **2019,** *842*, 59-65.
48. Kreuer, K. D.; Schuster, M.; Obliers, B.; Diat, O.; Traub, U.; Fuchs, A.; Klock, U.; Paddison, S. J.; Maier, J., Short-side-chain proton conducting perfluorosulfonic acid

ionomers: Why they perform better in PEM fuel cells. *Journal of Power Sources* **2008,** *178* (2), 499-509.
49. Danilczuk, M.; Schlick, S.; Coms, F. D., Cerium(III) as a Stabilizer of Perfluorinated Membranes Used in Fuel Cells: In Situ Detection of Early Events in the ESR Resonator. *Macromolecules* **2009,** *42* (22), 8943-8949.
50. Kudo, K.; Jinnouchi, R.; Morimoto, Y., Humidity and Temperature Dependences of Oxygen Transport Resistance of Nafion Thin Film on Platinum Electrode. *Electrochimica Acta* **2016,** *209*, 682-690.
51. Novitski, D.; Holdcroft, S., Determination of O(2) Mass Transport at the Pt | PFSA Ionomer Interface under Reduced Relative Humidity. *ACS Appl Mater Interfaces* **2015,** *7* (49), 27314-23.
52. Ye, X.; Wang, C. Y., Measurement of Water Transport Properties Through Membrane-Electrode Assemblies: I. Membranes. *Journal of the Electrochemical Society* **2007,** *154*.
53. He, C.; Yang-Neyerlin, A. C.; Pivovar, B. S., Probing Anion Exchange Membrane Fuel Cell Cathodes by Varying Electrocatalysts and Electrode Processing. *Journal of The Electrochemical Society* **2022,** *169* (2).
54. Wang, J.; Zhao, Y.; Setzler, B. P.; Rojas-Carbonell, S.; Ben Yehuda, C.; Amel, A.; Page, M.; Wang, L.; Hu, K.; Shi, L.; Gottesfeld, S.; Xu, B.; Yan, Y., Poly(aryl piperidinium) membranes and ionomers for hydroxide exchange membrane fuel cells. *Nature Energy* **2019,** *4* (5), 392-398.
55. Luo, X.; Rojas-Carbonell, S.; Yan, Y.; Kusoglu, A., Structure-transport relationships of poly(aryl piperidinium) anion-exchange membranes: Eeffect of anions and hydration. *Journal of Membrane Science* **2020,** *598*.
56. Luo, X.; Kushner, D. I.; Li, J.; Park, E. J.; Kim, Y. S.; Kusoglu, A., Anion Exchange Ionomers: Impact of Chemistry on Thin-Film Properties. *Advanced Functional Materials* **2021,** *31* (20).
57. Duan, Q.; Ge, S.; Wang, C.-Y., Water uptake, ionic conductivity and swelling properties of anion-exchange membrane. *Journal of Power Sources* **2013,** *243*, 773-778.
58. Cheng, X.; Zhang, J.; Tang, Y.; Song, C.; Shen, J.; Song, D.; Zhang, J., Hydrogen crossover in high-temperature PEM fuel cells. *Journal of Power Sources* **2007,** *167* (1), 25-31.
59. Parthasarathy, A.; Martin, C. R.; Srinivasan, S., Investigations of the O[sub 2] Reduction Reaction at the Platinum/Nafion® Interface Using a Solid-State Electrochemical Cell. *Journal of The Electrochemical Society* **1991,** *138* (4), 916-921.
60. Mohamed, H. F. M.; Ito, K.; Kobayashi, Y.; Takimoto, N.; Takeoka, Y.; Ohira, A., Free volume and permeabilities of O2 and H2 in Nafion membranes for polymer electrolyte fuel cells. *Polymer* **2008,** *49* (13-14), 3091-3097.
61. Weber, A. Z.; Kusoglu, A., Unexplained transport resistances for low-loaded fuel-cell catalyst layers. *J. Mater. Chem. A* **2014,** *2* (41), 17207-17211.
62. Chen, D.; Kongkanand, A.; Jorne, J., Proton Conduction and Oxygen Diffusion in Ultra-Thin Nafion Films in PEM Fuel Cell: How Thin? *Journal of The Electrochemical Society* **2019,** *166* (2), F24-F33.
63. Liu, H.; Epting, W. K.; Litster, S., Gas Transport Resistance in Polymer Electrolyte Thin Films on Oxygen Reduction Reaction Catalysts. *Langmuir* **2015,** *31* (36), 9853-8.
64. Perrin, J. C.; Lyonnard, S.; Volino, F., Quasielastic neutron scattering study of water dynamics in hydrated nafion membranes. *J Phys Chem C* **2007,** *111* (8), 3393-3404.

65. Zelsmann, H. R.; Pineri, M.; Thomas, M.; Escoubes, M., Water self-diffusion coefficient determination in an ion exchange membrane by optical measurement. *Journal of Applied Polymer Science* **1990,** *41* (78), 1673-1684.
66. Schneider, N. S.; Rivin, D., Steady state analysis of water vapor transport in ionomers. *Polymer* **2010,** *51* (3), 671-678.
67. Pivovar, B. S.; Smyrl, W. H.; Cussler, E. L., Electro-osmosis in Nafion 117, polystyrene sulfonic acid, and polybenzimidazole. *Journal of the Electrochemical Society* **2005,** *152* (1), A53-A60.
68. Zawodzinski, T. A.; Davey, J.; Valerio, J.; Gottesfeld, S., The water content dependence of electro-osmotic drag in proton-conducting polymer electrolytes. *Electrochimica Acta* **1995,** *40* (3), 297-302.
69. Ise, M.; Kreuer, K. D.; Maier, J., Electroosmotic drag in polymer electrolyte membranes: an electrophoretic NMR study. *Solid State Ionics* **1999,** *125* (1-4), 213-223.
70. Eastman, S. A.; Kim, S.; Page, K. A.; Rowe, B. W.; Kang, S.; Soles, C. L.; Yager, K. G., Effect of Confinement on Structure, Water Solubility, and Water Transport in Nafion Thin Films. *Macromolecules* **2012,** *45* (19), 7920-7930.
71. Davis, E. M.; Stafford, C. M.; Page, K. A., Elucidating Water Transport Mechanisms in Nafion Thin Films. *ACS Macro Lett* **2014,** *3* (10), 1029-1035.
72. Kongkanand, A., Interfacial Water Transport Measurements in Nafion Thin Films Using a Quartz-Crystal Microbalance. *The Journal of Physical Chemistry C* **2011,** *115* (22), 11318-11325.
73. Khalid, H.; Najibah, M.; Park, H. S.; Bae, C.; Henkensmeier, D., Properties of Anion Exchange Membranes with a Focus on Water Electrolysis. *Membranes (Basel)* **2022,** *12* (10).
74. Luo, X.; Wright, A.; Weissbach, T.; Holdcroft, S., Water permeation through anion exchange membranes. *Journal of Power Sources* **2018,** *375*, 442-451.
75. Myles, T. D.; Kiss, A. M.; Grew, K. N.; Peracchio, A. A.; Nelson, G. J.; Chiu, W. K. S., Calculation of Water Diffusion Coefficients in an Anion Exchange Membrane Using a Water Permeation Technique. *Journal of The Electrochemical Society* **2011,** *158* (7).
76. Melchior, J.-P.; Jalarvo, N. H., A Quasielastic Neutron Scattering Study of Water Diffusion in Model Anion Exchange Membranes over Localized and Extended Volume Increments. *The Journal of Physical Chemistry C* **2019,** *123* (23), 14195-14206.
77. Gunasekara, I.; Lee, M.; Abbott, D.; Mukerjee, S., Mass Transport and Oxygen Reduction Kinetics at an Anion Exchange Membrane Interface: Microelectrode Studies on Effect of Carbonate Exchange. *ECS Electrochemistry Letters* **2012,** *1* (2), F16-F19.
78. Gutru, R.; Turtayeva, Z.; Xu, F.; Maranzana, G.; Vigolo, B.; Desforges, A., A comprehensive review on water management strategies and developments in anion exchange membrane fuel cells. *International Journal of Hydrogen Energy* **2020,** *45* (38), 19642-19663.
79. Omasta, T. J.; Wang, L.; Peng, X.; Lewis, C. A.; Varcoe, J. R.; Mustain, W. E., Importance of balancing membrane and electrode water in anion exchange membrane fuel cells. *Journal of Power Sources* **2018,** *375*, 205-213.
80. Nara, H.; Momma, T.; Osaka, T., Impedance analysis of the effect of flooding in the cathode catalyst layer of the polymer electrolyte fuel cell. *Electrochimica Acta* **2013,** *113*, 720-729.

81. Pasaogullari, U.; Wang, C. Y., Two-phase modeling and flooding prediction of polymer electrolyte fuel cells. *Journal of the Electrochemical Society* **2005,** *152* (2), A380-A390.
82. Shen, J.; Xu, L.; Chang, H.; Tu, Z.; Chan, S. H., Partial flooding and its effect on the performance of a proton exchange membrane fuel cell. *Energy Conversion and Management* **2020,** *207*.
83. Owejan, J. P.; Trabold, T. A.; Mench, M. M., Oxygen transport resistance correlated to liquid water saturation in the gas diffusion layer of PEM fuel cells. *International Journal of Heat and Mass Transfer* **2014,** *71*, 585-592.
84. Wan, Z. H.; Zhong, Q.; Liu, S. F.; Jin, A. P.; Chen, Y. N.; Tan, J. T.; Pan, M., Determination of oxygen transport resistance in gas diffusion layer for polymer electrolyte fuel cells. *International Journal of Energy Research* **2018,** *42* (6), 2225-2233.
85. Williams, M. V.; Begg, E.; Bonville, L.; Kunz, H. R.; Fenton, J. M., Characterization of Gas Diffusion Layers for PEMFC. *Journal of The Electrochemical Society* **2004,** *151* (8).
86. Bard, A. J.; Faulkner, L. R., *Electrochemical Methods: Fundamentals and Applications*. 2nd ed.; John Wiley & Sons, Inc.: New York, 2001.
87. Bockris, J. O. M.; Reddy, A. K. N.; Gamboa-Aldeco, M. E., *Modern Electrochemistry 2A: Fundamentals of Electrodics*. 2 ed.; Springer US: 2000.
88. Ivanov, Y. B.; Levich, V. G., Study of unstable intermediates of electrode reactions using rotating disc electrode. *Doklady Akademii Nauk SSSR* **1959,** *126*, 1029.
89. Levich, V. G., *Physicochemical hydrodynamics*. Prentice-Hall: Englewood Cliffs, N.J., 1962.
90. Kulikovsky, A. A.; Berg, P., Positioning of a Reference Electrode in a PEM Fuel Cell. *Journal of The Electrochemical Society* **2015,** *162* (8), F843-F848.
91. Srinivasan, S.; Velev, O. A.; Parthasarathy, A.; Manko, D. J.; Appleby, A. J., High-Energy Efficiency and High-Power Density Proton-Exchange Membrane Fuel-Cells - Electrode-Kinetics and Mass-Transport. *Journal of Power Sources* **1991,** *36* (3), 299-320.
92. Parthasarathy, A.; Dave, B.; Srinivasan, S.; Appleby, A. J.; Martin, C. R., The Platinum Microelectrode Nafion Interface - an Electrochemical Impedance Spectroscopic Analysis of Oxygen Reduction Kinetics and Nafion Characteristics. *Journal of the Electrochemical Society* **1992,** *139* (6), 1634-1641.
93. Forster, R. J., Microelectrodes: new dimensions in electrochemistry. *Chem Soc Rev* **1994,** *23* (4), 289-297.
94. Nitopi, S.; Bertheussen, E.; Scott, S. B.; Liu, X.; Engstfeld, A. K.; Horch, S.; Seger, B.; Stephens, I. E. L.; Chan, K.; Hahn, C.; Norskov, J. K.; Jaramillo, T. F.; Chorkendorff, I., Progress and Perspectives of Electrochemical CO(2) Reduction on Copper in Aqueous Electrolyte. *Chem Rev* **2019,** *119* (12), 7610-7672.
95. Steimecke, M.; Seiffarth, G.; Bron, M., In Situ Characterization of Ni and Ni/Fe Thin Film Electrodes for Oxygen Evolution in Alkaline Media by a Raman-Coupled Scanning Electrochemical Microscope Setup. *Anal Chem* **2017,** *89* (20), 10679-10686.
96. Polcari, D.; Dauphin-Ducharme, P.; Mauzeroll, J., Scanning Electrochemical Microscopy: A Comprehensive Review of Experimental Parameters from 1989 to 2015. *Chem Rev* **2016,** *116* (22), 13234-13278.
97. Liu, W.; Zuckerbrod, D., In Situ Detection of Hydrogen Peroxide in PEM Fuel Cells. *Journal of The Electrochemical Society* **2005,** *152* (6).

98. Qiao, Y.; Qiao, Y.; Zou, L.; Ma, C.; Liu, J., Real-time monitoring of phenazines excretion in Pseudomonas aeruginosa microbial fuel cell anode using cavity microelectrodes. *Bioresour Technol* **2015,** *198*, 1-6.
99. Chlistunoff, J., Oxygen permeability of cast ionomer films from chronoamperometry on microelectrodes. *Journal of Power Sources* **2014,** *245*, 203-207.
100. Uribe, F. A.; Springer, T. E.; Gotesfeld, S., A Microelectrode Study of Oxygen Reduction at the Platinum/Recast-Nafion Film Interface. *Journal of The Electrochemical Society* **1992,** *139* (3), 765.
101. Yim, S.-D.; Chung, H. T.; Chlistunoff, J.; Kim, D.-S.; Fujimoto, C.; Yang, T.-H.; Kim, Y. S., A Microelectrode Study of Interfacial Reactions at the Platinum-Alkaline Polymer Interface. *Journal of The Electrochemical Society* **2015,** *162* (6), F499-F506.
102. Basura, V. I.; Beattie, P. D.; Holdcroft, S., Solid-state electrochemical oxygen reduction at Pt | Nafion® 117 and Pt | BAM3G™ 407 interfaces. *Journal of Electroanalytical Chemistry* **1998,** *458* (1-2), 1-5.
103. Petrovick, J. G.; Kushner, D. I.; Tesfaye, M.; Danilovic, N.; Radke, C. J.; Weber, A. Z., Mass-Transport Resistances of Acid and Alkaline Ionomer Layers: A Microelectrode Study Part 1 - Microelectrode Development. *ECS Transactions* **2019,** *92* (8), 77-85.
104. Trasatti, S.; Petrii, O. A., Real Surface-Area Measurements in Electrochemistry. *Journal of Electroanalytical Chemistry* **1992,** *327* (1-2), 353-376.
105. Jiang, J.; Kucernak, A., Investigations of fuel cell reactions at the composite microelectrode|solid polymer electrolyte interface. I. Hydrogen oxidation at the nanostructured Pt|Nafion® membrane interface. *Journal of Electroanalytical Chemistry* **2004,** *567* (1), 123-137.
106. Basura, V. I.; Chuy, C.; Beattie, P. D.; Holdcroft, S., Effect of equivalent weight on electrochemical mass transport properties of oxygen in proton exchange membranes based on sulfonated a,b,b-trifluorostyrene (BAM ®) and sulfonated styrene-(ethylene-butylene)-styrene triblock (DAIS-analytical) copolymers. *Journal of Electroanalytical Chemistry* **2001,** *501*, 77-88.
107. Büchi, F. N.; Wakizoe, M.; Srinivasan, S., Microelectrode Investigation of Oxygen Permeation in Perfluorinated Proton Exchange Membranes with Different Equivalent Weights. *Journal of The Electrochemical Society* **1996,** *143* (3), 927.
108. Novitski, D.; Kosakian, A.; Weissbach, T.; Secanell, M.; Holdcroft, S., Electrochemical Reduction of Dissolved Oxygen in Alkaline, Solid Polymer Electrolyte Films. *J Am Chem Soc* **2016,** *138* (47), 15465-15472.
109. Zhang, S.; Zhang, J.; Zhu, Z.; Liu, P.; Cao, F.; Chen, J.; He, Q.; Dou, M.; Nan, S.; Lu, S., Unusual influence of binder composition and phosphoric acid leaching on oxygen mass transport in catalyst layers of high-temperature proton exchange membrane fuel cells. *Journal of Power Sources* **2020,** *473*.
110. Winlove, C. P.; Parker, K. H.; Oxenham, R. K. C., The Measurement of Oxygen Diffusivity and Concentration by Chronoamperometry Using Microelectrodes. *Journal of Electroanalytical Chemistry* **1984,** *170* (1-2), 293-304.
111. Lawson, D. R.; Whiteley, L. D.; Martin, C. R.; Szentirmay, M. N.; Song, J. I., Oxygen Reduction at Nafion Film-Coated Platinum-Electrodes - Transport and Kinetics. *Journal of the Electrochemical Society* **1988,** *135* (9), 2247-2253.
112. Shoup, D.; Szabo, A., Chronoamperometric Current at Finite Disk Electrodes. *Journal of Electroanalytical Chemistry* **1982,** *140* (2), 237-245.

113. Kim, Y. S.; Einsla, B.; Sankir, M.; Harrison, W.; Pivovar, B. S., Structure–property–performance relationships of sulfonated poly(arylene ether sulfone)s as a polymer electrolyte for fuel cell applications. *Polymer* **2006,** *47* (11), 4026-4035.
114. Chlistunoff, J.; Pivovar, B., Effects of Ionomer Morphology on Oxygen Reduction on Pt. *Journal of The Electrochemical Society* **2015,** *162* (8), F890-F900.
115. Peron, J.; Mani, A.; Zhao, X.; Edwards, D.; Adachi, M.; Soboleva, T.; Shi, Z.; Xie, Z.; Navessin, T.; Holdcroft, S., Properties of Nafion® NR-211 membranes for PEMFCs. *Journal of Membrane Science* **2010,** *356* (1-2), 44-51.
116. Bird, R. B.; Stewart, W. E.; Lightfoot, E. N., *Transport Phenomena*. rev. 2nd ed.; John Wiley & Sons, Inc.: New York, 2007.
117. Borup, R.; Meyers, J.; Pivovar, B.; Kim, Y. S.; Mukundan, R.; Garland, N.; Myers, D.; Wilson, M.; Garzon, F.; Wood, D.; Zelenay, P.; More, K.; Stroh, K.; Zawodzinski, T.; Boncella, J.; McGrath, J. E.; Inaba, M.; Miyatake, K.; Hori, M.; Ota, K.; Ogumi, Z.; Miyata, S.; Nishikata, A.; Siroma, Z.; Uchimoto, Y.; Yasuda, K.; Kimijima, K.; Iwashita, N., Scientific aspects of polymer electrolyte fuel cell durability and degradation. *Chem Rev* **2007,** *107* (10), 3904-51.
118. Borup, R. L.; Kusoglu, A.; Neyerlin, K. C.; Mukundan, R.; Ahluwalia, R. K.; Cullen, D. A.; More, K. L.; Weber, A. Z.; Myers, D. J., Recent developments in catalyst-related PEM fuel cell durability. *Current Opinion in Electrochemistry* **2020,** *21*, 192-200.
119. Wood III, D. L.; Chlistunoff, J.; Majewski, J.; Borup, R. L., Nafion Structural Phenomena at Platinum and Carbon Interfaces. *J. Am. Chem. Soc.* **2009,** *131* (50), 18096-18104.
120. White, H. S.; Leddy, J.; Bard, A. J., Polymer Films on Electrodes. 8. Investiagtion of Charge-Transport Mechanisms in Nafion Polymer Electrodes. *J. Am. Chem. Soc.* **1982,** *104* (18), 4811-4817.
121. Zook, L. A.; Leddy, J., Density and solubility of nafion: recast, annealed, and commercial films. *Anal Chem* **1996,** *68* (21), 3793-6.
122. Tesfaye, M.; MacDonald, A. N.; Dudenas, P. J.; Kusoglu, A.; Weber, A. Z., Exploring substrate/ionomer interaction under oxidizing and reducing environments. *Electrochemistry Communications* **2018,** *87*, 86-90.
123. Sethuraman, V. A.; Khan, S.; Jur, J. S.; Haug, A. T.; Weidner, J. W., Measuring Oxygen, Carbon Monoxide and Hydrogen Sulfide Diffusion Coefficient and Solubility in Nafion Membranes. *Electrochimica Acta* **2009,** *54* (27), 6850-6860.
124. Mukaddam, M.; Litwiller, E.; Pinnau, I., Gas Sorption, Diffusion, and Permeation in Nafion. *Macromolecules* **2015,** *49* (1), 280-286.
125. Zhang, Z.; Chattot, R.; Bonorand, L.; Jetsrisuparb, K.; Buchmüller, Y.; Wokaun, A.; Gubler, L., Mass spectrometry to quantify and compare the gas barrier properties of radiation grafted membranes and Nafion®. *Journal of Membrane Science* **2014,** *472*, 55-66.
126. Sakai, T.; Takenaka, H.; Torikai, E., Gas Diffusion in the Dried and Hydrated Nations. *Journal of The Electrochemical Society* **1986,** *133*, 88-92.
127. Petrovick, J. G.; Anderson, G.; Kushner, D. I.; Danilovic, N.; Weber, A. Z., Methods—Using Microelectrodes to Explore Solid Polymer Electrolytes. *Journal of The Electrochemical Society* **2021**.

128. Bond, A. M.; Oldham, K. B.; Zoski, C. G., Theory of Electrochemical Processes at an Inlaid Disc Microelectrode Under Steady-State Conditions. *Journal of Electroanalytical Chemistry* **1988,** *245* (1-2), 71-104.
129. Parthasarathy, A.; Davé, B.; Srinivasan, S.; Appleby, A. J.; Martin, C. R., The Platinum Microelectrode/Nafion Interface: An Electrochemical Impedance Spectroscopic Analysis of Oxygen Reduction Kinetics and Nafion Characteristics. *Journal of The Electrochemical Society* **1992,** *139* (6), 1634.
130. Aoki, K.; Osteryoung, J., Diffusion-Controlled Current at the Stationary Finite Disk Electrode - Theory. *Journal of Electroanalytical Chemistry* **1981,** *122* (May), 19-35.
131. Aoki, K.; Osteryoung, J., Formulation of the Diffusion-Controlled Current at Very Small Stationary Disk Electrodes. *Journal of Electroanalytical Chemistry* **1984,** *160* (1-2), 335-339.
132. Basha, C. A.; Rajendran, L., Theories of Ultramicrodisc Electrodes: Review Article. *Int. J. Electrochem. Sci* **2006,** *1*, 268-282.
133. Evans, C. M.; Singh, M. R.; Lynd, N. A.; Segalman, R. A., Improving the Gas Barrier Properties of Nafion via Thermal Annealing: Evidence for Diffusion through Hydrophilic Channels and Matrix. *Macromolecules* **2015,** *48* (10), 3303-3309.
134. Crothers, A. R.; Radke, C. J.; Weber, A. Z., Impact of Nano- and Mesoscales on Macroscopic Cation Conductivity in Perfluorinated-Sulfonic-Acid Membranes. *The Journal of Physical Chemistry C* **2017,** *121* (51), 28262-28274.
135. Yasuda, H.; Lamaze, C. E.; Peterlin, A., Diffusive and Hydraulic Permeabilities of Water in Water-Swollen Polymer Membranes. *Journal of Polymer Science* **1971,** *9*, 1117-1131.
136. Currie, J. A., Gaseous diffusion in porous media. Part 2.-Dry granular materials. *Br. J. Appl. Phys* **1960,** *11* (8), 318.
137. Bergman, T. L.; Lavine, A. S.; Incropera, F. P.; Dewitt, D. P., *Fundamentals of Heat and Mass Transfer*. Seventh ed.; John Wiley & Sons, Inc.: Hoboken, NJ, 2011.
138. Sander, R., Compilation of Henry's law constants (version 4.0) for water as solvent. *Atmospheric Chemistry and Physics* **2015,** *15* (8), 4399-4981.
139. Beattie, P. D.; Basura, V. I.; Holdcroft, S., Temperature and pressure dependence of O_2 reduction at Pt|Nafion® 117 and Pt|BAM® 407 interfaces. *Journal of Electroanalytical Chemistry* **1999,** *468*, 180-192.
140. Parthasarathy, A.; Srinivasan, S.; Appleby, A. J.; Martin, C. R., Temperature-Dependence of the Electrode-Kinetics of Oxygen Reduction at the Platinum Nafion(R) Interface - a Microelectrode Investigation. *Journal of the Electrochemical Society* **1992,** *139* (9), 2530-2537.
141. Stewart, S. M.; Spernjak, D.; Borup, R.; Datye, A.; Garzon, F., Cerium Migration through Hydrogen Fuel Cells during Accelerated Stress Testing. *ECS Electrochemistry Letters* **2014,** *3* (4), F19-F22.
142. Fornaciari, J. C.; Gerhardt, M. R.; Zhou, J.; Regmi, Y. N.; Danilovic, N.; Bell, A. T.; Weber, A. Z., The Role of Water in Vapor-fed Proton-Exchange-Membrane Electrolysis. *Journal of The Electrochemical Society* **2020,** *167* (10).
143. Zhang, K.; Liang, X.; Wang, L.; Sun, K.; Wang, Y.; Xie, Z.; Wu, Q.; Bai, X.; Hamdy, M. S.; Chen, H.; Zou, X., Status and perspectives of key materials for PEM electrolyzer. *Nano Research Energy* **2022,** *1*.
144. Merle, G.; Wessling, M.; Nijmeijer, K., Anion exchange membranes for alkaline fuel cells: A review. *Journal of Membrane Science* **2011,** *377* (1-2), 1-35.

145. Henkensmeier, D.; Najibah, M.; Harms, C.; Žitka, J.; Hnát, J.; Bouzek, K., Overview: State-of-the Art Commercial Membranes for Anion Exchange Membrane Water Electrolysis. *Journal of Electrochemical Energy Conversion and Storage* **2021,** *18* (2).
146. Salvatore, D. A.; Gabardo, C. M.; Reyes, A.; O'Brien, C. P.; Holdcroft, S.; Pintauro, P.; Bahar, B.; Hickner, M.; Bae, C.; Sinton, D.; Sargent, E. H.; Berlinguette, C. P., Designing anion exchange membranes for CO2 electrolysers. *Nature Energy* **2021,** *6* (4), 339-348.
147. Bui, J. C.; Lees, E. W.; Pant, L. M.; Zenyuk, I. V.; Bell, A. T.; Weber, A. Z., Continuum Modeling of Porous Electrodes for Electrochemical Synthesis. *Chem Rev* **2022,** *122* (12), 11022-11084.
148. Kulkarni, A.; Giddey, S., Materials issues and recent developments in molten carbonate fuel cells. *Journal of Solid State Electrochemistry* **2012,** *16* (10), 3123-3146.
149. Weber, A. Z.; Borup, R. L.; Darling, R. M.; Das, P. K.; Dursch, T. J.; Gu, W.; Harvey, D.; Kusoglu, A.; Litster, S.; Mench, M. M.; Mukundan, R.; Owejan, J. P.; Pharoah, J. G.; Secanell, M.; Zenyuk, I. V., A Critical Review of Modeling Transport Phenomena in Polymer-Electrolyte Fuel Cells. *Journal of The Electrochemical Society* **2014,** *161* (12), F1254-F1299.
150. Weber, A. Z.; Newman, J., Modeling Transport in Polymer-Electrolyte Fuel Cells. *Chem Rev* **2004,** *104*, 4679-4726.
151. Owejan, J. P.; Gagliardo, J. J.; Sergi, J. M.; Kandlikar, S. G.; Trabold, T. A., Water management studies in PEM fuel cells, Part I: Fuel cell design and in situ water distributions. *International Journal of Hydrogen Energy* **2009,** *34* (8), 3436-3444.
152. Wang, X. R.; Ma, Y.; Gao, J.; Li, T.; Jiang, G. Z.; Sun, Z. Y., Review on water management methods for proton exchange membrane fuel cells. *International Journal of Hydrogen Energy* **2021,** *46* (22), 12206-12229.
153. Luo, X.; Kushner, D. I.; Kusoglu, A., Role of External and Internal Environments in Sustainion Membranes for Water and CO_2 Electrolysis. *Journal of Membrane Science (submitted)* **2023**.
154. Le Canut, J. M.; Abouatallah, R. M.; Harrington, D. A., Detection of membrane drying, fuel cell flooding, and anode catalyst poisoning on PEMFC stacks by electrochemical impedance spectroscopy. *Journal of the Electrochemical Society* **2006,** *153* (5), A857-A864.
155. Cheah, M. J.; Kevrekidis, I. G.; Benziger, J., Effect of interfacial water transport resistance on coupled proton and water transport across Nafion. *J Phys Chem B* **2011,** *115* (34), 10239-50.
156. Ge, S. H.; Yi, B. L.; Ming, P. W., Experimental determination of electro-osmotic drag coefficient in Nafion membrane for fuel cells. *Journal of the Electrochemical Society* **2006,** *153* (8), A1443-A1450.
157. Luo, Z.; Chang, Z.; Zhang, Y.; Liu, Z.; Li, J., Electro-osmotic drag coefficient and proton conductivity in Nafion® membrane for PEMFC. *International Journal of Hydrogen Energy* **2010,** *35* (7), 3120-3124.
158. Ren, X. M.; Gottesfeld, S., Electro-osmotic drag of water in poly(perfluorosulfonic acid) membranes. *Journal of the Electrochemical Society* **2001,** *148* (1), A87-A93.
159. Xu, F.; Leclerc, S.; Stemmelen, D.; Perrin, J.-C.; Retournard, A.; Canet, D., Study of electro-osmotic drag coefficients in Nafion membrane in acid, sodium and potassium forms by electrophoresis NMR. *Journal of Membrane Science* **2017,** *536*, 116-122.

160. Wang, X.; McClure, J. P.; Fedkiw, P. S., Transport properties of proton- and hydroxide-exchange membranes for fuel cells. *Electrochimica Acta* **2012,** *79*, 126-132.
161. Roy, A. L. Electrodes and Membranes for Alkaline Energy Storage and Conversion. University of Tennessee, Knoxville, United States -- Tennessee, 2018.
162. Tricker, A. W.; Lee, J. K.; Shin, J. R.; Danilovic, N.; Weber, A. Z.; Peng, X., Design and operating principles for high-performing anion exchange membrane water electrolyzers. *Journal of Power Sources* **2023,** *567*.
163. Petrovick, J. G.; Radke, C. J.; Weber, A. Z., Gas Mass-Transport Coefficients in Ionomer Membranes Using a Microelectrode. *ACS Meas Sci Au* **2022,** *2* (3), 208-218.
164. Jiang, R.; Mittelsteadt, C. K.; Gittleman, C. S., Through-Plane Proton Transport Resistance of Membrane and Ohmic Resistance Distribution in Fuel Cells. *Journal of The Electrochemical Society* **2009,** *156* (12).
165. Delacourt, C.; Newman, J., Mathematical modeling of a cation-exchange membrane containing two cations. *Journal of the Electrochemical Society* **2008,** *155* (11), B1210-B1217.
166. Chialvo, A. A.; Cummings, P. T.; Simonson, J. M.; Mesmer, R. E., Solvation in high-temperature electrolyte solutions. I. Hydration shell behavior from molecular simulation. *The Journal of Chemical Physics* **1999,** *110* (2), 1064-1074.
167. Nagasaka, M.; Yuzawa, H.; Kosugi, N., Interaction between Water and Alkali Metal Ions and Its Temperature Dependence Revealed by Oxygen K-Edge X-ray Absorption Spectroscopy. *J Phys Chem B* **2017,** *121* (48), 10957-10964.
168. Gierke, T. D.; Munn, G. E.; Wilson, F. C., The morphology in nafion perfluorinated membrane products, as determined by wide- and small-angle x-ray studies. *Journal of Polymer Science: Polymer Physics Edition* **1981,** *19* (11), 1687-1704.
169. Botti, A.; Bruni, F.; Imberti, S.; Ricci, M. A.; Soper, A. K., Solvation of hydroxyl ions in water. *Journal of Chemical Physics* **2003,** *119* (10), 5001-5004.
170. Tuckerman, M.; Laasonen, K.; Sprik, M.; Parrinello, M., Ab initio molecular dynamics simulation of the solvation and transport of hydronium and hydroxyl ions in water. *The Journal of Chemical Physics* **1995,** *103* (1), 150-161.
171. Yadav, S.; Chandra, A., Structural and Dynamical Nature of Hydration Shells of the Carbonate Ion in Water: An Ab Initio Molecular Dynamics Study. *J Phys Chem B* **2018,** *122* (4), 1495-1504.
172. Zeng, Y.; Li, A.; Yan, T., Hydrogen Bond Dynamics in the Solvation Shell on Proton Transfer in Aqueous Solution. *J Phys Chem B* **2020,** *124* (9), 1817-1823.
173. Okada, T.; Ayato, Y.; Yuasa, M.; Sekine, I., The Effect of Impurity Cations on the Transport Characteristics of Perfluorosulfonated Ionomer Membranes. *The Journal of Physical Chemistry B* **1999,** *103* (17), 3315-3322.
174. Okada, T.; Xie, G.; Gorseth, O.; Kjelstrup, S.; Nakamura, N.; Arimura, T., Ion and water transport characteristics of Nafion membranes as electrolytes. *Electrochimica Acta* **1998,** *43* (24), 3741-3747.
175. White, J. A.; Schwegler, E.; Galli, G.; Gygi, F., The solvation of Na+in water: First-principles simulations. *The Journal of Chemical Physics* **2000,** *113* (11), 4668-4673.
176. Kreuer, K. D.; Paddison, S. J.; Spohr, E.; Schuster, M., Transport in proton conductors for fuel-cell applications: simulations, elementary reactions, and phenomenology. *Chem Rev* **2004,** *104* (10), 4637-78.

177. Hickner, M. A. Transport and Structure in Fuel Cell Proton Exchange Membranes. Virginia Polytechnic Institute and State University, Blacksburg, Virginia, USA, 2003.
178. Gallagher, K. G.; Pivovar, B. S.; Fuller, T. F., Electro-osmosis and Water Uptake in Polymer Electrolytes in Equilibrium with Water Vapor at Low Temperatures. *Journal of The Electrochemical Society* **2009,** *156* (3).
179. Fuller, T. F. Solid-Polymer-Electrolyte Fuel Cells. Ph.D., University of California, Berkeley, United States -- California, 1992.
180. Crothers, A. R.; Darling, R. M.; Kusoglu, A.; Radke, C. J.; Weber, A. Z., Theory of Multicomponent Phenomena in Cation-Exchange Membranes: Part II. Transport Model and Validation. *Journal of The Electrochemical Society* **2020,** *167* (1).
181. Crothers, A. R.; Kusoglu, A.; Radke, C. J.; Weber, A. Z., Influence of Mesoscale Interactions on Proton, Water, and Electrokinetic Transport in Solvent-Filled Membranes: Theory and Simulation. *Langmuir* **2022,** *38* (34), 10362-10374.
182. Dullien, F. A. L., *Fluid Transport and Pore Structure*. 2nd ed.; Academic Press, Inc: San Diego, CA, 1991.
183. Ghanbarian, B.; Hunt, A. G.; Ewing, R. P.; Sahimi, M., Tortuosity in Porous Media: A Critical Review. *Soil Science Society of America Journal* **2013,** *77* (5), 1461-1477.
184. Weber, A. Z.; Newman, J., Transport in polymer-electrolyte membranes - II. Mathematical model. *Journal of the Electrochemical Society* **2004,** *151* (2), A311-A325.
185. Friedman, S. P., Soil properties influencing apparent electrical conductivity: a review. *Computers and Electronics in Agriculture* **2005,** *46* (1-3), 45-70.
186. Guan, L.; Jiménez, M. E. G.; Walowski, C.; Boushehri, A.; Prausnitz, J. M.; Radke, C. J., Permeability and partition coefficient of aqueous sodium chloride in soft contact lenses. *Journal of Applied Polymer Science* **2011,** *122* (3), 1457-1471.
187. Marino, M. G.; Melchior, J. P.; Wohlfarth, A.; Kreuer, K. D., Hydroxide, halide and water transport in a model anion exchange membrane. *Journal of Membrane Science* **2014,** *464*, 61-71.
188. Mansur, H. S.; Oréfice, R. L.; Mansur, A. A. P., Characterization of poly(vinyl alcohol)/poly(ethylene glycol) hydrogels and PVA-derived hybrids by small-angle X-ray scattering and FTIR spectroscopy. *Polymer* **2004,** *45* (21), 7193-7202.
189. Duan, Q.; Wang, H.; Benziger, J., Transport of liquid water through Nafion membranes. *Journal of Membrane Science* **2012,** *392-393*, 88-94.
190. Gerhardt, M. R.; Pant, L. M.; Weber, A. Z., Along-the-Channel Impacts of Water Management and Carbon-Dioxide Contamination in Hydroxide-Exchange-Membrane Fuel Cells: A Modeling Study. *Journal of The Electrochemical Society* **2019,** *166* (7), F3180-F3192.
191. Liu, J.; Kang, Z.; Li, D.; Pak, M.; Alia, S. M.; Fujimoto, C.; Bender, G.; Kim, Y. S.; Weber, A. Z., Elucidating the Role of Hydroxide Electrolyte on Anion-Exchange-Membrane Water Electrolyzer Performance. *Journal of The Electrochemical Society* **2021,** *168* (5).
192. Newman, J.; Thomas-Alyea, K., *Electrochemical Systems*. 3rd ed.; John Wiley & Sons: 2004.
193. Liu, M.; Suo, S.; Wu, J.; Gan, Y.; Ah Hanaor, D.; Chen, C. Q., Tailoring porous media for controllable capillary flow. *J Colloid Interface Sci* **2019,** *539*, 379-387.
194. Rumble, J. R., *CRC Handbook of Chemistry and Physics*. 103rd (Internet Version 2022) ed.; CRC Press/Taylor & Francis: Boca Raton, FL, 103rd edition (Internet Version 2022).

195. Chapman, T. W. The Transport Properties of Concentrated Electrolytic Solutions. Ph.D., University of California, Berkeley, United States -- California, 1967.
196. Hiemenz, P. C.; Rajagopalan, R., *Principles of Colloid and Surface Chemistry*. M. Dekker: New York, 1986.
197. Smith, J. M.; Van Ness, H. C.; Abbott, M. M., *Introduction to Chemical Engineering Thermodynamics*. 7th ed.; McGraw-Hill: New York, NY, 2005.
198. Nightingale, E. R., Phenomenological Theory of Ion Solvation - Effective Radii of Hydrated Ions. *J Phys Chem-Us* **1959,** *63* (9), 1381-1387.
199. More, K. L.; Borup, R. L.; Reeves, K. S., Identifying Contributing Degradation Phenomena in PEM Fuel Cell Membrane Electrode Assemblies Via Electron Microscopy. *ECS Transactions* **2006,** *3* (1), 717-733.
200. Thiele, S.; Zengerle, R.; Ziegler, C., Nano-morphology of a polymer electrolyte fuel cell catalyst layer—imaging, reconstruction and analysis. *Nano Research* **2011,** *4* (9), 849-860.
201. Berlinger, S. A.; Chowdhury, A.; Van Cleve, T.; He, A.; Dagan, N.; Neyerlin, K. C.; McCloskey, B. D.; Radke, C. J.; Weber, A. Z., Impact of Platinum Primary Particle Loading on Fuel Cell Performance: Insights from Catalyst/Ionomer Ink Interactions. *ACS Appl Mater Interfaces* **2022,** *14* (32), 36731-36740.
202. Huang, J.; Li, Z.; Zhang, J., Review of characterization and modeling of polymer electrolyte fuel cell catalyst layer: The blessing and curse of ionomer. *Frontiers in Energy* **2017,** *11* (3), 334-364.
203. Suter, T. A. M.; Smith, K.; Hack, J.; Rasha, L.; Rana, Z.; Angel, G. M. A.; Shearing, P. R.; Miller, T. S.; Brett, D. J. L., Engineering Catalyst Layers for Next-Generation Polymer Electrolyte Fuel Cells: A Review of Design, Materials, and Methods. *Advanced Energy Materials* **2021,** *11* (37).
204. Neyerlin, K. C.; Gu, W. B.; Jorne, J.; Gasteiger, H. A., Study of the exchange current density for the hydrogen oxidation and evolution reactions. *Journal of the Electrochemical Society* **2007,** *154* (7), B631-B635.
205. Sheng, W. C.; Gasteiger, H. A.; Shao-Horn, Y., Hydrogen Oxidation and Evolution Reaction Kinetics on Platinum: Acid vs Alkaline Electrolytes. *Journal of the Electrochemical Society* **2010,** *157* (11), B1529-B1536.
206. Chen, K. S.; Hickner, M. A.; Noble, D. R., Simplified models for predicting the onset of liquid water droplet instability at the gas diffusion layer/gas flow channel interface. *International Journal of Energy Research* **2005,** *29* (12), 1113-1132.
207. Chen, L.; He, Y.-L.; Tao, W.-Q., Effects of surface microstructures of gas diffusion layer on water droplet dynamic behaviors in a micro gas channel of proton exchange membrane fuel cells. *International Journal of Heat and Mass Transfer* **2013,** *60*, 252-262.
208. Das, P. K.; Grippin, A.; Kwong, A.; Weber, A. Z., Liquid-Water-Droplet Adhesion-Force Measurements on Fresh and Aged Fuel-Cell Gas-Diffusion Layers. *Journal of The Electrochemical Society* **2012,** *159* (5), B489-B496.
209. Obeisun, O. A.; Finegan, D. P.; Engebretsen, E.; Robinson, J. B.; Taiwo, O. O.; Hinds, G.; Shearing, P. R.; Brett, D. J. L., Ex-situ characterisation of water droplet dynamics on the surface of a fuel cell gas diffusion layer through wettability analysis and thermal characterisation. *International Journal of Hydrogen Energy* **2017,** *42* (7), 4404-4414.

210. Patel, V.; Battrell, L.; Anderson, R.; Zhu, N.; Zhang, L., Investigating effect of different gas diffusion layers on water droplet characteristics for proton exchange membrane (PEM) fuel cells. *International Journal of Hydrogen Energy* **2019,** *44* (33), 18340-18350.
211. Mularczyk, A.; Lin, Q.; Blunt, M. J.; Lamibrac, A.; Marone, F.; Schmidt, T. J.; Büchi, F. N.; Eller, J., Droplet and Percolation Network Interactions in a Fuel Cell Gas Diffusion Layer. *Journal of The Electrochemical Society* **2020,** *167* (8).
212. O'Hayre, R.; Cha, S.-W.; Colella, W. G.; Prinz, F. B., Chapter 6: Fuel Cell Modeling. In *Fuel Cell Fundamentals*, John Wiley & Sons: Hoboken, New Jersey, 2016; pp 203-236.
213. Vielstich, W.; Lamm, A.; Gasteiger, H. A., *Handbook of Fuel Cells: Fundamentals, Technology, and Applications*. John Wiley & Sons: Chichester, England, 2003; Vol. 1.
214. Darling, R. M., A Hierarchical Model for Oxygen Transport in Agglomerates in the Cathode Catalyst Layer of a Polymer-Electrolyte Fuel Cell. *Journal of The Electrochemical Society* **2018,** *165* (9), F571-F580.
215. Zhang, F.-Y.; Spernjak, D.; Prasad, A. K.; Advani, S. G., In Situ Characterization of the Catalyst Layer in a Polymer Electrolyte Membrane Fuel Cell. *Journal of The Electrochemical Society* **2007,** *154*, B1152.
216. Xu, Z.; Zhang, L.; Wilke, K.; Wang, E. N., Multiscale Dynamic Growth and Energy Transport of Droplets during Condensation. *Langmuir* **2018,** *34* (30), 9085-9095.
217. Nouri-Khorasani, A.; Tabu Ojong, E.; Smolinka, T.; Wilkinson, D. P., Model of oxygen bubbles and performance impact in the porous transport layer of PEM water electrolysis cells. *International Journal of Hydrogen Energy* **2017,** *42* (48), 28665-28680.
218. Angulo, A.; van der Linde, P.; Gardeniers, H.; Modestino, M.; Fernández Rivas, D., Influence of Bubbles on the Energy Conversion Efficiency of Electrochemical Reactors. *Joule* **2020,** *4* (3), 555-579.
219. Peeters, P.; Pieterse, G.; van Dongen, M. E. H., Multi-component droplet growth. II. A theoretical model. *Phys Fluids* **2004,** *16* (7), 2575-2586.
220. Zhao, Z.; Poulikakos, D., Heat transfer and fluid dynamics during the collision of a liquid droplet on a substrate,, I. Modeling. *International Journal of Heat and Mass Transfer* **1996,** *39* (13), 2771-2789.
221. Mohammadi, M.; Shahhosseini, S.; Bayat, M., Direct numerical simulation of water droplet coalescence in the oil. *International Journal of Heat and Fluid Flow* **2012,** *36*, 58-71.
222. Family, F.; Meakin, P., Kinetics of droplet growth processes: Simulations, theory, and experiments. *Phys Rev A Gen Phys* **1989,** *40* (7), 3836-3854.
223. Perera, R. T.; Arcadia, C. E.; Rosenstein, J. K., Probing the nucleation, growth, and evolution of hydrogen nanobubbles at single catalytic sites. *Electrochimica Acta* **2018,** *283*, 1773-1778.
224. Pant, L. M.; Gerhardt, M. R.; Macauley, N.; Mukundan, R.; Borup, R. L.; Weber, A. Z., Along-the-channel modeling and analysis of PEFCs at low stoichiometry: Development of a 1+2D model. *Electrochimica Acta* **2019,** *326*.
225. Goswami, S.; Klaus, S.; Benziger, J., Wetting and absorption of water drops on Nafion films. *Langmuir* **2008,** *24* (16), 8627-33.
226. Cullen, D. A.; Koestner, R.; Kukreja, R. S.; Liu, Z. Y.; Minko, S.; Trotsenko, O.; Tokarev, A.; Guetaz, L.; Meyer, H. M.; Parish, C. M.; More, K. L., Imaging and Microanalysis of Thin Ionomer Layers by Scanning Transmission Electron Microscopy. *Journal of The Electrochemical Society* **2014,** *161* (10), F1111-F1117.

227. Ramaswamy, N.; Gu, W.; Ziegelbauer, J. M.; Kumaraguru, S., Carbon Support Microstructure Impact on High Current Density Transport Resistances in PEMFC Cathode. *Journal of The Electrochemical Society* **2020,** *167* (6).
228. Pärnamäe, R.; Mareev, S.; Nikonenko, V.; Melnikov, S.; Sheldeshov, N.; Zabolotskii, V.; Hamelers, H. V. M.; Tedesco, M., Bipolar membranes: A review on principles, latest developments, and applications. *Journal of Membrane Science* **2021,** *617*.
229. Kusoglu, A.; Dursch, T. J.; Weber, A. Z., Nanostructure/Swelling Relationships of Bulk and Thin-Film PFSA Ionomers. *Advanced Functional Materials* **2016,** *26* (27), 4961-4975.